Three dimensional photonic crystals for optoelectronic applications

David Louis Maxime Poussin

Department of Materials
Imperial College London

Submitted in partial fulfilment of the requirements for the degree of *Doctor of Philosophy*

Declaration of Originality

I declare that the work presented in this PhD thesis is my own, unless explicitly stated and appropriately referenced.

Copyright Declaration

The copyright of this thesis rests with the author. Unless otherwise indicated, its contents are licensed under a Creative Commons Attribution-Non Commercial 4.0 International Licence (CC BY-NC).

Under this licence, you may copy and redistribute the material in any medium or format. You may also create and distribute modified versions of the work. This is on the condition that: you credit the author and do not use it, or any derivative works, for a commercial purpose.

When reusing or sharing this work, ensure you make the licence terms clear to others by naming the licence and linking to the licence text. Where a work has been adapted, you should indicate that the work has been changed and describe those changes.

Please seek permission from the copyright holder for uses of this work that are not included in this licence or permitted under UK Copyright Law.

Abstract

Inverse opals are nano-structures with three dimensional periodicity, which confers them a control on the light passing through them. The light can be forbidden to exist within the structure, giving a physical effect known as optical band-gap, which is the analogue of the electronic band-gap observed in semiconductors materials. For these reasons, these structures are part of a larger class of materials, called photonic crystals. In addition of the light control, inverse-opal structures offer a large surface area in an organised way, which makes them advantageous in specialised devices. Due to the complex fabrication process needed to produce high-quality inverse opal, only a limited amount of work has been done on their integration in optoelectronic devices. To complete this gap, this thesis aims to produce inverse opals made from new materials, for use in optoelectronic devices, such as solar cells and light emitting diodes.

This thesis is divided in 5 results chapters, as described hereafter. Chapter 3 details the fabrication procedures developed to obtain reproducible inverse opals on a large scale. The structures are made by using an opal template made of polystyrene nanoparticles, which shows excellent optical properties, which is then infiltrated with precursors. In chapter 4, a new concept for solar cell architecture is proposed, with the use of a fluorine tin oxide inverse opal as a three dimensional electrode, to optimise the charge collection, and lead halide perovskite as an absorbing layer. The infiltration of lead halide perovskite inside the inverse opal is very challenging due to the complex crystallisation of this material. A partial infiltration can be obtained with an optimised deposition method, and working solar cells have been made with this architecture.

Work to prepare large-scale crack-free inverse opal made of fluorine tin oxide is described chapter 5. Due to the high reactivity of the precursors used to make this material, a different approach of infiltration is made, with the synthesis and use of nano-crystals of this material. The structures made in this section show a great decrease in the amount of cracks, as well as very good periodicity. In chapter 6, a novel architecture for a light-emitting diode is proposed, which makes use of the optical properties of the inverse opal to sharpen the emission spectrum. A method to homogeneously coat the inverse opal by sol-gel has been optimised, and a standard OLED has been made, to confirm the choice of materials. The structures are simulated with a finite-difference-time-domain (FDTD) code, in order to study their optical properties. To finish, the work in chapter 7 reports the creation of very large scale structures of 15x15cm^2, which show good optical effects.

Dedication

To my parents, Franck & Solange, and to my love, Anna.

List of Figures

1.1 *Left :* Precious opal gemstone showing light opalescence. *Right:* Scanning electron microscopy of the surface of an Australian opal. Reproduced with permission from [1] and [2] respectively. 2

1.2 Section of a one-dimensional photonic crystal schematic. 4

1.3 Two-dimensional photonic crystal illustration (*left*), and unit-cell of the crystal previously represented (*right*). 5

1.4 Schematics of basic optical circuit, based on two dimension photonic crystal. A waveguide (*left*) and a spectral filter (*right*). 6

1.5 Three-dimensional photonic crystal schematic. 7

1.6 Schematic of light interaction within an opal. 9

1.7 *Left :* Photonic band diagram for a Gallium Arsenide (GaAs) bulk, with a dielectric constant $\epsilon = 13$, and *Right :* for a periodic multilayer structure alternating GaAs and air layer. Reproduced with permission from [3] 14

1.8 Representation of the First Brillouin Zone and the Irreducible Brillouin zone associated with a face centred cubic lattice. Reproduced with permission from [4] 16

1.9 Calculated optical band diagram for an inverse opal, in a fcc organisation, consisting of air spheres ($\epsilon = 1$) in a material with a high dielectric constant ($\epsilon = 13$). The yellow band indicates a complete photonic band gap, while the salmon-pink one indicates a partial band gap. Reproduced with permission from [3] 17

1.10 Photonic band diagram associated with a one-dimensional photonic crystal. The yellow band represents the photonic band gap, and the red segments indicate the slope of the curve for the considered frequencies. 18

1.11 *Left :* Hexagonal organisation of mono-dispersed nanoparticles with a size distribution of 3.8%. *Right:* Random organisation of non mono-dispersed nanoparticles, with a size distribution of 14.2%. Reproduced with permission from [5] 20

1.12 Attraction and repulsion forces between two negatively charged particles in solution. An electrostatic double layer is represented on both particles, by the addition of positive charges. 22

1.13 Potential between two charged nanoparticles, depending on the distance between them. The potential from the electrostatic forces is in blue, the one from the Van der Waals forces in red, and the sum of both in green. Important features such as primary and secondary minimum, as well as the energy barrier, are represented. 23

1.14 *Left :* Nanoparticles driven toward the meniscus due to convection forces. *Right :*Attraction forces between the nanoparticles due to the surface tension of water. 24

1.15 *Left :* Shape of the surface of water when a thin layer of glass is added at the end of the meniscus. *Right :* Schematic representation of the absence of a nanoparticle layer on an area, due to the pinching of the water film. Reproduced with permission from [6]. 25

1.16 *Left :* Face-centred-cubic structure *Right :* Hexagonal-compact structure. The size of the particles is arbitrary, and is set for an optimal comprehension of the structure. 25

1.17 *Left :* Unit cell of a hexagonal-compact structure, with spheres contacting each other. *Right :* Many cells in a hc structure The colours are only here for a better understanding of the planar organisation. . 26

1.18 *Left :* Unit cell of a face-centred-cubic structure, with spheres contacting each other. *Right :* Many cells with a fcc structure, with a [111] plan on the top. The colours are only here for a better understanding of the planar organisation. 26

1.19 *Left :* Large area of a colloid crystal seen from top, showing a [111] plan of a fcc structure. *Right :* Close view of a colloid crystal seen from the side, exhibiting both [111] and [100] plans. Reproduced with permission from [7] 27

1.20 Best research solar cells efficiency chart, for all technologies. Updated on September 2019, by the National Renewable Energy Laboratory (NREL). 31

1.21 (a) Schematic cross section of a solar cell, from bottom to top : the transparent conductive electrode in grey, the electron transport layer in blue, the active layer in red, the hole transport layer in green and the top electrode in yellow. The charge separation process due to absorbed light is represented. (b) Band diagram corresponding to the left structure, with the same colour code for the three semiconducting layers. The two electrodes are represented with a single line, indicating their Fermi-level value. 33

1.22 Inverse opal obtained in a one-step spin coating method. Left: Top view. Right, cross section. Reproduced with permission from [8]. . . 36

1.23 (a) Schematic cross section of a light-emitting diode, with from bottom to top : the transparent conductive electrode in grey, the electron transport layer in blue, the active layer in red, the hole transport layer in green and the top electrode in yellow. (b) Band diagram corresponding to the left structure, with the same colour code for the three semiconducting layers. The two electrodes are represented with a single line, indicating their Fermi-level value. 38

1.24 *Top:* Spontaneous emission, by random release of the system energy. *Bottom :* Stimulated emission, due to the interaction of a photon with an excited system. After the emission, the two photons are totally undistinguishable. 40

1.25 Double simultaneous lasing emission from a die-infiltrated inverse opal. The incident laser is the blue one, on the right of the picture, and the excited ones are the red and green on the left. Reproduced with permission from [9] 42

2.1 Schematic of interactions between the electron beam and the sample . 47

2.2 Electron diffraction on TEM on a single crystal (a), a polycrystal (b) and an amorphous sample (c). Reproduced with permission from [10]. 50

2.3 Schematic of Uv-Vis with rotating stage 51

2.4 Dynamic Light Scattering 52

2.5 Schematic of the spatial distribution of charges around a charged nanoparticle in solution. The potential corresponding to different layers of charges is represented in the bottom of the picture. 53

2.6 Formation of a film by spin coating. 1: Solution deposition. 2: Substrate spinning. 3: Evaporation. 4: Film formation. 57

2.7 Schematic ALD different stages for metal-oxide deposition 58

2.8 Precursors used in the Atomic Layer Deposition machine 58

2.9 Schematic of the vacuum chamber used for metal evaporation. 59

2.10 *a)* Path difference between two coherent beams, interacting with the first and the second layer of a crystal. *b)* X-ray gun and detector in a parallel position, to only take into account the crystal plane parallel to the surface of the sample. Reproduced with permission from [11] and [12] respectively. 60

2.11 Schematic of a differential scanning calorimetry measurement cell. Reproduced with permission from [13]. 61

2.12 *Left :* First Brillouin Zone and Irreducible Brillouin Zone (in blue) for the k-space associated with a 2D square lattice. *Right :* Irreducible Brillouin Zone, and discrete choice of specific k-values amongst the edges, represented by black dots. The Greek letters used Γ , M and X are typically used as names for the corners of the IBZ. 63

3.1 *a)* Dilution of a stock solution of PS-nanoparticles in DI water. *b)* Vertical deposition of a substrate inside the diluted suspension of PS-nanoparticles. *c)* Upon evaporation of the solution, formation of a film on the substrate due to the deposition of the nanoparticles. *d)* Full film on the surface of the substrate at the end of the evaporation. 68

3.2 Stability of temperature and relative humidity inside the humidity oven, for a *a)* low level of humidity of 20 % RH and a temperature of 65 °C for 48 hours, and *b)* a high level of humidity of 90 % RH and a temperature of 65 °C. 69

3.3 Distinct regions on a sample made with evaporation induced self assembly. Deposition from right to left. Reproduced with permission from [14]. 69

3.4 *a)* Photography of an opal presenting regular striped defects. *b)* SEM top view of a striped samples, showing the absence of material between the stripes, and *c)* cross section SEM of a stripe. 71

3.5 *a):* SEM top and *b):* magnified top view of an opal made of 250nm polystyrene nanoparticles, made by evaporation induced self assembly, with a temperature of 70°C and a relative humidity of 60 %. Observation under standard *c:* and magnified view *d:* of the same sample, with a 45° tilt. 71

3.6 Far *a)* and close *b)* top view SEM pictures, and cross section at 45° *c)* and 90° *d)* of a 250nm opal, made by evaporation-induced self assembly, as $60°C$, and 20% RH. The glass sample are treated with piranha solution prior to the deposition. 72

3.7 Zeta potential measurement of two batches of 211nm polystyrene nanoparticles. 74

3.8 *a)* COOH terminated nanoparticles, deposited under basic conditions ($50\mu l$ of 0.1M NaOh in 5ml of 0.1% suspension), exhibits a highly structured pattern. *b)* Magnified view of the opal, showing the regular triangular terraces due to the highly negative zeta potential. 75

3.9 211nm PS nanoparticles evaporated in a 24mm diameter vial (*left*) and a 19mm diameter vial (*right*). Both samples are evaporated in the same conditions, at a temperature of 60 °C, and a relative humidity of 20%. 77

3.10 Cross section SEM of an opal made in a *a)* PTFE vial and a *b)* glass vial. The deposition conditions are identical for both samples. 78

3.11 *a)* Picture of 250nm opal, showing a green colour due to its optical band-gap. *b)* Transmittance and reflectance UV-VIS measurements, in direct mode and with integrating sphere, of the previously shown opal. The optical band-gap corresponds to where the intensity dips in transmission, and with peaks in reflection. 80

3.12 UV-VIS reflectance spectra acquired at 8 different incident angles, for opals composed of polystyrene nanospheres of (a) 250 nm and (b) 488 nm in diameter. Maximum peak reflectance wavelength (red triangles) and fitting with the modified Bragg law (blue curve) for the 250nm (c) and the 488nm (d) opals. 82

3.13 High-order peak reflectance wavelength and fitting with the modified Bragg law for the 250-nm (a) and the 488-nm (b) opals. 84

3.14 *a)* Low and *b)* high magnification of a TiO_2 inverse opal, made by infiltration of a 250nm opals by a 0.2M solution of $TiBALDH$ in methanol, according to the procedure described section 3.4.1. TiO_2 inverse opal presenting *c)*, an insufficient amount of infiltrated precursors, and *d)*, an overlayer. All the sample are calcined at $500°C$ for 4 hours, with a temperature ramp of $1°C/min$. 88

3.15 Established process for the infiltration of solution inside an opal, with spin coating. 89

3.16 Low *a)* and high magnification *b)* of a silicon dioxide inverse opal, and a titanium dioxide inverse opal (c and d) after calcination, made with a one step method with 340nm PS nanoparticles. TEOS and TiBALDH are used as silicon and titanium precursors respectively. . 91

3.17 TGA and DSC measurements of polystyrene of 300nm nanoparticles in air. Maximum temperature of 800 °C, with a ramp rate of 10 K/min. 92

3.18 Opal with silicon precursor infiltrated, calcined at $20°C/min$, until 600 °C. *Left :* Top view. *Right :* Cross section. 92

4.1 *a)* FTO inverse opal, on a FTO substrate. *b)* Deposition of a continuous and uniform film of titanium dioxide inside the inverse opal, by ALD. *c)* Infiltration of the TiO_2-coated inverse opal by a pervoskite material, with formation of an over-layer on top of the structure. *d)* Deposition of the hole transport layer and of the second electrode, on top of the structure. 96

4.2 *a)* Top view of a solar cell with six evaporated contacts on top and a scratched part on the bottom, to reveal the underneath FTO layer. A measurement device is connected to the bottom FTO and to one of the upper electrode. *b)* Solar cell on an un-etched FTO. The measurement probe can pierce the layers and contact the bottom FTO, leading to a short circuit. *c)* Solar cell on etched FTO. Even if the measurement probe pierces trough the layers, it does not contact the FTO, and the solar cell can be measured. 97

4.3 Schematic of the FTO patterning method. *i)* The bare FTO substrate (*I)*) is covered by kapton tape, to protect the areas which should not be etched (*II)*). Zinc powder is deposited on the areas where etching is wanted (*III)*), and concentrated HCl (37%), is dropped on the sample(*IV)*). To finish, the sample is washed with DI water, and the kapton tape is removed(*V)*). 98

4.4 TGA and DSC measurements of dried tin tetrachloride pentahydrate and ammonium fluoride in a 10:1 ratio. Maximum temperature of 600 °C, with a ramp rate of 10 K/min. 99

4.5 Low (*a*) and high (*b*) magnification SEM of calcined FTO inverse opals, made from 250nm polystyrene nanoparticles. 99

4.6 Comparison of XRD peaks for a commercial FTO thin film (dark blue), and FTO inverse opal, made on glass substrate (light blue). . . 100

4.7 SEM cross section of a crack free SiO_2 inverse opal, infiltrated with 200 cycles of ZnO by ALD. Analysed by secondary electrons (*a* and *c*) and by backscattered electrons (*b* and *d*), at low (*a* and *b*) and high (*c* and *d*) magnification. The secondary and backscattered electrons data are acquired at the same time, on the same regions. 102

4.8 Cross section of a crack free SiO_2 inverse opal, infiltrated with *a)* 63 and *b)* 27 cycles of ZnO by ALD, analysed with backscattered electrons microscopy. Deposition made at $200°C$, with 3 seconds hold. 102

4.9 *a)* TEM analysis of a TiO_2-coated SnO_2 inverse opal. *b)* High magnification on a TiO_2-coated region. Two interference fringe sizes are indicated. *c)* Large-area electron diffraction of the coated inverse opal, and *d)* radial profile of the diffraction pattern. 104

4.10 STEM/EDX chemical maps for a FTO inverse opal coated with 10nm titanium dioxide by atomic layer deposition. Clockwise, from the top left right : Titanium, oxygen, tin and the superposition of the mapped elements with the dark field image. 105

4.11 Schematic of the projection effects appearing for a coated inverse opal. 106

4.12 Cross section *a)* and top view *b)* of a FTO inverse opal infiltrated with a 1.5M solution of $CH_3NH_3PbI_3$ in DMF/DMSO, spin coated at 4000rpm for 30 seconds, with diethyl ether anti-solvent dripping. Cross section *c)* and top view *d)* of a FTO inverse opal infiltrated with a 1M solution $CH_3NH_3PbI_3$, deposited in the same conditions. Both inverse opals are made by infiltration of a 250nm polystyrene nanoparticles opal template. 109

4.13 Cross section *a)* and top view *b)* of a SiO_2 inverse opal infiltrated with a 1.5M solution of $CH_3NH_3PbI_3$ in DMF/DMSO, spin coated at 2000rpm for 30 seconds. Inverse opal made by a one-step method. 111

4.14 *a)* Top view of a FTO inverse opal infiltrated with a 1.5M solution of $CH_3NH_3PbI_3$ in DMF/DMSO. The sample is spin coated for one second, and is then rested for one minute to evaporate, and increase the precursor concentration. This is followed by a spin coating at 4000rpm for 30 seconds, with anti-solvent diethyl ether dripping at 7 seconds. *b)* Enhanced view of pinholes on top of the film. Cross section of the sample on a defect free part *c)* , and on a cracked part *d)*. 112

4.15 Top *a)* and cross section view *b)* of a FTO inverse opal infiltrated with a 1.2M solution of $CH_3NH_3PbI_3$ in DMF/DMSO spin coated at 4000rpm for 30 seconds, with a 3bar nitrogen pressure applied on the sample during spin coating, for 15 seconds. Inverse opal made with a one step nano-crystal infiltration method. 114

4.16 Top *a)*, cross section *b)* and magnified cross section view *c)* of a FTO inverse opal infiltrated with a 1.2M solution of PbI_2 in DMF/DMSO spin coated at 2000rpm for 30 seconds, annealed at $60°C$ for 10 minutes, followed by an immersion inside a 10mg/ml solution of methyl ammonium in IPA. The immersion is followed by an annealing at $100°C$ for 15 minutes. Inverse opal made with a one step nano-crystals infiltration method. 116

4.17 *a)* SEM cross section of a full solar cell with overlayer, made with the solvent-retard method. *b)* Magnified view of the top of the solar cell with, from bottom to top, the perovskite layer, the PTAA layer in dark, and the gold layer in white. 117

4.18 I-V curve of an FTO inverse opal base solar cell, under 1.5 Sun illumination. The open circuit voltage (V_{oc}) and the short circuit current (J_{sc}) are represented. The blue rectangle represents the behaviour of an ideal cell of the obtained V_{oc} and J_{sc}, and is used to calculate the fill factor. 118

5.1 *a)* Mix of COOH-terminated PS-nanoparticles with a low amount of tin precursors, resulting in *b)* covalent bounds between the nanoparticles after the deposition. *c)* Mix of tin precursors with PS-nanoparticles, which produces *d)* an opal fully infiltrated with precursors. *e)* Mix of FTO-nanocrystals and PS-nanoparticles, resulting in an opal fully infiltrated with FTO-nanocrystals. 122

5.2 Large area (a) and magnified (b) SEM view of an opal made with a 5ml solution of PS-COOH particles (0.1% vol %) with 5μl of a 0.05M $SnCl_4$ solution as a cross-linker. Large area (c) and magnified (d) SEM view of an opal with the same solution as previously, where 5 μl of ethanolamine are added. Cracked structure obtained with stabilised tin cross linker (e), and enhanced view of the particles the the location of the cracks (f) 124

5.3 Magnified SEM view of opal samples made from a 5ml solution of PS-COOH particles (0.1% concentrated) with the addition of *a)*, 7.5μl of a 0.05M $SnCl_4$ and 7.5μl ethanolamine, *b)*, 10μl of a 0.05M $SnCl_4$ and 10μl ethanolamine, *c)*, 12.5μl of a 0.05M $SnCl_4$ and 12.5μl ethanolamine and *d,* 15μl of a 0.05M $SnCl_4$ and 15μl ethanolamine. 125

5.4 Magnified view of opal samples made from a 5ml solution of PS-COOH particles (0.1% concentrated), with 7.5 μl of a 0.05M solution of $SnCl_4$, stabilised by ethanolamine in a 2:1 (a) and a 3:1 ratio (b). 125

5.5 Inverse opal made with 5ml of 0.1% concentrated 200nm PS nanoparticles, with 15.6mg of tin tetrachloride pentahydrate. 1ml of a 2% solution of sodium dodecyl sulfate is added to the solution to prevent the aggregation of the nanoparticles. 127

5.6 Chemical structure of a l-lysine monomer, protonated with bromic acid, in a 1:1 ratio. 128

5.7 Size (*left*) and zeta-potential (*right*) of 200-nm polystyrene nanoparticles coated with poly-l-lysine. 130

5.8 *Left :* One-step deposition of a 5ml suspension of 0.1% concentrated PLL-coated PS nanoparticles (200nm), blended with 15.6mg of tin tetrachloride and 0.165 mg of ammonium fluoride. *Right :* Isolated ordered structure. 130

5.9 Zeta potential of $-NH_2$ terminated nanoparticles in pure DI water (red), and in a mixture of 5ml DI water with 10 µl concentrated hydrochloric acid (black). 132

5.10 Low (*a*) and high (*b*) magnification of a FTO structure formed in a one-step procedure with amine-terminated nanoparticles. Three-dimensional defect on top of the structure (*c*). 132

5.11 Opal formed by evaporation induced self assembly, with amine-terminated nanoparticles (*a*) and the measured diameters distribution (*b*). 133

5.12 TGA/DSC of FTO nano-crystals made by hydrothermal method, centrifuged at 10000 rpm for one hour, at 5°C (*a*). For comparison, the nano-crystals from the same batch are measured without the centrifugation step (*b*). For both sample, a small amount of the suspension is left to dry naturally to obtain a FTO nano-crystal powder, which is measured by TGA/DSC. 135

5.13 XRD of dried FTO nano-crystals. The FTO powder is held on a sample holder with double-sided sticky carbon tape. 136

5.14 TEM (*a*) and HRTEM (*b*) of FTO nano-crystals, deposited on a holey carbon grid. Two different atomic planes are indicated on the HRTEM image. SAED on a large area (*c*), forming concentric rings due to the many different orientations of the measured crystals. (*d*) Radial intensity of the SAED. 137

5.15 DLS intensity (*a*), DLS number (*b*) and zeta potential (*c*)results for a freshly made FTO nano-crystals suspension, stabilised with different amounts of TMAOH. (*a,b,c*) Same measurements, for a one week old FTO nano-crystals suspension, stabilised with the same amount of TMAOH. 138

5.16 Transparency evolution of a 200 ml FTO nano-crystals suspension, after the addition of 500 µl of TMAOH. From left to right : suspension immediately after the addition of the stabiliser, after 8 seconds, 15 seconds and 30 seconds. The stabilised suspension is diluted 50 times from the original suspension, after its purification by centrifugation. . 139

5.17 Order quality of inverse opals made from FTO suspensions with different amounts of TMAOH. The 200ml suspension are stabilised with *a)* 200 µl, *b)* 300 µl, *c)* 500 µl, *d)* 600 µl and *e)* 800 µl of TMAOH. . . 140

5.18 Low (*a*) and high (*b*) magnifications of an inverse opal made with a FTO suspension stabilised with 600 µl of TMAOH. 141

5.19 Cross sections at low and high magnification of a FTO inverse opal made with a FTO suspension stabilised with 200 µl of TMAOH (*a and b*), and with 800 µl of TMAOH (*c and d*) 142

5.20 Large-area SEM views exhibiting the defects created on the inverse opal (top row), and high magnification on a characteristic defect of the structure. The inverse opals are made with a 200ml FTO suspension stabilised with 200μl (*a and f*), 300μl (*b and g*), 500μl (*c and h*), 600μl (*d and i*) and 800μl (*e and j*) of TMAOH. 143

5.21 Opals made with 1.5ml (*a*), 1ml (*b*) and 500μl (*c*) of a 1ml TMAOH FTO suspension, diluted 50 times from the stock solution. The total volume used for the opal evaporation is maintained at 5ml, with a PS concentration of 0.1%. 143

5.22 FTO inverse opals made with 1ml (*a* and *b*) and 500μl (*c* and *d*) of a 1ml TMAOH FTO suspension, diluted 50 times from the stock solution. The total volume used for the opal evaporation is maintained at 5ml, with a PS concentration of 0.1%. 144

5.23 Molecule of citric acid (*a*), and deprotonated citric acid chelating a tin(IV) cation (*b*). Reproduced and adapted with permission from [15] 145

5.24 0.1M solution of tin tetrachloride in methanol, stabilised with citric acid concentrated at 0.25M (*left*) and 0.5M (*right*), let to rest for 48 hours. 146

5.25 Low (*a*) and high magnification (*b*) of a FTO inverse opal made in a one step method, with 211nm PS particles concentrated at 0.1% in 5ml water, with 1ml of FTO suspension stabilised with 800 µl of TMAOH. 10 µl of a solution of 0.1M tetrachloride in methanol and 0.4M citric acid, neutralised at Ph 7 with ammonia, is added to the suspension. 147

5.26 Low (left column) and high magnitude (right column) of a FTO inverse opal made in a one-step method, with 211-nm PS particles concentrated at 0.1% in 5 ml of water, with 1 ml of FTO suspension stabilised with 800 µl of TMAOH. 10 µl (*a and b*), and 40 µl (*c and d*) of a solution of 0.1M tetrachloride in methanol and 0.4M citric acid, neutralised at pH 7 with sodium hydroxide, is added to the suspension. 148

5.27 Schematic of the separation between the high and low zeta potential nanoparticles, in an autoclave placed vertically. 149

5.28 SEM images of a near-defect free FTO inverse opal, obtained by selection of high zeta potential nano-crystals, at *a)* high, *b)* medium and *c)* high magnification. 150

6.1 *Left :* Schematic of a multilayer device inside an inverse opal. *Right :* Magnification of the multilayer structure. 154

6.2 Fabrication process of a multilayer OLED for a standard substrate (*std-a)* to *std-e)*) and for an inverse opal substrate (*io-a)* to *io-e)*). From left to right, for both substrate : *a)* FTO substrate, *b)* deposition of nickel oxide by sol-gel, *c)* deposition of the active material by sol-gel, and deposition of zinc oxide and aluminium-doped zinc oxide, by ALD (*d)* and *e)* respectively). 156

6.3 *a)* Cross-section schematic of a multilayer device, where the electron transport layer and the outside electrode are deposited by ALD. The red circle indicates the area where a short circuit between the two electrodes is possible. *b)* Cross section of the same device as *a)*, but with an etched FTO electrode on the sides, to prevent short circuit. *c)* Top view of the etched FTO on glass a substrate. 157

6.4 Chemical structure of nickel(II) acetate tetra-hydrate. 157

6.5 Chemical structure of 4,4'-Bis(9-carbazolyl)-1,1'-biphenyl (CBP) (left) and of Bis(1-phenylisoquinoline)(acetylacetonate)iridium(III) (Ir(pic)2(acac) (right). Reproduced with permission from Ossila [16]. 158

6.6 *Left :* SEM picture of defect on a CBP/Ir(piq)2(acac) thin film annealed at 95 °C. *Right :*Magnification of picture on *left*, showing the discontinuity of the organic film(in dark), and the exposition of the FTO(in light colour). 159

6.7 *Left :* DSC scan of a CBP/Ir(piq)2(acac) blend in a 20:1 mass ratio. The heating and cooling rate are 10 °C/min. *Right :* XRD on a FTO/NiO(10nm)/CBP-Ir(piq)2(acac)(100nm) device, after annealing at 75 °C (blue curve) and 100 °C (red curve). 160

6.8 DSC of CBP powder, annealing and cooling at 10 °C/min, under nitrogen. 160

6.9 Chemical structure of 9,9'-Diphenyl-9H,9'H-3,3'-bicarbazole (BCzPH). Reproduced with permission from Ossila [16]. 161

6.10 Large (*left*) and close view (*right*) of a spin coated BCzPH/Ir(piq)2(acac) layer (20:1 mass ratio), after annealing at 95 °C. The molecules are dissolved in chloroform, and spin coated at 4000 rpm for 40 seconds, on a FTO/NiO substrate. 162

6.11 *Left :* Cross section of FTO/NiO/(BCzPH/Ir(piq)2(acac))/ZnO/AZO device. The layers are highlighted in different colours : golden, green, red, yellow and grey, for the bottom electrode, hole transport layer, active layer, electron transport layer and top electrode respectively. *Right :* Delamination of the active layer, on both the electron and hole transport layer. 162

6.12 Top (*left*) and 45° inclined view (*right*) of a 0.2M nickel acetate solution spin coated at 4000 rpm on a FTO inverse opal. The sample is calcined at 400 °C for 30 minutes after deposition. 164

6.13 Comparison between spin coating done on a flat substrate (*top row*) and on a three dimensional inverse opal (*bottom row*). Deposition of the solution on the substrate (*a and d*), spin coating and evaporation of the solution (*b and e*) and film formation on the substrate (*c and f*)164

6.14 Calculated required concentration of nickel acetate precursor to coat the inverse opal with a specified thickness of crystalline nickel oxide, for different inverse opal pore sizes. 166

6.15 Calculated required concentration of nickel acetate precursor to coat the inverse opal with a specified thickness of crystalline nickel oxide for an inverse opal with a pore size of 300 nm, corrected with different pore connections sizes. 167

6.16 FTO inverse opal with 488-nm pores, coated by a sandwiched infiltration of a 150mg/ml nickel acetate solution, immediately followed by an annealing at $300°C$. Top (a) and side (b) views of a coated structure without overlayer. (c) Large view of the structure, indicating irregular areas with over-layer (darker areas) and (d) magnification on inverse opals with overlayer. 169

6.17 FTO inverse opal with 488-nm pores, coated by a sandwiched infiltration of a 150 mg/ml nickel acetate solution, let to dry at room temperature for two days, followed by an annealing at $300°C$. (a) Medium and (b) high magnification of the structure after annealing. (c) Side view of the structure, and (d) observation of ball shaped nickel oxide deposition within the inverse opal. 170

6.18 Schematic of the homemade vertical drop deposition method. (a) Vertically placed sample, and solution dropped on top of it. (b) Spreading of the solution inside the structure driven by gravity and capillarity. (c) Formation of an excess of solution at the bottom of the sample, due to the surface tension of the solution. (d) Addition of a substrate directly in contact with the bottom of the sample, preventing the an excess of solution on the inverse opal. 171

6.19 488-nm FTO inverse opal, infiltrated with a 150 mg/ml nickel acetate solution in methanol, by vertical drop method. Top view at low (a) and high (b) magnification of the coated structure after annealing at 300 °C. Cross section of the coated inverse opal (c) and ultra high magnification on one coated pore in cross section (d), showing the rough surface due to the NIO coating. 172

6.20 *Left :* Reflectance Uv-Vis at different angles for a 488-nm FTO inverse opal prior (plain lines), and after (dashed lines) NiO deposition by vertical drop method. *Right :* Maximum peak position for the coated and uncoated structures. 173

6.21 STEM/EDX of a 488-nm FTO inverse opal coated with NiO by vertical drop method. Clock-wise, from the top right picture, Nickel, Oxygen, Tin, and the dark field image with the superposition of the three elements. 174

6.22 Calculated required concentration of CBP to coat the inverse opal to a specified thickness of crystalline CBP, for different inverse opal pore sizes. 175

6.23 Maximum contact model between nanoparticles. Only one layer with seven nanoparticles is represented. *Left :*Plane passing through the centre of the particles. *Middle:* Intermediate plane, showing space between the particles, *Right:* Minimal contact between the particles. The initial spherical form of the nanoparticles is represented, by superposition of colours, and the particles' limits are shown with red lines. 176

6.24 *Left:* Inverse opal schematic, associated with a compact opal model. In grey, the inverse opal and in red, a coated layer. *Right:* Packed opal, with an equilateral triangle linking the centres of the spheres, as well as the triangles' centre, at the point where the 3 spheres contact. R is the radius of the initial nanoparticle, and R_{lim} is the radius of the air sphere inside the inverse opal, in the limiting case where the air spheres contacts are punctual. 177

6.25 Optical band diagram of an inverse opal, made of air (n=1) and a material with refractive index n=1.9, simulated with MPB. The 15 first bands are represented. The partial band-gaps on the ΓL direction are highlighted in blue. 180

6.26 Optical band diagram of an inverse opal made of air (n=1), with a core material with a refractive index n=1.9, coated with a material with refractive index n=2.5, simulated with MPB. The coating's thickness is calculated according to equation 6.8. The first 15 bands are represented. The partial band-gaps on the ΓL direction are highlighted in blue 181

6.27 Optical band diagram of an inverse opal made of air (n=1), with a core material whose refractive index n=2.2, simulated with MPB. The 15 first bands are represented. The partial band-gaps on the ΓL direction are highlighted in blue. 182

6.28 (*a*) Initial step for the inverse-opal model's creation, from bottom to top: a block of glass (blue), a block of FTO representing the initial thin film (light grey) and a second block of FTO representing the inverse opal. (*b*) Addition of air spheres within the second layer of FTO. 184

6.29 (*a*) Hexagonal packing of seven particles, with an orthogonal axis centred on the middle particle. The red dots represents the position of the nanoparticles of the second layer. (*b*) Vertical distance between the centres of the nanoparticles from two different levels. (*c*) Coordinates of the nanoparticles represented in (*a*), depending of their diameter *D*. (*d*) Coordinates of the second layer of nanoparticles, obtained by a translation from the first layer coordinates. 185

6.30 *Left :* Schematic of the as-developed inverse opal model. Periodic Bloch boundary conditions are applied for the lateral faces, while perfectly matched layers (PML) are used for the bottom and top faces. The wave source is below the inverse opal (red line) and the wave detector is above it (blue line). *Right :* Model seen from top, with the size requirements for the x and y faces. k_1 and $_2$ are positive integers, which can be different. 186

6.31 Slices of the three-dimensional dielectric constant model, passing by the centre of the pores (top row) and off-centre of the pores (bottom row). The slices are through the x axis (*a* and *d*), the y axis (*b* and *e*) and the z axis (*c* and *e*). 187

6.32 *a)* Ratio of measured intensity on maximal intensity, and *b)* measured intensity only, for each step of a non-converging simulation. 188

6.33 Ratio of measured intensity on maximal intensity for a converging simulation, stopped when it reaches the specified target of 10^{-9} (indicated with a horizontal line). 189

6.34 Spectral intensity of the transmitted waves for a simulation (*a*) without any structure and (*b*) with the presence of an inverse opal cell. *c)* Normalisation of the spectra measured with the presence of the inverse opal, by the one obtained with an empty cell. 190

6.35 Normalised transmitted spectrum for a 5 layers inverse opal made of a n=2.2 dielectric material, for 8 different pore sizes, ranging from 270 nm (*top*) to 340 nm (*bottom*) in steps of 10 nm. The two band-gaps predicted by the mode solver are indicated with black dashed lines, and a third non-identified dip in the transmission spectra is indicated with a green dashed line. 191

6.36 Normalised transmitted spectrum for an inverse opal with pore sizes of 340nm, with a convergence target of 10^{-9} (*top*) and of 10^{-7} (*bottom*). 192

6.37 Bilayer inverse opal model creation. (a) Initial configuration, with a block of glass (in blue) a block of FTO representing the initial thin film (in light grey) and a second block of FTO (in dark grey). (b) Addition of nickel oxide spheres, centred on the standard coordinates, with greater radii than the final those of the pores, making the spheres overlap. (c) Addition of air spheres, placed within each of the nickel oxide spheres, with a radius corresponding to the final pore size. (d) Creation of open hemisphere on top of the inverse opal, with the addition of a block of air. (d) Final model, as the features outside the defined cell are removed by the simulations' boundary conditions. 193

7.1 Sketch of a slot die coater. A: Wet thickness. B: Coating gap. C: Die gap. 199

7.2 Slot die coater from (a) above and (b) from below. 200

7.3 Die seen from bottom (a) and mounted on the equipment (b). 201

7.4 *Left :* Loading of the solution from the main reservoir. *Right :* Dispense of the solution to the die. 201

7.5 Required wet thickness for a monolayer of polystyrene nanoparticles. Different concentrations of solutions are represented. 203

7.6 Optical microscope (a) and SEM (b) of slot die coated glass sample with 1.28 μm nanoparticles (sample 1.28-2 from table 7.1) 204

7.7 Required wet thickness for a monolayer of polystyrene nanoparticles. Different concentrations of solutions are represented. 205

7.8 Optical microscope (a) and SEM (b) of slot die coated glass sample with 800 nm nanoparticles (sample 800-1 from table 7.2) 205

7.9 (a) Optical effects due to a large aggregation during the solvent drying. (b) SEM analysis of the thick deposition area. 206

7.10 Uv-Vis transmission spectra of slot die coated 800nm particles, in thin and thick area. 206

7.11 Microscope view of a slow-coating of 800nm nanoparticles, exhibiting stick slip effect. The deposition is in the vertical direction. 208

7.12 Low (a) and high magnification (b) SEM view of a stripe of slow-coated 800nm nanoparticles. 208

7.13 Optical microscopy of samples S488-1 (a), S488-2 (b) and S488-3 (c) according to table 7.5. 209

7.14 SEM of samples S488-1 (a), S488-2 (b) and S488-3 (c) according to table 7.5. 210

7.15 Sample S488-3 under white light illumination, with a low (a) and a high incidence angle (b). 210

7.16 Uv-Vis reflection of slow-coated 488-nm particles, with different deposition parameters. 211

7.17 Optical microscopy of samples S250-1 (a), S250-2 (b) and S250-3 (c) according to table 7.6. 212

7.18 SEM of samples S250-1 (a), S250-2 (b) and S250-3 (c) according to table 7.6. 212

7.19 Uv-Vis reflection of slow-coated 250-nm particles, at three different speed. 213

7.20 Uv-Vis reflectance of slow-coated 250-nm particles, on a flexible plasma treated PET substrate. 213

7.21 Polystyrene nanoparticles drying and aggregating at the bottom of the die. 214

A.1 *a)* Schematic of beam interaction with an inclined plane in an opal, and *b)* enlargement of the area and description of the used angles within the yellow circle in *a)*. 225

B.1 Defects present on an opal made with the addition of FTO nano-crystals, stabilised with 800μl of TMAOH. 227

B.2 Defects present on an inverse opal after annealing, made with the addition of FTO nano-crystals stabilised with 800μl of TMAOH. . . 228

C.1 [100] plan of a fcc crystal on top of the sample, prior *a)* and *b)* after annealing. Sample made with the addition of FTO nano-crystals, stabilised with 200μl of TMAOH. 229

G.1 Authorisation for the use of an image from [5]. 244

G.2 Authorisation for the use of an image from [6]. 245

G.3 Authorisation for the use of an image from [7]. 245

G.4 Authorisation for the use of an image from [9] 246

G.5 Authorisation for the use of an image from [13] 246

G.6 Authorisation for the use of an image from [14]. 247

G.7 Authorisation for the use of an image from [10]. 247

List of Tables

3.1 250nm opal peaks for four different measurements. 81

3.2 Bragg-law fitting parameters for the maximum reflectance peak. . . . 83

3.3 Bragg law fitting parameters for the high order reflectance peak . . . 83

4.1 Coated SnO_2 peak positions measured with SAED. 105

6.1 0.2M nickel oxide solution composition 158

6.2 CBP/Ir(piq)2(acac) solution composition 159

6.3 Calculated size of nanoparticles, and spectral location of the bandgap of the corresponding inverse opal, for different coating thickness. The theoretical diameter of the nanoparticles and the location of the optical band-gap are calculated through equation 6.8 and 1.4 respectively. The calculations use an inverse opal made of materials of refractive index n=1 and n=1.9, in an fcc structure. 178

6.4 Optical band-gap frequencies measured from figure 6.24, and their corresponding wavelengths, for an inverse opal whose pores are 597 nm in diameter. 180

6.5 Optical band-gap frequencies measured from figure 6.26, and their corresponding wavelengths, for a coated inverse opal with a pore size of 597 nm. 181

6.6 Optical band-gap frequencies measured from figure 6.27, and their corresponding wavelengths, for a 597nm diameter pore size inverse opal. 181

7.1 1.28um nanoparticles coating, concentration of 1% per weight 203

7.2 800nm nanoparticles coating, concentration of 0.8% per weight 203

7.3 800nm special coatings, concentration of 0.8% per weight 206

7.4 800nm slow coating, concentration of 0.8% by weight 207

7.5 488nm slow coating, concentration of 1.2% by weight 209

7.6 250nm slow coating 211

7.7 Flexible substrate coating 212

Contents

List of Figures

List of Tables

1 Introduction **1**

1.1 Photonic crystals 1

1.1.1 History 1

1.1.2 Photonic crystal classification 3

1.2 Optical properties 8

1.2.1 Bragg reflections 8

1.2.2 Optical band theory 11

1.2.3 Slow photon effect 17

1.3 Three-dimensional photonic crystal fabrication 19

1.3.1 Polystyrene nanoparticles 19

1.3.2 DLVO theory 21

1.3.3 Opal formation method 23

1.3.4 Inverse opal formation methods 28

1.3.5 Crack-free structures 29

1.4 Applications in devices 30

1.4.1 Solar cells 30

1.4.2 Light-emitting devices 37

1.4.3 Other applications of inverse opal in devices 42

2 Instrumentation **47**

2.1 Electron Microscope 47

2.1.1 SEM 47

2.1.2 TEM 49

2.2 Optical measurements 50

2.2.1 Uv-Vis spectroscopy 50

2.2.2 Dynamic light scattering - Zeta potential 51

2.2.3 Zeta potential 53

2.3 Centrifugation 54

2.4 Humidity-Controlled Oven 55

2.5 Film-deposition methods 56

2.5.1 Spin-coating 56

2.5.2 Atomic-Layer Deposition 57

2.5.3 Metal evaporation 59

2.6 Structural Characterisation 60

2.6.1 XRD 60

2.6.2 TGA/DSC 61

2.7 Simulations 62

2.7.1 MPB 62

2.7.2 MEEP 64

3 Opal and Inverse Opal Fabrication **67**

3.1 Evaporation-Induced Self Assembly 67

3.2 Opal fabrication 70

3.2.1 Temperature and relative humidity 70

3.2.2 Surface treatment 73

3.2.3 Zeta potential and solution pH 74
3.2.4 Vial characteristics 76
3.2.5 Conclusion - Protocol 79
3.3 Optical characterisation of opals 79
3.3.1 UV-VIS spectroscopy 79
3.3.2 Angle-resolved UV-VIS 81
3.3.3 Conclusions 84
3.4 Inverse-opal growth 85
3.4.1 Precursor infiltration 85
3.4.2 One-step method 88
3.4.3 Calcination and template removal 91

4 Fluorine Tin Oxide Inverse Opals as a Scaffold for Perovskite Solar Cells 93

4.1 Mesoscopic solar cells 93
4.1.1 State of the art 93
4.1.2 Motivation of the project 94
4.2 Coated-scaffold fabrication 96
4.2.1 Fluorine tin oxide scaffold 96
4.2.2 Titanium dioxide coating 100
4.3 Perovskite infiltration 106
4.3.1 Infiltrated substrates 107
4.3.2 Visual controls 107
4.3.3 Antisolvent dripping 108
4.3.4 Antisolvent free deposition 110
4.3.5 Solvent retardation method 111
4.3.6 Alternative crystallisation methods 113
4.3.7 Two-step deposition 114

4.4 Solar-cell power conversion efficienicy . . . 116
4.5 Conclusions . . . 118

5 Crack-free FTO Inverse opal 121

5.1 Fabrication process overview . . . 121
5.2 Crack-free polystyrene template . . . 122
5.3 One-pot method with tin oxide precursors . . . 126
5.3.1 Zeta potential and solution stability . . . 126
5.3.2 Particles coating with positively charged polymer . . . 128
5.3.3 Aminated Polystyrene nanoparticles . . . 131
5.4 FTO crystalline nanoparticles . . . 133
5.4.1 Fabrication and characterisation . . . 134
5.4.2 One-step co-infiltration . . . 139
5.5 Conclusion . . . 150

6 OLEDs with Inverse Opal Structure 153

6.1 Motivation . . . 153
6.1.1 Materials . . . 154
6.2 Standard OLED fabrication . . . 156
6.3 Coating challenges . . . 163
6.4 Structure simulation . . . 175
6.4.1 Simulation model . . . 175
6.4.2 Band-gap analysis . . . 179
6.4.3 FDTD model . . . 182
6.4.4 FDTD results . . . 186
6.4.5 Three-dimensional multilayer coating model . . . 192
6.5 Conclusions . . . 193

7 Large-scale processing **197**

7.1 Motivation for upscaling 197

7.2 Slot die coating 199

7.2.1 Working principle 199

7.2.2 Equipment 199

7.3 Experimental 200

7.3.1 Classical coating 201

7.3.2 Slow coating 207

7.3.3 Flexible substrate 212

7.3.4 Conclusions 213

8 Conclusions **215**

9 Future work **219**

A Bragg law for tilted opal **225**

B Inverse-opal defects **227**

C Inverse-opal square packing **229**

D MPB **231**

E MEEP - standard inverse opal **233**

F MEEP - multilayer inverse opal **237**

G Permission documents **243**

Chapter 1

Introduction

1.1 Photonic crystals

1.1.1 History

"There's plenty of room at the bottom". It is by these words that the physicist Richard Feynman, December 29th 1959, expressed all the potential given by nanotechnology, and all the engineering done at the nanoscale [17]. More than half a century later, the progresses of nanotechnology in electronics have given compact computers, based on transistors working close to the atomic scale, solar panels and light-emitting displays(LED), to cite only some technologies. All of them rely on semiconductor materials, which are materials possessing an electronic band-gap, where electrons with a specific energy are forbidden. This feature, which is a fundamental prerequisite of working transistors, solar cells and LEDs, is due to the atomic periodicity of the material [18].

The applications resulting from semiconducting materials come from an accurate control over a fundamental particle, the electron. One can wonder if this property of forbidden states can be extended to others particles, such as the photon, the fundamental particle of light. Such structures could give a better efficiency for many devices using optics, by giving more control on the light involved in the device.

To design structures with the equivalent of a band-gap for light, the periodicity of semiconducting materials has to be been taken into consideration. However, the periodicity cannot be at the same scale, because of the differences between the wavelength of electrons and optical photons. An electron of 1eV has approximately a wavelength of 1 nm, while the wavelength of a 1eV photon is approximately 1000nm. For this reason, the periodic structure has to be scaled up, to be in the same order of magnitude as the light wavelength it has to interact with.

Contrary to semiconducting material, which rely on the spatial periodicity of atoms arranged as crystals, a periodic structure with a period above 100nm cannot easily be formed by atomic arrays, and has to be made by nano-engineering.

Due to the similarities these structures share with natural crystals, they are named photonic crystals, and the band of forbidden energy states created is called photonic band-gap.

As we shall see in part 1.1.2, photonic crystals with different periodic organisation can be made, leading to different optical properties. In addition, as explained in part 1.2, contrary to materials with an electronic band-gap, where light is absorbed and then re-emitted, light within a photonic band-gap is purely refracted or reflected. This refraction-reflection is also different from a classical mirror, which is based on the reflection of light on polished metals, where light, which is partially an electromagnetic wave, creates collective oscillations of electrons, known as plasmons. These plasmons can then re-create another light wave, which leads to their de-excitation. It should be noted that for semiconductor materials and for metals, light can be absorbed by the material, but the processes for these two different class of material are totally different.

In the two processes described above, light is first absorbed, before getting re-emitted at a lower frequency. Due to this absorption, a part of the energy of the initial light beam is lost in the material with which it interacts, and is converted to heat. However, in a photonic crystal, where no absorption occurs, the reflection of a light beam is total, and no energy is lost. This difference is not clearly noticeable when only one reflection occurs, as with a standard mirror, but makes all the difference when a large number of refractions of the same light beam occurs. In this case, a standard mirror made of metals would greatly absorb the light beam, while a photonic crystal would preserve its initial energy.

As is often the case in the history of human innovation, nature has been a source of inspiration to create such materials. The most famous example of a naturally created photonic crystal, is the precious gemstone opal, shown in figure 1.1 (*left*). This precious stone exhibits different colours within a single gem, and the colours change when the stone is tilted. The reason for these colours is the presence of many silicon dioxide spherical nanoparticles, organised in a periodical way (figure 1.1 *right*). Depending on the way this photonic crystal is oriented, and the size of the particles, different colours can be reflected.

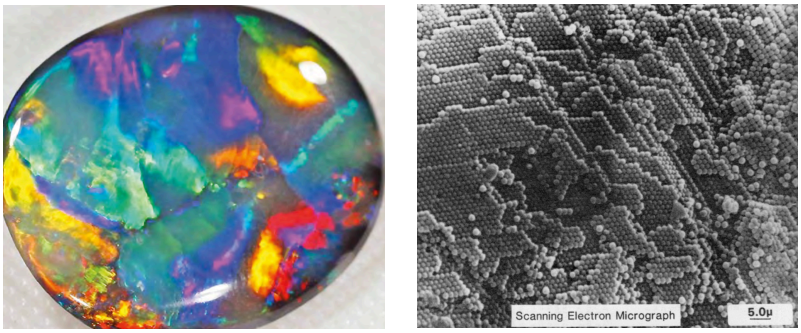


Figure 1.1: *Left :* Precious opal gemstone showing light opalescence. *Right:* Scanning electron microscopy of the surface of an Australian opal. Reproduced with permission from [1] and [2] respectively.

The colours of the precious opal stone come from a different phenomenon,

known as structural colour, than the ones of the other precious stones such as sapphire, ruby or emerald. For these precious stones, their colour comes from the material they are made of, with light being absorbed by it, whereas for the precious opal, the light is not absorbed, but only reflected due to the photonic crystal structure. If the nanoparticles composing the opal are not well organised, the stone is called a common opal, or"potch", and does not exhibit the same range of colours as the precious one, but posseses a uniform colour.

1.1.2 Photonic crystal classification

A crystal is periodic over the 3-dimensions, creating a band-gap for electrons in 3-dimensions. As photonic crystals have dimensions in the order of 100nm and above, they can be constructed with classical nanotechnology fabrication methods. This allows better control of the final structure, and also freedom about the periodicity of the structure. Different architectures of photonic crystals can then be created, with periodicity along one, two, or three dimensions.

We describe in this section the main architectures for photonic crystals depending of their periodicity, and with it, the main advances in each architecture. The one and two dimensional *PhC* are only briefly described, as this thesis uses three dimensional *PhC* (3D-PhC).

One dimension

The simplest architecture for a photonic crystal is the one-dimensional one. In a 1D PhC, a periodic pattern of two materials with different refractive indices is repeated along one direction, as shown in figure 1.2, where two materials with different refractive indices $n1$ and $n2$ are periodically repeated following the z axis. The materials are unchanged for the x and y axis and are considered of infinite size in these directions in the theoretical case.

In real cases, the dimensions of the structure in x and y are of course limited. However, if these dimensions are large compared to the wavelength of the light passing through the structure, an infinite-length approximation in both the x and y directions can be used to describe the photonic crystal.

As the periodicity of such a structure is only along the z axis, only light beams on this axis can be affected by the photonic band-gap. However, as we detail in 1.2, a light beam which has a non zero projection on the axis, is still affected by the photonic band-gap. However, this band-gap is different compared to the one for light beams that run normal to the PhC, along the z axis. In addition, for inclined light beams, the effect of the band-gap is weaker, and less light is reflected, for the same sample thickness. A light beam which lies only in the xy plan, is not affected at all by the band-gap of the one dimensional photonic crystal. Other effects can be applied on this light beam, such as a waveguide effect, but no forbidden band-gap exists.

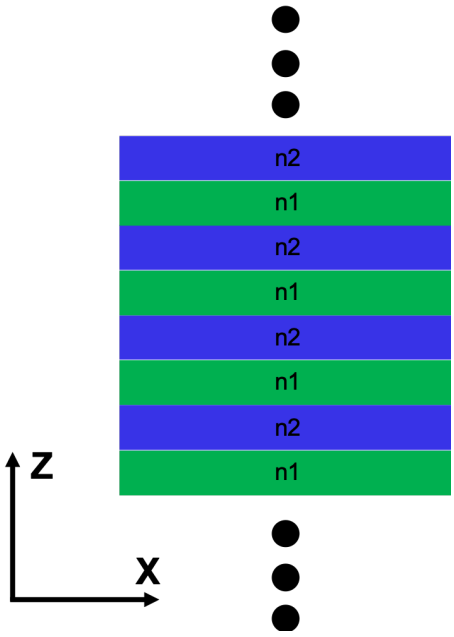


Figure 1.2: Section of a one-dimensional photonic crystal schematic.

Because a photonic band-gap does not exist for light coming from every direction, the term partial band-gap, or stop-band, is employed for one dimensional PhC (1D-PhC). Indeed, the term band-gap, originally coming from the solid state physics, indicates a band that is energy forbidden for electrons, for all directions of propagation.

With their relative simplicity, both to study and to produce, one dimensional PhC have been the first to be analysed. The initial work for these structures comes from Lord Rayleigh in 1887, where a theoretical analysis on a periodic structure made of two dielectric with different refractive index, predicts that a band of frequency cannot exist inside it [19]. At that time, the term photonic crystal was not yet used, as the structure imagined by Lord Rayleigh cannot be compared to a common crystal.

A way to explain the physics happening inside $1DPhC$ is to use the Bragg relation, initially made to calculate diffraction of X-rays due to crystals. Indeed, we can view visible light inside a photonic crystal structure as a scaled up version of X-rays inside a standard crystal. Due to the linearity of the Maxwell equations, the Bragg relation is still applicable for systems with different dimensions that standard crystals. The dimensions for the visible light and photonic crystal are around hundreds of nanometers, whereas for the X-rays and crystal, it is close to an Angstrom (0.1 nanometer).

Using the Bragg equation, and taking into account all the reflections and refractions happening inside the periodic structure, we can calculate that constructive and destructive interferences appear, in the same logic as in Lord Rayleigh pioneer work [19]. A constructive interference for a reflected beam, indicates that the beam is totally reflected, and thus not transmitted, exhibiting the same optical band-gap previously described. Because of this analogy, $1DPhC$ are also called

"Distributed Bragg Reflector" (DBR), because of the distribution of layer inducing a strong reflection, or simply "Bragg Mirror".

Bragg mirrors can nowadays be prepared with many different dielectric materials, such as nanoparticles or polymer for instance [20]. Due to their extremely high reflectivity, they can be used to form optical cavities, where two Bragg mirrors sandwiche a volume [21]. Light within a certain wavelength range is then trapped between the two DBR, and can be amplified without losses, due to the absence of absorption on each DBR. A common application of optical cavities is lasers [22]. DBR are also used when extra high reflectivity is needed, in optical experiments for instance. Many of the mirrors or filters used on an optical bench can be made from DBR [23].

Two dimensions

A two-dimensional photonic crystal (2D-PhC) posses two axes of periodicity, as schematically represented on figure 1.3 (*left*). These axes do not have to be of the same length, nor perpendicular with respect to one another. With an analogy to crystallography, we can define a unit cell of this 2D PhC, represented in 1.3 (*right*). The final photonic crystal is the repetition of the unit-cell, following the periodicity axes.

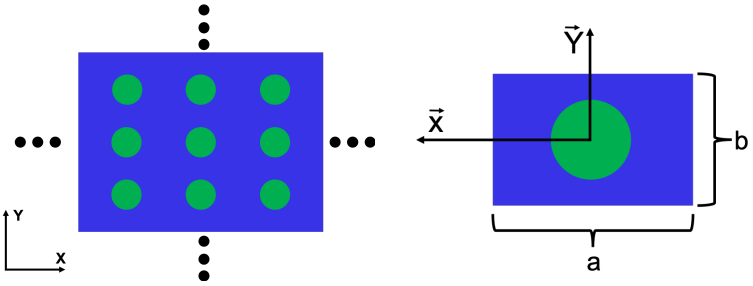


Figure 1.3: Two-dimensional photonic crystal illustration (*left*), and unit-cell of the crystal previously represented (*right*).

As for the one-dimensional photonic crystal, one dimension, the z axis in our case, is not specified, and is considered infinite for the theoretical case, to not make it interfere. For real structures, if this dimension is too small it can interfere with the propagation of light inside it. Dimensions well above the used wavelength are used to avoid these unwanted effects, which gives micrometers size thickness to these structures (with visible light, which is around 400-800nm).

To define the energy range in which the light cannot exist in the structure, we use the term stop-band, as previously explained. Indeed, we can see that there is no complete band-gap affecting light in the three directions, as for instance, light on the z-axis would not be affected by any periodicity of the structure.

Light beams in the xy plane are affected by the photonic stop-band, as the periodicity of the structure is within this plane. However, depending of the direction of a light beam, different stop-band occurs. For instance, a light beam along the

x axis, and one along the y axis, are not affected by the same periodicity value (if these two values are different). This results in a different stop-band for light on the x axis or the y axis.

These periodical structures are much more difficult to analyse theoretically and to produce, which is why they have been reported for the first time only much later in 1992, in a paper of Joannopoulos *et al.* [24]. However, due to elaborate techniques coming from microelectronics, the fabrication of such structures is now much easier, and extremely accurate.

Two-dimensional photonic crystal can prevent light within a designed stop-band to pass through it. However, if parts of the structure are removed, light can propagate through them, yet is still confined by the rest of the photonic crystal, as symbolised figure 1.4 (*left*). With such structures, light can be guided in complex ways, with low losses. A filter can also be implemented with a 2D photonic crystal, as shown in figure 1.4 (*right*). If the PhC represented on the figure has a band gap for red wavelength, we can see that red light is totally reflected, while blue light, not affected by the band-gap, is totally transmitted.

With these two basic elements previously described, and others that we do not describe here, such as optical diode [25], an optical circuit where the light is guided, filtered, and controlled at the nanoscale, can be created [26].

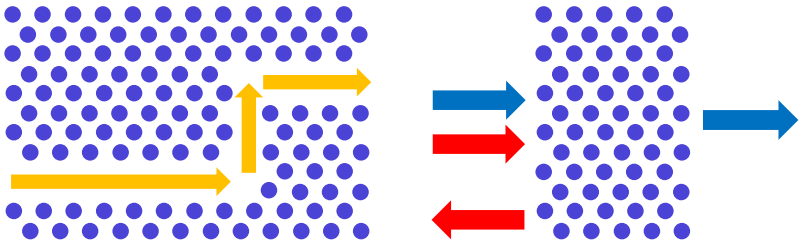


Figure 1.4: Schematics of basic optical circuit, based on two dimension photonic crystal. A waveguide (*left*) and a spectral filter (*right*).

A different and exotic application of 2D photonic crystal is to confine light inside an optical fibre [27]. The PhC is this time composed of tubes of air inside an optical fibre, parallel to the fibre. This technique allows better confinement than the classical core-shell structure, and can reduce losses to a very low value [28].

Three dimensions

As a continuation of the previously described one- and two-dimensional photonic crystal (figure 1.5) a three-dimensional photonic crystal (3D-PhC) has 3 axes of symmetry, which are non-coplanar, do not necessarily have the same length, and are not necessarily perpendicular to each other. With a direct analogy to crystallography, we can define a unit-cell which the smallest unit necessary to describe the crystal.

Contrary to the two previous cases, this time there are three axes of periodicity, and light beams coming from any directions can be affected by the periodicity

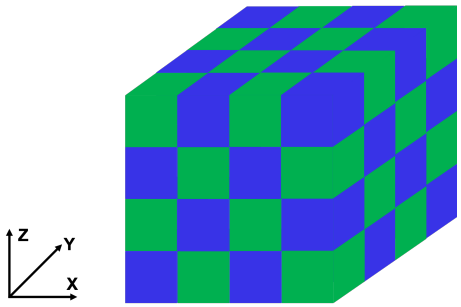


Figure 1.5: Three-dimensional photonic crystal schematic.

of the structure. Potentially, such a structure can posses a complete optical band-gap, forbidding light within a certain energy range from being transmitted no matter what the direction.

However, a complete band-gap is not necessarily achieved with any three dimensional PhC. All the directions do not always posses a band-gap, and even if it is the case, all the individual stop-bands might not cover the same energy range, preventing a complete band-gap for all directions. Examples of this are shown in part 1.2.

Because of their complexity, 3D PhC have only been studied long since their one dimensional counterparts were studied. It was exactly 100 years after the initial work by Lord Rayleigh in 1887, that Yablonovitch theorised a structure which would prevent the propagation of some electromagnetic waves (light), in all directions in 3D space [29]. To prove this effect, Yablonovitch built the first three-dimensional periodic material, by drilling holes with regular angles, into a block of matter [30]. Because the drill is a mechanical method, the characteristic size of this structure was of the order of millimetres.

As the equations of optics are linear, this structure exhibits photonic effects for waves with the same order of magnitudes, which are the microwaves. As this structure was totally new, it has been named after its creator, the *Yablonovite*. After drilling, the holes forms a crystal similar to a diamond lattice. As a result, the *Yablonovite* exhibits a complete band-gap in the radio-wave range, and is the first material that could do so.

With this initial success, showing that it is possible to obtain a complete band-gap, three-dimensional periodic material, gained a lot of interests, and other methods to build them, and to scale them down to visible wavelengths, got developed.

To reach wavelengths close to visible light, the mechanical building method has to be changed, as nanotechnology methods are more suitable. One of the earliest methods to build 3D PhC was to use colloids, formed with spherical nanoparticles. If these particles are mono-dispersed, meaning that they are all with the same diameter, they can self-assemble while drying, into a regular and periodic structure, also known as a colloidal crystal. As these structures are periodic and formed of two materials with different refractive index (colloid and air), they can exhibit a Photonic

Band-Gap (PBG) [31]. Colloidal crystals are extremely similar to natural precious opals, and for this reason, they are often called (artificial) opal for simplicity.

As shall be explained in part 1.2, the so-called inverse opal shows stronger optical effect compared to the regular opal, as it can have a complete PBG, if the contrast of refractive index is high enough. An inverse opal can be seen as the inverse version of an opal, where the high- and low-refractive-index material are reversed. It is formed by using an opal template, which is then infiltrated with other material, as detailed in 1.3. It is similar to *Yablonovite*, in the sense that it is composed of spheroidal cavities inside a transparent solid dielectric matrix.

A complete PBG for light at a wavelength of 1.5 μm has been detected, for an inverse opal made of silicon [32]. While the materials to build opal with colloid crystal are limited to the available mono-dispersed colloids, mostly polystyrene (PS) and silicon dioxide (SiO_2), an inverse opal can be formed from a wide range of materials. Semiconductor inverse opals, such as silicon dioxide (SiO_2) [33], titanium dioxide (TiO_2)[34], tin dioxide (SnO_2) [35] and many others [36], have been reported. Carbon [37], zinc [38] and also $III - IV$ semiconductors such as gallium arsenide ($GaAs$) [39] can also be used as a material to build inverse opal. Polymers have also been reported [40], which gives interesting possibilities for flexible [41] and bio-compatible devices [42].

Another possible way to obtain a three-dimensional periodic structure is the woodpile architecture. As it names indicates, this structure looks like a pile of wood, deposited in cross stacking : each layer is perpendicular to the previous one. This architecture can be made using conventional photolithography derived from microelectronics [43], which offers extremely accurate reproducibility, and good control of dimensions. Different materials can be used for woodpile, such as semiconductors [44] or polymers [45].

1.2 Optical properties

We detail in this part the physics of photonic crystals, and the origin of the PBG. We first begin to explain the photonic band-gap effect, using wave-optics and Bragg's law, as this theory is simpler to describe, and can be used as an introduction. Then, the more complete theory, involving Maxwell's equations, is detailed, which leads to a more accurate characterisation of these photonic structures. In addition, we describe an effect that we did not yet address, namely the "slow-photon effect".

1.2.1 Bragg reflections

Using some classical notions from X-ray diffractions, adapted to the opal system, it is possible to calculate which wavelength the PBG will reflect. This method employs the optics of waves, viewing light beams as periodic waves.

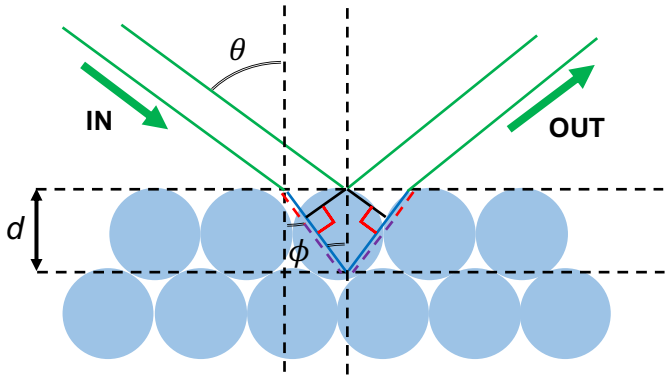


Figure 1.6: Schematic of light interaction within an opal.

We represent in the scheme figure 1.6, two parallel light waves interacting with an opal. In this scheme, the opal nanoparticles are represented in a smaller version that they should be in reality, for the sake of visibility of the other compounds. Only two layers of particles are represented, but the following demonstration is still true for more layers.

The incident light comes from the left arrow of the scheme, and the two waves are in phase, and come from the same coherent source. After reflection on the nanoparticles, described hereafter, the waves propagate to the right of the schematic. The relative phase ϕ between these two waves can vary from 0 to 2π, which lead to constructive interferences when $\phi = 0$. The case where we have constructive interference, represented on the schematic figure 1.6, gives a strong directed reflection, which we can also be interpreted as no transmission.

The angles at which the constructive interferences occurs, can be calculated with the Bragg law, $k\lambda = 2d\cos(\theta)$, with k an integer. However, there is a difference between X-ray diffraction (detailed in 2.6.1), where the X-rays scatter on the electronic clouds around the atoms, and the opal made of nanoparticles, where the light scatter on the particles. For the XRD, it is considered that the X-ray has the same frequency (and wavelength) in the air and inside the structure, which gives a simple Bragg law. However, for the visible light, the interaction with materials is much more important, as shown with the existence of the refractive index n, which can change the speed and the direction of light inside a material.

For this reason, the waves inside the material are represented in blue in figure 1.6, to exhibit their different direction and wavelength compared to the external waves. The angles θ and ϕ represents the angle of the incident wave and the refracted waves respectively, compared to the normal. We also have to modify the traditional Bragg law, to take into account the effect of the material on the wavelengths (which may itself depend on wavelength, i.e. dispersion).

The path difference between the two waves is indicated with dashed purple line on figure 1.6. The red dashed lines also represents a path difference between the waves, which is not present in XRD. However, this effect is not taken into account for the following analysis. By naming λ_{opal}, the wavelength inside the material, and using the angle ϕ to calculate the path difference, we obtain the equation 1.1, which

is a modified form of the Bragg's law. However, these values are not convenient, as they are not the one applied on the system, which are θ and the wavelength in the air.

$$k\lambda_{opal} = 2d\cos(\phi) \tag{1.1}$$

In order to link all the values together, an effective refractive index n_{eff} is calculated, by making the average of the contribution from the nanoparticles and from the air. We make the assumption that the opal structure is in a face centred cubic phase (f.c.c), which is the most compact phase, occupying 74% of the space. The effective refractive index can now be calculated, as $n_{eff}^2 = 0.74 * n_{particle}^2 + 0.26 * n_{air}^2$, in which n_{air} can be taken equal to one.

The wavelength of light changes when it passes from air to a medium with a different refractive index, and can be calculated with the equation 1.2. The refraction of the light can be calculated with the well known Snell's law (equation 1.3).

$$\lambda_{opal} = \frac{\lambda_{air}}{n_{eff}} \tag{1.2}$$

$$n_{air}\sin(\theta) = n_{eff}\sin(\phi) \tag{1.3}$$

The equations 1.2 and 1.3 are then inserted into equation 1.1, to remove the intermediate values. A small trigonometry manipulation is used to make $\sin(\phi)$ appear instead of $\cos(\phi)$ in equation 1.1, with the equality $\cos = \sqrt{1-\sin^2}$. We can then obtain the equation 1.4, which indicates which wavelength is reflected, depending on the incident angle.

$$k\lambda_{air} = 2d\sqrt{{n_{eff}}^2 - \sin(\theta)^2} \tag{1.4}$$

We can see that, with the well-known Bragg and Snell laws, it is possible to calculate at which wavelength the light is reflected, and thus blocked by the Bragg mirror. This calculation shows good accuracy with experimental results. However, it does not completely describe the optical effects occurring in the system, as the equation 1.4 predicts that the PBG only concerns one wavelength, and thus should be extremely sharp and the reflections peaks should be similar to the ones of XRD. Instead, a light in a wide energy range is reflected on Bragg mirrors, indicating that the previous calculation is incomplete, and some effects are missing.

To obtain the final result 1.4, we make the simple assumption that light behaves like a wave, without regarding the nature of this wave. Light is an electromagnetic wave, interacting with its environment, because of the electric and magnetic field from which it is composed. By taking into account this nature of

light, a new theory describing more accurately the origin of the photonic band gap can be established.

1.2.2 Optical band theory

The complete theory of the origin of the optical band gap occurring in photonic crystal is described in this part. A theoretical work about the the general propagation of light in periodic structure is firstly described. The results are then applied on one-dimensional photonic crystal, which are easier to describe and can be compared to the results obtained previously [3]. The theory is then used to describe three dimensional photonic crystal, which are at the centre of this thesis. To finish, an effect not described until now and emerging from this new theory, called the slow photon effect, is described.

As this thesis does not focus on the physics of light inside photonic crystals, but only on its consequences and its applications for devices, some parts requiring deep understanding of light physics can be overlooked, and only partially described.

Theoretical preliminaries

The propagation of electromagnetic waves in a media is governed by the four equations of Maxwell (eq. 1.5). The four unknowns **E**,**D**,**B** and **H** represent the electric field, the displacement field, the magnetic flux and the magnetic field respectively, while ρ and **J** are known and represent the free charges and the current density respectively. The bold characters in the equations stands for vectors, and thus represent 3 variables each.

$$\begin{aligned} \nabla \bullet \mathbf{B} &= 0 \\ \nabla \bullet \mathbf{D} &= \rho \\ \nabla \times \mathbf{E} + \frac{\partial \mathbf{B}}{\partial t} &= 0 \\ \nabla \times \mathbf{H} - \frac{\partial \mathbf{D}}{\partial t} &= \mathbf{J} \end{aligned} \tag{1.5}$$

One of the main difficulties in solving these equations lies in the cross terms, making impossible a direct resolution for any of the variables. In addition, the absence of direct relation between the different unknowns prevent any simplifications. With specific and adapted simplifications, one can however re-arrange the Maxwell equations in a form that make them solvable for one variable.

To allow simplifications of Maxwell's equations, we consider a simple linear lossless dielectric medium. Because of the lossless characteristic of the medium, we can deduce that there are no free charges in the system, as these charges could interact with light and absorb it (e.g. plasmons), and thus $\rho = 0$. For the same reason, no electrical currents are created due to the passage of light, leading to

$\mathbf{J} = 0$. The next simplification occurs by taking into the relations between $\mathbf{D}$ and $\mathbf{E}$, and between $\mathbf{B}$ and $\mathbf{H}$. Due to the fact that a linear material is used, we know that $\mathbf{D} = \epsilon_\mathbf{0}\epsilon(\mathbf{r})\mathbf{E}$, with $\epsilon(\mathbf{r})$ being real and positive, due to the transparency of the materials we study. A similar relation occurs between $\mathbf{B}$ and $\mathbf{H}$, and considering that most of the materials do not exhibit strong magnetic behaviour, we can approximate $\mu(\mathbf{r}) = 1$, and thus $\mathbf{B} = \mu_\mathbf{0}\mathbf{H}$. With these assumptions, the previous set of equations 1.5, is now simplified as equations 1.6.

$$\begin{aligned} \nabla \bullet \mathbf{H} &= 0 \\ \nabla \bullet (\epsilon(\mathbf{r})\mathbf{E}) &= 0 \\ \nabla \times \mathbf{E} + \mu_\mathbf{0}\frac{\partial \mathbf{H}}{\partial t} &= 0 \\ \nabla \times \mathbf{H} - \epsilon_\mathbf{0}\epsilon(\mathbf{r})\frac{\partial \mathbf{E}}{\partial t} &= 0 \end{aligned} \tag{1.6}$$

A last important simplification can be done by separating the space and time dependancy of the used vectorial functions $\mathbf{E}$ and $\mathbf{H}$, which we now write in their full form, $\mathbf{E}(\mathbf{r}, \mathbf{t})$ and $\mathbf{H}(\mathbf{r}, \mathbf{t})$. According to the Fourier theorem, any function can be decomposed in an infinite sum of periodic functions, such as cosine functions, as written in equation 1.7 :

$$\mathbf{H}(\mathbf{r}, \mathbf{t}) = \sum_\omega \mathbf{H}_\omega(\mathbf{r}) cos(\omega t) \tag{1.7}$$

Instead of cosine functions, it is more convenient to use complex numbers and exponential functions, due to ease of derivation and integrations. When this technique is used, one has to remember that only a part of the new equation, either real or imaginary, describe the original system. Using exponential notations, equation 1.7, is now written :

$$\mathbf{H}(\mathbf{r}, \mathbf{t}) = \sum_\omega \mathbf{H}_\omega(\mathbf{r}) \exp^{i\omega t} \tag{1.8}$$

The equations 1.6 could be re-written using the infinite sum of exponentials 1.8 functions instead of $\mathbf{E}(\mathbf{r}, \mathbf{t})$ and $\mathbf{H}(\mathbf{r}, \mathbf{t})$. However, due to the linearity of the Maxwell equations, we can actually decompose equation 1.6 in an infinite sum of equations, one for each ω (mode), in equation 1.8. These new equations are just equation 1.6, with $\mathbf{H}(\mathbf{r}, \mathbf{t}) = \mathbf{H}_\omega(\mathbf{r}) \exp^{i\omega t}$ and an equivalent relation for $\mathbf{E(r,t)}$. In this form, the space and the time dependencies of the fields are separated and new simplifications can occur, considering that a derivation on space consider a term dependant on time as a constant, and vice-versa. Applying this new form for the fields, give us the equation 1.9 :

$$\begin{aligned} \nabla \bullet \mathbf{H}_\omega(\mathbf{r}) &= 0 \\ \nabla \bullet (\epsilon(\mathbf{r})\mathbf{E}_\omega(\mathbf{r})) &= 0 \\ \nabla \times \mathbf{E}_\omega(\mathbf{r}) + \mu_\mathbf{0} i\omega H_\omega(r) &= 0 \\ \nabla \times \mathbf{H}_\omega(\mathbf{r}) - \epsilon_\mathbf{0}\epsilon(\mathbf{r}) i\omega E_\omega(r) &= 0 \end{aligned} \tag{1.9}$$

We can now de-couple the crossed equations in 1.9. If we choose to solve them for the magnetic field $\mathbf{H}(\mathbf{r})$, we first isolate $E_\omega(r)$ on the last equation, and we then substitute it in the third equation. Remembering that we have the equality $c^2\epsilon_0\mu_0 = 1$, we obtain equation 1.10 below, known as the wave equation.

$$\nabla \times (\frac{1}{\epsilon(\mathbf{r})}\nabla \times \mathbf{H}_\omega(\mathbf{r})) = (\frac{\omega}{c})^2 \mathbf{H}_\omega(\mathbf{r}) \tag{1.10}$$

This equation is scale invariant, which means that if we solve it for a given $\epsilon(r)$, we can easily solve it for any dilation or compression in space of this dielectric function, because the eigenvalues will only change by a certain factor. In other words, if an eigenvalue is found with $\epsilon(r)$ as the dielectric function, for any new dielectric function $\epsilon(rs)$, with s a positive number, the corresponding eigenvalues will be the same as the original problem, multiplied by the factor s.

It can be noted that the master equation is equivalent to solving an eigenvalue equation, with $(\frac{\omega}{c})^2$ as the eigenvalue and $\mathbf{H}(\mathbf{r})$ as an eigenvector. The solving of this equation is the whole core of the photonic crystal theory. We can see it in the following way : given a certain frequency ω, we can calculate if there is any associated magnetic field $\mathbf{H}(\mathbf{r})$. If there is none, it means that this frequency cannot exist in the material, indicating the presence of a photonic band-gap. By repeating such calculations over many frequencies, the whole range of energy where the PBG is present can be found.

One dimension

The case of a one dimensional photonic crystal is firstly described, which allows simplification on the master equation 1.10. The periodicity of this structure allows some assumptions about the magnetic field $\mathbf{H}(\mathbf{r})$. We use the axis z as the periodicity direction. If we note $\mathbf{a}$ the smallest vector to describe the periodicity of the system, we have $\epsilon(\mathbf{r} + \mathbf{a}) = \epsilon(\mathbf{r})$, and by extension, multiples of the vector $\mathbf{a}$ by an integer will also satisfy this relation.

It is also useful to define the vector $\mathbf{k}$, which represents the spatial variations of the field. This vector is the the space equivalent of the scalar ω, which describes the time variation. Each $\mathbf{k}$ vector is associated to one field, and if we suppose we are in free space, the equation 1.11, describes the spatial variation of a field associated with a certain $\mathbf{k}$ vector. The vector $\mathbf{H_0}$ indicates the direction and intensity of the magnetic field.

$$\mathbf{H_k}(\mathbf{r}) = \mathbf{H_0} \exp^{\mathbf{ikr}} \tag{1.11}$$

In this equation, both **k** and **r** are vectors in space, but if we consider only the field on the z axis, we can simplify **kr** by $k_z z$.

The equation 1.11 can be extended to a field in a periodic dielectric structure, by the addition of a periodic function $u_z(z)$ which has the same periodicity as the dielectric structure. In our case, $u_z(z + a) = u_z(z)$, and the resulting field is expressed as the equation 1.12.

$$H_k(z) = H_0 \exp^{ik_z z} u_z(z) \tag{1.12}$$

The equation 1.12 is also known as a Bloch wave, and is analogous to the description of electron waves in a crystal [18]. It can easily be extended in three dimensions, with the addition of more periodic functions. The full description of all the possible waves thus requires many different k vectors, going in all directions of the so called k-space. The k-space is a well known and useful notion in solid-state physics, to describe electron behaviour in a crystal. Because the unit of k is the inverse of a distance, this space is also called the inverse space.

However, due to the periodicity of the equation 1.12, many of these k are actually redundant, and the system can be fully described with only a small interval of k values. As the periodicity of our structure is a, the minimal interval for the k values is $\frac{-\pi}{a} \leq k \leq \frac{\pi}{a}$. This small interval is called the First Brillouin Zone (FBZ) [18].

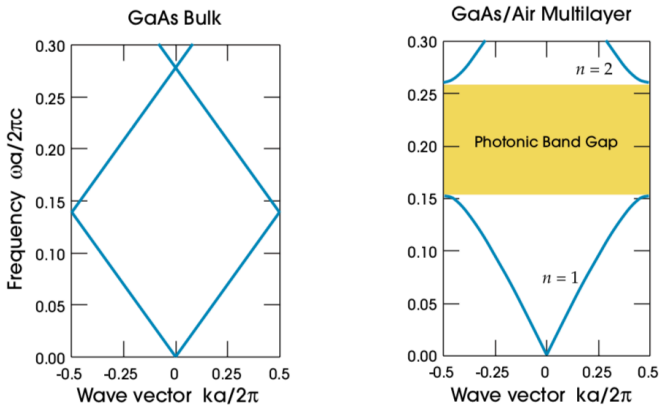


Figure 1.7: *Left :* Photonic band diagram for a Gallium Arsenide (GaAs) bulk, with a dielectric constant $\epsilon = 13$, and *Right :* for a periodic multilayer structure alternating GaAs and air layer. Reproduced with permission from [3]

By calculating for all k from the FBZ, the associated frequencies ω with the 1.10, the figures 1.7 can be constructed. On the horizontal axis of these figures, the values of k inside the FBZ are represented, while the frequencies are represented on the vertical axis. The left figure represents the associated frequencies for each value of k inside the FBZ, for a uniform bulk of Gallium Arsenide (GaAS). All the

frequencies have at least one corresponding wave-vector k, meaning that they can exist inside the material, as it is expected from a homogeneous material. However, for a one dimensional photonic crystal, made by alternating layers of air and GaAs, a forbidden band for the frequencies (in yellow on figure 1.7 appears. As no corresponding wave-vectors can be associated for the frequencies inside this band, they cannot exist in the material, which shows the existence of a PBG for this structure.

Three dimensions

The theory previously detailed for one 1d-PhC can be extended for 2D and 3D-PhC. It of course implies more calculations, due to the larger number of symmetries, and also a more complex way of presenting the results, because of large number of different possible $k-vectors$ passing through the structure. As this thesis only focusses on 3D-PhC, only this architecture is detailed hereafter.

The master equation 1.10 is still valid for three dimensional PhC, but the magnetic field representation with Bloch functions is now adapted to the increased number of periodicities. Equation 1.13 describing a general magnetic field in the 3d PhC is now a function of a three dimensional $k-vector$, and uses function $u(\mathbf{r})$, periodic in all three dimensions, following the PhC's own periodicity.

$$\mathbf{H_k}(\mathbf{r}) = \mathbf{H_0} \exp^{i\mathbf{kr}} u(\mathbf{r}) \tag{1.13}$$

The method for the calculation of the photonic band structure is the same as in the 1D case : for each vector k, a corresponding magnetic field is built, and the associated frequencies are calculated with the master equation 1.10. However, if all the possible k values could be represented on a line for the 1D case, this is not the case anymore for the 3D structure. The associated $k-space$ for a three dimensional structure is also in three dimension, meaning that the k-values are now represented in a volume.

Because of the periodicity of the structure, there is also an associated first Brillouin zone in the reverse space. Its shape can be quite complicated, as can be seen on figure 1.8, where the FBZ associated with a face-centred cubic lattice (fcc) is represented. An important axis on figure 1.8 is the ΓL one, as it corresponds to the [111] plane of the fcc in real space. In addition, it can be noticed that there are some invariance by symmetry for the considered structure. These symmetries make some of the $k-values$ inside the FBZ redundant, and thus, the range of $k-values$ necessary to fully describe the system is restricted. An irreducible Brillouin zone can be defined as the minimal volume in k-space for which any vector in k-space is related to a single vector in the irreducible Brillouin zone by symmetry operations. The irreducible Brillouin zone is represented in red in figure 1.8 and is delimited by the points Γ, L, U, X, W and K.

In spite of this drastic reduction of variables needed to be calculated, the irreducible Brillouin zone is still a volume, and it is time consuming to calculate all the possible values, and the representation of the results is also challenging. For

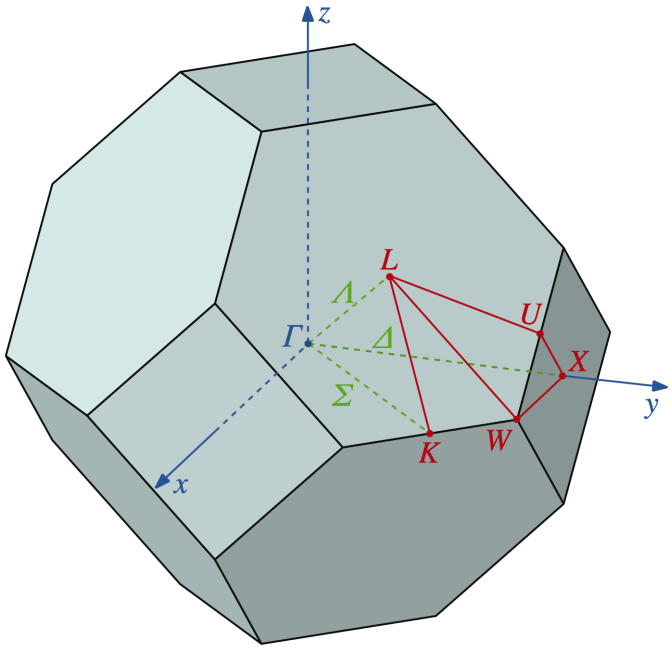


Figure 1.8: Representation of the First Brillouin Zone and the Irreducible Brillouin zone associated with a face centred cubic lattice. Reproduced with permission from [4]

this reason, it is commonly decided to make the calculations for the photonic band diagram only on the edges of the volume defining the irreducible Brillouin zone. The results can then be presented as in the figure 1.9, where each section of the figure represents an edge of the irreducible Brillouin zone, like ΓL, LU or XW for instance. It can be thought that by doing so, many of the data are missing, and mistakes can occur due to their omission. However, for most of the cases, all the "interesting" points, meaning maximum or minimum of possible band-gap, occurs on the edges, and even more on the corners, of the irreducible Brillouin zone.

Figure 1.9 is an example of what an optical band diagram looks like, with different features that we describe hereafter. The corresponding structure is an inverse opal, in a face-centred cubic structure, where the medium forming the matrix has a dielectric constant $\epsilon = 13$, and the spheres are made of air. This result is obtained by simulation, with the software package MIT Photonic Bandgap (MPB), described in section 2.7.1. It can be seen that for the frequencies within the yellow band, there are no associated k *values*. In consequence, these frequencies cannot exist within this inverse opal, for all directions, which indicates that there is a complete photonic band gap for these frequencies. For the frequencies within the red band, we can see that there are no existing fields for the ΓU edge, meaning that, for light with this direction, these frequencies are forbidden in the photonic crystal. However, for all the other edges, there is always at least one possible $k - value$, and so the wave can exist for these directions, indicating that there is only a partial band gap for this structure.

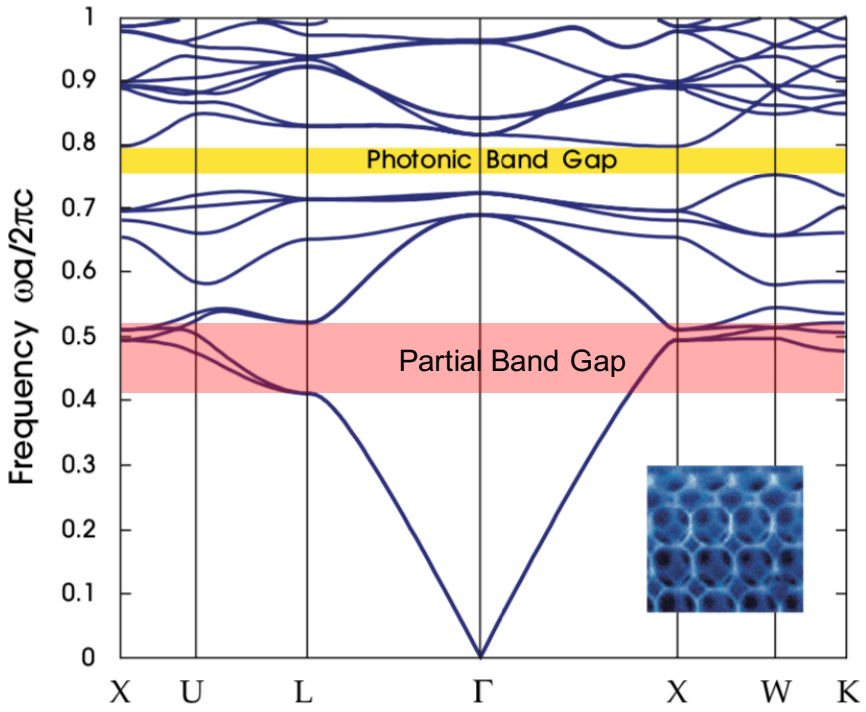


Figure 1.9: Calculated optical band diagram for an inverse opal, in a fcc organisation, consisting of air spheres ($\epsilon = 1$) in a material with a high dielectric constant ($\epsilon = 13$). The yellow band indicates a complete photonic band gap, while the salmon-pink one indicates a partial band gap. Reproduced with permission from [3]

1.2.3 Slow photon effect

In the two previous sections, an explanation of the origin of the photonic band-gap inside one and three dimensional photonic crystal is given. It is supposed that, for photons with energies outside the PBG, nothing particularly happens, and they are simply transmitted through the crystal. However, between the normally transmitted light and the totally reflected one, there is an intermediate state which is described here.

The speed of light in the material, also called the group velocity, can be calculated with the equation 1.14, which is the partial derivation of the frequency compared to the wave vector. Instead of calculating this derivative, which requires either the exact equation linking ω to k, or many different values of these parameters, it is possible to use the previously established band diagrams, to qualitatively explain why the group velocity is changing.

$$v_g = \frac{\partial \omega}{\partial k} \tag{1.14}$$

The schematic of a classical band diagram is represented figure 1.10, with the yellow band representing the PBG. The value of the derivate of ω compared to k at a certain frequency, can be seen as the local slope of the curve linking them. As

it can be seen, the value of this slope is constant for frequencies far from the band gap, and is represented on the schematic at the frequency ω_1. As the frequency gets closer to the PBG, the slope of the curves, and thus the group velocity, decreases, as shown at the frequency ω_2, which has a lower group velocity than ω_1. For a frequency extremely close to the band gap, such as ω_3, the group velocity is close to zero, meaning that the light is almost stoped, hence the name "slow-photon". The figure 1.10 only details the group velocity the frequencies below the band gap, but the exact same effect occurs for frequencies above it.

The band diagram of the bulk GaAs left of figure 1.7 shows no such effect, as there is no visible change of the slope of the curve. Indeed, a standard material cannot exhibit a slow-photon effect, as it needs particular conditions to appear. The use a slow light can be of a great use for many optical devices, to enhance absorption [46] or for making photons interact with each other [47], and photonic crystals are a good structure to create this effect [48].

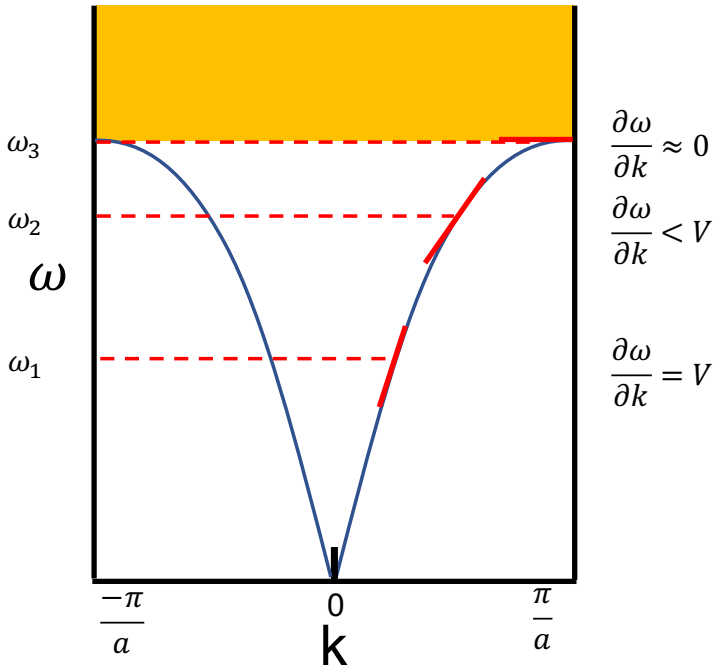


Figure 1.10: Photonic band diagram associated with a one-dimensional photonic crystal. The yellow band represents the photonic band gap, and the red segments indicate the slope of the curve for the considered frequencies.

The slow light is not homogeneously flowing inside the photonic crystal, but is concentrated either in the high or the low refractive index material. The energy of the light with frequencies just below the PBG, is concentrated on the high refractive index material, while for frequencies just above the PBG, the energy is mostly in the low refractive index material. As the simplest architecture for a photonic crystal uses only a dielectric material and air, for the high and low refractive index materials respectively, the band bellow the band gap is often called the dielectric band, while the one above it is called the air band because of where the energy is located when the light is in these bands. An analogy can be made between the dielectric and air band, and the valence and conduction band from the classical electronic band

theory.

Another way to differentiate the two sides of the band gap, is to use the corresponding wavelength size differences. As the frequencies from the dielectric band are smaller than the ones of the air band, the corresponding wavelengths are larger. A common way in optics to compare wavelength sizes is to use the red and blue colour from the visible spectrum, with red indicating a large wavelength, while blue is for a small one. With these terms, the slow photon effect happening at the edge of the dielectric band (large wavelength), is said to occur at the red-edge, while the one happening at the edge of the air band is at the blue-edge.

The explanation for the slow-light effect are given here for a one-dimensional photonic crystal, as easier diagram and figures can be used. However, this effect and the associated explanations stay true for three dimensional PhC. As for the band gap, the slow photon is exhibited for different frequencies, depending on the direction of the incoming light.

1.3 Three-dimensional photonic crystal fabrication

In this section, the main fabrication techniques to prepare 3D-PhC, particularly inverse opals, are described. As we shall see, these techniques employ polystyrene nanoparticles, which can form opal 3D PhC under specific conditions. These opals can then be used as a sacrificial template to build inverse opal, from a wide range of materials.

We first briefly describe in this section how the used nanoparticles are made, and their specificities. The theory explaining how particles interact with each other in solution is them detailed, as it is directly related to opal formation. To finish, the main techniques to build opals from nanoparticles are described, as well as inverse opal fabrication techniques.

1.3.1 Polystyrene nanoparticles

As this thesis is mostly based on material science, the nanoparticles used are bought from two companies, Microparticles Gmbh [49], and Bangs laboratories [50]. The fabrication of polymer based nanoparticles is a complex chemistry process, which could not be achieved in our laboratory. A specification of the particles' provenance is given each time they are reported on the thesis.

To obtain a periodic structure from nanoparticles at least two fundamental conditions are required. Firstly, the nanoparticles have to be mono-dispersed, meaning that they should all have the same size. In reality, it is impossible to obtain exactly the same size for many nanoparticles, and they always present a size distribution (S.D.). However, as long as this size distribution is small enough, a

periodic stricture can be formed. As we can see on figure 1.11, the structure on the left is highly periodic because the size distribution of the nanoparticles has a small value of 3.8%. However, on the right of this picture is presented a structure made with nanoparticles presenting an important S.D. of 14.2%, resulting in a random organisation.

The second condition to obtain an organised periodic structure from nanoparticles is that all nanoparticles must have the same shape. If different shapes are present, such has spheric or ellipsoidal, no organised structure can be made, even if all the particles present have the same average size.

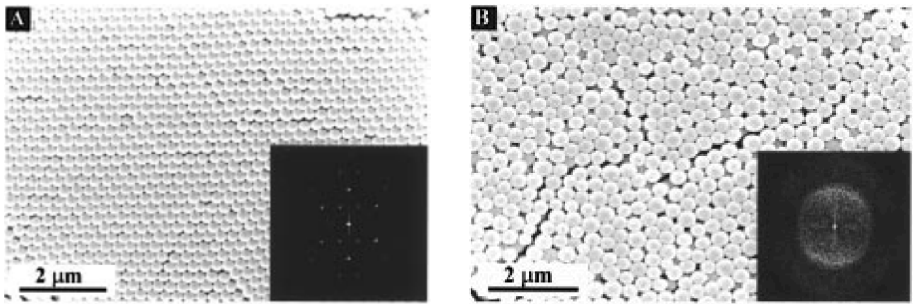


Figure 1.11: *Left :* Hexagonal organisation of mono-dispersed nanoparticles with a size distribution of 3.8%. *Right:* Random organisation of non mono-dispersed nanoparticles, with a size distribution of 14.2%. Reproduced with permission from [5]

Two main methods are used to make mono-dispersed polystyrene nanoparticles, in a spherical shape. The first method is called dispersion polymerisation, and uses that fact that a monomer and a polymer made of this monomer can have different solubility in the same solvent. In this method, monomers are dissolved and a polymerisation reaction is then started with the addition of an initiator. As the polymer is formed, it precipitates out of solution. Many nanoparticles are then formed in the solution, because of the aggregation of the initially formed polymer chains. These particles are then getting bigger in size, with the addition of more monomers, which polymerise with the polymers forming the particles. With a precise control over the monomer concentration, the temperature, the solvent and initiator used, to cite only a few parameters, extremely mono-dispersed and smooth nanoparticles can be obtained [51].

The second method is known as emulsion polymerisation, which, as its name indicates, uses an emulsion to induce the formation of nanoparticles. An emulsion is defined as a heterogeneous mixture between two liquids, which are not miscible in each other. A common example is oil and water, which are not miscible, but if mixed energetically, fine droplets of oil can formed inside water (or the opposite). The emulsion polymerisation uses two solvents which are not miscible, one in which the monomer is soluble, and one in which it is not. By forming an emulsion, the monomer concentrates inside the droplets of the solvent they are miscible in, and a polymerisation reactions starts with these "aggregates" of monomer, leading the the formation of polymer nanoparticles. These methods allow the fabrication of polystyrene nanoparticles with controllable size, from the micrometer range [52], to the nanometer [53].

The previous methods are only examples of the processes invented to make polystyrene nanoparticles, and can of course be extended to other polymers. Nanoparticles can also be made with inorganic materials, which as silicon dioxide, with a method known as the Stöber process, which is not described here [54].

A common point between all methods to make nanoparticles, is about the stability of the formed nanoparticles. If nothing is done, the particles can aggregate during their formation process, or even when they are completely formed. To avoid this, the particles have to strongly repel each other, which is done by the addition of stabilisers or surfactant, which gives the particles an electric charge on their surfaces. The theory explaining the stability of nanoparticles in solution, known as the DLVO theory, is detailed hereafter, as it is an important concept for the formation of opals.

1.3.2 DLVO theory

The DLVO theory takes its names from its creators, Boris **D**erjaguin, Lev **L**andau, Evert **V**erwey and Theodoor **O**verbeek and its aim is to explain the stability of colloids in solution [55]. Its main idea relies on the opposition of two forces between the individual nanoparticles : the Van der Wals forces, which are attractive, and the electrostatic forces, which are repulsive in this case.

Van der Wals forces are weak forces, existing between atoms or molecules. These forces originate from electric dipoles or fluctuations in the electron clouds of the atom/molecule, resulting in an attractive force between them. They are strong when the two elements are close, but quickly diminish with distance. In addition, the Van der Wals forces are additive, which means that the total force between two nanoparticles is the sum of all individual interactions between the polymers forming them.

The electrostatic forces are present because the charges on the surfaces of the nanoparticles are supposedly negative for this explanation. The nanoparticles are actually surrounded by many free charges, both positive and negative, which are attracted due to the nanoparticles' charge. This situation, called an electrical double layer, is explained in detail in 2.2.3, and is only symbolised by some charges on figure 1.12. In result, the net potential from the nanoparticles surface is screened, and the importance of the screening depends on the solution. In spite of this screening, the particles are still negative, and repel each other due to electrostatic forces. These forces also decrease with the distance.

The interactions between two (negatively) charged particles are summarised in figure 1.12. As explained previously, positive charges are attracted by the negative surface of the nanoparticles, and are represented on this figure. The potential due to the electrostatic forces and the van der walls forces can be calculated, and their sum indicates the energy potential between two charged particles. An example of a typical potential curve, as well as the Van der Waals and electrostatic contribution, are represented figure 1.13.

It can be observed that the the total potential, in green on figure 1.13,

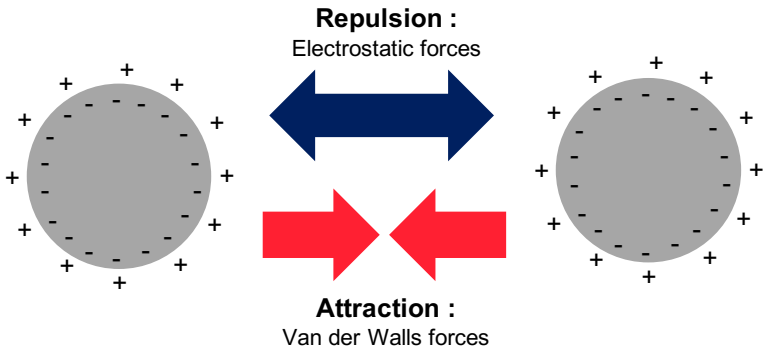


Figure 1.12: Attraction and repulsion forces between two negatively charged particles in solution. An electrostatic double layer is represented on both particles, by the addition of positive charges.

presents two minimum, which indicates two stables distance between the particles. The Primary minimum occurs when the distance is null, meaning the two particles are in contact. In this configuration, the van der walls forces completely overcome the electrostatic repulsion, and thus the two particles stays in contact. The attraction force is so strong, that this configuration is irreversible, meaning that the particles cannot separate.

The second minimum is further, and is not as deep or as stable as the primary one. The particles can still move and change the distance between themselves, with thermal energy. For a particle to pass from the secondary minimum to the primary one, it has to overcome an energy barrier, indicated on the figure. For a colloidal suspension with a high energy barrier, barely no particles are trapped in the primary minimum, as they do not have the energy to overcome the barrier. Thus, such a solution is very stable, and no aggregation occurs between the particles, which can only be at the secondary minimum, or at further distance.

The value of the energy barrier is dependant of an important amount of parameters, both depending on the colloids and the solution. To cite a few, we have the surface charges on the colloids, which changes the total charge of the particle, the amount of free ion in the solution, which increases the screening of the charges, and the dielectric constant of the solvent. These parameters all influence the value of the zeta potential, described in 2.2.3. An elevated temperature provides more energy to the particles, increasing the probability of overcoming the energy barrier.

In a solution with colloids having a small zeta-potential, i.e. a small barrier energy, permanent aggregation between particles occur relatively fast. These aggregates becomes bigger over time, as new particles get added to them. However, a colloid solution with a high zeta potential, and at low temperature, can be stable and present no aggregation for a very long time, as no particles can overcome the energy barrier.

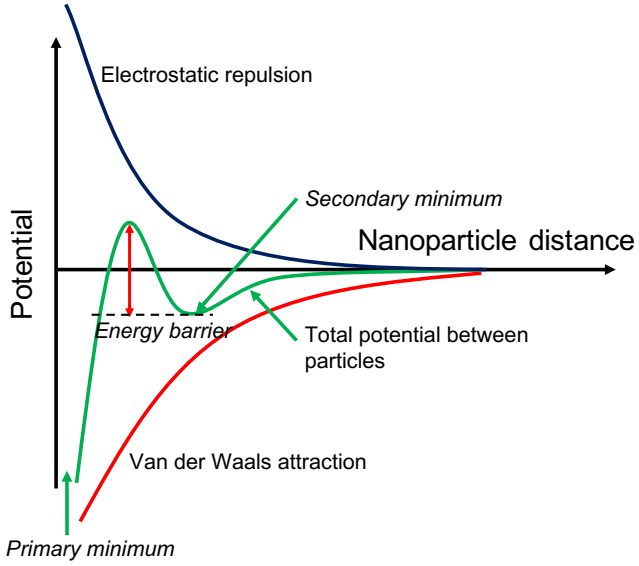


Figure 1.13: Potential between two charged nanoparticles, depending on the distance between them. The potential from the electrostatic forces is in blue, the one from the Van der Waals forces in red, and the sum of both in green. Important features such as primary and secondary minimum, as well as the energy barrier, are represented.

1.3.3 Opal formation method

Amongst all the methods to grow colloidal crystals [56], one of the most famous one is called evaporation induced self assembly (EISA), where a substrate is immersed vertically, or with a small angle, in the solution [5]. A meniscus is formed at the interface between the substrate, the solution and the air, as shown schematically in the left of figure 1.14. Due to the small thickness of the meniscus, the evaporation of the solvent has an important effect on this area. It creates convective flux, which drives the particles to the meniscus, leading to a larger concentration of particles in this area.

Due to the higher concentration of particle in the meniscus, the particles are all at at close distance from each other, but cannot aggregate, as explained by the DLVO theory. However, a new force has to be taken into consideration, the surface tension of water. Surface tension can be defined as the ability of a liquid to minimise its surface. As the cohesion between the water molecule is extremely strong, due to the hydrogen bonding between them, water has one of the highest surface tensions out of all liquids, with a value of 72 mN/m at 25 °C.

Surface tension gives another effect, named the capillary effect, which is well known for famous effects such as getting water "sucked" into a block of sugar, or for the ascension of water inside small glass tubes, as if it were ignoring gravity. The capillary effect originates from the combination of the surface tension, which minimises the surface area of a liquid, and the adhesion forces between the liquid and a hydrophilic surface, which wants to maximise the contact between the liquid and the surface. If we take the example of the ascension of water inside a glass tube, the adhesion forces creates a meniscus at the contact between glass and water. As

this meniscus increases the surface between air and water, the level of water rises to decrease it, due to the cohesion forces between the water molecule. Due to this new level of water, the meniscus goes even higher, increasing the total surface again, and so on. This ascension eventually stoped when an equilibrium with the force of gravity is found.

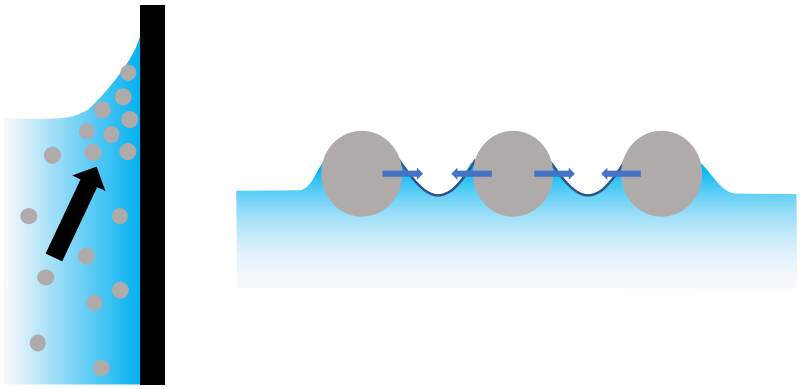


Figure 1.14: *Left :* Nanoparticles driven toward the meniscus due to convection forces. *Right :*Attraction forces between the nanoparticles due to the surface tension of water.

Because of the high density of nanoparticles in the meniscus, water can be "trapped" between the particles. Because of evaporation, the volume of water between the nanoparticles is reduced, the surface between water and air is increased. In order to reduce this surface, the capillary effects brings the nanoparticles closer. As the surface tension of water is high, it is strong enough to overcome the repulsion barrier between the nanoparticles and making them contact each other. As this procedure is similar for all the particles is solution, and is also true between the particles and the surface, a stacking of particles starts to appear.

This nanoparticle layer is formed in the meniscus, and gets bigger over time, as new particles driven by the convection forces are directed toward the meniscus, and then get added to the layer, by capillary forces. However, the meniscus itself is moving, due to the evaporation of water, which allows the nanoparticles stacking area to move on the substrate, leading to a complete film.

One of the major problems which can occur during the movement of the meniscus, is the so called stick-slip effect[57]. When the solvent level goes down, the basis of the meniscus also goes down, but its top part can still stay at the initial level, and also gets deformed due to the newly created nanoparticle layer [6]. This situation is represented on the left of figure 1.15, with a glass block replacing the nanoparticle layer, for reasons of clarity. The shape of the surface of the liquid can be described with Laplace's equation, commonly used in static mechanics [6]. When the height difference between the two levels is too great, the meniscus is "pinched", leading to a variation of its position. The area between the two levels of the meniscus is not covered by nanoparticles, leading to a substrate where isolated lines of nanoparticles are created, as seen on the right of figure 1.15.

The particles assembled by capillarity are not randomly stacked, but present a long range order. As the minimal energy between two particles is when they are

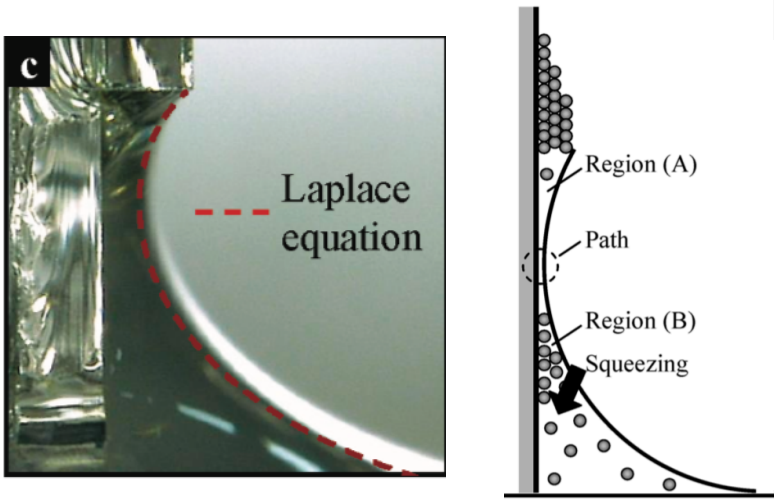


Figure 1.15: *Left :* Shape of the surface of water when a thin layer of glass is added at the end of the meniscus. *Right :* Schematic representation of the absence of a nanoparticle layer on an area, due to the pinching of the water film. Reproduced with permission from [6].

touching, it can be deduced that the minimum energy for a group of identical particles occurs when they are all as close as possible. As a system tries to go to its state of least energy, the particles assembled by capillarity should be as packed as possible.

To identify what configuration of particles allows a high packing, a source of inspiration can be the field of crystallography, which studies the organisations of the atoms inside materials. Amongst all the possible structures, the ones that present the highest degree of packing are the face-centred-cubic structure (fcc), and the hexagonal close packing (hcp) structure, represented schematically on the left and right of figure 1.16, respectively. For a real colloidal crystal, the particles are in contact with each other, and in this situation, they occupy 74% of the space.

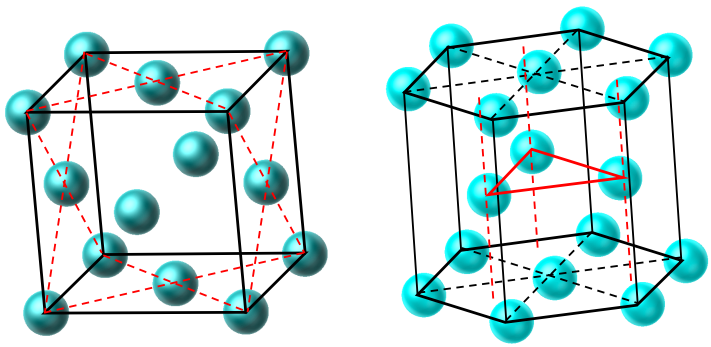


Figure 1.16: *Left :* Face-centred-cubic structure *Right :* Hexagonal-compact structure. The size of the particles is arbitrary, and is set for an optimal comprehension of the structure.

These two structures look relatively different from their unit-cell point of view. However, if many consecutive cells are represented, a similar pattern is

observed between these structures. On the left of figure 1.17, is represented a unit cell of a hc structure, with contacting spheres, and many consecutive units cells are represented on the right of this figure. On the large area structure, a clear hexagonal pattern made by the particles is observed, as well as a stacking of layer in a ABABAB... structure, symbolised by the red and blue colours.

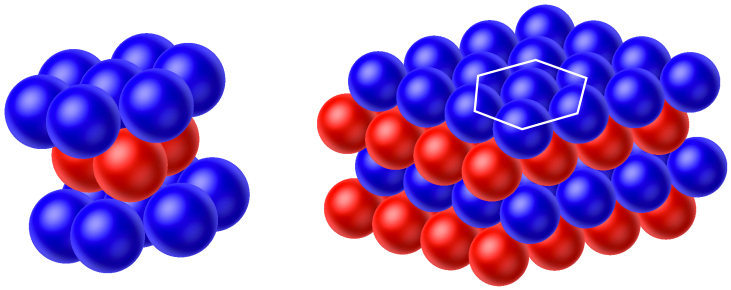


Figure 1.17: *Left :* Unit cell of a hexagonal-compact structure, with spheres contacting each other. *Right :* Many cells in a hc structure The colours are only here for a better understanding of the planar organisation.

On the left of figure 1.18, an fcc unit cell with contacting spheres is represented, and many consecutive unit cells are displayed on the right of this figure. The large area structure is represented at a different angle from the unit cell one, and the link between the two orientations can be done with the colours code, which is identical for both structures. The structure on the right of figure 1.18 is displayed with the [111] plan facing up. As it can be seen, this structure also exhibits a hexagonal pattern if seen from the [111] plan, and the layer stacking follows a ABCABCA... structure, each plane being symbolised by a different colour.

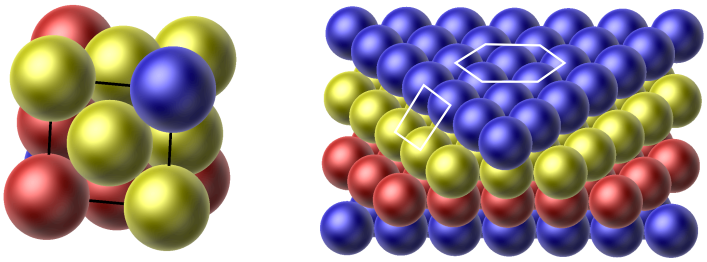


Figure 1.18: *Left :* Unit cell of a face-centred-cubic structure, with spheres contacting each other. *Right :* Many cells with a fcc structure, with a [111] plan on the top. The colours are only here for a better understanding of the planar organisation.

Even if these two structures are extremely similar, the fcc structure is slightly more stable, as theoretical works show that its energy is smaller by $0.005R$, with R the perfect gas constant[58]. This result is also confirmed by simulation[59], where it is expected that the fcc phase dominates the crystal structure, with still some parts showing hexagonal structure. The defects of stacking, due to the presence of different phases inside the crystal, are also expected to heal themselves [60], which would result in a pure fcc phase.

These results are confirmed with experimental work, where the face centred cubic phase is dominant [7], and can be distinguished from the hexagonal compact phase, by looking at the [100] plan, which presents a square organisation, as it can be seen on figure 1.19.

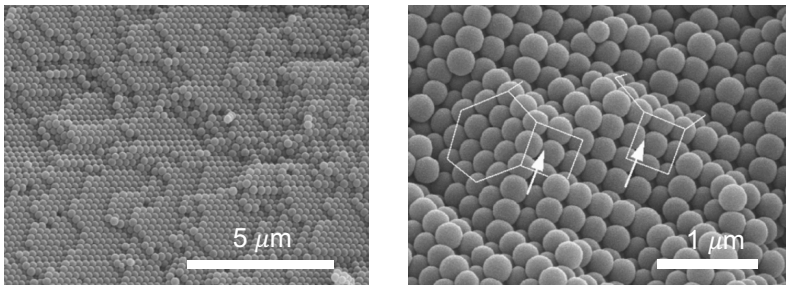


Figure 1.19: *Left :* Large area of a colloid crystal seen from top, showing a [111] plan of a fcc structure. *Right :* Close view of a colloid crystal seen from the side, exhibiting both [111] and [100] plans. Reproduced with permission from [7]

By decreasing the temperature, or with the addition of surfactant into the solution, a body centred cubic phase can be seen [61]. Even if this structure is not as stable as the fcc one, it can still appear because the surfactant decreases the surface tension of water, and the cold reduced temperature limits the available energy of the particles. These combined effects can prevent the crystal from reaching its most stable form, and only allow the formation of a less stable form.

Theory also predicts the formation of other possible structures for colloidal crystals [62, 63], by changing parameters such as the surface tension, or the addition of electrolyte in the solution, and some of these phases have been observed experimentally [64].

As a final word, it can be seen that the evaporation induced self assembly allows the production of large-area, periodic structures made of nanoparticles, and these structures can exhibit good photonic effects[5]. Due to the slow speed of this method, related to the evaporation of water, the crystal have a long time to self assemble, which lead to a low amount of defects, and large grain sizes.

In addition of the EISA, several other methods can be used to produce opal. Some of these methods uses the same physical principle as previously described (capillary effect) to make the particles form crystals. Spin-coating [65], dip-coating[66], or blade coatings [67] are examples of methods, who can be used to produce opal from nanoparticle suspensions. Other ways to force the particles to stick together is the centrifugation [68, 69], or the electrophoretic method [70], which uses an electric field to force the particles to go on the substrate. It is important to note that all these methods are relatively fast compared to the evaporation induced self assembly, which relies on the natural evaporation of water. For this reason, the crystals formed with these other methods can produce domains in different orientations, making the sample polycrystalline.

A last method for making opals uses monolayers of nanoparticles[71]. One first forms a floating layer of nanoparticles on the surface of water, with a careful deposition of a concentrated solution on water. The surface tension of water then

pushes the particles together, forming floating two dimensional photonic crystals on water. This floating crystal can then be deposited on a substrate, with a fishing process for instance. By repeating this method many times on the same sample, the two dimensional crystals stack together, and form a three dimensional opal. It can also be noted that the formation and utilisation of two dimensional crystals made of nanoparticles are of a great use in nano-patterning, and is called nano-sphere lithography [72].

1.3.4 Inverse opal formation methods

The inverse of the previously described structure is the inverse opal, where the place of the high and low refractive index material are switched. The common method for producing an inverse opal, is to start from an opal, and to fill the gap between the particles with another material. The initial nanoparticles are then removed, and only the newly injected material stays, giving the inverse opal. Different methods exists to fill the gaps between the particles, such as chemical vapour deposition (CVD) [73], atomic layer deposition(ALD) [74], electrodeposition [75], or sol gel methods. As this thesis only employs solutions for the infiltration of precursor, it is the only method described here.

The infiltration of a solution inside an opal can be done because of the good porosity and capillarity of this structure [76], due to its regularity and the important amount of surfaces driving the flow of the liquid. If the infiltrated structure is calcined directly after a standard precursor infiltration, the final structure presents poor characteristics, as an important over-layer is formed on top of the inverse opal, due to unwanted precursors. In order to remove the excess of precursors, spin-coating or dip coating can be used. Also employing solution infiltration inside an opal, electrodeposition can be used to grow an inverse opal, and because the thickness of the structure is controlled by the time of the deposition, the creation of an over-layer can be avoided.

The solution infiltration can also be done by putting a flat material on top of the opal, pressing the whole structure, which is now like a sandwich[77]. The solution is injected from the side of the structure, and because of strong capillary forces between the substrate and the material on top of the structure, the solution easily goes inside the structure. In addition, the top material prevents the formation of an over-layer, because it is pressed on top of the opal, and the solution cannot accumulate there.

The calcination of precursors from an amorphous to a crystalline form induces a shrinking of the material. Because this shrinking happens in the three dimensions, the volume of the inverse opal is reduced, while the substrate on which it is deposited does not shrink. The difference of shrinking between the inverse opal and its substrate creates stress within the structure, which eventually leads to the creation of cracks.

Work by Curti *et al.* [78] showed the difference in shrinking between an

opal infiltrated with standard precursors, and with crystalline nanoparticles. The latter shows a limited amount of cracks, due to its low shrinking, because of already crystalline particles instead of amorphous one. However, the infiltration of nano-crystals is longer and requires a specific method, due to the difficulties of the infiltration inside the opal.

1.3.5 Crack-free structures

As seen previously, both the formed opal and inverse opal present cracks, both because of the shrinking of the polystyrene nanoparticles during the drying of the opal, and because of the conversion of the precursor from an amorphous to a crystalline phase. These cracks have an impact on the optical properties, and reduce the total surface of the opal.

To suppress cracks during the opal formation, Shi *et al.* introduced a ligand which chemically binds the nanoparticles, and so prevents the stress to cause cracks appear [79]. To do so, nanoparticles with carboxyl groups ($COOH$) on the surface are used. The ligand is a molecule based on zirconium, which can make more than one covalent bond with the carboxyl groups of the nanoparticles. During the drying of the opal, the zirconium ligand reacts with the nanoparticle surface groups, making covalent bounds between them, and preventing them to be separated due to stress. This method shows crack free structure on a large scale, as well as improved optical characteristic of the opal. Following the same idea of liganding in the solution, Yi *et al.* made a structure presenting no cracks, and with a low angle dependency for the light reflection [80]. This method relies on the formation of small local colloid crystals, oriented in many directions. The final structure has no cracks due to the linking between the particles, and a homogeneous reflection, because of the distribution of the crystals orientation. However, the resulting reflection peak width is large compared to a classical ordered crystal.

A crack-free opal can also be obtained, with the use of a super hydrophobic substrate, with a colloidal suspension deposited on top [81]. Because the nanoparticles are not fixed on the hydrophobic substrate during the evaporation of the solvent, the crystals which are already formed can freely move and go in contact with others crystals, preventing cracks to appear. The resulting opals present a sharper reflection peak, indicating the good quality of the band gap, and a direct correlation between the surface energy of the substrate and reflection peak sharpening is observed.

Crack-free inverse opal are also a well studied topic, because of the better optical properties of inverse opal compared to opal, and also because of the wide range of possible material to build these structures. In 2010, Hatton *et al.* presented a method to build a large area, crack free inverse opal made of silicon dioxide [82]. To do so, a precursor of silicon dioxide named tetraethyl orthosilicate (TEOS), is added inside the colloidal suspension. During the self assembly of the nanoparticles, these precursors stay between the particles, which prevents them from cracking during drying. In addition, the concentration of precursor between the particles is

high compared to a standard infiltration by sol gel. The structure is then slowly calcinated, and due to the high fraction of precursors, the induced shrinking is relatively low. For this reason, the mechanical stress is also low, and is not enough to create cracks inside the structure, leading to crack-free inverse opal. However, the stress is still present, and its effect can be seen when the structure is too thick, as cracks starts to appear after a certain number of layers. Interestingly these cracks follow some specific directions, depending on the orientation of the crystal.

Structures made by this method can only be made of certain materials, to avoid the formation of cracks[83]. Silicon dioxide is a good material for this, as it is an amorphous material, which does not shrink as much as a crystalline one during the calcination phase. To increase the diversity of the possible material used to make crack free inverse opal, the same group showed that, by adding already formed nano-crystals to the standard precursor solution [84], the shrinking is greatly reduced, and thus the cracks are also limited. This method allows the making of crack-free opal made of titanium dioxide (TiO_2), and zirconium dioxide (ZrO_2) for instance. Monomers can also be employed instead of inorganic precursors, which allows for the creation, after polymerisation of the monomers and removal of the nanoparticles, of a crack-free polymer inverse opal[85].

The method of adding precursors can also be modified to make crack free opal, by removing only the precursor and not the nanoparticles, after the self assembly [86].

1.4 Applications in devices

1.4.1 Solar cells

History

The initial discovery leading to the solar cells as we know them today took place in 1839, where Alexandre Becquerel discovered the photovoltaic effect, where voltage and current are created in a material under light illumination. This first observation happened with an electrochemical cell, consisting of two metal plaques immersed in a solution. Shortly after this discovery, the first solid-state solar cell was created, using selenium as an active layer. A better understanding of the photovoltaic effect and its origin happened after the discovery and subsequent researches on the photoelectric effect, where electrons are ejected outside the material because of light absorption. The explanation of the photoelectric effect gave Albert Einstein his Nobel Prize in 1921.

After more than a century of researches and discoveries in laboratories, solar cells were used in a real-world application in 1959, with the installation of solar panels on the satellite Vanguard 1, which was followed in 1962 by the satellite Telstar, also powered by solar panels. For these machines, solar cells are the only unlimited source of energy possible, and this fact led to a lot of investment to build

larger and more efficient solar panels. This innovation revealed that the photovoltaic effect could be more than just a scientific curiosity, but could provide a clean and unlimited source of energy.

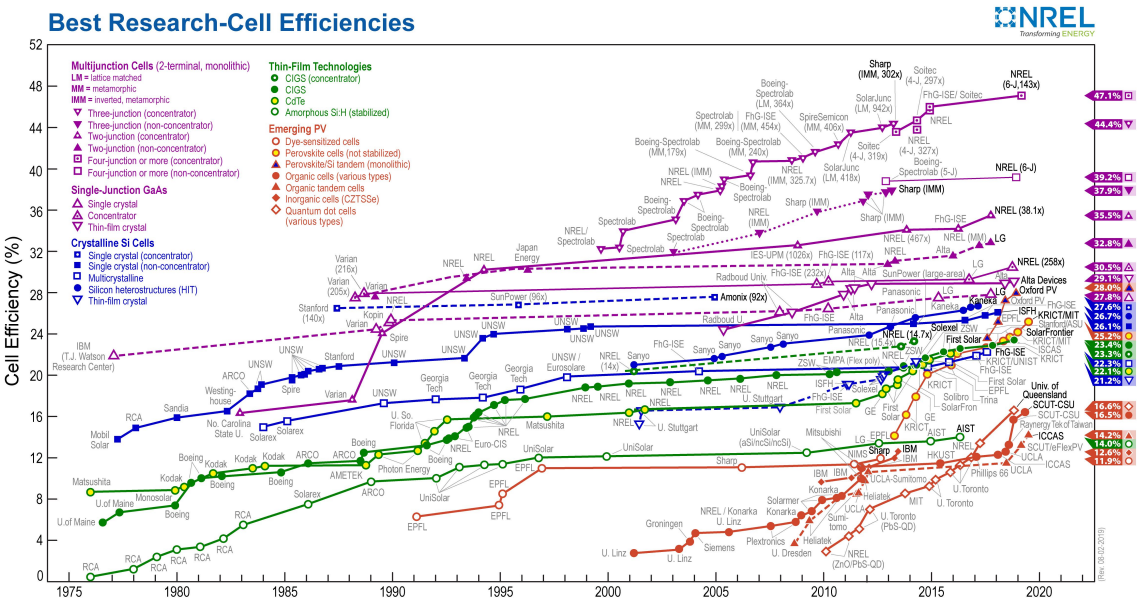


Figure 1.20: Best research solar cells efficiency chart, for all technologies. Updated on September 2019, by the National Renewable Energy Laboratory (NREL).

With their popularisation by space industries, solar cells became a major research topic and their efficiency kept increasing over the years, as it can be seen on figure 1.20. Many possible technologies and materials are currently studied, to improve both cost and performance. However, silicon solar cells keep dominating the market because of their good performance and the well-known fabrication process with silicon. In addition, the price of silicon solar cell keep decreasing, which sustains their domination of the market [87].

In spite of the domination of silicon solar cells, new photovoltaic technologies are actively studied. The main emerging technologies are summarised in figure 1.20, where they are written in red. As it can be seen, all the emerging photovoltaics technologies are all on the bottom right of the figure, both because of their recent discovery, but also because of their relatively low efficiency. However, their efficiencies are quickly rising and have already overcome some of the previously developed technologies, such as amorphous silicon, or even multi-crystalline silicon. Amongst the emerging technologies, some of the fastest growing and promising are the organic solar cell, passing from 2% in 2001 to 16.5% efficiency today, and the quantum dot solar cel, passing from around 2% in 2010, to 16.6% currently. The currently most studied emerging technology is the perovskite solar cell, which has an extremely fast growing efficiency, passing from 13% to 25.2% in less than 10 years.

In addition of their rapidly increasing efficiency, other factors motivate the study of these new technologies. Instead of the high vacuum and high temperature required in the fabrication process of silicon and inorganic solar cells, the emerging technologies can be fabricated by standard solution process. In addition to reducing the energy cost of production, the solution deposition method gives the possibility

of printing solar cells, which allows a faster fabrication process. The use of a flexible substrate such as PET is also possible with solution processed solar cell, allowing flexible and light solar panels.

Working principles

As described previously, many different technologies exist for solar cells. Thought there are important differences between all of them, the core principles of the technology stay similar. In this section, we first describe the global physical mechanism behind solar cells, followed by their potential limitations.

Semiconductor materials are the core material of solar cells and the theory explaining their properties is called band theory. The similarity between the band theory and the optical theory of photonic crystals can be noted, both theories starting from periodicity in materials, creating forbidden states for particles within a certain energy range. In addition of their electric properties, semiconductor materials also interact with light. When a photon passes through a semiconductor, its energy can be transferred to an electron, and the outcome of this exchange depends of the energy of the incident photon [88]. We call E the energy of the photon, and E_g the band gap energy. If we have $E \geq E_g$, the energy of the photon can be transferred to an electron at the top of the valence band, which can be excited and go to the conduction band. However, if $E < E_g$, the electron cannot be excited, as his new energy would be within the forbidden band gap, and so, the photon passes through the semiconductor material without being absorbed.

The space left by the electron is called a hole, and is as important as the electron itself for the solar cell. A hole is not a particle, as it is only an empty space left by an electron. However, we can consider it as a quasi-particle, with a mass m_h and a positive charge $+e$, on which the classical laws of physic apply. We can see the utility of such a model, by making an analogy with bubbles in any gaseous drink. To analyse the movement of a bubble, it is much simpler to analyse the property of the bubble, which is just an absence of liquid, rather than studying the movement of all the liquid particles around it.

The purpose of a solar cell is the collection of the excited electron/hole pairs created with the absorption of photons. Once these charges are extracted from the cell, they can be used to directly power a device connected to the solar cell, or to charge an energy-storing device, such as a battery.

A simplified scheme of a solar cell seen from the side is represented in figure 1.21 *a*. In this schematic, we have the following colour code : in grey and yellow the electrodes, in red the semiconducting material for light absorption, and in blue and green the electron transport layer and the hole transport layer respectively, whose role is described here-after. The corresponding band structures of all these layers are represented on figure 1.21 *b*, with the same colour code for the semiconducting layer and the electron- and hole-transport layer (red, blue and green respectively). By convention, the electrodes are not represented by bands, which are not relevant to conductive materials, but only by their Fermi-level value, symbolised by a black

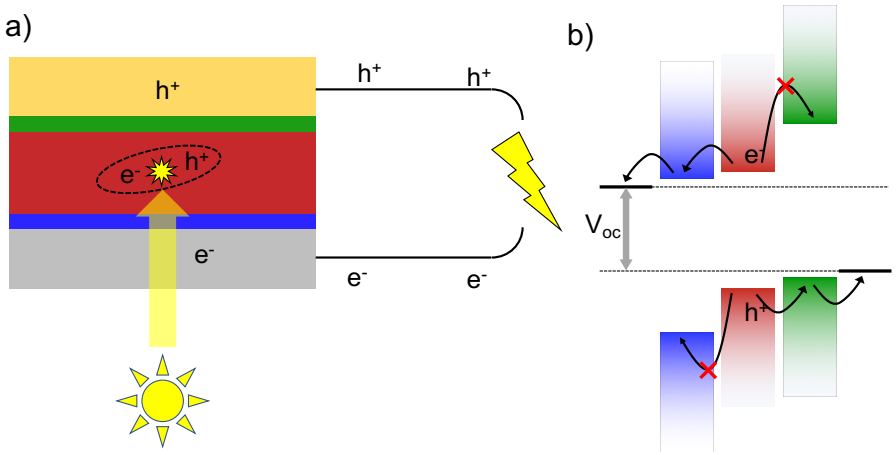


Figure 1.21: (*a*) Schematic cross section of a solar cell, from bottom to top : the transparent conductive electrode in grey, the electron transport layer in blue, the active layer in red, the hole transport layer in green and the top electrode in yellow. The charge separation process due to absorbed light is represented. (*b*) Band diagram corresponding to the left structure, with the same colour code for the three semiconducting layers. The two electrodes are represented with a single line, indicating their Fermi-level value.

horizontal line in the schematic.

Classical metallic electrodes, such as gold or silver, reflect light very well. If both electrodes were made from metal, light could not reach the semiconductor layer. For that reason, one of the electrodes has to be transparent and conductive at the same time. A category of material, called transparent conductive oxide (TCO), in which we can find Fluorine doped Tin oxide (FTO), Indium doped Tin oxide (ITO) or Aluminium doped Zinc oxide (AZO), affords both a good conductivity, and a good transparency for visible light. These materials have a large band gap (3eV for tin oxide, 3.2eV for zinc oxide), which prevents the absorption of visible light, and are also strongly doped to increase the amount of free electrons, and so, the conductivity of the material. The doping is both intrinsic (vacancy in the oxide material), and extrinsic (addition of fluorine, tin or aluminium). One of the electrodes of the solar cell, which we consider the bottom electrode, is made from one of these materials.

After the absorption of a photon in the semiconductor layer, a free electron and a free hole are created, as schematically represented in figure 1.21 *a*. Energetically, the free electron is at the bottom of the conduction band, while the hole is on top of the valence band. It is important to remember that both electron and hole always try to minimise their energy, however, they do not do it in the same way. The electron decreases its energy by going "down" on the band diagram, which is the same idea as an excited electron in an isolated atom, moving to a lower electronic orbital. The hole being an absence of electron, has an opposite behaviour, and is moving "up" in the band diagram.

It is energetically favourable for the electron to move into the electron-transport layer, as the ETL's conduction band edge has a lower energy than that of

the semiconductor material. From there, it can then go to the electrode, as its Fermi-level is even lower. The hole cannot go the same way, as the top of the valence band of the electron transport layer is deeper than that of the semiconductor, preventing the hole to pass. Instead, it heads to the other electrode, passing through the hole transport layer. In this way, all the electrons are going to one electrode, while the holes are going to the other one. Due to the difference of potential between the two electrodes, this device can then be used to power an electric device.

The process described previously is of course ideal, and many effects limit its efficiency. One of the most famous limits in the field of solar cell is known as the Shockley-Queisser limit, which states that the maximum efficiency for a solar cell is 33.7%, by having a bandgap of 1.34eV (assuming standard illumination) [89]. The main reasons for the Shockley-Queisser limit, are that electrons with an energy below the band-gap are not absorbed, while those with an energy above it are absorbed, but their excess of energy is lost due to the relaxation of the excited electrons and holes. By taking into account the energy distribution of the solar flux, the optimal bandgap position can be deduced.

Many solar cell efficiencies presented in figure 1.21 are above the 33.7% limit. This is because the Shockley-Queisser limit is only valid for a single junction solar cell, under standard illumination. New cell architectures, including tandem solar cells, concentrated solar cells or those employing multiple electron generation, can overcome this limit.

In addition to the limits associated with the presence of the band-gap, other losses occur within a solar cell. Due to their opposite charges, the excited electron and holes attract each other and can recombine, dissipating the previously absorbed photon energy. To reduce this effect, the charges have to be separated quickly and reach their respective transport layer, which is done when the charges have a good mobility, a low number of energy traps are present in the material, and the thickness of the device is small enough. In addition, a material with a high dielectric constant increases the screening between the charges, reducing their attraction.

Photonic crystal application

The optical properties of photonic crystals, i.e. the presence of an optical band gap and slow photon effect, can be used to improve the properties of a solar cell. In addition, in the case of a three-dimensional opal, the large surface area provided by such a structure gives important advantages.

Due to the necessarily small thicknesses of the absorbing layer of semiconductor material in a solar cell, a portion of the incoming light can pass through it without being absorbed. The addition of a reflecting surface after the solar cell allows the non-absorbed light to be sent back to the semiconductor layer, increasing the total absorption, and so the efficiency of the cell. In a conventional solar cell, the metallic electrode is used as a reflector, but this solution implies losses associated with the reflection on a metallic material. Due to the purely elastic reflection occurring in photonic crystals, such reflectors do not absorb light, leading to no

energy loss and thus more light is sent back to the solar cell, increasing its potential efficiency.

The easiest type of photonic crystal to implement on the back of a solar cell is the one dimensional Bragg mirror[90]. An increase of 20% efficiency for the solar cell can be achieved with such mirrors,[91] due to their good reflectivity. In order to further increase the absorbed light with an optical device on the back of the solar cell, it is also possible to combine a Bragg mirror with a diffraction grating [92]. By doing so, the light is both strongly reflected, and also deviated by large angles, increasing the reflected photon's distance of travel through the absorbing layer.

Three-dimensional photonic crystals, such as opals and inverse opals, can also be used a back reflectors for solar cells [93, 94]. By selecting the correct dimensions, it is possible to have a device exhibiting both reflection and diffraction for the spectral range of interest [95]. Inverse opals can also be used in dye-sensitised solar cells (DSSC), where the equivalent of the hole transport layer is a liquid electrolyte. Due to its porous nature, inverse opal can be infiltrated by the electrolyte, without preventing the movement of the ions in the solution. In that way, the opal is integrated within the device itself while still acting as a reflector [96]. To cover a greater spectral range, inverse opals with different pores size can be stacked, creating a reflector acting on a wide range of frequencies [97, 98] .

The use of the slow-light effect to increase absorption in the solar cell have found limited applications, due to the complex architectures required for such a device. In addition the slow light only act on a sharp spectral range, for a given PhC. Nevertheless, Bragg mirrors designed to use the slow light effect have been reported for silicon solar cell [99], enhancing absorption for a part of the spectrum. This effect can also be used for new solar cell technologies, where it can be combined with novel materials to obtain a quantum efficiency (amount of excited electrons per incoming photon) exceeding 100% [100]. The use of inverse opal exploiting the slow light effect in solar cells have also been reported, with inorganic perovskite as an active layer [101], and with a copper oxide inverse opal infiltrated with zinc oxide [102].

Finally, a possibility for the use of high surface-area-to-volume ratio photonic crystals in solar cells, is to use inverse opal as a matrix to be filled. To do so, the dimensions of the pores of the inverse opal must be small, around 100nm, to ensure a large surface-to-area ratio. At these dimensions, and with the refractive index used for non-absorbing materials ($n < 2.5$), the optical band gap can no longer be in the visible range, according to equation to 1.4, and thus, the inverse opal is only used as a high-surface-to-area-ratio material, rather than an optical device.

Instead of a randomly organised mesoporous layer made with titanium dioxide nanoparticles, used in perovskite solar cells as an electron transport layer, an inverse opal made from the same material can be used as a novel solar cell architecture. Such an architecture gives more control on the morphology of the layer, while maintaining a large surface area. Work from Chen in 2015 [8] presents the first use of a titanium dioxide inverse opal ($TiO_2 - IO$) in a perovskite solar

cell. In this work, the $TiO_2 - IO$ is made by a spin coating method, by spin coating at the same time both the polystyrene nanoparticles used as a template and the precursors for the titanium dioxide. This one-step method is very quick, but the inverse opal obtained with it is not highly ordered, and is relatively thin (Figure 1.22). Despite this, the champion device with this architecture shows an efficiency of 13.11% higher than its mesoporous counterpart, with an efficiency of 11% [8]. Both devices architecture use a two step deposition for the perovskite layer, with the same conditions.

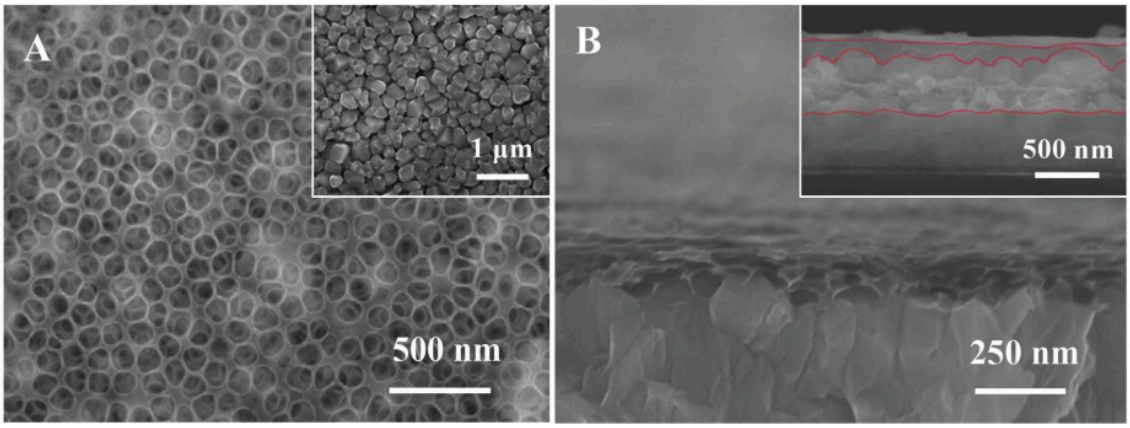


Figure 1.22: Inverse opal obtained in a one-step spin coating method. Left: Top view. Right, cross section. Reproduced with permission from [8].

In a similar idea, Ha *et al.* used a more ordered $TiO_2 - IO$ as an electron transport layer for a perovskite solar cell [103]. In their work, the polystyrene template is deposited by a modified blade-coating method, leading to ordered structures of controllable thickness [104]. These inverse opals have a thickness between $500nm$ and $1\mu m$ and are infiltrated with perovskite, in a one step method. With this architecture, the well-known hysteresis observed during perovskite solar cell measurement is greatly reduced, while the champion device shows an efficiency at 17.1%.

An inverse opal made of titanium dioxide can also be used in a DSSC [105, 106] where instead of being filled with a solid material, the inverse opal is filled with an electrolyte. A different architecture of the previously reported ones, can be seen in a work from Yuan *et al.* [107], where the inverse opal is made of a transparent conductive oxide, in this case fluorine tin-oxide (FTO). This inverse opal is then filled with TiO_2 nanoparticles, by dipping it into a bath of TiO_2 precursors, followed by calcination. This structure used in a DSSC, shows greater current collection and efficiency compared to its equivalent made only in TiO_2, for the same thickness and pore sizes. The reason for this efficiency improvement is a decreased resistance of the whole device. Titanium dioxide is a poor conductor, so the resistance of a full device, including the electrolyte and the whole layer of TiO_2 nanoparticles, is very high. By using a three dimensional $FTO - IO$ filled with nanoparticles, the resistance greatly decreases, due to the fact that every nanoparticle is now close to the electrode, and thus, the charges do not have to pass through the full layer of TiO_2.

1.4.2 Light-emitting devices

In this section, we review the advantages of using photonic crystal for organic light-emitting devices, such as organic light-emitting diode (OLED) and organic laser. We only study organic based devices, as the inorganic light emitting diode and inorganic lasers forms a totally different field, and only the organic devices are studied in this thesis.

History

The field of emitting devices started with the discovery of the electroluminescence effect by Henry Round in 1907 [108]. This effect can be seen, in a simple approach, as the opposite of the photovoltaic effect described in part 1.4.1. The electroluminescence effect generates light from an electric current passing through a material. This effect should not be confused with the incandescence effect that we can see in some light bulbs, where an electric current passing through a metal, generates heat, and this heat emits light by incandescence. The electroluminescence effect is a direct conversion of electric current to light.

Electroluminescent effects were discovered in organic compounds, such as molecules and polymers, by Andre Bernanose in the 50s [109, 110, 111]. The early emitting devices made with these new materials showed poor efficiency, mostly due to the poor electrical conductivity of the organic materials. However, in 1990, pioneering work from Burroughes *et al.* showed the creation of an efficient green OLED, creating the opportunity for more complex and efficient devices [112]. This new thin-film technology has been decreased in size, and can be used as self-emissive pixels in displays, giving OLED displays. The OLED TVs are brighter than their inorganic counterparts, and provide deep black levels.

As said previously, both molecules and polymers can show an electroluminescent effect. Each category of materials have their own advantages that we briefly present here. The semiconducting materials can easily form crystals, which have better properties than an amorphous phase, both in term of electric conductivity, and light emission. In addition, these molecules can be evaporated to form films with accurate thickness, and controllable crystallinity. On the other hand, polymers do not exhibit full crystallinity, but can be semicrystalline, with different stacking between the polymer chains. An advantage of the absence of full crystallinity is the possibility of having flexible films, and to a larger extent, flexible devices. Due to their heavy molecular masses, polymers cannot be evaporated, and have to be dissolved to be deposited, using a wide range of techniques, such as spin coating, slot-die coating or roll-to-roll deposition to cite only a few.

Because of their better properties when deposited by evaporation, this method is used in conventional OLED display. However, polymers are also studied, both because of the possibility of creating flexible displays, and also for their easier deposition method. One could use solution deposition, to print devices in the same way magazine are printed, instead of the time-and-energy-consuming vacuum

evaporation method.

OLED Working principle

As outlined previously, the working principle of an OLED can be seen as being the opposite as that of a solar cell. Instead of light being absorbed and generating electricity, a light-emitting diode uses electricity to produce light.

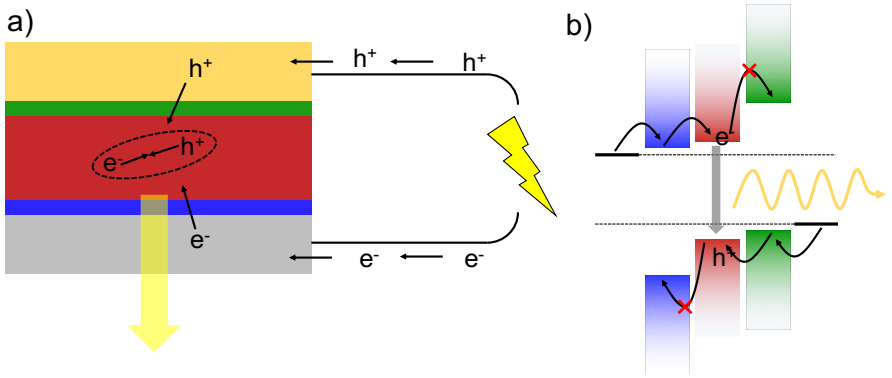


Figure 1.23: (a) Schematic cross section of a light-emitting diode, with from bottom to top : the transparent conductive electrode in grey, the electron transport layer in blue, the active layer in red, the hole transport layer in green and the top electrode in yellow. (b) Band diagram corresponding to the left structure, with the same colour code for the three semiconducting layers. The two electrodes are represented with a single line, indicating their Fermi-level value.

A simplified schematic of a light-emitting diode is presented on figure 1.23 (a), as well as the corresponding band diagram on figure 1.23 (b). In both schematics, the direction of electrons and holes are represented with arrows. It can be noticed that the schematics for the LED and the solar cell are extremely similar, due to their reversed working principle.

The LED described in figure 1.23 (a) is composed of two electrodes, an active layer (red) where the light is generated, and two interlayers (blue and green) whose functions is slightly different from those of a solar cell, and will be detailed later. One of the electrodes has to be transparent, to allow the light generated inside the device to be extracted. This transparent conductive layer can be made from a TCO, just like the case of a solar cell. As detailed in both the band diagram and the schematic, the charges are injected from the electrodes. If we take the example of an electron : after getting injected from the bottom electrode, the electron pass through the first interlayer, in blue, and then to the active layer, in red. We have a similar charge movement for the hole, which passes from the top electrode, to the green interlayer, and to the active layer.

When both electron and holes are present in the same layer, there is a possibility for them to recombine. A recombination can be either radiative or non-radiative, leading in a creation of a photon, or some phonons respectively. We do not detail the phenomena behind the probability of a radiative or non-radiative loss,

and the methods to avoid non-radiative recombinations, as this is not in the scope of this thesis.

In the previous description of the working principle of an OLED, we assume that both electron and hole stay inside the active layer and recombine in this one. However, due to the difference of potential applied between the electrodes, the charges would go naturally from one electrode to the other, without stopping in any particular layer. It is to prevent this effect that the two layers, represented in green and blue, are added to the structure. If we take the example of an electron, the transfer from the electrode to the electron transport layer, and then to the active layer are possible due to the small difference in energy between their conduction band level. However, the electron cannot pass the hole transport layer (green layer), as it does not have enough energy to go in its conduction band. For this reason, the electron stays in the active layer, as it cannot pass the hole transport layer. For a similar reason, and with the valence band of the electron transport layer, the hole is also blocked in the active layer of the OLED. As the electron and hole transport layer are more used in this structure as blocking layer to prevent charges to pass, they are called hole and electron blocking layer respectively.

It should be noted that the presented structure is the one of a simple LED, to present the essential concepts of this technology. Nowadays, most of the LED architectures posses many more layers, to improve performance, stability or even light extraction.

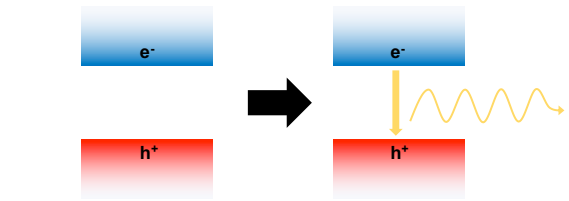
LASER Working principle

The word laser is an acronym which stands for "Light Amplified by Stimulated Emission of Radiation". Behind this name stands a physical effect coming from quantum mechanics, called stimulated emission, which we are describing hereafter.

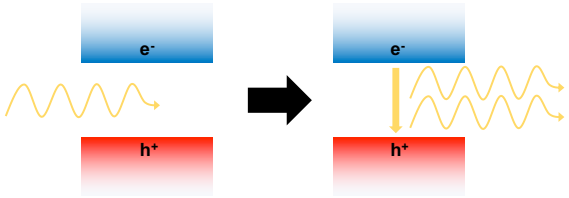
The previously described effect, where an excited electron leaves the conduction band, recombine with a hole from the valence band and emits a photon, is called spontaneous emission, and is represented figure on 1.24a. The term spontaneous refers to the fact that this emission of light does not require any external excitation to occur, and also to the fact that the emission time cannot be predicted.

The stimulated emission occurs when a photon of the same energy as the band gap of the material, pass close to an excited electron in the conduction band. The photon can stimulate this electron to release its energy, with the emission of a photon. This new photon has the particularity that it is perfectly similar to the original photon, in term of direction, wavelength and even phase. It is impossible to distinguish the initial and the new photon after a stimulated emission. It is important to notice that the incoming photon is not absorbed by the material, but is only triggering the emission of a new identical photon [113].

In summary, the light emission due to an excited atom can be done either by spontaneous or stimulated emission. The dominant process is determined by the number of photon present in the material.



(a) Spontaneous emission



(b) Stimulated emission

Figure 1.24: *Top:* Spontaneous emission, by random release of the system energy. *Bottom :* Stimulated emission, due to the interaction of a photon with an excited system. After the emission, the two photons are totally undistinguishable.

Without going into the details of the underlying principles, we can explain why either stimulated of spontaneous emission is the dominant process. If the photon density inside the material is very low, the excited electrons have a very low chance of being close to a photon, which could trigger a stimulated emission, during the time they stay excited. For this reason, the main emission way will be spontaneous, when the photon density is low. On the other hand, when the photon density is high enough, most of the excited electrons will be close to a photon at any time, and so, a stimulated emission can occur. The required energy to inject in the material to have a necessary photon density is called the threshold energy.

However, the emitted photon, either by stimulated or stimulated emission, can be re-absorbed by the media. To avoid this effect, the gain media needs to be in inversion of population, which means that more electrons need to be present at a high energy level, rather than a lower one. The electronic population is said to be inverted, compared to a standard material in equilibrium at a positive thermodynamic temperature, where the majority of the electrons are in the ground level, and only few are present at higher energies.

During population inversion, fewer electrons are present in the lower energy level, and so, the absorption of light, due to the excitation of these electrons, becomes less probable compared to the emission of light. In this way, the system emits more light than it absorbs. To create an inversion of population, the optical media needs to be pumped, meaning that a lot of energy has to be injected into it, to promote many electrons to the higher level. The pumping can be done electrically, or optically, with the use of another laser to excite the medium.

An additional feature of a laser is the creation of on optical cavity, in order in increase the density of photons inside the optical gain medium. A simple optical cavity can be composed of two mirrors, with one of the mirror being semi-transparent, with the optical gain medium between them. Light generated inside the optical medium bounces back on forth between both mirrors, increasing with

every passage the number of photons emitted by stimulated emission, so generating a great number of coherent photons. A part of the light can then be extracted by the semi-transparent mirror, and be used for other applications.

Photonic crystal

The use of photonic crystals in light-emissive devices allows accurate control of the emitted light [114]. This control can be spatial, with the light being emitted in a preferential direction, and spectral, with the reduction of the bandwidth. When combining emissive materials with three-dimensional light control, different architectures are conceivable, which are reviewed here below.

As previously explained, an optical cavity is necessary for the creation of a laser. Due to the presence of a band-gap in specific directions through a 3D PhC, the light is reflected in these directions, and the structure can be used as a very compact mirror. Compared to a metallic mirror where losses happen due to plasmons, the light is physically reflected in a PhC, and no losses occur. This is particularly important for a laser, where a photon inside the cavity interacts with the mirrors many times. Using this effect, it is possible to sandwich a layer of emissive material between two opals, which have a OBG matching the emission of the sandwiched material [115, 116]. The emissive layer is excited by an external laser, which is known as optical pumping. When the pumping reaches a sufficient intensity, a lasing effect is observed, which is characterised by a narrow spectrum and an emission strongly oriented in the [111] direction of the opal. A lower energy threshold to obtain the lasing effect can be reached by using two inverse opals for the optical cavity [117], due to the stronger optical band-gap of these structures.

A second way to use the optical cavity provided by an inverse opal, is to infiltrate the structure with emissive dyes, and to optically pump it. Under excitation by an external laser, a dye-infiltrated inverse opal exhibit an emission whose spectrum depends on the angle it is measured[118]. When a sufficient amount of energy is given to the system, a lasing effect is observed, which is once again oriented in the [111] direction of the crystal[119, 120]. In addition, due to the high order of periodicity of inverse opals, other stop-bands, corresponding to different plans in the structure, are present. With the correct choice of emissive materials, multiple band-gaps can be used as optical cavity, and lasing at different wavelengths and directions can occur simultaneously[9] (figure 1.25). A work by Furumi *et al.*, uses an opal made of non-close-packed nanoparticles, embedded in a gel doped with dyes[121]. Due to the non-close-packed opal and the presence of gel, this structure can be deformed, creating different band-gaps depending of the applied pressure. When excited with en external laser, a laser is observed, whose frequency depends on the pressure applied on the structure, which can be tunable.

The inverse opal itself can be made of an active material, which often have high refractive index, increasing even more the optical effects of the structure. In a work by Scharrer *et al.*, a lasing effect in an inverse opal made of zinc oxide is reported.[122] This structure does not use the first band gap, but one of higher order,

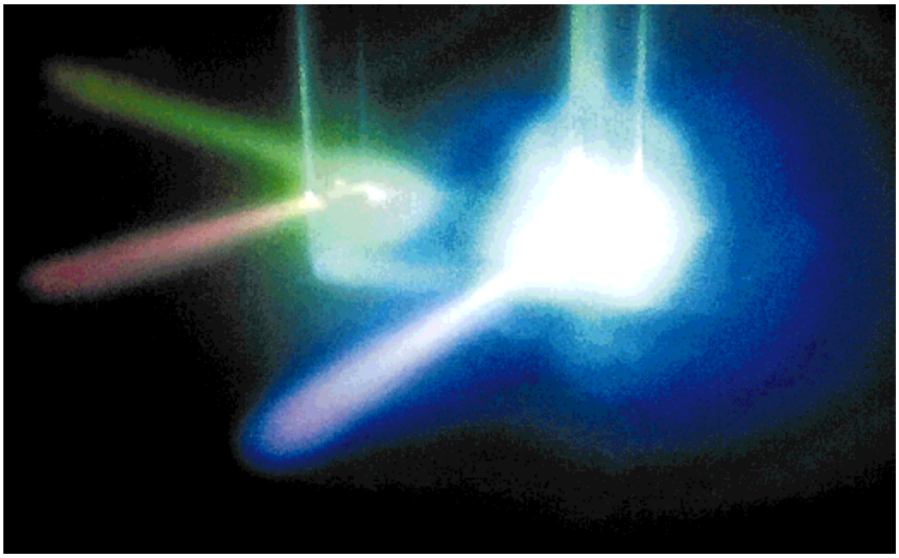


Figure 1.25: Double simultaneous lasing emission from a die-infiltrated inverse opal. The incident laser is the blue one, on the right of the picture, and the excited ones are the red and green on the left. Reproduced with permission from [9]

which matches the high energy of the emitted ultraviolet light. Pursuing the same idea, the well-studied lead halide perovskite material, which is further described in chapter 4, can be used to make inverse opals, which can emit laser under optical pumping [123] . Due to their high tunability, the desired emission wavelength can be obtained, by varying the composition of the perovskite.

All of the previously described structures emit light upon optical pumping, made by another laser. In addition of requiring additional equipment, the final system can hardly be reduced in size. A work by Ozin *et al.*, presents the use of one dimensional PhC as a reflector for an OLED[124]. The PhC serves as one of the electrodes, and is composed of alternating layers of conductive thin film and conductive nanoparticles film, where the refractive index of each is different. A partial optical cavity matching the emission of the active layer is created in that way, what results in the sharpening of the emitted spectrum. This work shows the possibility of integrating photonic crystals within standard devices, to improve their performances.

1.4.3 Other applications of inverse opal in devices

Inverse opals are exploited in many devices in addition to solar cells and emitting devices, for their optical as well as other properties. A quick review of these applications and the advantages of the use of photonic crystal is provided in this section. As these devices are not studied in this thesis, their working principles are only briefly explained.

Photocatalysis

The word photocatalysis comes from the concatenation of two words, the greek word *photo*, which means light, and *catalysis*,from the greek word *katalusis*, which originally mean dissolution, but is now defined as a material which can change the rate of a chemical reaction, without being altered. Photocatalysis can then be defined as the acceleration of a chemical reaction driven by light, with the help of a catalytic material [125]. Photocatalytic systems can be under different forms, such as homogeneous catalysis, where the catalytic material is mixed with the solution, and heterogeneous catalysis where two different phases are present, with commonly the catalyst in solid form[126].

Many different kinds of photocatalysis exist, either naturally or created in laboratory, and the most famous of the photocatalysts is the photosynthesis, where plants consume carbon dioxide and water, to produce sugar and oxygen. This conversion does not happen spontaneously, but the absorption of photons during the photosynthesis gives enough energy for it to occur. Amongst all the possible reactions driven by light, water splitting, which creates oxygen and hydrogen from water, is one of the most promising, in term of industrial applications for low-cost hydrogen production [127]. It should be noted that other forms of photocatalysis are possible, such as the transformation of nitrogen to ammonia [128], or the degradation of organic pollutants [129] .

A photocatalytic devices works in an analogous way to that of a solar cell. Photons are absorbed by a semiconductor material, which promotes electrons from the valence band to the conduction band. In a solar cell, these excited electrons can directly power a device, or transfer their energy to a battery. In a photocatalytic cell, the excited electrons (and holes) participate in chemical reactions of oxydo-reduction. For these reactions to happen, both the electrons and holes need to have a certain energy, which depends on the position of the energy bands of the semiconductors, which limits the use of potential materials.

The use of inverse opal is extremely developed in the field of photocatalysis, both because of the slow photon effect, which enhances light absorption, and for the large surface area between the solution and the active material. The former point is a fundamental difference between photocatalytic systems and solar cells : in photocatalytic systems, the electrode, represented by the solution, is in contact with the absorbing material, meaning that either the electron or the hole, has only a short distance to travel, while in a solar cell, both charges have to travel a long distance before reaching their respective electrodes.

Titanium dioxide is one of the most studied materials in water splitting heterogeneous photocatalysis, due to its well positioned conduction and valence bands, as well as its good surface properties [130, 131]. Due to its low light absorption, and only in the ultraviolet range, this material is often used in combination with others. Titanium dioxide inverse opal have been reported, which can be coated with gold nanoparticles to exploit plasmonics in combination with the slow light effect [132, 133]. Another possibility is to make the inverse opal in a material with a good conductivity, such as fluorine doped tin oxide, and to then coat the structure with

TiO_2 [134, 135]. In this way, the charge extraction from the TiO_2 coating to the core of the inverse opal is enhanced, which reduces the recombination rate and thus enhances the efficiency of the device.

Inverse opal for photocatalysis have been reported using others materials, such as tungsten trioxide (WO_3), which can be used as the core of the inverse opal [136], or as a coating layer [137] , bismuth vanadate ($BiVO_4$) [138] , or zinc oxide (ZnO) [139]. Most of these works use bilayer structures to enhance charge separation, and increase device performance. An inverse opal photocatalytic device can also be combined with a standard solar cell, to increase its performances [140].

To enhance light absorption, Eftekhari *et al.* use a stack of inverse opal with different sizes, to both slow down the light and reflect it if not absorbed [141]. A Bragg mirror can also be used to reflect only a part of the visible spectrum, which allows a spectral filtration of the incident light. In this way, Shi *et al.* demonstrate a tandem photocatalytic with a Bragg mirror between the two active layers, allowing reflection of short wavelength photons, which can then be reabsorbed by the first layer, yet a total transparency for photons at other wavelengths, which can be absorbed by the second layer[142].

Most of the work presented in this part uses the red edge of the optical-band-gap to obtain the slow photon effect, because most of the energy of the electromagnetic field is concentrated in the high-index material at this edge. However, by doing so, a fraction of the light which could be absorbed is reflected by the band-gap. Another possibility is to use the blue edge of the inverse opal to slow down the light, which places the photonic band-gap at high wavelength which are not absorbed. Even if the field is this time concentrated in the low-refractive-index material, absorption is still possible due to a loose confinement to this medium [46]. It should also be added that to obtain the slow-photon effect in the desired range, high-quality optical structures are required, which implies a low number of cracks, and a low dispersion in the size of the pores[143].

Chemical sensors

Inverse opals can be used as chemical sensors, by using either their optical or structural properties. When fabricated in organic materials, the dimensions of inverted opals are flexible, which allows their optical properties to be modified reversibly. If a material sensitive to a certain chemical is used as the core of the inverse opal, putting the structure in the chemicals presence can make it swell or shrink, changing its optical properties, which can easily be detected with a Uv-Vis spectrometer or simply by the naked eye. The detection of different chemicals using these properties of inverse opals have been reported, such as ethanol [144] or acid/base compounds such as ammonia or hydrochloric acid [145, 146, 40].

The slow-photon property of the inverse opal can also be used for chemical detection. If a material whose absorption can be altered by the presence of a chemical is present inside the inverse opal, the slow-photon effect increases its global absorption, increasing the sensitivity of detection. Using this method, very small

amounts of TNT have been detected by an inverse opal coated with a TNT-sensitve polymer[147]. The detection limit is much lower than with a standard thin film, both because of the large surface provided by the PhC, and by the absorption enhancement due to the slow photon effect. The important surface area of inverse opal can alone be used to greatly improved the detection of chemicals, using either absorption [148, 149], or the change of electric conductivity of the inverse opal core material [35].

Energy storage and production

With their high spatial order, porosity and surface area, inverse opals are very interesting for energy-storage devices such as batteries, or energy-production devices, namely fuel cells. A battery can be described as a converter of electric energy to chemical energy during its charging, and the opposite during its use (discharge). It is composed of three parts : an anode, a cathode, and a membrane between them to avoid a direct contact between the electrodes and to let ions pass through it. One of the currently most studied batteries is the lithium ion battery, and its mechanism is briefly described here. During the charge, lithium cations, present in the cathode pass through the membrane and are stored in the anode. To complete the electric circuit, electrons go in the opposite, in an external circuit. During discharge, the charges movement is reversed, and the electrons in the external circuit can be used to power a device.

For both the charge and the discharge, the electrodes need to be very porous and able to store (or release) a large number of ions to increase the energy-density performance of the battery. Because of their high porosity and organisation, inverse opal make great candidates for use both as anodes [150, 151, 152] and cathodes [153]. It is shown that thanks to their properties, inverse opals exhibit greater ion and electron transport compared to randomly organised porous structures. Inverse opal can also be used for the ions' conductive membrane separating the two electrodes [154], as it both assures a good ion conductivity and prevents any contact between the electrodes. Last but not least, the optical properties of the inverse opal can also be used to monitor the status of the battery, such as charge or discharge, or eventual damage to it[155].

A fuel cell is a device for converting the chemical energy of an oxidant reducer couple into electric energy. It is different from the discharge cycle of a battery, as the reacting compounds are not stored within it, but are added from external supplies. One of the most used ox-red couple is oxygen-hydrogen, with oxygen as the oxidant and hydrogen as the reducer. Under normal conditions, the reaction of these two compounds is highly exothermic, and produces water. In a fuel cell, the compounds are added from both sides of the cell, which are separated by an ion-permeable membrane, letting only the ions pass while the electrons pass by an external circuit which can be used to power other devices. Inverse opals can be used on both sides of the cell, firstly because of their porosity, letting gas freely pass through them, and secondly because of their high order, allowing the charges to have a good mobility [156].

A last application in the energy storage of inverse opal is the possibility of making super-capacitors, which exhibit great performance due to the opals unique properties[157].

Chapter 2

Instrumentation

2.1 Electron Microscope

2.1.1 SEM

Scanning electron microscopy (SEM) is one of the most standard characterisation methods to obtain topological information of a sample, with a resolution that can reach around 10nm. In the SEM, electrons extracted from an electron gun are accelerated to a high voltage (from 5kV to 20kV), and are focused into a beam, directed at the sample. The interaction between the beam and the sample gives many different signals, which are summarised in figure 2.1.

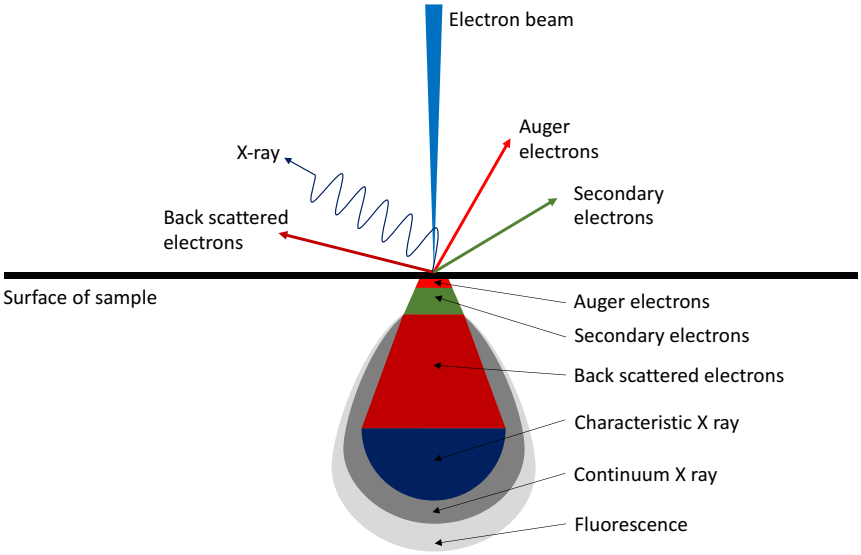


Figure 2.1: Schematic of interactions between the electron beam and the sample

All the different signals give different information about the sample, relating to either its structure (i.e. the spatial arrangement of atoms) or its chemical

composition.

The most widely used signal in SEM is that provided by the secondary electrons (SE). The secondary electrons are created when primary electrons from the beam interact with the electron cloud in the sample. A primary electron can give a part of its energy to another electron which is then ejected from its location. If this electron goes in the right direction, it can then reach the surface of the sample and be detected. Not all the secondary electrons reach the surface, because of possible re-absorption by the sample. For this reason, only the secondary electrons near the surface of the sample will be detected.

The SEM scans the sample in a raster pattern. At each pixel, the intensity of the secondary electrons is recorded and a map can then be plotted. As said previously, the detected SE comes from the surface of the sample, but may or may not be detected depending of the local surface topology. Indeed, electrons coming from a "hill" of the sample can go freely to the detector, while electrons coming from a "valley" will be blocked by shadows effects. Due to these effects, the recorded map of the intensity of SE gives a topological map of the surface of the sample.

In addition to SE, other signals can be extracted by SEM. One of the most used one is X-ray emission, analysed by a technique known as energy dispersive spectroscopy (EDS or EDX). The X-ray emission occurs after the ejection of an electron from an atomic shell : an electron with higher energy will take its place, and the difference of energy can be released in the form of an X-ray. The energy of the emitted X-ray only depends on the difference between two energy levels of an atom, and so, each atom can be characterised by the spectrum of X-rays emitted.

As indicated in figure 2.1, the detected X-rays comes from a deep volume in the bulk. This is due to the weak interaction between the bulk and the X-rays, letting most of them reach the surface and escape. For this reason, this technique does not give surface sensitive information, and is not as spatially accurate as SE. We mostly use it in this thesis for bulk composition analysis.

Other information can be obtained by detecting back scattered electrons (BSE), which are electrons from the primary beam, scattered by atom in the sample. This scattering occurs because the negative electron is deviated by the positive nucleus of the atoms around it. If the deflection is great enough, the electron can get back to the surface of the sample, and reach a detector. The scattering intensity is directly related to the amount of positive charge present in the nucleus, and so, to the atomic number of the atom. This technique cannot indicate precisely which atoms are in the sample. However, if an intensity contrast is observed, one can understand where heavy and light atoms are located in the sample.

For SEM, samples have be conductive, in order to avoid electron accumulation, which will lead to charging, and to a poor imaging resolution. To image semi conductors or insulators, a thin coating of conductive material, usually chromium, has to be applied to allow an easy transfer of electrons to the detector and a discharging route for the primary beam to the ground.

2.1.2 TEM

Transmission electron microscopy (TEM) allows materials characterisation down to the atomic scale, by accelerating electrons at a high voltage, from 80kV to 300kV for the used microscope. This high voltage gives the electrons, according to the De Broglie relation, an extremely small wavelength, smaller than the inter atomic distance. With these small wavelengths, it becomes possible to image features of less than one nanometre.

TEM differs from SEM not only because of the higher voltage used to accelerate the electrons, but also because with this technique, electrons are passing through the sample, and are analysed after this interaction. The results will this time represent the whole sample, which is projected on a 2 dimensional plane. Because the electrons have to be transmitted through the analysed sample, it has to be electron transparent, which is achieved by making it extremely thin - a "foil", of around 100nm in thickness.

Depending on the composition of the sample, the electrons passing through it will interact with different regions in different ways. For example, dense areas or heavy atoms, will interact more with the beam, resulting in fewer electrons being detected. The final results can be seen as a vertical projection of the sample, with the signal intensity representing different materials or phases.

If a crystalline samples is analysed, it is also possible to see crystalline domains directly on TEM. Indeed, because of the wavelength used being smaller than inter atomic plans, diffraction of the electron with the crystal will occur, and lattice fringes can be seen with high-enough magnification. Depending on the crystal orientation relative to the beam, electrons can be diffracted on different planes, leading to a better characterisation of the crystal. If the electrons diffract off more than one plan for the same crystal, the interferences due to the diffraction will react between each other, and new patterns, different from lattice fringes, will occur. Interpretation is thus not straight forward.

In addition to the imaging mode previously described, a TEM can be used in diffraction mode. In this mode, the focus length of the imaging lens is changed, which results in the diffractions spots being projected on the screen, instead of the image of the sample. This mode, also called selected area electron diffraction (SAED), will make electrons diffract off all of the crystals in a selected area. As the selected area can contain a large number of atoms, the measurement of the diffraction pattern is very accurate. The distance between atomic plans (d-spacing), can be measured with a great accuracy with this method.

Depending on the samples, different diffraction patterns can occur. In the case of a mono-crystal, the diffraction spot consists in separated individual points, corresponding to different plans of the crystal (figure 2.2 *a*). If a poly-crystalline sample is analysed, two cases can happen. Either the number of crystals is small, and each contribution of diffraction can be seen, and in that case the pattern will be composed of many points. Or either the amount of crystal is very large, and in that case the diffraction spots will start to form continuous pattern (instead of discrete

ones), which will lead to concentric smeared rings, with each ring corresponding to a different crystalline plan (figure 2.2 b). If the samples is not crystalline, a blurry ring, characteristic of amorphous area will appear (figure 2.2 c).

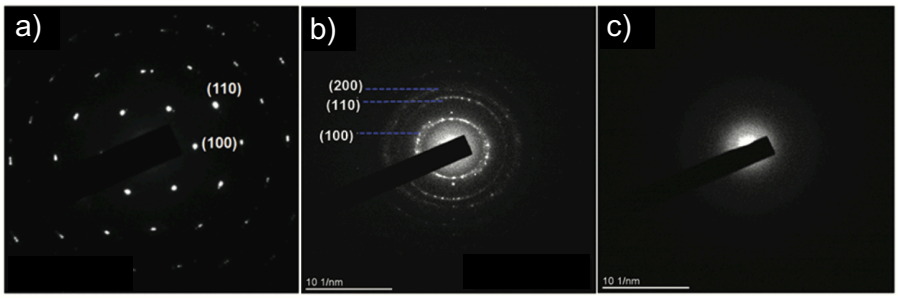


Figure 2.2: Electron diffraction on TEM on a single crystal (a), a polycrystal (b) and an amorphous sample (c). Reproduced with permission from [10].

For the previously mentioned TEM utilisation, the electron beam is localised on a small area, and the image is obtained with the analysis of the whole beam. It is also possible to use the instrument as a scanning TEM (STEM), where the beam is focused in a probe, which will scan the sample pixel by pixel, in the same way as SEM. At each scan of the probe, the emitted X-ray (same emission process as SEM), can be analysed, giving spatial information about the composition of the sample. Contrary to SEM, where the X-ray information is poorly localised, the one obtained in STEM is spatially extremely accurate, as the X-rays are emitted only where the beam is passing. This good spatial localisation allows a chemical mapping to be done, with nanometer accuracy.

2.2 Optical measurements

2.2.1 Uv-Vis spectroscopy

Ultraviolet-visible spectroscopy (Uv-Vis) is a simple technique, providing a lot of information, over a large range of wavelengths, about an optical sample.

The basic principle of Uv-Vis spectroscopy, is to fire monochromatic light at a sample, and to measure what percentage of the initial beam is transmitted through or reflected off the sample. The sample is analysed in this way with monochromatic light covering the whole range of ultraviolet and visible light. The production of a monochromatic light is done with a white light diffracted off a diffraction grating. The diffracted light is then passed through a slit, enabling the selection of a monochromatic light.

There are many possible interactions that the beam can have with the sample : the light can be either transmitted, reflected, or absorbed in the material. In case of transmission or reflection, it can be in the same direction as the initial beam (direct light), or any other direction (diffused light). In order to detect the direct and the diffuse light at the same time, a detector in the full half space (transmission

or reflection) is required. To do so, an integrating sphere, which is a sphere coated on the inside with a non-absorbing material, can be use. This tool will trap the light transmitted (or reflected), in all directions, until it reaches a detector, leading to complete information about the transmitted/reflected light.

When reflected and transmitted fractions of light are measured with an integrating sphere, if their sum is not 1, it means that a fraction of light is absorbed inside the material, leading the the equation 2.1, where A, R, T stand for absorption, reflection and transmission respectively.

$$A = 1 - R - T \tag{2.1}$$

In a conventional Uv-Vis spectrometer, light is sent perpendicularly to the sample. With the optical materials (opals) studied in this thesis, the angle of incidence on the sample is critical for the resulting spectrum. To overcome this limit, Uv-Vis measurements with a rotating sample holder and rotating detector, are also performed, which enables the acquisition of spectra at different angles between light and sample. In this rotating Uv-Vis, no integrating sphere is installed, and only direct transmission or reflection is measured.

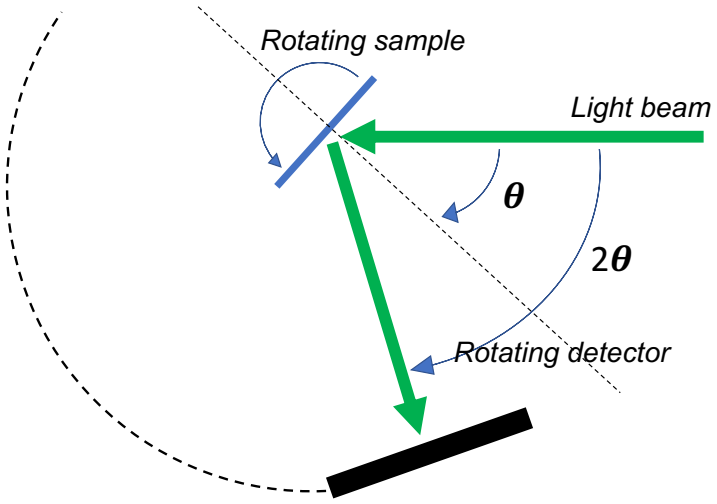


Figure 2.3: Schematic of Uv-Vis with rotating stage

2.2.2 Dynamic light scattering - Zeta potential

Dynamic light scattering (DLS) enables the direct measurement of nanoparticles sizes and their distribution in solution. The same instrument can also be used to measure zeta-potential, which is an important characteristic of nanoparticles, which will be shortly described in section 2.2.3.

The analysed sample is in liquid phase, contained within a cuvette. A laser, with a wavelength of 633nm for the machine used in this thesis, is incident on the cuvette. Because of the particles in the solution, this light will be scattered in all directions. The intensity of the scattered light is measured at one specific angle, and is recorded with time. In the machine used, the back scattered intensity is measured, at an angle of 173.3°.

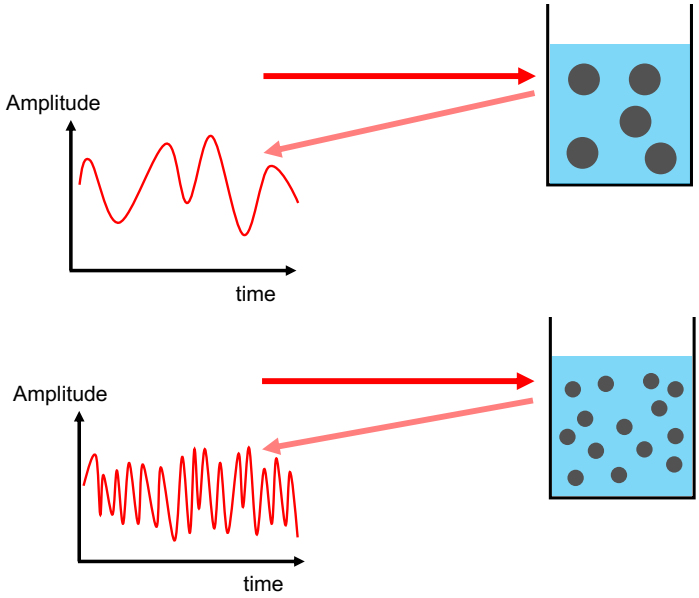


Figure 2.4: Dynamic Light Scattering

Due to the movement of particles inside the solution, the intensity of the measured scattered light will vary with time. For the same experimental conditions (temperature, solvent), the variations of intensity will be "faster" for small particles, and "slower" for big particles, because of their different Brownian movement. To quantify the variation of intensity with time, an autocorrelation function is applied to the measured intensity, which enables the extraction of the decay rate, characteristic of the signal. This decay rate can then be linked to the diffusion coefficient, which is linked to the nanoparticles sizes, according the Stokes-Einstein equation 2.2 [158, 159], with T the temperature, η the solvent viscosity, k_B the Boltzmann constant, and r the radius of the nanoparticles.

$$D = \frac{k_B T}{6\pi\eta r} \tag{2.2}$$

In this brief description, only the case of a solution containing mono-dispersed particles is explained. However, it is possible to measure solutions with different size of particles, and the ratio between the particles can be obtained. The detection range of the instrument can go from around 10 nm, to 5 μm.

2.2.3 Zeta potential

The Zeta-potential, or electrokinetic potential, is a characteristic value for nanoparticles analysis.

For nanoparticles in solutions to be stable, they have to repel each other. If they do not, they will enter in contact with each other due to Brownian motion, and might agglomerate because of Van der Walls forces. Such a solution quickly starts to form agglomerates of nanoparticles, and does not behave as a suspension anymore. In order for the particles to repel each other, their surface is charged, and because of electrostatic forces, those charges repel each other if the particles get too close to each other[160].

The Zeta potential is directly related to the stability of the nanoparticles in solution, and is linked to the surface charges previously mentioned. It is expressed in mV, and a solution of nanoparticles is considered stable, if the Zeta-potential is below -30mV, or above 30mV.

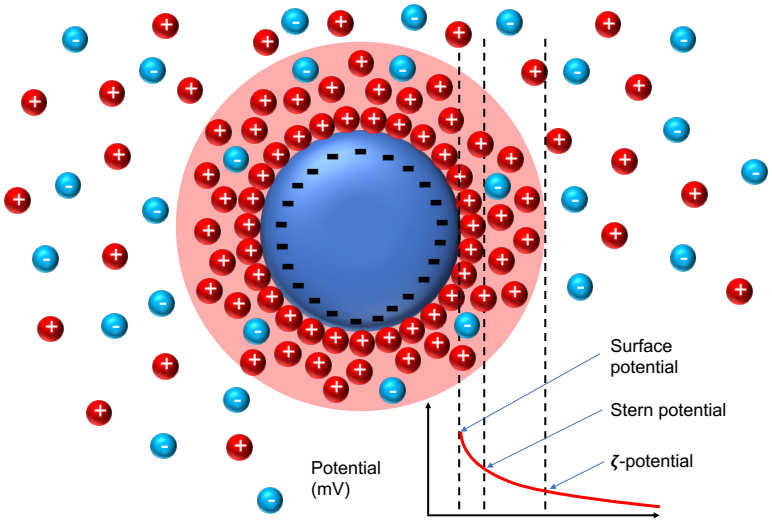


Figure 2.5: Schematic of the spatial distribution of charges around a charged nanoparticle in solution. The potential corresponding to different layers of charges is represented in the bottom of the picture.

The value of the zeta-potential on a nanoparticle is calculated indirectly. Because of the charges on the nanoparticles, the nanoparticles can be accelerated under an electric field, which force their motion to be directed in an unique direction, oppositely to a standard Brownian motion. The measurement of the resulting speed is done with a laser, whose frequency will slightly change when it is scattered by the moving nanoparticles, because of the Doppler effect. An accurate measurement of this Doppler shift is done by mixing the scattered beam, to a reference beam from the initial laser. The known values of the velocity V, and the applied field E, lead to the electrophoretic mobility μ_e, according to equation 2.3

$$\mu_e = \frac{V}{E} \tag{2.3}$$

The knowledge of μ_e, can then lead to the calculation of the zeta potential ζ, with the use of the Henry equation 2.4, with ϵ_r the dielectric constant of the solvent, ϵ_0 the permittivity of vacuum, η the solvent viscosity, and f(Ka), the Henry function.

$$\mu_e = \frac{2\epsilon_r \epsilon_0 \zeta f(Ka)}{\eta} \tag{2.4}$$

The Henry function being difficult to calculate [161], this expression is often simplified, in the case of a layer of charges whose thickness is small compared to the particle's diameter, giving the Helmholtz-Smoluchowski equation 2.5 , or in the opposite case of a layer that is thick compared to the particle's diameter, the simplification gives the Huckel equation 2.6

$$\mu_e = \frac{\epsilon_r \epsilon_0 \zeta}{\eta} \tag{2.5}$$

$$\mu_e = \frac{2\epsilon_r \epsilon_0 \zeta}{3\eta} \tag{2.6}$$

2.3 Centrifugation

The centrifugation method is a common way to force the sedimentation of nanoparticles in suspension. Common materials such as sand or any powder with micrometer dimensions, will naturally sediment when they are in suspension in a solvent, due to gravity forces. The sedimentation occurs relatively quickly with these materials, on the timescale of minutes to hours.

However, for nanoparticles a few hundred nanometers in diameters and below, Brownian motion needs to be taken into account in addition to the gravity. Brownian motion is due to the collision between the nanoparticles, and the molecules of the solvent, which all move into different directions, with different velocities. Due to the random transfer of momentum from the molecules to the nanoparticles, the movement of the nanoparticles is erratic in three dimensions.

Brownian motion creates a random movement in all directions, and thus can make the particles move oppositely to gravity. For particles with a size above a few micrometers, the effect of Brownian motion compared to gravity is negligible. However, for particles under this size, gravity is much weaker for individual particles, and Brownian motion dominates the overall motion. For this reason, for nanoparticles of this size, sedimentation takes an extremely long time to occur, or might never happen for the smallest particles.

In order to make nanoparticles sediment, a centrifuge puts the samples at a very high rotational speed. Due to the rotation, a centrifugal force is applied on the

suspension, and more precisely to the molecules and nanoparticles inside it. This force is directed to the outside, and its value is calculated according to equation 2.7 [162], with m the mass of the considered element, molecule or nanoparticle, ω the rotational speed of the centrifuge, and R the distance between the sample and the centre of the rotation.

$$F_{centri} = m\omega^2 R \tag{2.7}$$

The centrifugal force, whose value can be controlled with the rotation speed, can reach an extremely large value compared to gravity. This force now overcomes that of Brownian motion in keeping the particles suspended, and pushes all the nanoparticles in the same direction, driving sedimentation. For smaller particles, a larger force, and so a greater speed, is required, due to their smaller masses. The equipment used in his thesis, an Eppendorf 5804 R, can reach rotation speeds up to 10000 rpm. In addition, there is also the possibility of cooling down the whole system, to reduce the thermal energy and so, the importance of the Brownian motion. By reducing this effect, a weaker force is required for successful sedimentation of the nanoparticles.

Due to the high rotational speed of the moving part of the centrifuge, some precautions have to be taken while using this equipment. Firstly, the centrifuge must be well balanced, which means that if a sample is loaded, a sample with a similar mass and volume has to be loaded on the opposite side to the first sample. Each sample will apply a force on the centrifuge while rotating, and if the whole system is well balanced, these forces cancel each other. If it is not the case, the resulting force can damage or even destroy the centrifuge. For the same reason, the samples have to be well maintained in specific holders, to avoid any movement or vibration during the centrifugation, which could lead to the same consequences previously described.

2.4 Humidity-Controlled Oven

In order to accurately control the conditions of evaporation of the suspensions used in this thesis, a humidity oven (or incubator) was used. With this equipment, it is possible to control both the temperature and the relative humidity in a stable way, with an accuracy of $\pm 0.1°C$ and $\pm 0.5\%$ of relative humidity, for a long period of time.

The relative humidity of damp air is expressed as a percentage, and is defined as being the partial pressure of water in the air, divided by the maximum partial pressure of water possible at that temperature, before condensation of water, as expressed in equation 2.8. At the maximum partial pressure, the air is fully saturated of water, and any water vapour added immediately condenses out. As explained, the relative humidity ratio takes into account the temperature of the air. When the temperature is increased, a larger maximal partial pressure of water is possible, and so, more water can be present in the atmosphere. It is also important

to notice that, for the same value of relative humidity at 30 °C and at 60 °C for instance, the total amount of water present is different : indeed, the maximal partial pressure of water being higher at high temperature, more water is present at 60 °C, for the same percentage of relative humidity (as it is canonically defined).

$$RH = \frac{p_{H_2O}}{p_{max,H_2O}} \tag{2.8}$$

The oven used allows temperature from room temperature to 95 $°C$, with a control on relative humidity from 20% to 95%. To reach its target in both temperature and relative humidity, the humidity oven first increases its temperature until the set point, which has the effect of decreasing the relative humidity. Then, water vapour, coming from external water tanks, is injected into the humidity oven, until the target value for the relative humidity is reached. This procedure takes between 30 minutes and one hour for the oven used, depending of the values of both targets.

2.5 Film-deposition methods

2.5.1 Spin-coating

Spin coating is one of the most known and common techniques to deposit thin films of different material such as metal-oxides, polymers or molecules, on a variety of substrates. It can be used with small samples at a laboratory scale, but also at industrial scale on larger wafers.

A solution with dissolved materials inside is firstly spread on the sample, covering the whole surface of it. Then, the substrate begins to spin at a defined speed, for a chosen amount of time. Because of the spinning, centrifugal forces will be applied on the solution, and most of it will be ejected outside of the substrate. Because of capillarity forces, an amount of the solution stays on the substrate, and forms a flat wet layer. During the spin coating, the solvent also evaporates and the dissolved materials starts to form a film on the substrate, by aggregation. Due to the small wet thickness of the film created by the spinning, this evaporation step is relatively quick, with most of the solvent evaporated in some seconds.

It can be seen that behind its apparent simplicity, the final thickness of a spin coated film depends on many factors, such as : spin speed, spin time, solvent used, material concentration, substrate surface energy, temperature and even humidity of the air. However, it is found that for a "long" spinning time (more than 30 seconds), and with a stable environment, the final thickness is proportional to the inverse root of the spinning speed. In order to target a specific thickness for a material, a calibration linking final thickness to spinning speed has to be done. The speed can then be adjusted to obtain the wanted thickness.

In this description, we only describe a single-step spin coating, at a fixed speed. However, for complex deposition, many steps can be required, with different

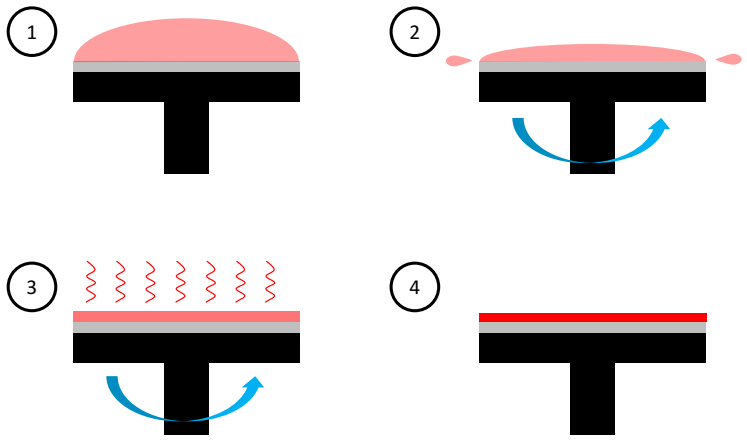


Figure 2.6: Formation of a film by spin coating. 1: Solution deposition. 2: Substrate spinning. 3: Evaporation. 4: Film formation.

time, speed and acceleration.

2.5.2 Atomic-Layer Deposition

Atomic-layer deposition (ALD) is a relatively modern deposition technique, in which a material can be deposited with a thickness controlled down to the atomic level. This technique can provide an extremely conformal coating, even on samples with complicated topology. The deposition is done by a sequential gas injection of specially designed precursors.

To make a typical (AB) compound by ALD, two precursors are needed : a precursor containing the atom A and a precursor containing the atom B. These precursors are designed not to react with themselves or with the same category of precursor. However, they are required to react with the other precursors.

A standard cycle of deposition is represented in figure 2.7. On the first step, a full layer of precursor A is created, by reaction with the active groups on the surface of the sample. During this reaction, side products are created, and need to be removed from the chamber, with a nitrogen purge. Due to the particular nature of the precursor, a perfect monolayer is achieved, and active groups for the precursor B are present on the surface. The precursor B is then released, making a perfect monolayer, and creating new actives groups for precursor A on the surface. In that way, the cycle can be repeated as many times as it is needed. Between each precursor release, a purge is needed, to remove the unreacted precursors, and also the created biproducts (waste).

Before the first precursor's release, active groups need to be present at the

surface to allow the reaction of the precursor, and the formation of a monolayer. The substrates used in this thesis are all oxide compounds (silicon dioxide or fluorine-tin-oxide) and hydrophilic treatment such as Uv-Ozone, creates hydroxyl groups on the surface of the sample, which then react with the first precursor.

The described ALD cycle is only ideal, with a monolayer growth, if the deposition temperature is inside the so-called ALD window. If the temperature is too high or too low, an incorrect growth will occur, with parasitic effect that will disturb the ALD deposition.

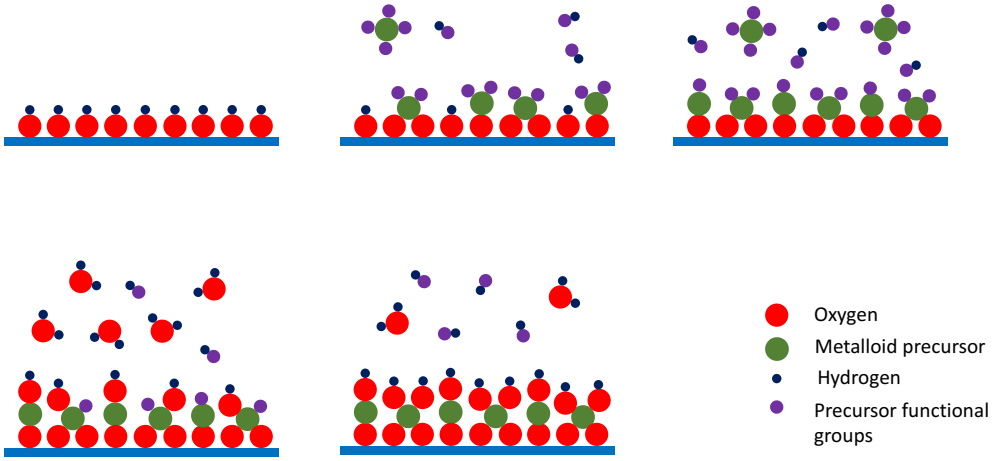
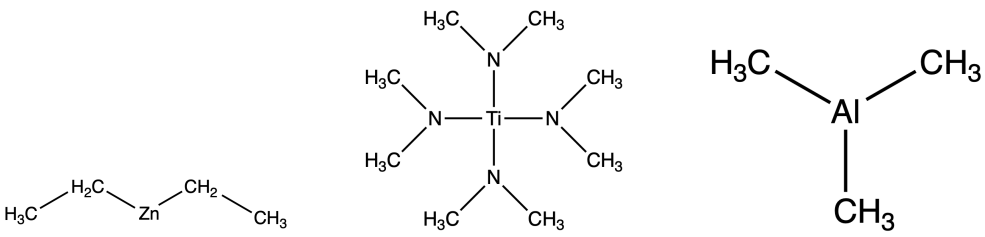


Figure 2.7: Schematic ALD different stages for metal-oxide deposition

The ALD used in this thesis is a homemade machine, built by a previous PhD student. It is designed to deposit metal-oxide compounds, in a chamber with a maximum temperature of 200°C. A total of 3 materials can be deposited with this setup : zinc oxide, titanium oxide and aluminium oxide, using diethyl zinc (DEZ), tetrakis(dimethylamido)titanium (TDMAT) and trimethylaluminum (TMA) respectively as a metal precursor, and water as an oxygen precursor.



(a) DEZ (b) TDMAT (c) TMA

Figure 2.8: Precursors used in the Atomic Layer Deposition machine

The previously mentioned materials can be doped, by mixing different precursors during the deposition. For instance, one cycle of aluminium oxide every 10

cycles of zinc oxide, is a way to make aluminium doped zinc oxide, which is a transparent conductive oxide (TCO). It is also possible to dope materials by changing the deposition temperature, which will lead to more or fewer vacancies inside the material.

2.5.3 Metal evaporation

To deposit a homogeneous layer of metal on a sample, the evaporation method is one of the most useful methods. The whole process is done under high vacuum, inside a chamber which is itself inside a glovebox, and which is schematised in figure 2.9. Pellets of metallic materials are deposit on a conductive holder, also called a boat, through which an intense current is passed. This current increases the temperature of the boat and the pellets, until the evaporation of the latter.

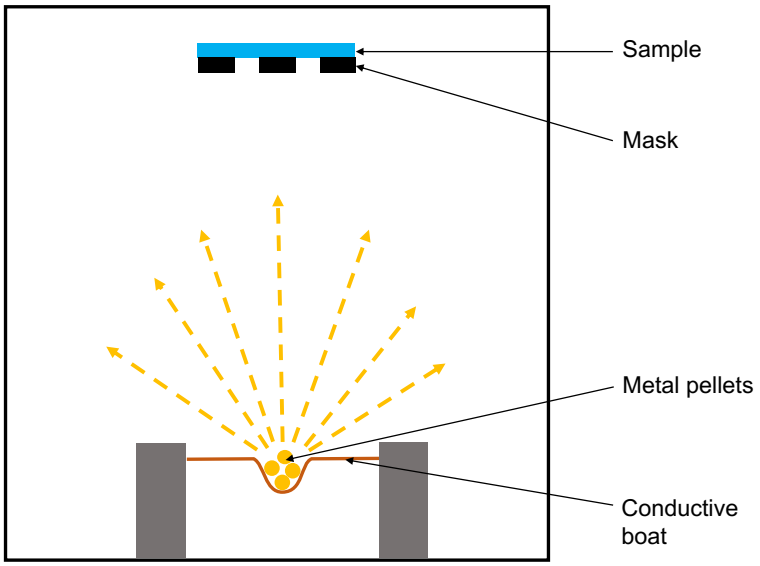


Figure 2.9: Schematic of the vacuum chamber used for metal evaporation.

The evaporated metallic atoms then travel in a straight direction, until they arrive on a surface, where they deposit. The sample is placed face down, to allow a deposition on its active face. A mask can be placed in front of the sample, which allows the deposition of the metallic atoms only on a selected area, creating a pattern on the sample.

To control the deposited thickness on the sample, a quartz balance is present in the chamber, with its active face directing toward the metallic pellets. Knowing the distance of the balance to the pellets, the rate of evaporation of the metallic atoms can be deduced, which enables an accurate control of the deposition.

2.6 Structural Characterisation

2.6.1 XRD

The X-ray diffraction (XRD) is one of the most well known techniques to characterise crystalline materials. In this technique, X-rays with a known wavelength are sent to a sample. Due to the order of the atoms in a crystal, and of the similar length between the atomic plans and the X-ray wavelength, a diffraction phenomenon occurs, where the x-rays are strongly reflected for specific angles.

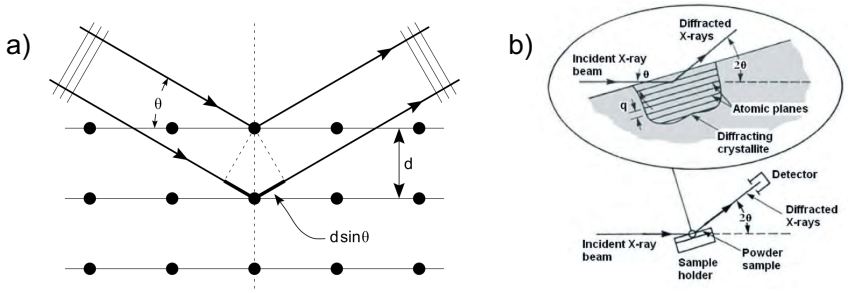


Figure 2.10: *a)* Path difference between two coherent beams, interacting with the first and the second layer of a crystal. *b)* X-ray gun and detector in a parallel position, to only take into account the crystal plane parallel to the surface of the sample. Reproduced with permission from [11] and [12] respectively.

The incoming X-rays are shown schematically in figure 2.10 *a)* coming from the left. These rays are in phase, and the wavefront is oriented perpendicular to the direction of the beam. A part of the beam is reflected by the first atomic layer, while another part is reflected by the second. Because of the different distance taken by the different parts of the beam, they now have a different phase. However, if the path difference equals a multiple of the wavelength, the different parts of the beams are in phase, which results in a strong diffraction intensity in the reflected direction of the incoming light. With trigonometric considerations, the path difference between the two parts of the beam is calculated as $2dsin\theta$ (figure 2.10) . When this difference is equal at an integer multiplied by the wavelength, there is constructive interferences. This condition is known as Bragg's law, and is expressed in equation 2.9.

$$m\lambda = 2dsin\theta \tag{2.9}$$

This analysis of a polycrystalline thin film by XRD is also known as powder diffraction, because of the many orientations of the crystals composing the film, in the same way as a randomly organised powder. Due to their multiple directions, an incident X-ray beam is diffracted towards many different angles at each angle of measurement. To avoid unwanted signals, the detector is placed symmetrically to the x-ray tube. In this way, only the samples which have crystal plans parallel to the substrate are measured (figure 2.10 *b*).

The analysis is done my measuring the diffracted x-ray intensity for many θ angles. At every variation of the incident angle, the detector is also moved, to

conserve the symmetry of the system. For incident angles which satisfy the Bragg law, an intense reflection peak is observed. The result of the acquisition is represented as the measured intensity versus the acquisition angle (expressed in 2θ), and consists of sharp peak positioned at different angles. By measuring the position of these peaks, and knowing the wavelength of the incident X-ray, the inter-planar distance between different atomic plans can be deduced using equation 2.9. With these values, the nature of the analysed crystal can be deduced, by comparison with references tables.

2.6.2 TGA/DSC

Differential scanning calorimetry (DSC) and thermogravimetric analysis (TGA), are used to detect some temperature-related properties of materials, such as melting and crystallisation temperature, or decomposition temperature. These two techniques are different, but give complementary results for a wide range of materials. For this reason, some equipment can do them both at the same time, on the same sample. We describe here both techniques separately, then explain how they can be combined in one measurement.

In DSC, we measure the amount of energy required to increase the temperature of a sample, or oppositely, the energy released when the sample is cooled down. When no phase reaction or phase change occurs, the energy required to increase the temperature of a material is directly related to its heat capacity. However, if an endothermic (exothermic) process happens, the energy required to increase the temperature of the material will increase (decrease). The analysis of the peaks or trench positions that results from the difference of energy required, indicates what kind of process happens in the material, and at what temperature.

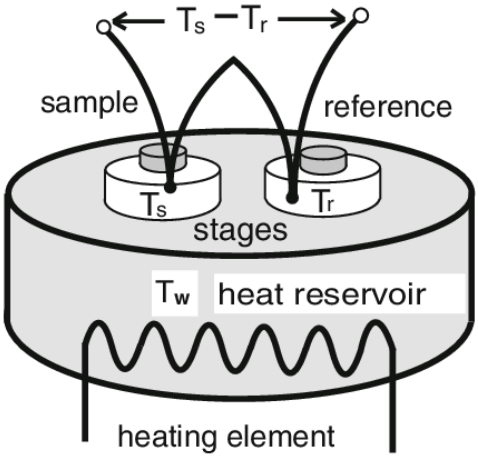


Figure 2.11: Schematic of a differential scanning calorimetry measurement cell. Reproduced with permission from [13].

In order to measure in an accurate way the energy transferred to a material, a system described schematically figure 2.11 is used. The heating reservoir is

considered as being very large compared to the sample and the reference, and these two elements do not affect its temperature. By measuring at the same time the difference of temperature between the reference and the sample, one can calculate the heat capacity of the sample, and detect its phase change.

Thermogravimetric analysis measures the loss of mass occurring in a material under annealing. The mass loss can occur due to evaporation of some component of the sample, or because of chemical reactions within the material itself or with its gaseous environment (if not pre-evacuated and sealed), indicating degradation of the material. The mass change is measured by using a precision frequency balance, whose own frequency varies with the mass of the sample.

To use both TGA and DSC simultaneously, a frequency balance with an integrated temperature measurement probe is used. In this system, two sample holders are used, and one is kept empty to be used as a reference system for the DSC. The system is used in air for standard measurements, but nitrogen can also be used.

2.7 Simulations

In this thesis, two freely available and open-source software packages, named MIT Photonic Bandgap (MPB) and MIT Electromagnetic Equation Propagation (MEEP) are used to simulate the interaction between light and photonic crystals. These two software packages provide solutions for two different kind of systems, with two different methods.

Due to the large amount of data that needs to be processed to solve some systems, not all simulations can be executed on personal computers because of the lack of calculation power and thus the excessive time required to complete the simulation. Instead, High Performance Computing (HPC) is used, and the calculations are done on a supercomputer at Imperial College London. The use of HPC allows the run of many simulations in the same time, as well as parallel calculations, which drastically reduces the required time needed to complete calculations.

2.7.1 MPB

MPB is a freely available software package which is used for the calculation of the optical band-gaps of periodic dielectric structures. It solves the master equation 1.10 for different values of k, which provides the frequency eigenstates associated with each k-vector. An optical band-gap (OBG) can be identified when no k-vectors are associated with a given frequency.

The procedure to use this software package is described hereafter.

1) The user first have to describe the dielectric function $\epsilon(\mathbf{r})$ of the struc-

ture. Because the structure used are periodic in three dimensions, this is done by fully describing the unit cell, and by specifying the three lattices vectors, if we use a crystallographic analogy. The unit cell is specified in a continuous way, with ideal structures such as sphere or blocks, but is then discretised in a three dimensional mesh. The size of the mesh is left to the user, and an optimum between accuracy and computation time has to be found.

Because of the previously mentioned scale-invariant property of the master equation, MPB uses unitary distances to define the structure. In this way, any structure with the same dilated or compressed dielectric function can be solved by a simple multiplication of the final result.

2) The wave-numbers k, for which we want the fields to be computed, have to be specified by the user. The most common way to select relevant values for k, is to find the coordinates of the edges of the Irreducible Brillouin Zone (IBZ), and to interpolate a defined number of points along each axis, as it is shown in figure 2.12. The IBZ is not calculated by the software, but it can easily be found for most of the structures, in pre-calculated tables.

It should be noted that with this discretisation method, we only uses k-values which are on the edges of the IBZ, and we forget the ones which are purely inside it. It is acceptable to do so in most of the simple cases, because many of the interesting effects takes place for k-values on the edges and on the corners of the IBZ.

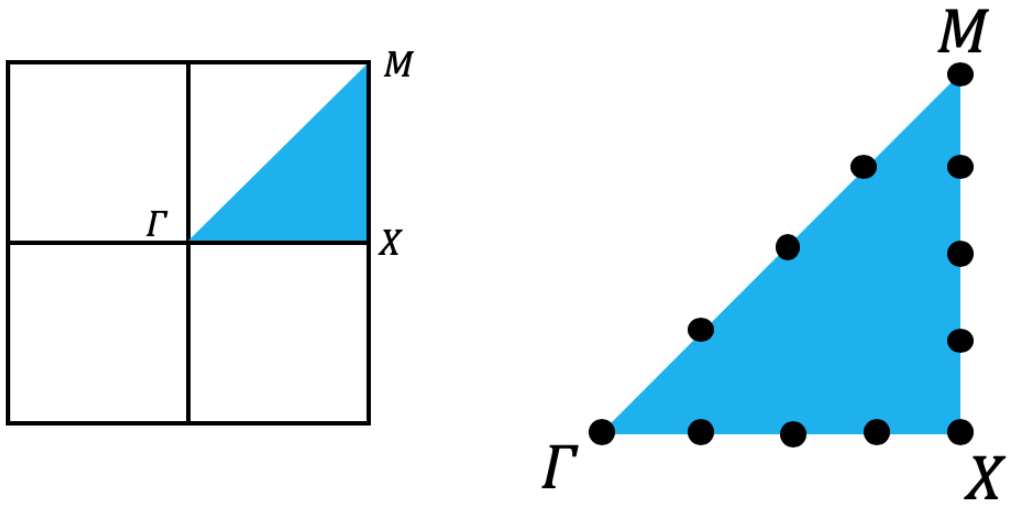


Figure 2.12: *Left :* First Brillouin Zone and Irreducible Brillouin Zone (in blue) for the k-space associated with a 2D square lattice. *Right :* Irreducible Brillouin Zone, and discrete choice of specific k-values amongst the edges, represented by black dots. The Greek letters used Γ , M and X are typically used as names for the corners of the IBZ.

3) For each value of k which we are interested in, MPB will solve the master equation 1.10, which is an eigenvalue problem, with the eigenvalue $(\frac{\omega}{c})^2$ and $H(r)$

as an eigenvector. This procedure is facilitated by the known approximate form of $H(r)$, expressed in equation 1.12, in one dimension. For each value of k, there is a series of solutions to the master equation, each corresponding to a different eigenvalue, and they represent different modes of light. MPB finds the solutions of the master equation one after the other, for increasing value of ω. The number of solutions, or "modes", calculated needs to be specified by the user.

The output files from the software take the form of a table, in which each selected k-value is associated with a list of eigen-frequencies. The frequencies are given in $\frac{c}{a}$ unit, with values for $a = 1$ for the initial simulation. Depending on the scale of the structure, the value of a is changed, to obtain the correct frequencies.

A standard calculation with MPB is relatively fast, but the required time will increase with the dimensions. The calculation of 20 k-values for a three dimensional structure, with 5 frequencies for each, takes approximately two hours.

2.7.2 MEEP

MEEP is the second specialised software used in this thesis, and is also dedicated to optical simulations. Contrary to MPB, MEEP is not solving an infinite structure in the spectral domain, but is simulating a field propagation in a finite structure. Because the Maxwell equations cannot be solved analytically for complex structures, MEEP uses a method called Finite-Difference Time-Domain (FDTD), in which space and time are discretised.

In FDTD, the three-dimensional structure is divided into many small cubes, in a regular way. If we consider a random cube in the structure, its faces have the coordinates x, y, z for three of them, and $x + dx, y + dy, z + dz$ for the three others, where dx, dy and dz are considered as small, in regards of the dimensions of the structure.

For the FDTD method, the approximation 2.10 is used, allowing a simplification in the solution of Maxwell's equations 1.5. For simplification, we only describe a one-dimensional case, with a function E only depending on x and t.

The equation given as an example simplifies the derivation on the x direction, and is also true for the derivation in time, using $E(x, t)$ and $E(x, t + dt)$.

$$\frac{dE}{dx}(x,t) \approx \frac{E(x+dx,t) - E(x,t)}{dx} \tag{2.10}$$

If we consider a one-dimensional case, knowing $E(x, t)$ and $E(x + dx, t)$ and using equation 2.10, the values of $E(x, t + dt)$ and $E(x + dx, t + dt)$ can be deduced, by taking into account the parameters of the structure inside the segment $[x, x + dx]$. By this method, we can deduce the value of E for all the calculated points, and their evolution with time.

For the three-dimensional case, the small cube defined previously, which we call a finite element, is used for the simplification of Maxwell's equations. The knowledge of the value of E on all the faces of the cube for a defined time t, as well as the known values of the dielectric constant inside the finite element, gives us the values of E for the time $t + dt$. By repeating this operation on all the finite elements of the defined structure, and for a chosen time, the fields propagation is calculated.

Unlike MPB, MEEP allows many materials for the definition of the structure, which can have real or complex dielectric constants, or even the presence of a current density for instance.

The calculated fields posses known values only at the vertices delimiting the shapes of the finite elements. If one requires a better accuracy, the size of the elements can be reduced, thus providing more data-points. However, this solution can become easily time consuming. An improvement of 2 of the finite distances used, increases by 8 (=2*2*2) the amount of required values to be calculated. In addition, the time-step is also divided by two, because a shorter distance between vertices implies a shorter time of propagation between them. In total, a factor-of-2 decrease in the size of each finite elements, increases by 16 the time needed to perform the calculation.

The standard way to use MEEP is to first define at least one source inside the structure. The source can be either monochromatic, where a field with a single frequency is generated, or polychromatic. For the polychromatic case, a pulse is generated, and by Fourier decomposition, we know that this pulse is composed of many frequencies. The frequencies chosen by the user for the polychromatic source are generated by changing the size and the shape of the pulse.

The signal then needs to be measured on at least one area. The defined area is integrating the measured energy passing through it with time, by calculating the Poynting vector on each of the finite elements touching the area. In the polychromatic case, a Fourier transform is automatically done by MEEP, to convert the information coming from the pulse, into frequencies.

Chapter 3

Opal and Inverse Opal Fabrication

This chapter presents initial results of optimisations carried out to produce opal photonic crystals, which are necessary to make inverse opal in a second step. An optical analysis of these structures in also made, in two different ways. To finish, two methods of precursors infiltration inside opal are presented, as well as the calcination of these infiltrated precursor to make crystalline inverse opal.

As this thesis focuses on the use of inverse opal for devices, the work presented in this chapter only aims to provide a reliable and repeatable method to produce inverse opal. The assembly mechanisms and physical process are not studied in detail, and the following analysis does not aim to study the impact of all the variations in parameters, nor giving the most optimised way of producing such structures. The impact of the different parameters on the self assembly of colloidal crystals can be found elsewhere [163].

3.1 Evaporation-Induced Self Assembly

In this work, the photonic crystals are exclusively prepared by evaporation-induced self assembly, the theory of which is given section 1.3.3. In brief, a substrate is placed inside a vessel containing an aqueous suspension of monodispersed nanoparticles, and is then heated to evaporate the water. Upon evaporation, the nanoparticles are driven to the meniscus at the interface between the substrate and the water surface, and they self assemble in a periodic structure. The thickness of the formed opal is highly dependant of the nanoparticles' concentration, as well as the evaporation rate of the water[164][165].

A schematic of the process of fabrication of opals by evaporation induced self assembly is shown in figure 3.1. A diluted suspension of PS-nanoparticles is firstly made inside a vial, and a substrate is then vertically immersed inside the suspension (figures 3.1 *a* and *b* respectively). The suspension is then let to dry completely, which progressively form a film on the substrate, due to the self-assembly of the nanoparticles (figures 3.1 *c* and *d*).

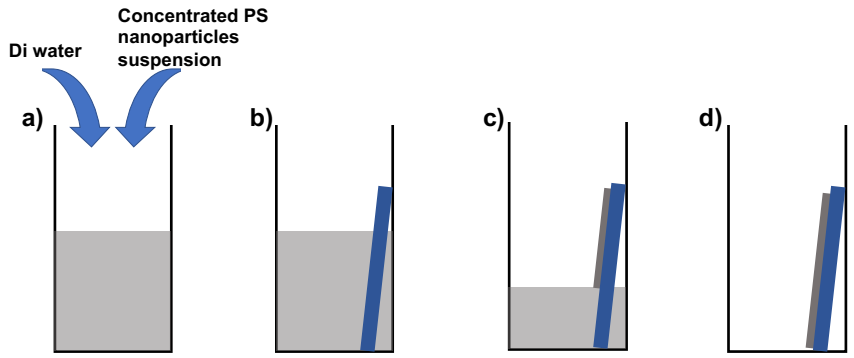


Figure 3.1: *a)* Dilution of a stock solution of PS-nanoparticles in DI water. *b)* Vertical deposition of a substrate inside the diluted suspension of PS-nanoparticles. *c)* Upon evaporation of the solution, formation of a film on the substrate due to the deposition of the nanoparticles. *d)* Full film on the surface of the substrate at the end of the evaporation.

In order to obtain repeatable results, the solutions are evaporated under a controlled atmosphere, in an oven where the temperature is homogeneous and stable[5]. By doing so, the solution temperature is also homogeneous. It should be noted that another solution is to use a hot plate, which produces a hot temperature on the bottom of the vial, and a colder one on the top due to the air, giving a temperature gradient. This can be beneficial for the self-assembly due to convective fluxes inside the solution, but because the atmosphere temperature is not controlled, this method can lead to variable results.

The relative humidity also needs to be controlled, to adjust the evaporation rate of water. For this reason, a humidity controlled oven is used in this study. In addition to providing a stable atmosphere with low or high relative humidity for an extended period of time (figure 3.2), the samples are within a closed area, protected from any external perturbations. It should be noted that when no power is provided to the equipment, the temperature slowly decreases to room temperature, as seen figure 3.2 *a)*, where the temperature is maintained for a fixed duration of 48 hours only.

Before reaching the given set-points for temperature and relative humidity, a transient phase is observed. During this phase, the temperature is firstly increased until the given set-point is reached, which also has the effect of decreasing the relative humidity within the chamber. When the temperature set-point is reached, the relative humidity is then increased to its own set-point. This whole procedure can take approximately one hour, as shown on figure 3.2 *b)*, with the initial decrease of the RH, followed by its increase until reaching its set-point. Due to its relatively short time compared to the total evaporation time (more than 48 hours), this phase does not prevent the good deposition of the nanoparticles.

The humidity oven is placed directly on the floor of the laboratory, but far from the walking area, to minimise vibrations which could disturb the self-assembly. This equipment allows the samples to be produced in batches, due to its large size of approximately 100L. The samples are always put at the same place, approximately at

the centre of the oven, in order to minimise any potential variations of temperature and humidity. The air pressure can also be controlled to improve the quality of the deposition[166], however this possibility is not studied here.

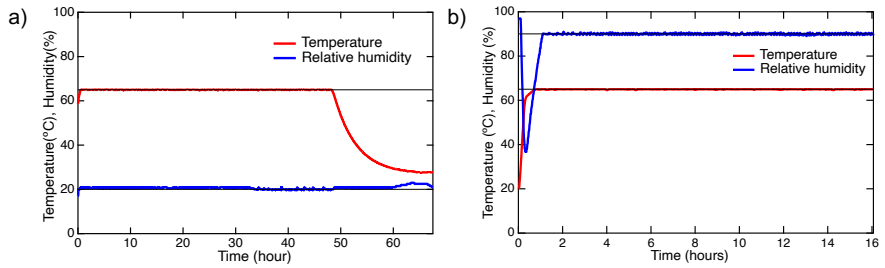


Figure 3.2: Stability of temperature and relative humidity inside the humidity oven, for a *a)* low level of humidity of 20 % RH and a temperature of 65 °C for 48 hours, and *b)* a high level of humidity of 90 % RH and a temperature of 65 °C.

As seen in the literature, evaporation-induced self-assembly does not create a sample with a homogeneous thickness. Three zones can be seen in an average sample, as seen figure 3.3, and the thickness of the opal increases when reaching the bottom of the sample. This increase of thickness is due to the variation of the concentration of nanoparticles in solution, which increases with time. Indeed, as the concentration of PS-nanoparticles is increased due to the evaporation of water, and decreased by the assembly of the nanoparticles on the sample, its value changes over time if the rates associated with these two effects are not identical.

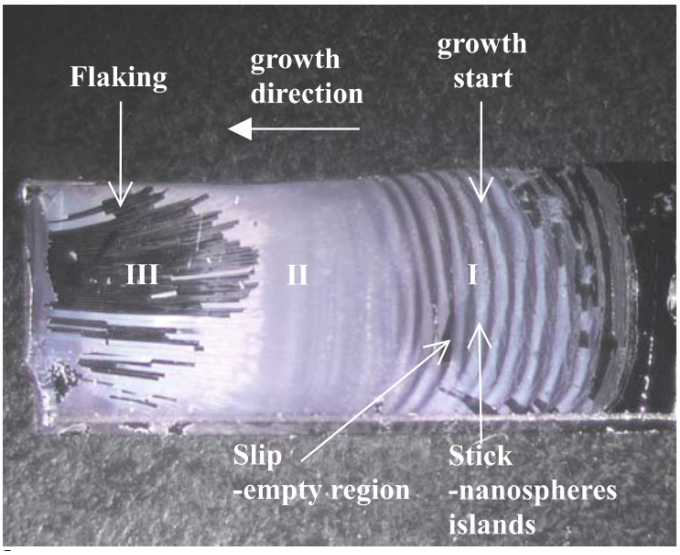


Figure 3.3: Distinct regions on a sample made with evaporation induced self assembly. Deposition from right to left. Reproduced with permission from [14].

The inhomogeneous thickness of the opal sample can be a problem for the realisation of devices. However, as it will be seen in chapter 4, the devices made in this thesis have a square shape, and a size of approximately 1x1cm^2. The samples made by evaporation induced self assembly are rectangular, and so, need to be cut after deposition to have a square shape which can be used as a device. For this reason, the dimensions of the initial sample are bigger than the final device, and

are of approximately 1x2.5cm^2. When the extremities of the samples are removed, it both gives the sample the correct size for a device, and removes inhomogeneous parts from it. As only the centre part of the sample made with EISA is thus used, only this part is taken into account for all the analysis in the thesis.

3.2 Opal fabrication

A brief work on the deposition of nanoparticles by EISA and the optimisation of the main parameters are presented hereafter. As explained previously, the goal of this section is not to study individually the impact of each parameter, but to find a reliable method to obtain opal photonic crystals. For this reason, several parameters can be changed at the same time, and not separately to study their individual contribution.

If not specified, the substrate is a glass substrate of 1x2.5cm^2, which is cleaned by residing for 10 minutes in an acetone bath under sonication, followed by a cleaning with isopropanol for 10 minutes under the same conditions. The sample is then dried with an air gun. The container used for the suspension of nanoparticles is a borosilicate specimen tube with a height of 50mm and a diameter of 19mm, which is also cleaned by isopropanol prior to utilisation. The nanoparticles used in this section have a diameter of 250 nm, unless specified.

3.2.1 Temperature and relative humidity

Temperature and relative humidity are two of the most important characteristics which determin the quality of an opal. Both these parameters can be controlled with great accuracy and for a long time inside a humidity oven.

If relative humidity is not controlled, temperature alone does not significantly influence the thickness of the deposited opal. If the temperature is increased, the evaporation of the water is faster, but the nanoparticles have more kinetic energy, and thus can self assemble faster. As these two effects balance each other out, the thickness of the final opal is not greatly influenced. However, a high kinetic energy, and thus a high temperature, is preferable for the opal formation, as nanoparticles with high energy can reach more easily their equilibrium position, giving a better opal.

When a temperature of 70°C was used for the opal formation, without any control on the relative humidity value, the 5 ml of suspended nanoparticles (250nm, 0.1% concentrated) is totally evaporated in one day. Due to the fast evaporation speed, a stick slip effect occurs during the deposition, and the sample is composed of regular horizontal stripes, as seen figure 3.4, with very weak photonic effects occurring on these stripes [6].

In order to reduce the evaporation rate of water without decreasing the

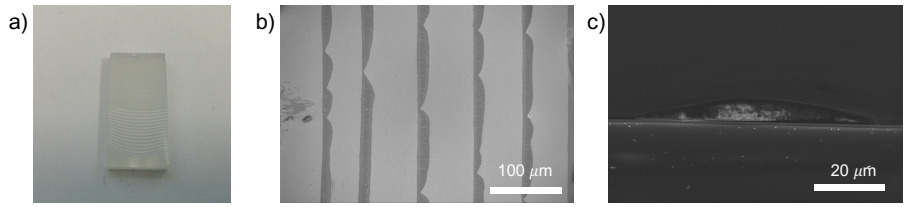


Figure 3.4: *a)* Photography of an opal presenting regular striped defects. *b)* SEM top view of a striped samples, showing the absence of material between the stripes, and *c)* cross section SEM of a stripe.

temperature, a controlled amount of relative humidity (RH) is introduced in the oven. The equipment takes into account the water evaporated from the nanoparticles suspension, in order to maintain a stable value for the RH. With the same temperature of 70 $°C$, but this time with a RH value of 60%, the 5ml of suspension takes this time approximately one week to evaporate, *i.e.* an average growth rate of 5mm per day.

The samples made in this way do not exhibit stripes, and are homogeneous over large areas. They also exhibit good photonic effects, on their centre part, which are analysed in the next section. The structures are analysed by electron microscopy on the middle area, which is the area considered for inverse opal making. Because of the insulating property of polystyrene, the samples are coated with 10nm of chromium prior to the analysis. The samples are imaged from the top, and from an angle of 45°. The results are presented figure 3.5.

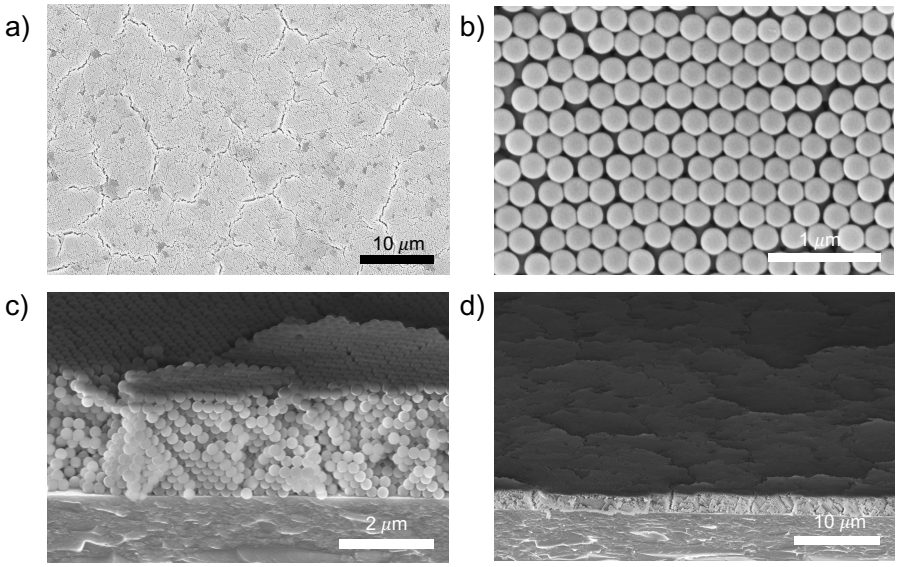


Figure 3.5: *a):* SEM top and *b):* magnified top view of an opal made of 250nm polystyrene nanoparticles, made by evaporation induced self assembly, with a temperature of 70°C and a relative humidity of 60 %. Observation under standard *c:* and magnified view *d:* of the same sample, with a 45° tilt.

The observed photonic crystals are homogeneous and continuous over a large area. Randomly oriented cracks are presents all over the surface, which are due to the drying of the nanoparticles after deposition. The particles are deposited in

an organised way, and are forming hexagonal structures, corresponding to the [111] plan of a face centred cubic structure (figure 3.5 *a)*). They are not tightly packed together, and a certain amount of irregularities are present in the packing, making it not totally periodic (figure 3.5 *b)*). The thickness of the sample is approximately $3\mu m$ at the considered area, and a good order is still observed in the inside of the sample. Some particles ,which can be seen close to the surface of the sample (figure 3.5 *c)*), are disposed in a square packing shape which is the [100] plan of the fcc packing. From a further view, it can be seen that the cracks are not flat on the surface, but create hills at their locations (figure 3.5 *d)*).

The opals made at 70 $°C$ and with 60% RH present optical effects, as well as a correct organisation of the nanoparticles and a good homogeneity of the film. However, these samples take a long time to deposit, with an evaporation time of more than one week, and the packing of the nanoparticles can still be improved. To do so, the relative humidity is decreased to 20%, and the temperature to 60°C, which makes a complete evaporation in two days, without any horizontal stripes. In addition, the samples are treated with piranha solution, which greatly enhances the wetability of the substrate, as well as the mobility of the nanoparticles on it. Due to this higher mobility, the nanoparticles can be organised into a more ordered structure. The effect of the piranha solution, as well as the protocol to make it, use it and dispose it, is described in the next part.

This method of fabrication for the opal provides an extremely homogeneous sample, with regular cracks present along the direction of the deposition (figure 3.6 *a)*). The nanoparticles are closely packed together, and long-range order is observed (figure 3.6 *b)*). The flatness of the sample can be seen on an inclined view at 70°, where no particular topology is observed (figure 3.6 *c)*). The structure is very well ordered internally, as seen with the many hexagonal pattern seen from a cross section observation (figure 3.6 *d)*).

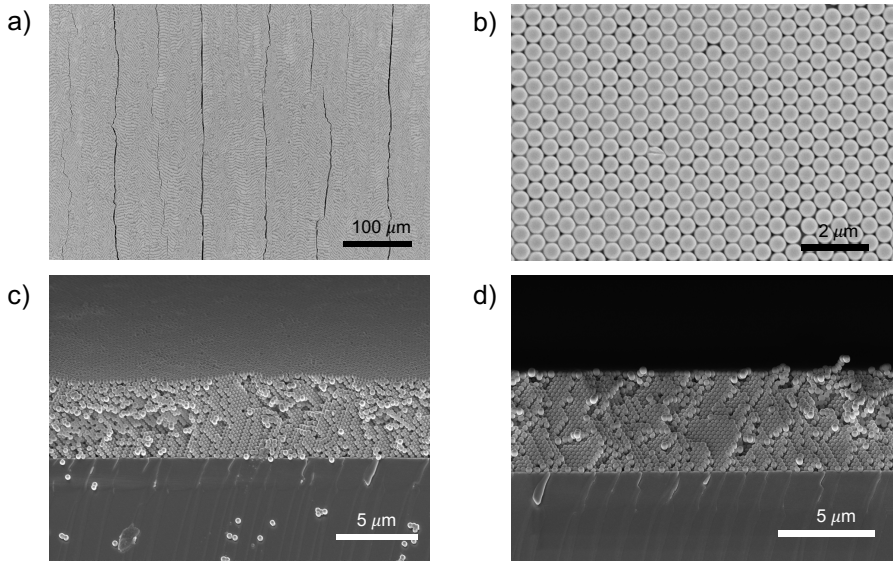


Figure 3.6: Far *a)* and close *b)* top view SEM pictures, and cross section at 45° *c)* and 90° *d)* of a 250nm opal, made by evaporation-induced self assembly, as 60°C, and 20% RH. The glass sample are treated with piranha solution prior to the deposition.

The choice of these parameters for temperature and relative humidity, as well as the surface treatment with piranha solution, provide excellent order and packing of the opal, as seen from top and cross section views. These three-dimensional periodic structures also provide good optical effects and are homogeneous over a long range, as seen by eyes.

3.2.2 Surface treatment

Borosilicate glass is naturally hydrophilic, with a surface energy of 83.4 mJ/m^2 [167]. The hydrophilicity of this material can be increased with the use of chemical or physical treatment. The surface energy of the substrate in the EISA method is a very important parameter, both for the meniscus shape and for the mobility of the nanoparticles on the surface of the sample, and to minimise its value is important in order to obtain a good quality opal.

A well-known technique for increasing the hydrophilicity of a material is UV-Ozone treatment, in which samples are put in a sealed space, under air. Ultraviolet light is emitted inside this space, and reacts with the di-oxygen molecules of the air, creating ozone according to equation 3.1. The newly created ozone can then be decomposed into highly reactive oxygen radicals, which react with the surface of the sample, oxidising unwanted materials on it, such as oil or solvent residues. After oxidation, the contaminants are vaporised into air, giving a clean surface and a very hydrophilic sample.

$$3O_2 \rightarrow 2O_3 \tag{3.1}$$

Even though the $UV - O_3$ method gives a more hydrophilic sample after treatment, it is possible to obtain better results with chemical methods. Amongst the possible methods, it is chosen to use the treatment by piranha solution, which both removes contaminants from the surface of the sample, and hydrolyses it, increasing even more the hydrophilicity[168]. Piranha solution is a very dangerous method, and has to be handled with care, with all the necessary personal protection.

The piranha solution is based on the creation of Caro acid, of formula H_2SO_5 which is one of the strongest oxidants. This acid is highly explosive and has a low boiling point of $45°C$, which makes it impossible to be bought directly. Instead, it is directly made in the laboratory by mixing sulphuric acid (H_2SO_4 , 95%) and hydrogen peroxide (H_2O_2, 37%), in a 3:1 ratio. This ratio has to be strictly respected, as a higher amount of H_2O_2 can make the solution explosive. The mixture is made by adding 30ml of H_2SO_4 in a beaker under a fume cupboard, followed by the slow addition of 10ml of H_2O_2. This reaction is very exothermic, and fumes are released from the solution.

Due to the strong reaction between piranha solution and any organic compound, the samples are carefully washed with acetone, isopropanol and DI water,

each time for 10 minutes in a sonicator, prior to their deposition in the piranha solution. The samples are left to react for at least three hours, with the solution being heated at $80°C$ during the whole time, to maintain its reactivity.

After the piranha treatment, the samples are carefully taken out of the solution, using teflon tweezers. They are then copiously rinsed using DI water, and dried using an air gun. Due to the extremely high hydrophilicity of the sample, the drying has to be done carefully in order to remove any drops of water. The samples are then directly dunked into the suspension of nanoparticles.

Due to its high reactivity, the piranha solution cannot be disposed in a conventional way like other chemicals. After being used, it is heavily diluted with DI water, and is let to rest for a full day. It is then slowly poured in the sink, with large amount of water to dilute even more the solution.

3.2.3 Zeta potential and solution pH

A suspension of nanoparticles with a zeta potential below -30mV (above 30mV) is considered as stable [169], since the nanoparticles repel each other sufficiently. The zeta potential plays an important role in the formation of colloidal crystal, as two stable suspensions can give different results. Different batchs of nanoparticle suspensions, from different supplier or not, can have different zeta potentials. An example is given in figure 3.7, where nanoparticles of 211nm from MicroParticles GmBh, have a zeta potential of -36mV, while nanoparticles of 211nm from Bangs Laboratories have a zeta potential of -45mV.

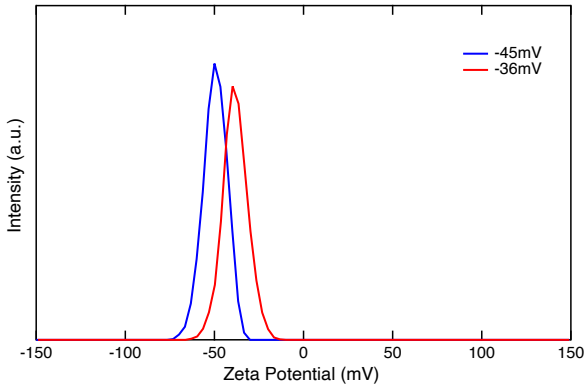


Figure 3.7: Zeta potential measurement of two batches of 211nm polystyrene nanoparticles.

For these two sets of particles, when processed at the same conditions of temperature and relative humidity, the suspension with the zeta potential of -45mV forms a good colloidal crystal, while for the other one, a striped structure similar to the one shown figure 3.4, is obtained. Although the two suspensions are stable in standard conditions, they behave differently during evaporation-induced self-assembly. As explained by the DLVO theory (section 1.3.2), the particles are stable in solution because they repel each other enough to not get trapped and stuck

together. However, in the meniscus where the evaporation happens, the density of nanoparticles is much higher than in suspension. In addition, the surface tension of water brings the nanoparticles close together, which eventually leads them to stick to each other. In these conditions, the nanoparticles with a higher zeta potential repel each other for a longer time, which allows them to form a structure with the lowest potential, which is a packed colloidal crystal. On the other hand, the nanoparticles with a weaker zeta potential aggregate faster, which can lead to a disordered structure. Due to this faster aggregation, a stick slip effect can occur, where a thick region of disordered particles is formed, followed by an empty area, due to the meniscus moving too fast.

Such suspensions of nanoparticles can still be used, by adding a small amount of base to it, which lowers the zeta potential. By doing so, the suspension becomes more stable, and a correct self assembly occurs in the meniscus. When a very low zeta potential is reached, the nanoparticles are so stable that they still form a hexagonal packing between them, but triangular shapes are also observed on top of the structure. An example is given figure 3.8, where PS particles terminated with COOH groups concentrated at 0.1%, with an addition of $50\mu l$ of 0.1M NaOH in a 5ml suspension, form many triangular shapes all over the sample. As explained previously, the nanoparticles form a compact hexagonal shape to decrease the total energy between them. However, before the particles come into contact and overcome the potential barrier, due to the strong repulsion between them, the nanoparticles can form structures which maximise the distance between themselves. Instead of a flat homogeneous surface, the triangular shape deposited on top of the surface, can increase the average distance between all the particles.

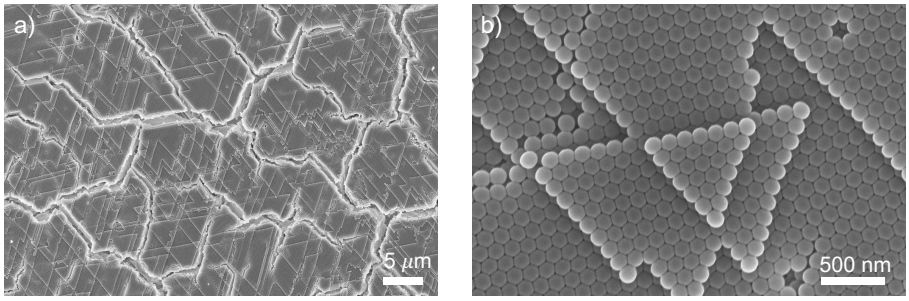


Figure 3.8: *a)* COOH terminated nanoparticles, deposited under basic conditions ($50\mu l$ of 0.1M NaOh in 5ml of 0.1% suspension), exhibits a highly structured pattern. *b)* Magnified view of the opal, showing the regular triangular terraces due to the highly negative zeta potential.

On the other hand, any addition of acid in a suspension of negatively charged nanoparticles, would reduces their zeta-potential, which reduce the quality of the formed colloidal crystal. This addition of acid can of course be done by adding an acidic solution in the suspension, but it can also occur because of an acidic atmosphere, which condenses into the suspension. As detailed in chapter 5, acidic solution can be used for evaporation induced self assembly, for the formation of specials opals or inverse opals. After the evaporation, the molecules of water, but also the ones responsible for the acidity, stay in the atmosphere of the incubator. The opening and closing of the door of the incubator, to remove a batch of samples and insert a new one, does not renew perfectly its atmosphere, due to the absence of air

flux inside the machine. The solutions of the new batch of sample, can become more acidic, due to the condensation the acidic molecule of the incubator's atmosphere inside them, leading to a bad self assembly.

To prevent this, the incubator is purged, after each deposition involving acidic solutions. To do so, a lot of water vapour is injected into the incubator atmosphere, to reach a relative humidity of 95%, and a temperature of 65 $°C$. When these conditions are reached, the door of the incubator is opened, and a lot of vapour comes out of it, due to the difference of relative humidity between inside and outside. With this humidity, most of the acidic compounds present inside the incubator are also removed. The door is let open until the relative humidity reaches a stable value, and this process is then repeated 3 times in total.

3.2.4 Vial characteristics

An easily forgotten aspect of the EISA method is the vial itself, and its different characteristics. Different vials have been tested in this thesis, to detect which parameters can influence the opal formation, and to select the vial giving the best resulting structures.

Firstly, the shape of the vial containing the liquid has been tested. Standard cylindrical vials possess a screw thread at their top, to enable a lid to be screwed on top. The neck of the vial, where the thread is located, is narrower than the rest of the vial, to have a cylindrical shape when the lid is screwed on it. While necessary for a standard utilisation of a vial, this neck influences the evaporation during the EISA. Having a smaller opening than the main body of the vial, is retaining humidity inside it, which can lead to a humidity saturated environment, which can interfere with a good deposition. For this reason, we choose to perform evaporation with vials having a wide opening, without any thread, which is not needed for our experiments. They can be specimen tubes, or simply beakers, as both provide a large opening.

The size of these vials is now considered. The size of the substrates being approximately 1x2.5cm^2, only vials which can contain substrates of these dimensions are considered. As previously mentioned, the substrate is totally immersed in the solution, to avoid any loss of coverage. For this reason, a vial with a greater height than the sample is needed. For the choice of the vial width, we compared the deposition done in a vial of 19mm diameter to that done in one of 24mm diameter, under the same conditions and with the same solution. The vial of 24mm diameter requires more volume to fill it up to at the same level and totally cover the sample.

The evaporation made in the wider vials does not lead to a homogeneous deposition, but rather gives stripes of white colour, indicating a disorder in the structure (figure 3.9). The white lines can be explained with the stick-slip effect which occurs if the concentration of nanoparticles is not high enough, or if the deposition speed is too fast. In the case of this experiment, the nanoparticle concentration in both vials is the same, so the reason for the stick sleep effect occurring is the

different evaporation rate between the 2 vials.

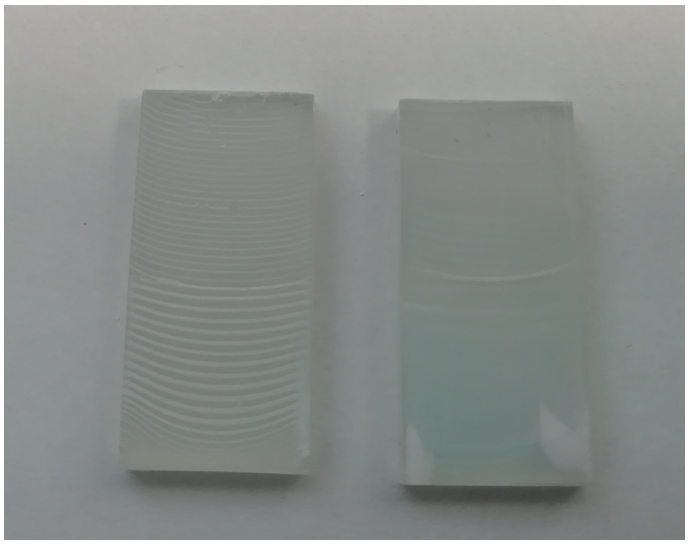


Figure 3.9: 211nm PS nanoparticles evaporated in a 24mm diameter vial (*left*) and a 19mm diameter vial (*right*). Both samples are evaporated in the same conditions, at a temperature of 60 °C, and a relative humidity of 20%.

This result leads us to the hypothesis that the relative humidity measured inside the incubator is not the same as the one inside the specimen tube. The incubator is closed and there is no fan inside it, so no air flux is present inside it. In this case, the only mechanism providing movement of species is diffusion, which is a slow process. The vial acts as a source of humidity in our case. The atmosphere inside of it probably always has a higher relative humidity than the rest of the environment, indeed, the diffusion alone cannot equilibrate the difference in humidity.

In the case of a wider vial, there is more space for the diffusion to occur and to let the humidity escape the vial. With a lower relative humidity inside the vial, the water evaporates faster, explaining why we have a stick slip effect with a wide vial, while we do not with a smaller one. This effect could be avoided by reducing the speed at which the water evaporates, either by decreasing the temperature, or by increasing the relative humidity inside the incubator. However, because a lower temperature would give a less ordered structure, we prefer using the vial with a small opening at higher temperature. In addition, a bigger vial requires a greater volume of suspension to cover the substrate totally, which consumes more material.

The last parameter of this study is the material of the vial itself. During the evaporation of the solvent, the nanoparticles are deposited on the substrate, but also on the vial. For this reason, different vial materials lead to different deposition on their surface, affecting the amount of nanoparticles in the suspension, and influencing the deposition on the substrate.

Two materials have been tested for the vials, borosilicate, which is hydrophilic, and polytetrafluoroethylene, also known as PTFE, or Teflon, which is strongly hydrophobic. The borosilicate vial is a specimen tube of 19mm diameter, while the PTFE container is a beaker, of 22mm diameter. Both containers are

filled with the same concentration of 250nm nanoparticles (0.1% concentration), and evaporated under controlled conditions, with a temperature of $60°C$ and a relative humidity of 20 %.

After complete evaporation, the surface of the borosilicate vial presents an intense green colour, due to the deposition of the nanoparticles in an opal structure. On the other hand, the PTFE beaker does not present any colour, and no deposited materials is seen on its surface. Indeed, due to its hydrophobicity, the hydrophilic PS nanoparticles are not attracted by it. The sample made with the borosilicate vial presents the same green colour as the surface of the vial, and can be seen through. The one made from the PTFE beaker also presents a green colour if observed at the correct angle (specular reflection), but is completely opaque, and shows a strong white appearance when observed from any other direction.

The white colour, as well as the opacity of the last sample, is characteristic of a strong light scattering. When looked in cross section, the sample made inside the PTFE beaker is approximately 4 times thicker than the sample made with the borosilicate specimen tube (figure 3.10). It is supposed that the substrate width, which we call d, is approximately half the diameter of the specimen tube, and that the polystyrene nanoparticles are deposited equivalently back and front of the substrate. The perimeter of the specimen tube is $2d\pi$, which can be approximated in $6d$. In these conditions, the surface in contact with the solution meniscus for the borosilicate vial, where the deposition occur, is equal to $2d$, due to the two sides of the substrate, plus $6d$ due to the specimen tube, which gives a total of $8d$. For the PTFE beaker, the length with a meniscus is only $2d$, due to nanoparticles not depositing on the surface of the beaker. The deposition thus occurs over a surface that is 4 times smaller in area, in the case of using a PTFE vial. However, because the same quantity of nanoparticles are deposited, due to the same concentration of nanoparticles used, the final thickness is theoretically four times greater in the case of a PTFE beaker, which corresponds well with the observation.

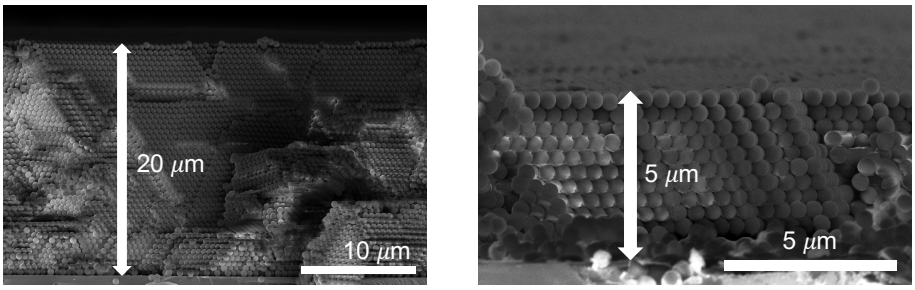


Figure 3.10: Cross section SEM of an opal made in a *a)* PTFE vial and a *b)* glass vial. The deposition conditions are identical for both samples.

The use of a PTFE beaker prevents the loss of nanoparticles depositing on the surface of the vial, which are not used for the rest of the experiments. As seen before, the deposited thickness is approximately four times those obtained with a borosilicate vial. Lower concentrations can be used with PTFE beakers to obtain the same thickness, so saving material. However, as the amount of material deposited is greater with a PTFE beaker, the variation of thickness of the opal is also much more sensitive. Indeed, a small variation in the nanoparticle concentration or in the

evaporation conditions changes the thickness of the sample by an amount that is four times larger than the one occurring with a borosilicate vial.

As the goal of this chapter is to obtain opal in a reproducible way, a borosilicate specimen tube is preferred over a PTFE beaker. Even if more material is needed, with the most important part lost by being deposited on the vial, this method allows a more robust and stable deposition.

3.2.5 Conclusion - Protocol

Evaporation-induced self assembly is an extremely sensitive technique, which requires everything to be controlled in order to obtain good and repeatable results. The found conditions are valid for a glass sample of 1x2.5cm^2, whose size is chosen to produce1x1cm^2 later on. Borosilicate specimen tubes with 50mm height and 19mm diameter are used to hold the nanoparticles and the sample.

Prior to any evaporation, the humidity oven is purged in order to remove any contamination which can be present in the atmosphere, due to a previous evaporation. This purge is done by saturating the oven in humidity and by suddenly opening the door, to let the humidity escape. This process is repeated three times, at high temperature.

The glass samples are cleaned with, in order, acetone, isopropanol and water, each time during 10 minutes under sonication. The samples are then treated with piranha solution, for three hours at 80°C. In the meantime, the specimen tube is cleaned with isopropanol, and dried with an air gun. It is then filled with 5ml of DI water, and a certain volume of concentrated PS suspension of nanoparticles is added to it, while the solution is stirred for at least one hour.

The samples treated by piranha solution are cleaned using copious amounts of DI water, and are dried with an air gun. They are then delicately placed vertically inside the specimen tube with the suspension of nanoparticles, whose magnetic stirrer has been removed. The samples are then placed inside the purged humidity oven, at 60°C and with a relative humidity of 20%, for approximately 2 days. After this duration, all the solvent is evaporated, and strong optical effects can be seen on both the specimen tube and the sample.

3.3 Optical characterisation of opals

3.3.1 UV-VIS spectroscopy

Electron microscopy is a very useful technique for characterising the opals' organisation and defects at the nanoscale, but only on a very small area. For a large-area (more than 1mm^2) characterisation, optical methods are employed, both

because of the larger area covered by a light beam, and because of the light properties of the opal.

One of the most well-known techniques is UV-VIS spectrocopy. To a completely characterise the optical structure, four measurements are made : direct transmission, where only the non-deflected beam is measured, total transmission where the whole transmitted light is measured, and their equivalents for reflection. By adding the total transmission and reflection, the absorbed light can be deduced.

An opal made of PS-nanoparticles of 250nm, fabricated with the method established in the previous parts ($60°C$ and RH of 20%) is fully characterised with this method. By eye, this structure presents an intense green reflection over a large area (figure 3.11 *a)*). The four measurements made with UV-VIS, as well as the sum of the total transmission and reflectance, are represented figure 3.11 *b)*.

The observed peaks are due to the optical band-gap, and they are all located at around 540 nm, which corresponds to the green colour as seen by eye. Small differences exist between the positions of the peaks, given table 3.1, which can be due to a bad alignment of the sample on the holder, making it not perfectly perpendicular to the beam. Indeed, as the sample has to be removed and replaced for each measurement, dust or small particles can give it an unwanted tilt, changing every time. This effect is not important for standard thin-film absorption, as the concerned material are most of time isotropic and thus the angle at which the light beam is absorbed does not matter, but can slightly alter the measurement of a photonic crystal due to its angular dependance. In addition to sample mis-alignment, it should be noted that transmittance measurements are done with the sample oriented perpendicularly to the light beam, while for the reflectance measurements, an angle of 7° is introduced by the system. This difference introduces a small shift between the transmitted and reflected peaks.

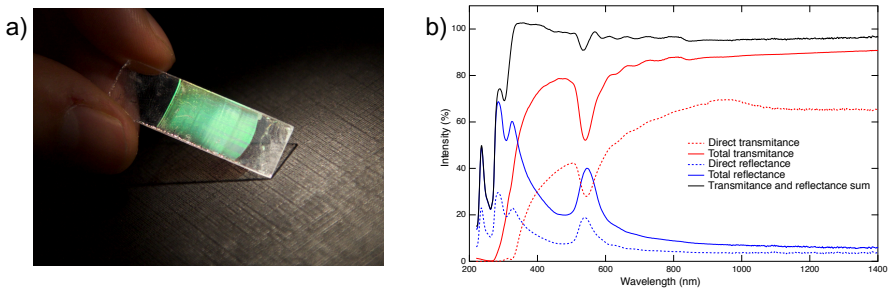


Figure 3.11: *a)* Picture of 250nm opal, showing a green colour due to its optical band-gap. *b)* Transmittance and reflectance UV-VIS measurements, in direct mode and with integrating sphere, of the previously shown opal. The optical band-gap corresponds to where the intensity dips in transmission, and with peaks in reflection.

One of the first inferences can be extracted from optical characterisation of the opal, is that the total and the direct measurements are not equal, which is due to light scattering. The scattered light is still impacted by the optical band-gap of the structure, because of the larger peak in the total measurement, compared to the direct one. The scattering is primarily due to the cracks in the opal, seen figure 3.6, but can also be caused by internal defects inside the structure. Due to the small

Table 3.1: 250nm opal peaks for four different measurements.

Measurement	Peak centre
Direct transmission	541nm
Total transmission	544nm
Direct reflection	539nm
Total reflection	545nm

thickness of the sample (approximately $5\mu m$), the optical band-gap does not stop all the incoming light but only a fraction of it.

The sum of the total transmission and reflection, should equal 100%, if the material does not absorb light. The polystyrene nanoparticles and the glass substrate both absorb in the UV range, which is why a total absorption is observed in this region of wavelengths. In the region around the optical band-gap, fluctuations appear in the sum of light intensity, while no light is absorbed there. This is because of the previously mentioned effects of sample misalignment, which creates a small difference between the observed peaks. Because of this, the added peaks do not correspond to exactly the same optical band-gap, which creates some error in the summation of the intensities, leading to the observed fluctuations. At approximately 380nm, a total light intensity above 100% is observed. This is due to the fact that at each measurement, the analysed area can vary, and the thickness of the opal with it, and so, the intensity of the transmission and reflection. For the wavelengths above 600nm, a stable total intensity at around 95% is observed. Once again, this intensity should be at 100 %, but a small shift exists due to manual misalignment, and change of analysed area.

The analysed opal presents a bright green colour, which is measured at $542 \pm 3nm$ by UV-VIS. If calculated using equation 1.4, with a refractive index of 1.5 for polystyrene, and a supposed 74% volume occupied by the nanoparticles, a theoretical reflection wavelength of 559nm is obtained, which is extremely close to the one measured experimentally. The measured value is slightly lower than the calculated one, which is mainly due to sintering of the nanoparticles, which reduces the distance between them.

3.3.2 Angle-resolved UV-VIS

In order to characterise the inverse opal in a more accurate way and taking into account its anisotropy, an angle resolved UV-VIS is used. By changing the incident angle at which the light reaches the photonic crystal, the position of the optical stop band changes, which changes the wavelength where the maximum reflection occurs.

Measurements are made using a Bentham UV-VIS, with a manually adjusted stage and detector, which are changed for each angle. Because of the tilt of the sample, the spot of the light beam is not circular, but oval-shaped. This shape

is then even more accentuated when it reaches the detector. As the detector has a size of approximately $1mm^2$, a certain fraction of the reflected light is not measured. Because this fraction is changing with the angle variation, due to the change in the spot shape, the intensity of the final signal depends on the angle at which the measurement is made. For this reason, all the spectra at normalised with their maximum value, to remove this effect.

The normalised reflection spectra, at 8 different incident angles, of two opals made with 250nm and 488nm PS nanoparticles are presented in figure 3.12, *a)* and *b)* respectively. As the incident angle increases, the peak of maximum reflection is blue-shifted, dropping from approximately 550nm to 430nm for the 250nm opal, corresponding to the change from a green to a blue colour. The data obtained for the opal made off 488nm nanoparticles present a main reflection peak in the same wavelength area (590nm to 450nm). This is because of the size of the particles used, which are approximately twice as large as the ones used for the 250nm opal. The observed peaks are 2^{nd} order, which are similar to those of 1^{st} order for nanoparticles of half the size, according to equation 1.4. Small waves can be seen in the region on the right of the main reflection peaks, especially for the measurement done at small angles. These are due to Fabry Perot oscillations, due to light bouncing back inside the opal film, and creating interferences. This shows that the film has a good homogeneity, as too many defects would scatter the light and prevent the appearance of interferences effects.

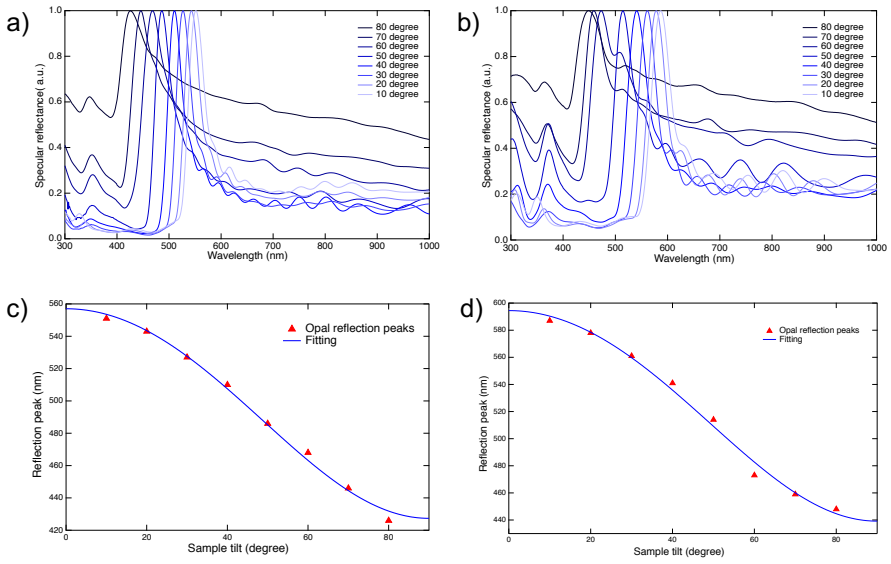


Figure 3.12: UV-VIS reflectance spectra acquired at 8 different incident angles, for opals composed of polystyrene nanospheres of (a) 250 nm and (b) 488 nm in diameter. Maximum peak reflectance wavelength (red triangles) and fitting with the modified Bragg law (blue curve) for the 250nm (c) and the 488nm (d) opals.

The wavelength of maximum intensity of the reflection peak is extracted for each angle, and plotted in figures 3.12 *c)* and *d)*. These wavelengths are then fitted with equation 1.4, with the refractive index and the nanoparticles size as two unknowns. The fitting is done by a minimisation of chi-square. The results of the fitting are presented in table 3.2, where the volume occupancy of the nanoparticles

is calculated using $n_{eff}^2 = n_{PS}^2 x + n_{air}^2(1-x)$, with x the volume occupied by the nanoparticles, n_{PS} the refractive index of PS, taken as 1.58, and n_{air} the refractive index of air, with a value of one. The fitting are done for the order-one reflection ($k = 1$ in equation 1.4) for the 250-nm opal, and for the order-two ($k = 2$) reflection for the 488-nm opal.

Table 3.2: Bragg-law fitting parameters for the maximum reflectance peak.

Nanoparticles size	250nm	488nm
Calculated size	219nm	491nm
Effective refractive index	1.56	1.48
Volume occupancy	0.96	0.83

The fitting curves are very close to the experimental data. The fitting results for the opal made with the 250-nm spheres are quite off from expectations, with a measured size of 219 nm and a very high volume occupancy of 96%, compared to a theoretical 250 nm and 76%. This high occupied volume can be explained due to an important sintering of the nanoparticles between them, creating a smaller distance between them. In addition, because of this sintering, the nanoparticles are compressed, which can alter the refractive index. If the refractive index of the nanoparticles is increased, the calculated volume occupancy decreases according to the equation $n_{eff}^2 = n_{PS}^2 x + n_{air}^2(1-x)$. On the other hand, the data obtained for the 488-nm opal are very close of the expected values of this structure.

At a shorter wavelength of the main reflection peaks, a smaller peak is present, for the opals of both size. The position of this peak varies with the incident angle, with a red-shift at the beginning, followed by a blue shift. The particular shift of these peaks is due to the fact that the planes creating them are not parallel to the surface of the structure. If the angle between the plane and the surface is α, it can be shown that the diffracted wavelengths are calculated with equation 3.2 (calculations described in appendix A).

$$k\lambda_{air} = 2d_{\alpha}(\cos(\alpha)\sqrt{n_{eff}^2 - \sin^2(\theta)} - \sin(\alpha)\sin(\theta)) \tag{3.2}$$

The planes creating the reflection peaks are supposed to be the 220 plane of the fcc structure. The distance between two consecutive 220 plans is $D\frac{\sqrt{2}}{\sqrt{8}}$, with D the nanoparticle diameter, according to crystallographic theory. The equation 3.2, is fitted to the experimental data, with D, n_{eff} and α as variables. The result of the fitting is presented figure 3.13; the variables are given in table 3.3.

Table 3.3: Bragg law fitting parameters for the high order reflectance peak

Nanoparticles size	250nm	488nm
Calculated size	210nm	468nm
Effective refractive index	1.67	1.59
Plane angle	27.2 °	26.4 °

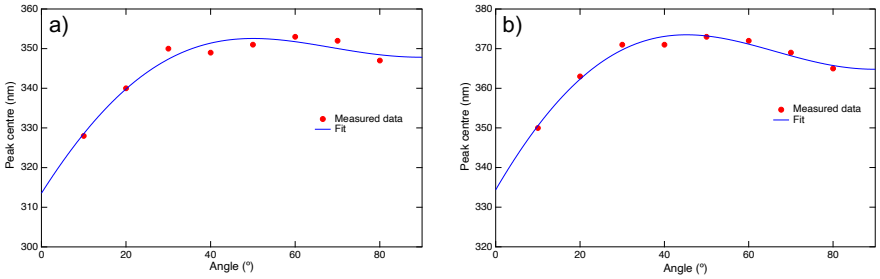


Figure 3.13: High-order peak reflectance wavelength and fitting with the modified Bragg law for the 250-nm (a) and the 488-nm (b) opals.

The fitting is close to the experimental data, and the values found for the nanoparticles sizes and effective refractive index are also close to the ones found previously (table 3.2). The refractive indices found for both particles sizes are higher than that of bare polystyrene (1.58). However, as explained previously, if we consider that the nanoparticles are compressed, the effective refractive index of the structure is increased on account of polystyrene filling a greater fraction of the volume (greater than the hard-sphere packing fraction of 74 %). The angle between the surface of the sample and the plane responsible of this peak, are very close for both sizes. However, these values are quite far from the theoretical angle between the 111 and the 220 plan, which is approximately 35°. The reasons for this difference have not been investigated, but can be due to coupling between the different planes of the structure, or internal reflection between the different plans [170]. These additional effects make the structure more difficult to analyse fully.

Peaks created by -111 planes (and similar), can be measured with the angle resolved UV-Vis method [170]. Such peaks are probably present in the acquired spectra figure 3.12, and some of them can be guessed, especially for the 488nm opal, at 60 and 70 °, on the right of the main peaks. However, because of the Fabry Perot oscillations due to the small thickness of the samples, these peaks cannot be clearly identified for most of the spectrum.

3.3.3 Conclusions

The analysis made with two different UV-Vis methods, confirms the good quality of the made opal, over a large scale. The opals present a clearly defined band-gap with a small width, but not all the light is reflected, due to the small thickness of the structures. Scattering is present on the structure, due to cracks observed on SEM, and results in a specular reflection which is approximately half the total reflection.

Study made with an angle resolved UV-Vis shows the very good quality and order of the opal, with a shift of the main reflected peaks with a change in the angle of incidence. This change corresponds with a good accuracy to the theoretical one, calculated using the Bragg-Snell law. In addition, higher-order reflection peaks have been measured, which confirms the quality of the colloidal crystal.

3.4 Inverse-opal growth

3.4.1 Precursor infiltration

To make an inverse opal, a polystyrene nanoparticle opal can be used as a template, which is infiltrated with a chosen material, as described in 1.3.4. Because of its simple and quick use, and the low amount of required solution, spin coating has been used in this thesis in order to infiltrate the opal samples. A well infiltrated opal should present no over-layer, and has to be homogeneously filled with precursors, meaning that every region of the sample has the same amount of precursors between the nanoparticles. Because the opal used as templates are photonic crystals and present optical effects, these effects can be used to asses the quality of the infiltration over a large area. The control of the infiltration is done by visual observations, which are described hereafter.

Visual control - Precursor infiltration

A non-infiltrated opal presents a reflection whose spectral centre can be approximated by equation 1.4. As previously seen, an opal made with 250-nm polystyrene nanoparticles, in a face-centred-cubic system with the [111] face parallel to the substrate, reflects at around 550nm, corresponding to a green colour, when the light hits the sample at the normal direction. Assuming the used substrate for the opal is transparent, the reflected colour is the same if seen from the top of the sample, or through the substrate.

If the solution infiltration is homogeneous within the sample, the effective refractive index in changed. Indeed, the effective refractive index prior to the infiltration, is a weighted average between the refractive index of the polystyrene, and that of air, equal to one. After infiltration, the refractive index of air is replaced by the one of the infiltratin solution, which is higher than one. Because of this, the effective refractive index is increased, leading to a reflected wavelength which is red-shifted. The change of colour of the opal can thus be used to validate the correct and homogeneous infiltration within the opal.

Visual control - Over-layer formation

The formation or not of an over-layer above the opal can also be verified visually, after the spin coating. Two cases can be distinguished : either a full film is formed on top of the sample, or due to a too small amount of material applied, only isolated islands are formed.

In the case where isolated islands are formed, scattering becomes greater on top of the opal. This scattering is particularly visible due to the reflected light coming from the opal. In the case of particularly big aggregates forming on top of the structure, these can be seen by eye. If a continuous layer is formed, an

iridescence, due to Fabry-Perot interferences, is visible on top of the sample. Due to the reflected light coming from the opal, the iridescence can be hard to detect, because of the difference of intensity. To detect it in an easier way, the sample can be placed under a bright light, and seen from a very wide angle. As previously, a visual analysis can be used to detect potential defects and any unwanted over-layer on the structure.

Experimental parameters

In order to have a good infiltration of the solution inside the opal, a solvent with a low surface tension is used. As the surface tension is low, the molecules of the solvent do not have strong interactions between them, and the creation of additional surfaces does not cost too great an energy. This is a required condition for the infiltration of an opal, which presents a large surface area. Amongst the solvents, methanol presents a low surface tension ($22.50 mN.m^{-1}$), and is a polar molecule, dissolving many precursors. For these reasons, it is chosen as a solvent for the infiltration of the opals structures.

The initial infiltrations are done with titanium bis(ammnonium lactato) ($TiBALDH$) as a precursor for titanium dioxide. Three concentrations of the precursor in methanol are tested, 0.1M, 0.2M and 0.5M, to asses to quality of the final inverse opal, and the presence of eventual defects. The solvent infiltration inside the opal is done by depositing a drop of the solution on the side of the sample. From this point, the solvent naturally spreads through the opals, by capillary effect. If the whole surface is not covered with the initial drop of solution, more of it is added at the same location, until all the opal is infiltrated.

Because air is naturally present between the nanoparticles, the deposition of the solution on top of the opal, leading to a film on top of it, would prevent the air from escaping. If air pockets are still present after the deposition of the solution, they stay trapped within the structure, and the solution precursors cannot take their place, leading to an incomplete infiltration. For the same reason, the solution is added slowly on the side of the sample, and is let to spread inside it. If a too large amount is added too quickly, and a film is formed on the top of the structure before the complete infiltration, trapping air within the sample.

After the slow infiltration done from the side of the sample, a change of colour of the opal is observed, both from the top of the sample, and through the glass substrate. As discussed previously, this homogeneous change of colour, from both sides of the sample, indicate a complete infiltration of the opal. The opal infiltration done in this way, gives a homogeneous result, from both sides of a sample. This was done for the three considered concentrations (0.1M, 0.2M, 0.5M), and for three different opal sizes, 250 nm, 320 nm and 488 nm.

The infiltrated samples are then spin coated, in order to remove the excess of solution on the top of the opal, without removing the infiltrated solution. The parameters used for the spin coating steps are dependant of the concentration of the solution and the nanoparticles sizes used in the opal. For all the spin coatings,

the spinning time is maintained at 60 seconds, the acceleration at 1000 rpm/s^2, and only the spin speed is adjusted.

After the spin coating step, the samples must present no over-layer, which can be checked by visual means, as previously explained. If any over-layer or residue are present on top of the opal after the spinning, additional solution is immediately added on the sample. The addition of the solution can dissolve the deposited materials, which are not strongly bound. The sample is then spun again at a higher velocity, until no more defects are seen on the top of it. The samples infiltrated with the 0.5M solution, for all the particle sizes studied, always present an overlayer, even with the highest spin-coating speed, which is 10000rpm for the used system. Such a concentration can thus not be used for opal infiltration, with the spin-coating technique.

The post-spinning infiltrated samples, which do not present any defects, are annealed at 60°C for 30 minutes, in order to both evaporate the solvent, and to create bonds between the precursors. At the end of this step, the colour of the opal is slightly blue shifted because of the decrease of the effective refractive index, due to the evaporation of the methanol. The infiltration, spin coating and annealing steps are then repeated, to increase the filling of the precursors between the nanoparticles. These steps are repeated until no further change in the colour of the sample occurs, indicating that the precursors filling it have reached its saturation.

For both concentration, 0.1M and 0.2M, this method leads to an opal which is fully infiltrated without over-layer. When using the 0.2M solutions, 3-4 steps of infiltration are typically needed to reach saturation, the 0.1M concentrated solution required many more steps. In addition, when using the 0.1M solution, a too fast spin coating speed provides a very weak infiltration, seen by a weak change of colour, which is probably due to the solution being ejected out of the opal. For these reasons, a solution made of 0.2M of precursor in methanol gives the best results for infiltration with the spin coating method. And it is was thereupon decided to use this solution, for all the sizes of nanoparticle studied.

The infiltrated samples are then calcined at $500°C$ for 4 hours, to remove the polystyrene nanoparticles and to crystallise the precursors. This procedure is described in detail on section 3.4.3. Inverse opals made by infiltration of a 250nm opal with a 0.2M solution of $TiBALDH$ in methanol, are presented in figure 3.14 *a)* and *b)*. The structures made with the previously described method present a very good order at the nanoscale, but an increased number of cracks compared to the original opal, which is due to the shrinking of the infiltrated precursors, from amorphous to crystalline. For comparison, TiO_2 inverse opals made with an insufficient amount of infiltrated precursors, and with an overlayer, are presented in figure 3.14 *c)* and *c)* respectively.

For an opal made of nanoparticles of 250nm, 3 spin coating steps are necessary when using a 0.2M concentrated solutions, with spin speeds of 5000rpm, 6000rpm and 7000rpm. It can be necessary to clean the back side of the sample after the spin coating, in case some of the solution leaked. If the spin speed is maintained constant for the 3 spin coating, over-layers appears at the second or third

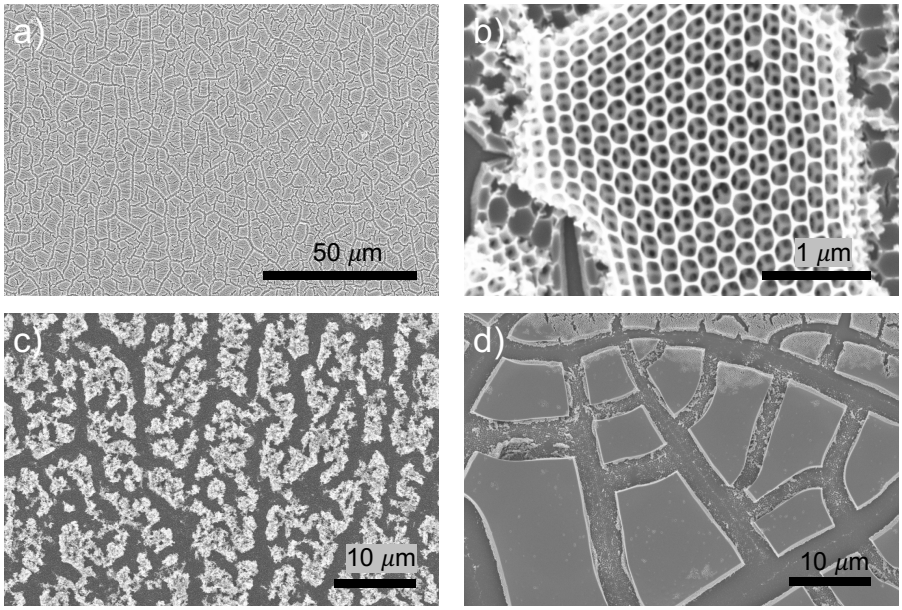


Figure 3.14: *a)* Low and *b)* high magnification of a TiO_2 inverse opal, made by infiltration of a 250nm opals by a 0.2M solution of $TiBALDH$ in methanol, according to the procedure described section 3.4.1. TiO_2 inverse opal presenting *c)*, an insufficient amount of infiltrated precursors, and *d)*, an overlayer. All the sample are calcined at $500°C$ for 4 hours, with a temperature ramp of $1°C/min$.

spin. It is supposed that because of the previous infiltration inside the structure, the surface energy of the opal is changed, which makes the deposition faster. In addition, reactions can occur between the infiltrated precursors and the ones in solution, which once again increases the probability of over-layer creation. For this reason, the spin speed is increased after each step.

A summary of all the steps previously described is given figure 3.15, under the form of an algorithm. The used opals can be made of nanoparticles of any sizes, and solution uses methanol as a solvent, as a precursor concentrated at 0.2M.

The previous conditions can still be used for opal made with nanoparticles of other sizes (320nm and 488nm). Additional infiltrations are however required, due to the greater amount of space between the particles to be filled. It should be noted that the optimal conditions for the infiltrations of opals with the spin coating method have not been searched. Indeed, a lower speed might be enough to prevent the formation of an over-layer, at least for the opal made of 488-nm spheres. However, as the purpose of this thesis is the utilisation and application of inverse opal for optoelectronics devices, the optimal conditions to build them have not been searched; rather, only one repeatable reliable method has been identified.

3.4.2 One-step method

Another way of infiltrating precursors inside an opal, without the creation of an over-layer, is to add some metal oxide precursors in the suspension

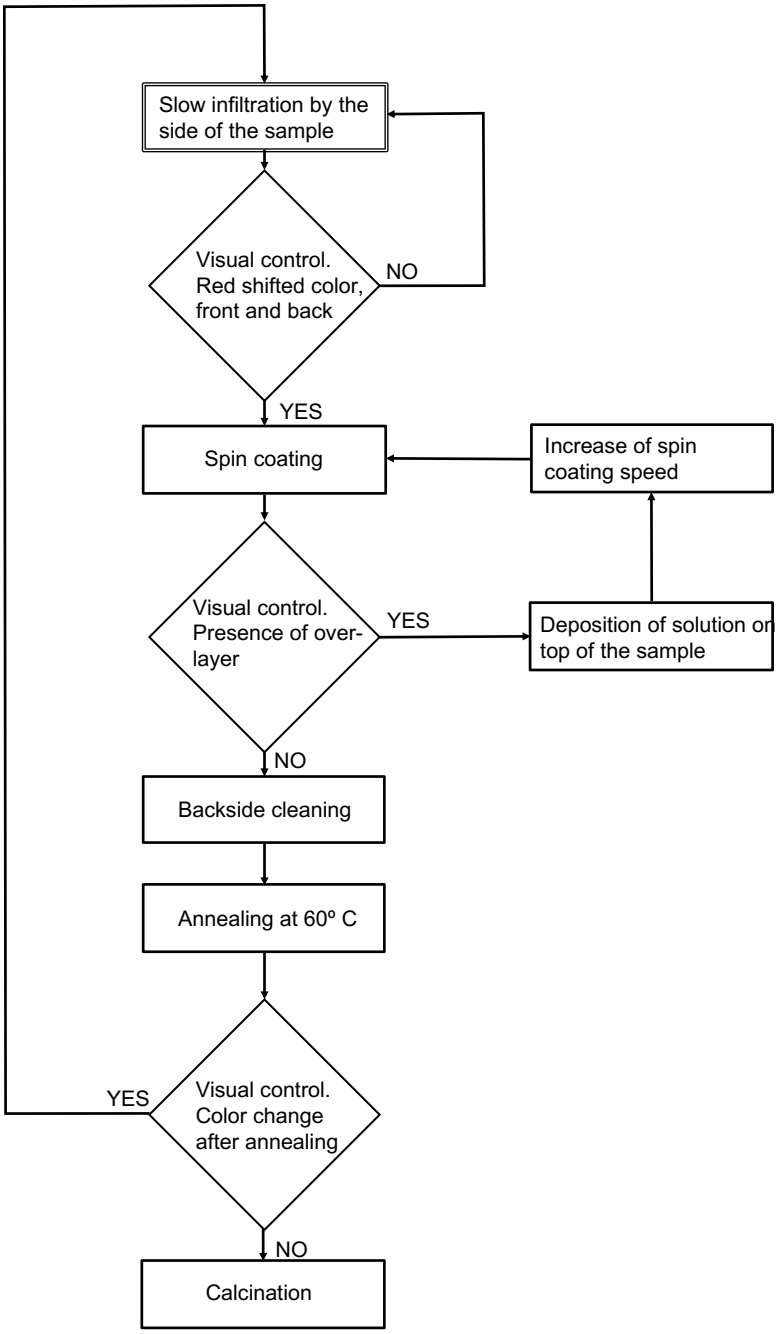


Figure 3.15: Established process for the infiltration of solution inside an opal, with spin coating.

of polystyrene nanoparticles, as described in the article of Hatton *et al.* [82]. The physical processes happening during this one step method are described in section 1.3.5.

One of the most well-known precursors for metal-oxide, is tetraethyl orthosilicate (TEOS), which is used to make silicon dioxide. This precursor is initially in the liquid phase, and hydrolyses if put directly into water, which would lead to quick aggregation and formation of nanoparticles. It is thus initially mixed with ethanol, in which it does not react, in order to dilute it to slow down the speed of the hydrolysis reaction. However, the precursor still has to hydrolyse to form the

matrix, and thus, hydrochloric acid is added to the mixture, to act as a catalyst. The TEOS solution is made of a 1:1:1.5 ratio by weight of TEOS, 0.1M HCl and ethanol respectively [82]. To make this solution, 0.27ml of TEOS, 0.25ml of 0.1M HCl in water and 0.48ml of EtOH are mixed, and are stirred at room temperature for at least one hour.

37.5 µl of the TEOS mix solution is added to a 5ml suspension of 0.1% concentrated PS nanoparticles in water. The final solution is left to stir for at least 2 hours at room temperature, and is then sonicated for 30 minutes, to break up any residual aggregates. A piranha treated glass sample is vertically deposited in the vial, and is then let to evaporate under controlled conditions, with a temperature of $60°C$ and a relative humidity of 20%.

After total evaporation, the samples are removed from the humidity oven, and the first noticeable difference is the total transparency of the sample, over its whole length. This transparency is due to two reasons : firstly, the light is not scattered due to the absence of cracks, and secondly, as the structure is totally filled, the difference of refractive index between the nanoparticles and the precursors area is extremely small, leading to a very weak optical band-gap. The one step method gives a sample which is homogeneous in term of precursor filling, and which also presents no cracks (figures 3.16 *a)* and *b)*). This is possibly due to the high stability of the TEOS solution in water, which stays stable for some days, even at $60°C$.

If a less stable precursor is used, it can start to react during the evaporation, which can alter the self-assembly of the nanoparticles, as well as the good filling of the precursors. As a precursor of TiO_2, Titanium(IV) bis(ammonium lactato) dihydroxide (TiBALDH), has been tested for the one step method. This precursor is initially diluted in water, with a concentration of 50%. In order to have the same molar ratio of precursor to nanoparticles as the recipe using TEOS, 22 µl of the TiBALDH solution is introduced in a 5ml suspension of 0.1% concentrated PS-nanoparticles.

After two days of evaporation, using the same conditions of temperature and relative humidity as standard evaporations, the solution is totally evaporated. The visual aspect of the samples this time highly depends on the size of the used particles, indicating the extreme sensitivity of this method. The samples using 520-nm particles are still transparent but somewhat cloudy, indicating the presence of cracks within the sample, while the samples using 196nm and 320nm nanoparticles exhibited a strong white colour, indicating that cracks are present, as well as an important disorder inside the structure (figures 3.16 *c)* and *d)*). It is hypothesised that these differences are not due to the size of the nanoparticles, but to the other elements brought by them, such as ions. Indeed, the used nanoparticles are negatively charged on their surface, which means that a certain amount of positive ions are released from the surface groups. For the same mass concentration, a suspension of 196-nm nanoparticles has a far greater surface area compared to one made of 520-nm nanoparticles, which means that the amount of released ions is greater for small-sized nanoparticles. These ions can then interfere with the introduced precursors by reducing their individual zeta potential, which reduces the repulsion and can increase the rate of reactions between them.

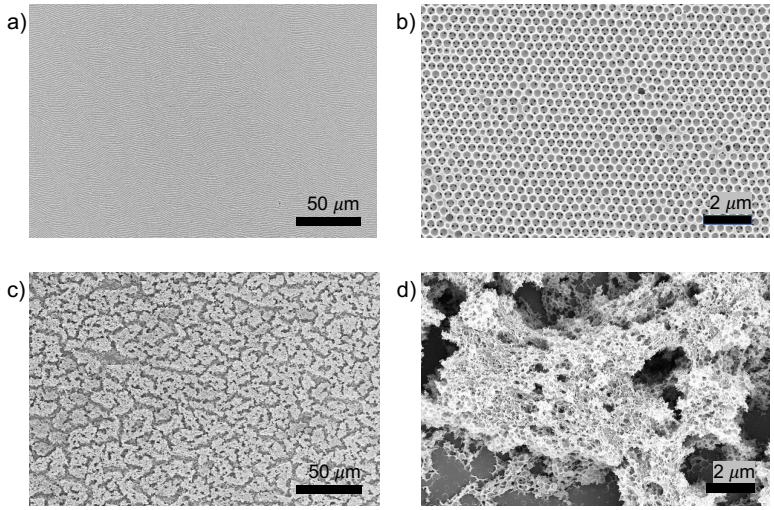


Figure 3.16: Low *a)* and high magnification *b)* of a silicon dioxide inverse opal, and a titanium dioxide inverse opal (*c* and *d*) after calcination, made with a one step method with 340nm PS nanoparticles. TEOS and TiBALDH are used as silicon and titanium precursors respectively.

In conclusion, the one-step method can give very good results in terms of precursors infiltration and cracks reduction, as seen with the total transparency of the infiltrated opal after evaporation. However, because the introduced precursors have to stay stable for a long duration, a very good stability is required. This stability can be adapted with the introduction of additional compounds, such as ethanol or hydrochloric acid. If the used precursor is not stable, this leads to a bad self-assembly of the nanoparticles, preventing optical effects.

3.4.3 Calcination and template removal

In order to remove the polystyrene nanoparticles, and to crystallised the deposited materials, the infiltrated structure is annealed at high temperature, for a defined time and with a controlled temperature ramp.

To know which temperature is required to completely remove the polystyrene template, dried nanoparticles are analysed with TGA-DSC. The analysed sample is simply made by dropping 1ml of 5% concentrated 250nm nanoparticles on a petri dish, and leaving it to dry naturally. The TGA and DSC results are presented in figure 3.17. A small mass loss occurs on the sample at approximately $100°C$, corresponding to the evaporation of water still present in the sample. The DSC shows an important phase change at 360 $°C$ (endothermic process), which corresponds to the calcination of the polystyrene, giving an important loss of mass of the sample. At $400°C$, only 2% of the original mass is remaining, while at $500°C$ only traces are still present.

The temperature ramp also needs to be controlled, with a slow ramp being more favourable for a good quality inverse opal. Two opals made in the same conditions, infiltrated with silicon dioxide precursor with a one-step method, have

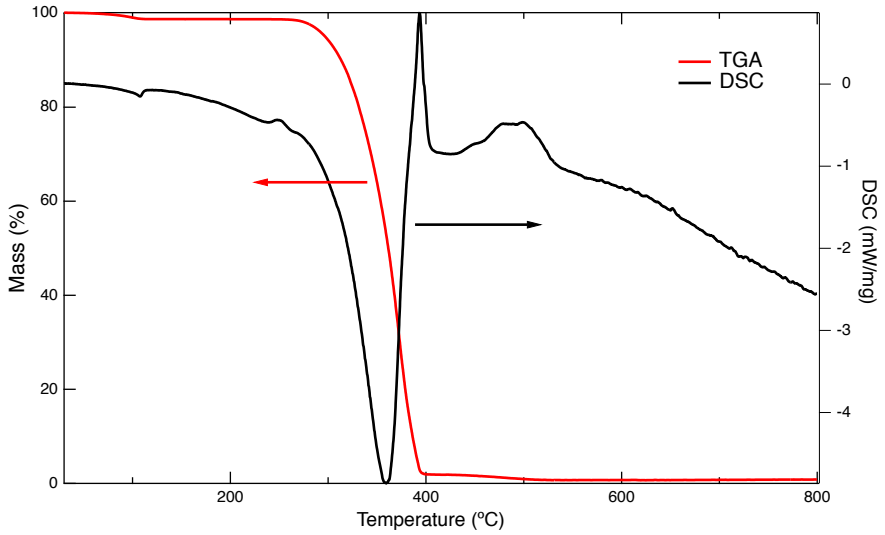


Figure 3.17: TGA and DSC measurements of polystyrene of 300nm nanoparticles in air. Maximum temperature of 800 °C, with a ramp rate of 10 K/min.

been calcined at the same temperature of 600 $°C$, for the same duration, but with temperature ramp of 20 $°/min$ for one of them, and only 1 $°/min$ for the other.

The sample calcined at 20 $°/min$ still shows an ordered structure from the top, but does not look like an inverse opal (figure 3.18 *a)*). When seen in cross section, the structure presents smooth and irregular shapes, and no clear order can be seen. It is supposed that, due to the fast annealing, the polystyrene nanoparticles are calcined faster than the reaction between the silicon precursors, which leads to the removal of the template before the inverse opal is completely formed. With an absence of template, the precursors are forming shapes which are mostly disordered. In addition, gas coming from the template escapes very quickly, which increases the disorder of the formed inverse opal.

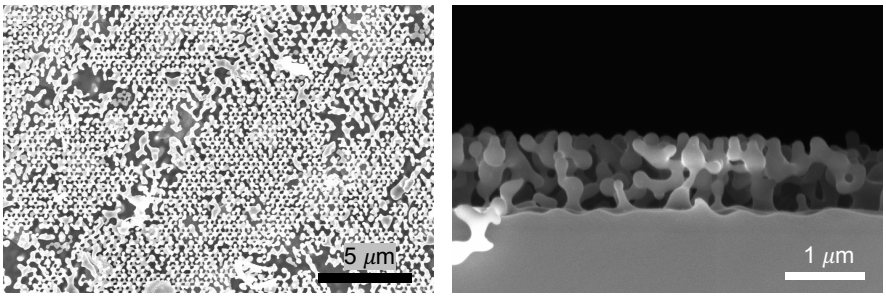


Figure 3.18: Opal with silicon precursor infiltrated, calcined at 20$°C/min$, until 600 °C. *Left :* Top view. *Right :* Cross section.

If the infiltrating material between the polystyrene nanoparticles does not require calcination, either because it is already crystalline, or because it is an organic material that would be destroyed, the nanoparticles have to be removed in another way. One possibility is the dissolution of the nanoparticles, using a solvent that does not dissolve the inverse opal itself [171].

Chapter 4

Fluorine Tin Oxide Inverse Opals as a Scaffold for Perovskite Solar Cells

The XRD measurements presented in this chapter have been done by Mr Bob Xu.

4.1 Mesoscopic solar cells

4.1.1 State of the art

Firstly used as sensitisers for solar cells in 2009 [172], then as an active layer by Snaith *et al.*[173], perovskite materials exhibit excellent performances within solar cells, with a rapid growing solar conversion efficiency [174][175], and is currently one of the major research topics in the solar-cell field. The latest reported efficiency for a single junction perovskite device is 25.2%, which is very close to the current record of standard silicon solar cells[176].

The reasons for the high performances of perovskite solar cell, including their electrical and optical properties, are not discussed here in detail, but much research is dedicated to it [177, 178, 179]. We only describe them shortly in this thesis, to provide some relevant background knowledge about these materials.

The term perovskite, used in the solar cell context, is actually only a short-name, for a category of inorganic-organic hybrid materials, which each crystallise into perovskite structure[175]. The inorganic part is commonly a lead-halide compound, with a negative charge, in the form PbX_3^-, where X stands for a halide, such as Chloride (Cl) , Bromide (Br) or Iodine (I). To equilibrate the charge, the organic part carries a positive charge. The most common compounds for it are methyl-ammonium ($CH_3NH_3^+$), Formamidinium ($CH(NH_2)_2^+$) or the caesium cation (Cs^+).

The choice of the organic and the inorganic compounds strongly influences the optical and electrical properties of the material[180][181], as well as its stability[182]. An important characteristic of the organic-inorganic hybrid perovskite is the possibility to mix the compounds for the choice of the halide, or the cation. For instance, a structure such as $PbBr_{3-x}I_x$ with x between 0 and 3, can be obtained by choosing the correct amount of materials during the material synthesis. In spite of all these possible variations, the most studied perovskite structure is one of the first discovered, the methyl-ammonium lead iodide perovskite ($CH_3NH_3PbI_3$), which is often simply called *MAPI*.

One of the reason for the good efficiencies of perovskite solar cells, is the low amount of trap states[183], as well as the long diffusion lengths for the charges[184]. In spite of its good characteristics, recombinations still happens in perovskite solar cell, reducing its maximum efficiency. To minimise this effect, some solar cells use architectures with a mesoporous titanium layer infiltrated with perovskite, in which the separation of the charges is increased due to the proximity of the electron transport layer[185] .

4.1.2 Motivation of the project

In spite of the good performance of perovskite solar cells with a TiO_2 scaffold, the randomness of the layer prevents a perfect transfer of the charges to the electrodes. For this reason, other architectures are studied to replace this layer, and the inverse opal is one of them.

Only a limited amount of work using inverse opal in a perovskite solar cell has been published [8, 103]. In these works, the inverse opal is made of TiO_2 and is used as an electron transport layer, with the goal of reducing the distance travelled for the charges. In addition, due to the ordered inverse opal structure, the path to the electrode is optimised, and there are less risks of trapping the charges within the meso-porous layer. However charges inside titanium dioxide do not have a good mobility, which makes them take a long time to reach the electrode. During this time, it is possible that a recombination with a hole within the perovskite happens, due to the important surface area between TiO_2 and the perovskite.

To prevent recombination occuring, as well as increasing the charge mobility within the inverse opal, it is proposed to make an inverse opal from a conductive material, which is coated by an electron transport layer. In this configuration, the core of the inverse opal plays the role of the electrode, while the coating is the ETL. In this way, the excited charges still have a short distance to reach the inverse opal, and at the contact with the TiO_2 coating, the electron is transferred to the ETL and then to the inverse opal core, which has a lower Fermi level due to its conductive behaviour. As the electrons are in the conductive core of the inverse opal and the holes inside the perovskite, they are separated by the TiO_2, that prevents recombination between them.

To maximise the performance of such a 3D solar cell, it is important to

ensure a complete filling of the inverse opal with the perovskite[186]. Otherwise, isolated perovskite dyes can be deposited in some ares of the inverse opal, resulting in an important amount of charges recombination in these dyes [187]. For this reason, instead of a randomly organised mesoporous layer, nano-rods can be used as a transport layer as such a structure is easier to fill with perovskite [188].

Due to the three-dimensional electrode within the perovskite, the realisation of a thick perovskite solar cell is possible, which can increase the light absorption, especially in the longer-wavelength region, such as red (700nm). In conventional devices, the increase of the perovskite thickness results in a lower efficiency, that is due to optical interferences, or greater charge recombination due to the distance to the electrodes. Another advantage of the use of a thick perovskite layer, is the possibility of a hole-transport-layer-free solar cell, as barely no electrons are still present on the top area of the solar cell[189]. Due to the known impact of the hole transport layer on the stability of the perovskite, its removal could greatly enhance stability.

To realise the desired structure previously described, an inverse opal made of a conductive transparent oxide needs to be prepared, in order to avoid light absorption by the electrode. In addition, the substrate used should be of the same material as the inverse opal, to allow a good contact and connection between the two. Fluorine tin oxide and indium tin oxide are two of the most well known transparent conductive oxides, and are good potential candidates for making a transparent inverse opals. However, as explained in the previous chapter, the substrate where the opal is made is treated with piranha solution to make it hydrophilic. As ITO is dissolved when in contact with acid, it cannot be used as a substrate. For this reason, FTO is used as a substrate and for the inverse opal to build on top of it.

The deposition of the electron transport layer is chosen to be done by atomic layer deposition, because of the good conformity given by this deposition method [190]. Both zinc oxide and titanium dioxide can be deposited using the ALD in our lab. Due to the instability of perovskite deposited on ZnO [191], it is chosen to use TiO_2 for the inverse opal coating. Due to its well known and optimised deposition method, the standard $MAPI$ perovskite is chosen as the active layer of the fabricated solar cell.

The wanted structure as well as the intermediate fabrication steps are schematically represented figure 4.1. The first step is to make a FTO-inverse opal, which is then uniformly coated with titanium dioxide, acting here as an electron transport layer (figures 4.1 *a* and *b* respectively). A perovskite material is then infiltrated inside the coated inverse opal. The perovskite completely fills the inside of the structure, and also forms a thin over-layer (figure 4.1 *c*). To complete the structure, the hole transport layer and the top electrode are deposited on the structure, by spin coating and metal evaporation respectively (figure 4.1 *d*).

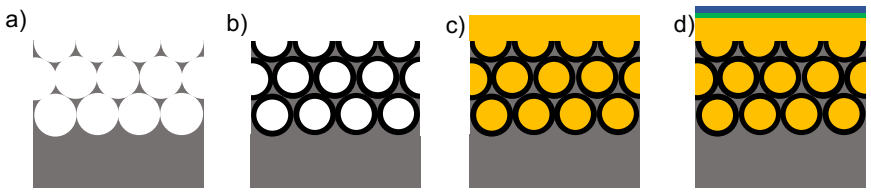


Figure 4.1: *a)* FTO inverse opal, on a FTO substrate. *b)* Deposition of a continuous and uniform film of titanium dioxide inside the inverse opal, by ALD. *c)* Infiltration of the TiO_2-coated inverse opal by a pervoskite material, with formation of an overlayer on top of the structure. *d)* Deposition of the hole transport layer and of the second electrode, on top of the structure.

4.2 Coated-scaffold fabrication

4.2.1 Fluorine tin oxide scaffold

The FTO substrates are provided in large pieces of 10x10cm^2, which have a thickness of 2.7mm. To create the desired size of substrate(1x2.5cm^2) from these pieces, a diamond pen and a tile breaker are used. Because of the high transparency of this material, the FTO coated side is identified by using an ohm-meter (multimeter), and a small mark is made on the back side of the sample using a diamond pen.

A complete solar cell (figure 4.2 *a)*) has often multiple electrodes, which allow different sites to be tested. The tests are done by connecting the bottom electrode (FTO), and one of the top electrodes, to a measurement device. The bottom electrode is contacted by scratching the deposited layers of the solar cell, to reveal the buried FTO. Due to the extremely small thickness of a thin film solar cell (less than 1μm), it is possible that the measurement probe contacting the top layer, pierces through it, and reaches the bottom layers. If the FTO layer is contacted by this probe, a short circuit occurs, due to the two probes being connected by a conductive layer (figure 4.2 *b)*), and the measurement of the solar cell is impossible. To avoid this case, the FTO is etched on the sides of the solar cell. Even if the probe pierces the layers, it can only contact the glass substrate, which does not lead to a short circuit (figure 4.2 *c)*), so enabling measurement of the solar cell.

As discussed, FTO is resistant to etching, as there is no reaction with simple acids. A known method to etch it, is to cover it with zinc powder, and then to add concentrated hydrochloric acid (figure 4.3)[192]. In order to protect the areas which should not be etched, kapton tape is deposited on them. A strong pressure is applied on the edges of the tape to avoid the acid seeping under it, which would create unwanted etching. Zinc powder is then deposited to cover all the areas which need etching, followed by the drop-wise addition of 37% HCl. Once the reaction is over, and all the zinc powder is consumed, the samples are copiously rinsed with DI water, and the kapton tape is finally removed.

After the etching, the patterned FTO samples are cleaned, using acetone,

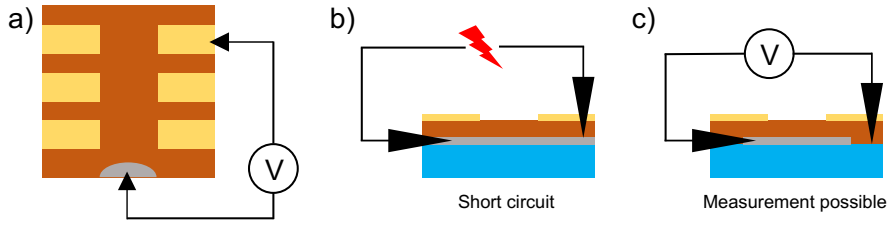


Figure 4.2: *a)* Top view of a solar cell with six evaporated contacts on top and a scratched part on the bottom, to reveal the underneath FTO layer. A measurement device is connected to the bottom FTO and to one of the upper electrode. *b)* Solar cell on an un-etched FTO. The measurement probe can pierce the layers and contact the bottom FTO, leading to a short circuit. *c)* Solar cell on etched FTO. Even if the measurement probe pierces trough the layers, it does not contact the FTO, and the solar cell can be measured.

isopropanol and water, for 10 minutes each, under sonication. The samples are then treated by piranha solution for three hours, at $85°C$. As previously said, the FTO is not attacked by the piranha solution, and the patterning is still intact after the treatment. After being copiously rinsed with DI water and dried with an air gun, the samples are vertically disposed in specimen tubes. The suspension consists of 250nm PS-nanoparticles (BangsLaboratories), concentrated at 0.1%, and stirred for at least one hour, and sonicated for 30 minutes prior to the samples' introduction. The evaporation is done at $60°C$, with a relative humidity of 20%, for two days.

After evaporation, the samples present an intense green colour, which is confirmation of good deposition of nanoparticles on the FTO coated substrates. The nanoparticles deposited on the edges of the sample, where the FTO has been etched, are removed using a tissue lightly soaked with acetone, which can dissolve polystyrene. The tissue is folded in a triangular shape, in order to accurately remove the particles on a specific area, and is only lightly soaked, to prevent the acetone spreading to the rest of the opal. It should be noted that a directly patterned opal can be obtained, with spatially localised chemical treatment of the substrate[193], preventing the use of chemical mechanical cleaning which can damage the structure. Once the green colour on these areas is no longer visible, and no defects due to PS residuals are seen, the original samples are cut into a 1cm x 1cm sample, using the diamond pen with a tile breaker. This is followed by an annealing of the samples at $85°C$ for 3 hours, in order to increase the sintering between the nanoparticles.

A well known precursor to make tin (IV) oxide (SnO_2), is tin (IV) tetrachloride pentahydrate ($SnCl_4.5H_2O$)[194, 134, 137]. As seen in the preliminary tests to infiltrate inverse opal (section 3.4.1) a low surface energy solvent is favourable for the infiltration. Methanol can dissolve $SnCl_4.5H_2O$, and has an extremely low surface energy, which makes it a very good choice. A 0.2M solution of tin tetrachloride pentahydrate is made by mixing 2ml of methanol, with 140mg of the precursor, which is stirred until completely dissolved, which takes approximately 30 minutes. To add fluorine as a dopant to this structure, ammonium fluoride (NH_4F) is added to the solution, in a 10:1 molar ratio compared to the tin precursor, which is done by adding 1.5mg of NH_4F to the previously made solution.

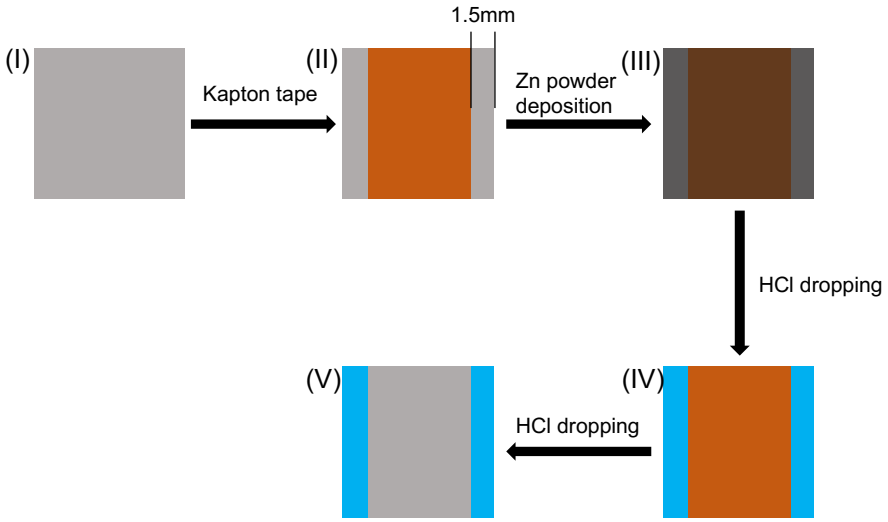


Figure 4.3: Schematic of the FTO patterning method. *i)* The bare FTO substrate (*I)*) is covered by kapton tape, to protect the areas which should not be etched (*II)*). Zinc powder is deposited on the areas where etching is wanted (*III)*), and concentrated HCl (37%), is dropped on the sample(*IV)*). To finish, the sample is washed with DI water, and the kapton tape is removed(*V)*).

According to the protocol established in the previous chapter (figure 3.15), the 250-nm opals are infiltrated by spin coating, using the 0.2M tin precursor in methanol. In order to avoid any tin oxide deposition on the FTO etched areas, which could lead to a short circuit in the completed solar cell, these areas are wiped with a tissue lightly soaked in methanol after each spin coating. When the infiltration is completed, the sample exhibits a red-orange colour, compared to its initial green.

To determine the temperature needed for the crystallisation of the solution in tin oxide, 2ml of a 0.2M solution are let to evaporate on a petri dish. The resulting powder is tested in a TGA/DSC apparatus, heating from room temperature to 600°C, at a rate of 10°C/min. The mass loss starts at approximately 100°C, and is supposed to be initially water residuals, trapped within the powder (figure 4.4). At 300°C, an endothermic peak is visible on the DSC spectra, indicating that a reaction of crystallisation occurs. The slope of the mass loss increases at that same temperature. At approximately 400°C, the rate of mass loss is drastically reduced, what is believed to be the end of the tin (IV) oxide crystal formation. Above this temperature, the mass still slowly decreases, and the DSC indicates that an endothermic reaction is still happening. It is believed that the endothermic reaction and the mass loss at high temperature are due to the creation of defects within the tin oxide, for instance oxygen vacancies, which are responsible for the conductivity of this material.

As the precursor is completely crystalline at $400°C$, and the polystyrene is completely carbonised at $500°C$, it is chosen to anneal the infiltrated opals at $500°C$ with a ramp rate of $1°/min$, in order to obtain a FTO inverse opal. The samples are left at $500°C$ for four hours, to ensure the complete conversion of the tin precursor into crystals.

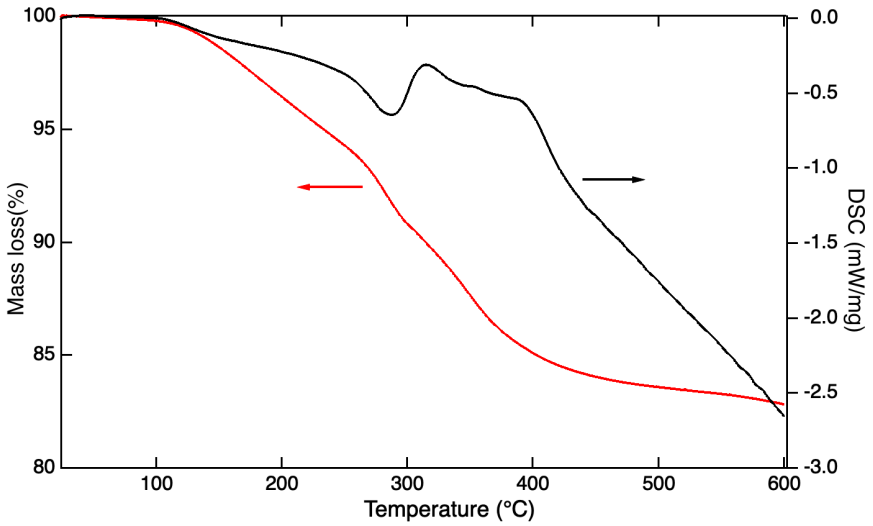


Figure 4.4: TGA and DSC measurements of dried tin tetrachloride pentahydrate and ammonium fluoride in a 10:1 ratio. Maximum temperature of 600 °C, with a ramp rate of 10 K/min.

After calcination, the samples appear transparent, with some blueish colours when examined under white light, which is a good confirmation of remaining order in the structure. When observed under SEM, no over layer is observed on the whole structure. Many cracks are present over the structure, due to the shrinking of the precursor during crystallisation(figure 4.5 *a)*). Two kinds of cracks can be observed : the larger ones, with a width of approximately 3-4μm are supposed to be due to a combination of the precursors shrinking, as well as the initial cracks of the opal, due to the shrinking of the PS nanoparticles. The smaller cracks, appearing inside the inverse opal domains, are only due to the shrinking of the precursors.

When observed with high magnification (figure 4.5 *b)*), the inverse opal shows a very good order, and a clear hexagonal packing. The connection between the pores are very good and large, which even allows the visualisation of the second layer of the structure. No coating is applied on the structure before the SEM, and yet no charging is observed during the microscopy, indicating the good conductivity of the FTO inverse opal.

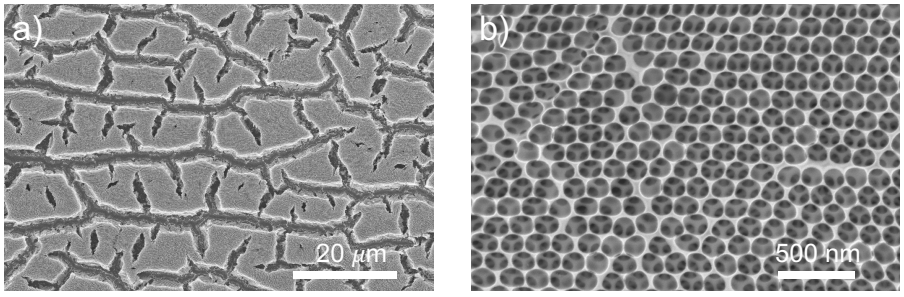


Figure 4.5: Low (a) and high (b) magnification SEM of calcined FTO inverse opals, made from 250nm polystyrene nanoparticles.

To asses the crystallinity of the structure, XRD has been carried out on the FTO inverse opal, which were this time made on a glass substrate to prevent

any signal coming from the FTO substrate. To compare these results, XRD is also carried out on a standard commercial FTO substrate. The two measurements shows exactly the same crystalline peaks at the same angles, indicating that the calcined inverse opal is made of pure FTO (figure 4.6). However, the peaks from the inverse opal structure appears to have a bigger width than the ones from the standard commercial substrate. This difference can be due to both the size of the crystals, which are smaller compared to the coated film due to the template made of PS nanoparticles, or because of residual stress within the crystals.

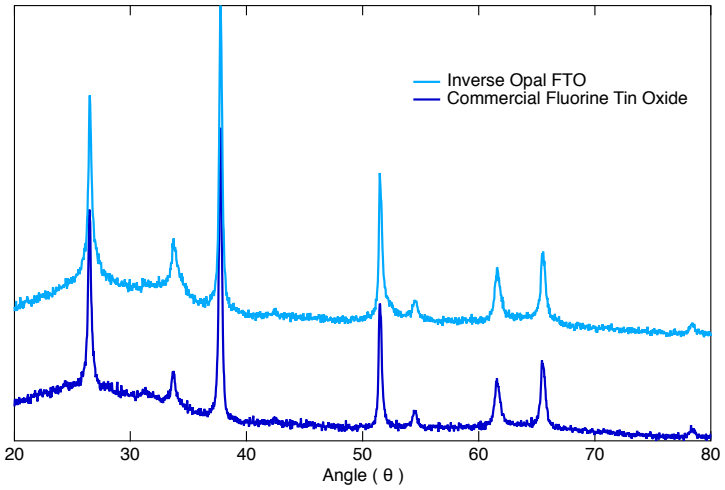


Figure 4.6: Comparison of XRD peaks for a commercial FTO thin film (dark blue), and FTO inverse opal, made on glass substrate (light blue).

4.2.2 Titanium dioxide coating

A part of the work of this section was made in a two-week secondment in the group of Prof. Gitti Frey, in the Technion Israel Institute of Technology, in Haifa. The ZnO deposition, as well as the analysis by SEM using secondary and backscattered electrons, have been made by Artem Levitsky, in Prof. Frey's group.

To create a uniform coating inside the inverse opal, atomic layer deposition (ALD), a very well known technique[195], was used. To assess the accuracy of this method, and its efficiency in the small-sized opal used in this thesis, the inverse opal is analysed with a high resolution SEM. As the final goal of this project is to make a coating on a crack-free FTO structure to maximise the surface of the solar cell, the coating are firstly done on a crack-free structure to asses the possibility of such a coating. Indeed, a cracked structure offers more possibilities for the gas precursor to penetrate the inside of the structure, while for a crack-free structure, the precursors can only enter by the top of the inverse opal, increasing the difficulties to have a complete coating.

The inverse opal made of FTO shows a certain number of cracks, due to shrinkage of the precursors and of the PS nanoparticles. For this reason, the inverse opal used to asses the possibility of coating by ALD is made in silicon dioxide with the one step method, as described in section 3.4.2. The nanoparticles used for these

crack-free samples have a size of 250nm, with a concentration of 0.1%, the rest of the conditions being identical to those stated in section 3.4.2. The samples are made on silicon, to allow an easier breaking to observe the cross sections. The desired material for the uniform coating of the inverse opal is titanium dioxide, but because the ALD used in the lab in Technion could not deposit this material, the experiments were made using zinc oxide, using diethyl ether and water as precursors.

During a normal cycle of ALD, the precursors are released from their container and pass through the chamber containing the samples, before getting pumped out. This method gives good conformal coatings on flat films, but a gradient of deposition can occur within three-dimensional structures [196]. To prevent this, it is also possible to keep the precursors within the chamber for a longer amount of time, to make it reacts with the sample for a longer time. When this "hold" is applied, the pressure inside the chamber keeps increasing, due to nitrogen which keeps being introduced within the chamber, without being exhausted. With a high temperature and a long time for the precursors to stay in contact with the sample, it is more probable that the precursors can react with the full surface of the inverse opal, even the bottom part that can be difficult to reach. The hold time is limited by the pressure reached within the chamber: If this becomes too high, the system automatically evacuates the gases and stops the deposition, as a safety mechanism.

Prior to the deposition, the samples are treated with $UV - O_3$, in order to increase the number of active sites that can react with the precursors. The $UV - O_3$ used in Technion is firstly filled with pure oxygen, to increase the effects of the ultraviolet reaction on oxygen. The samples are treated in this way for 10 minutes.

The first deposition is carried out on the crack free SiO_2 inverse opal, treated with $UV - O_3$, and at $200°C$ for 200 cycles of DEZ and H_2O. The hold time for each pulse is 3 seconds, and there is a 30 seconds purge between each pulse. After the deposition, the samples are broken with a sharp tungsten pen, in order to observe cross sections. The classical observation done with SEM uses secondary electrons, and gives information mostly about the topology and the phases on the samples. As in this case, SiO_2 and ZnO are closely related materials as they are both oxides, they can be difficult to distinguish using secondary electrons imaging. For this reason, backscattered electrons, who are more sensitive to the atomic mass contrast of the materials, is used to image the sample. As zinc has a higher atomic number than silicon, (30 and 14 respectively), zinc oxide is expected to interact stronger with the back scattered electrons, giving a stronger signal for the ZnO coated area. The samples are observed on a LEO Gemini 1525.

The sample made with 200 cycles is fully coated in a homogeneous way (figure 4.7 *a)* and *b)*). The apparent defects on the inverse opal organisation are due to the fact that the cross section is not aligned with the inverse opal crystal direction, as it follows the silicon substrate crystalline plans. The signals coming from the secondary and the backscattered electrons are acquired at the same time, which allows a direct comparison between the two signals. On the secondary electron signal (figure 4.7 *c)*), small crystal can be seem in the inside of the inverse opal, indicating the crystallisation of the ZnO after its deposition. The good contrast obtained with backscattered electrons allows the measurement of the deposited layer

with a good accuracy, as reported on figure 4.7 *d)*. The measured thickness of the coated layer can vary due to the non perfect cross section direction, but is still extremely homogeneous over the sample, with an average thickness of $26 \pm 2nm$.

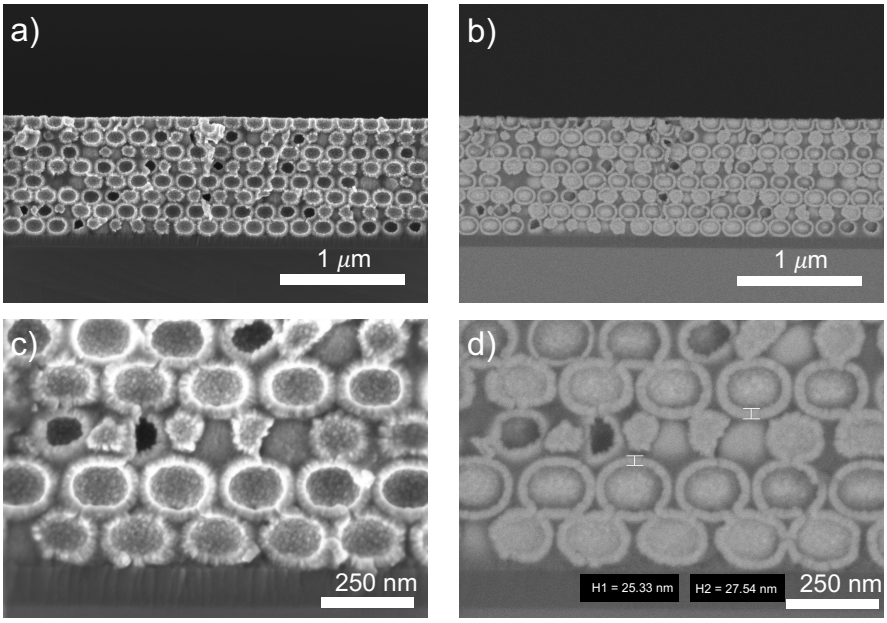


Figure 4.7: SEM cross section of a crack free SiO_2 inverse opal, infiltrated with 200 cycles of ZnO by ALD. Analysed by secondary electrons (*a* and *c*) and by backscattered electrons (*b* and *d*), at low (*a* and *b*) and high (*c* and *d*) magnification. The secondary and backscattered electrons data are acquired at the same time, on the same regions.

By decreasing the amount of cycles used in the ALD deposition, the coated thickness can be reduced. Additional samples have been made with 63 and 27 cycles, which also show a homogeneous coating inside the sample, as seen on figures 4.8 *a)* and *b)* respectively. The thickness can be measured on the sample made with 63 cycles, and is equal to $9.3 \pm 1nm$. It can be noticed that the ratio of cycles between 200 and 63 is equal to $\frac{200}{63} \approx 3.17$, which is close to the ratio of the thickness of these two samples, $\frac{26}{9.3} \approx 2.8$. This indicates that the growth per cycle of the ZnO is similar for the two depositions, indicating the good deposition of the material in both cases.

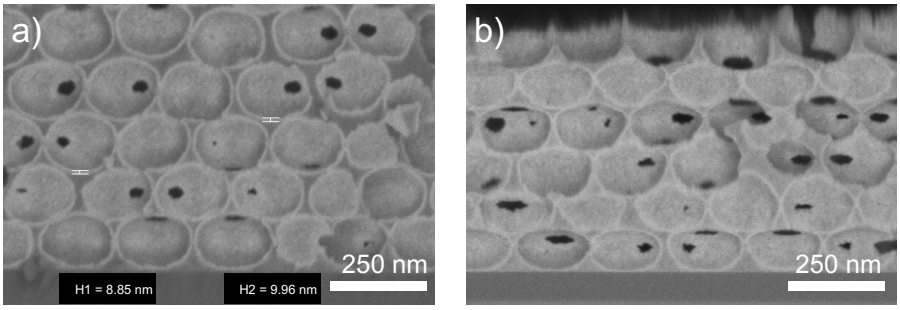


Figure 4.8: Cross section of a crack free SiO_2 inverse opal, infiltrated with *a)* 63 and *b)* 27 cycles of ZnO by ALD, analysed with backscattered electrons microscopy. Deposition made at $200°C$, with 3 seconds hold.

The sample made with only 27 cycles, still presents the signs of a good deposition, as indicated by the bright rings inside the inverse opal, figure 4.8 *b)*. The deposition appears to be continuous, however, its thickness is too small to be accurately measured by SEM. It is expected to be approximately 3.5nm, by using the same ratio as previously, which is below the resolution limit of the machine. The deposition of zinc oxide by ALD using a hold of 3 seconds and a temperature of 200°, shows conformal results within the SiO_2 inverse opal, and a homogeneous growth rate.

The ALD technique is now used to deposit TiO_2 inside FTO inverse opal, in order to make the electron transport layer of the desired solar cell design. These deposition are made is the homemade ALD in the group laboratory. The FTO inverse opal are made with 250-nm nanoparticles.

The deposition by ALD of TiO_2 uses tetrakis(dimethylamido)titanium (TDMAT) for the titanium and H_2O for the oxygen. It is confirmed by other group members' preliminary work, that this deposition is in the ALD window for a temperature of $150°C$, which is thus the temperature used for this study. The targeted thickness for this layer is 10nm, and 100 cycles of precursors are used to reach this value. The same hold time of three seconds is used to keep the precursors within the chamber. To finish, the FTO inverse opal is treated by $UV - O_3$ for 30 minutes prior to the ALD deposition. A longer time is chosen because the uv-ozone in the group laboratory operates in air, and not in oxygen, which reduces the efficiency of the method.

The samples are not analysed by SEM because of its lack of resolution to distinguish the TiO_2 layer from the FTO inverse opal. To distinguish such small layers, TEM is a very good method, which can be associated with STEM and EDX, in order to chemically map the sample at the nanoscale.

In order to make an analysis with TEM, samples are deposited on a copper grid, which is then placed inside the microscope. Due to the nature of the inverse opal, this structure can easily by scratched from the substrate, and the residuals can be deposited on the TEM grid. Due to the small size of the pieces deposited, a particular grid is used, where most of the empty spaces of the grid are covered with a thin layer of carbon, preventing the small pieces to pass through it. The grid, called holey carbon TEM grid, is still transparent for the electrons, due to the very small thickness of the carbon layer.

The samples are scratched in a clean specimen tube filled with 2ml of isopropanol. The scratching is done with a metallic spatula. When most of the surface of the sample is scratched, the specimen tube with the sample inside is sonicated for 30 minutes, in order to break any aggregates between the broken pieces. $10\mu l$ of this solution is then deposited on the holey carbon grid, and is let to evaporate at room temperature. The scratched samples are all of different sizes. Due to the nature of TEM, which focus on a plane, it is better to choose a small sample, to avoid having blurred areas in the planes which are far from the focus plane. In addition, due to the projection of the 3D sample in a 2D plan, too much information can overlap if the chosen sample is too thick, making the result hard to

interpret.

A scratched part of the coated sample analysed by TEM is presented in figure 4.9 *a)*. The pores present an average size of 200nm, smaller than the initial 250nm PS nanoparticles, which is due to both the shrinking of the PS nanoparticles and the shrinking of the precursors during crystallisation. The interface between the pores and the air is analysed at higher magnification to observe interferences fringes (figure 4.9 *b)*). Due to the projection of the 3D structure into a plane, it is challenging to only observe the TiO_2 coating crystals, however, by only analysing the interfaces visible on the picture, it is assumed that titanium dioxide crystal can be isolated. Two different fringe distances can be observed at the interface, with values of 2.017 and 2.573 Å, that we can identify as the [210] and [101] planes of the TiO_2 rutile phase [197]. However, due to the small amount of available crystal to analyse, the presence of TiO_2 cannot be verified over the whole surface of the inverse opal.

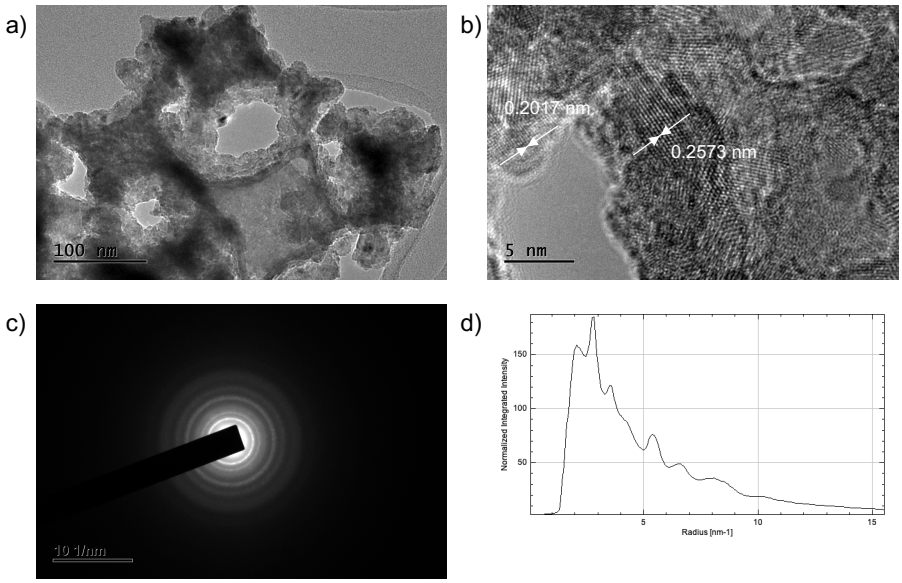


Figure 4.9: *a)* TEM analysis of a TiO_2-coated SnO_2 inverse opal. *b)* High magnification on a TiO_2-coated region. Two interference fringe sizes are indicated. *c)* Large-area electron diffraction of the coated inverse opal, and *d)* radial profile of the diffraction pattern.

To assess the crystallinity of the deposited TiO_2 selected area electron diffraction (SAED) is done on a large amount of samples, which results in a circular diffraction pattern , whose radial profile is extracted (figure 4.9 *c)* and *d)* respectively). Due to the thickness of the analysed sample, many crystals are not in focus, resulting in a diffraction pattern with widin peaks, which can result in a loss in accuracy. The summary of the peaks is given table 4.1, and the peaks can all be identified as a plane of tin dioxide [198]. Due to the very small volume of deposited TiO_2 compared to SnO_2, and the loss of accuracy due to the thickness of the sample, no peaks from titanium dioxide could be identified with this method.

To obtain a better confirmation of the presence of titanium dioxide on the surface of the inverse opal, STEM/EDX is used to provide chemical information at

Table 4.1: Coated SnO_2 peak positions measured with SAED.

Inverse distance (nm^{-1})	d-spacing (nm)	Identified SnO_2 peak
2.9	0.345	[110]
3.59	0.278	[101]
4.21	0.237	[200]
5.45	0.183	[211]
6.62	0.151	[310]

the nanoscale. The three main elements relevant to check for this studies are tin, oxygen and titanium. The chemical maps of tin and oxygen (figure 4.10), which are the main constituents of the inverse opal, are homogeneous and are matching with the sample image acquired with a dark field detector.

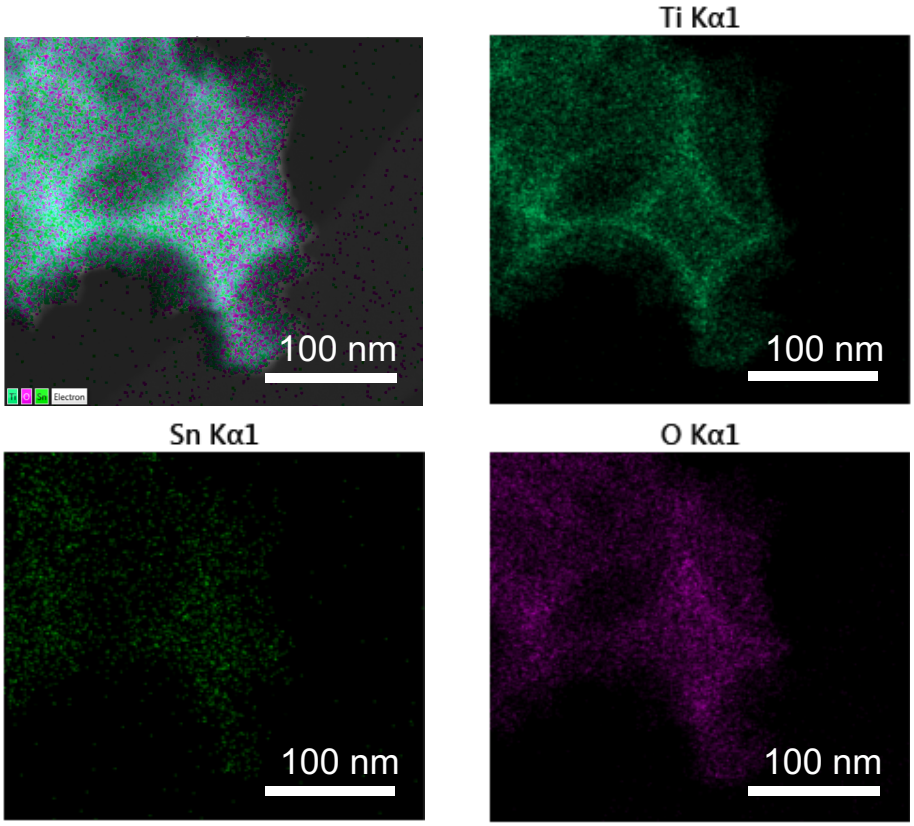


Figure 4.10: STEM/EDX chemical maps for a FTO inverse opal coated with 10nm titanium dioxide by atomic layer deposition. Clockwise, from the top left right : Titanium, oxygen, tin and the superposition of the mapped elements with the dark field image.

However, the chemical map of titanium, which is only present in the ALD coating, presents more intense areas, which are disposed on curved lines(figure 4.10). As the TEM results are a projection from 3D to 2D, such effects can appear, as schematised in figure 4.11. If the coating is very thin and orthogonal to the beam, its image appears very feint compared to that of the bulk inverse opal, as only a small volume of it is projected. However, if the film lies parallel to the beam, then

the projected volume is much larger, which leads to a larger signal. Other pieces sample have been analysed using the same method, giving identical intense lines corresponding to titanium.

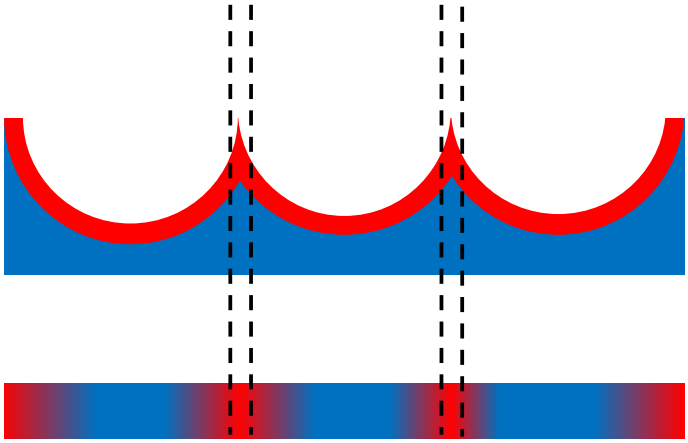


Figure 4.11: Schematic of the projection effects appearing for a coated inverse opal.

The obtained results for titanium on STEM/EDX agree with the idea of a three-dimensional film projected on a two-dimensional plan, which supports the idea that the TiO_2 coating is conformal on the inverse opal. Due to this behaviour being present on many parts of the samples, it is hypothesised that the coating is present over the entire surface of the inverse opal.

In conclusion, a conformal coating of TiO_2 have been obtained inside a FTO inverse opal with small sizes of pores. This coating is produced by atomic layer deposition, with the precursors being kept inside the chamber for a hold time of three seconds for each cycle of ALD. This provides a longer time for their diffusion inside the tortuous inverse opal.

4.3 Perovskite infiltration

In order to make a complete solar cell with the desired architecture, lead-halide perovskite has to be infiltrated inside the TiO_2 coated FTO inverse opal. The infiltrated structure needs to have an over-layer of perovskite to avoid short circuits between the conductive FTO inverse opal and the top electrode, which is deposited later. In addition, it is preferable that the perovskite fully infiltrates the inverse opal, to have a maximal absorption of light, and to avoid any dye absorption which would lead to charge recombination.

The deposition recipes to infiltrate inside inverse opal are made by mimicking the deposition recipes made in our group for standard planar solar cells. These depositions by spin coating ,which results in mirror-like films with a thickness of approximately 400nm, are described hereafter. The deposition recipes are valid for MAPI perovskite.

A 1.5M solution of methyl ammonium lead iodide is firstly made by dissolving 691 mg of lead iodide and 238 mg of methyl ammonium iodide, in a solution of 9:1.1 volume ratio between DMF and DMSO [199]. The DMSO is added in an equimolar ratio with the lead iodide, and its presence stabilises the precursors, creating a more homogeneous film after spin coating [200]. The solution is prepared inside a glovebox, and is then let to stir overnight. When the precursors are totally dissolved, the solution has an intense yellow colour.

To make a film of perovskite, 30 µl of the previously made solution, is spread over a sample. The sample is then spin coated at 4000rpm, for 30 seconds. At 7 seconds, 400 µl of diethyl ether is quickly dropped on the top of the sample. This method, called anti-solvent dripping, allows a fast and controlled crystallisation of the top of the perovskite sample, leading to a flat surface for this layer. The sample, which is yellowish after the spin-coating, is annealed at $100°C$ for 15 minutes, and quickly becomes black, because of the formation of $CH_3NH_3PbI_3$.

4.3.1 Infiltrated substrates

The work made to infiltrate inverse opal with perovskite solution has been carried over an extended duration of this thesis. During this period, other projects were carried on, including one related to the fabrication of crack-reduced FTO inverse opal. For this reason, the FTO inverse opals presented in this section were made with different methods of fabrication.

Most of the work on perovskite infiltration has been done using FTO inverse opal made as previously described in section 4.2. However, as a new method for fabricating high-quality inverse opal was established, these inverse opals are used for the latest results of this chapter. This crack-reduced method for inverse opal fabrication is the topic of chapter 5.

Some parameters determining the final perovskite film, such as the surface tension or the ease of infiltration of the solution inside the inverse opal, are different for the two methods for fabricating the inverse opals. However, it is believed that the impact of these changes are minor for the formation of the films, due to the similar materials and pore sizes, compared to the changes of deposition methods. The fabrication method for the infiltrated inverse opal is specified for each section.

4.3.2 Visual controls

The classical control made after a perovskite spin coating consists in checking if the top of the sample behaves like a mirror, indicating the extreme flatness of its surface. However for infiltrated inverse opal, the challenges of deposition are different, and so two others direct visual tests are directly made after the deposition and annealing of the perovskite material.

To assess the amount of material deposited inside and on top of the inverse

opal, the sample is placed in front of an intense orange light source, and viewed in transmission. As this colour is absorbed, if most of the light can be seen through the samples, it indicates the low amount of deposited materials. A flat film made with a standard method absorbs most of the orange light from a thickness of approximately 500nm. If an infiltrated inverse opal of approximately 1 µm does not absorb most of this light, it indicates a low degree of infiltration, and the need to change the deposition method.

Even though the previous observation gives information about the amount of deposited precursor, it is not enough to qualify the perovskite infiltration inside the inverse opal. Most of the deposited material can form an over-layer, which is also absorbing the light, and only a low amount of perovskite is infiltrated. To detect if the perovskite infiltrates the inverse opal to the bottom, the sample is observed from its back. If the sample is not totally infiltrated, the light coming from its back is interacting with a non-infiltrated inverse opal, before being absorbed by perovskite. Due to this initial interaction, the sample appears slightly greyish when seen from the backside, due to the light scattering on the cracks of the inverse opal. If the perovskite is fully infiltrated, the sample appears black from the back, due to the direct absorption of light.

4.3.3 Antisolvent dripping

As for the infiltration of polystyrene opals with precursors, the infiltration of inverse opal with the perovskite solution is done by depositing a drop of solution on the side of the sample. By capillary effect, the solution is slowly spread into the inverse opal, due to its good wetability [201, 202, 203]. If not all the inverse opal is infiltrated, additional drops of solution are deposited on the same area. After the infiltration, the inverse opal reflects a greenish colour (in addition to the yellow colour of the solution), which is due to the increase of the effective refractive index. This greenish colour can also be seen from the back of the sample, indicating the total infiltration of the perovskite solution through all the inverse opal. The infiltration is done for two concentrations of $CH_3NH_3PbI_3$, 1M and 1.5M, which both provide an identical infiltration.

The sample is spin coated with the same recipe used for a planar sample, i.e., spin coating at 4000 rpm for 30 seconds, with 400 µl of diethyl ether dropped vertically on the sample at 7 seconds. Just after the anti-solvent dripping step, it is observed that the sample passes from barely transparent, to slightly white. The sample is then immediately annealed at 100°C for 15 minutes, where it quickly turns black. After annealing, the sample made with the high-concentrated 1.5M solution is slightly transparent to the orange light, indicating a weak thickness of deposited perovskite, and has a greyish colour when seen from the back, showing that the crystalline perovskite is not present at the bottom of the sample. On the other hand, the sample made with the 1M solution, is seen as black from the back, but is also slightly transparent to the orange light, which indicates a weak perovskite deposition, mostly on the bottom of the structure.

The SEM cross section and top view are presented figure 4.12. The observations by microscopy confirm the hypothesis made by visual inspections : the perovskite is mostly on top of the inverse opal for the 1.5M solution, with the presence of a small over-layer, while it is mostly on the bottom for the 1M solution, without any visible over-layer (figures 4.12 *a)* and *c)* respectively). For both concentrations, the inverse opal is not fully covered with perovskite, and the cracks pattern can still be seen from top. The perovskite layer is not flat but follows the topology of the cracked inverse opal. A careful observation of the cross section of the sample made with 1.5M concentrated solution, reveals that the infiltrated perovskite takes the form of spheres on the top of the structure, which is not seen for the sample made with 1M solution.

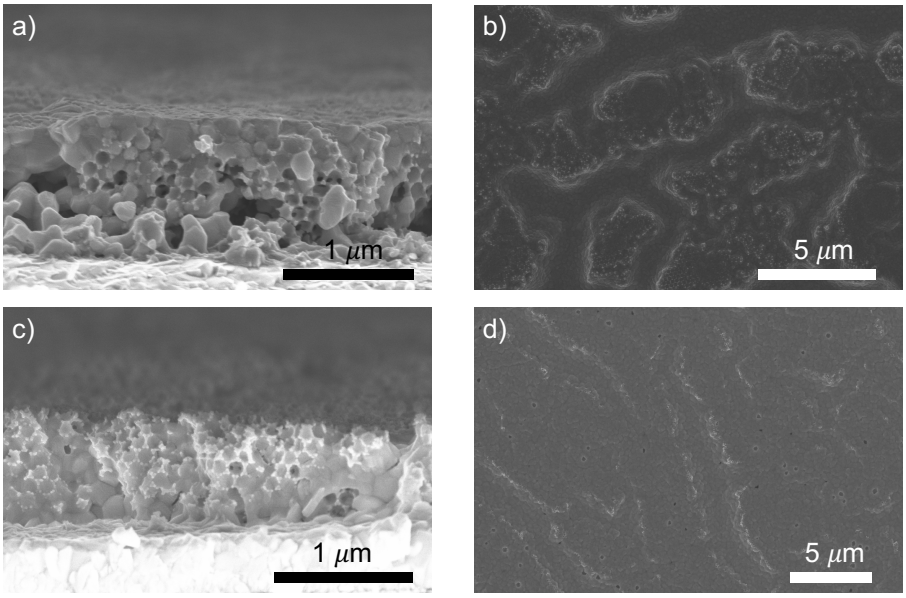


Figure 4.12: Cross section *a)* and top view *b)* of a FTO inverse opal infiltrated with a 1.5M solution of $CH_3NH_3PbI_3$ in DMF/DMSO, spin coated at 4000rpm for 30 seconds, with diethyl ether anti-solvent dripping. Cross section *c)* and top view *d)* of a FTO inverse opal infiltrated with a 1M solution $CH_3NH_3PbI_3$, deposited in the same conditions. Both inverse opals are made by infiltration of a 250nm polystyrene nanoparticles opal template.

To explain the difference of shapes between the perovskite within the inverse opal for the two samples, it is important to describe the process of the film formation as it occurrs inside the inverse opal, which is different from a standard film. In a standard flat film, the precursors come from the whole liquid film formed during spin coating, and then aggregate to form a thinner film. However, the precursors forming the "film" deposited inside the inverse opal comes from the inside of the inverse opal, which thus limits the amount. For this reason, a solution with a higher concentration brings more precursor within the inverse opal, and the final crystal is denser. If a high enough concentration is reached, the formed crystal takes the whole possible space, and so takes the form of a sphere. On the other hand, when the concentration is lower, the film is only formed on the surface of the inverse opal and does not occupy the whole of the availble space. For this reason, it appears flat on the SEM pictures.

It is also hypothesised that the anti-solvent dripping decreases even more the concentration of perovskite precursors within the inverse opal. As the anti-solvent is dropped on the spinning substrate, it also infiltrates the inverse opal and might dilute the already infiltrated solution. The white colour taken by the sample immediately after the anti-solvent dripping, is expected to be due to aggregation of perovskite precursors, which do not take the full space of the inverse opal, and so the cracks again begin to scatter light.

The second difference between the two films is where the perovskite material is located on the inverse opal. As seen in figure 4.12, the material is concentrated on the bottom of the inverse opal of the 1M solution deposition, while it is on top of the structure for the 1.5M one. In the case of the 1.5M sample, an over-layer is created by the anti-solvent step. It is hypothesised that after the creation of the over-layer, which relies on a quick forced nucleation, the precursors within the inverse opal participate in the growth of the crystals in the over-layer, and are thus driven toward the top of the structure. This behaviour happens because of the presence of perovskite crystals in the over-layer, due to the anti-solvent dripping, whereas there are not much perovskite crystals inside the inverse opal. No over-layer is observed for the 1M concentrated solution, probably due to a too-low concentration. Because of the supposed absence of a zone with many crystals seeds, the precursors are driven to the bottom of the sample by natural sedimentation, forming a film after solvent evaporation.

In order to keep more material on the sample, spin coating with lower speed was attempted. However, because of the speed reduction, the anti-solvent is less ejected from the sample during the dripping step, and thus more of it is infiltrated within the inverse opal. This leads to a greater dilution of the solution, which decreases even more the filling of the structure.

As observed with these depositions, the anti-solvent dripping method does not seem adapted to a complete inverse opal infiltration, due to the removal of precursors inside the inverse opal by the anti-solvent. Because of this decrease in concentration, the perovskite precursors do not completely fill the inverse opal after crystallisation, which either leave a fraction of the structure completely unfilled, or only form a film on the it.

4.3.4 Antisolvent free deposition

To assess the effect of the concentration decrease due to the antisolvent, samples without antisolvent dripping methods are explored. As no anti-solvent is used, the speed of the spin coating is also decreased, in order to have more materials on the sample. A concentration of 1.5M is used, with a spin speed of 2000rpm for 30 seconds, followed by 15 minutes of annealing at $100°C$. Inverse opals made of perovskite using spin coating without anti-solvent have been reported[123, 204], showing the potential of this method. However it should be noticed that these structures do not display any over-layer.

For the visual tests, the sample shows very good characteristics, as it absorbs most of the orange light passing through it, and appears well black when seen from the back. However, the samples made without anti-solvent dripping exhibit light scattering from the top, indicating the absence of over-layer on them. The SEM cross sections and top views (figure 4.13) confirm the visual observations that no over-layer is present, which is because of the absence of quenching to force the crystallisation. However, the perovskite is well infiltrated inside the inverse opal, with an infiltration reaching the bottom of the structure. In addition, it is completely filling the inverse opal, which is seen with the presence of many perovskite spheres inside it.

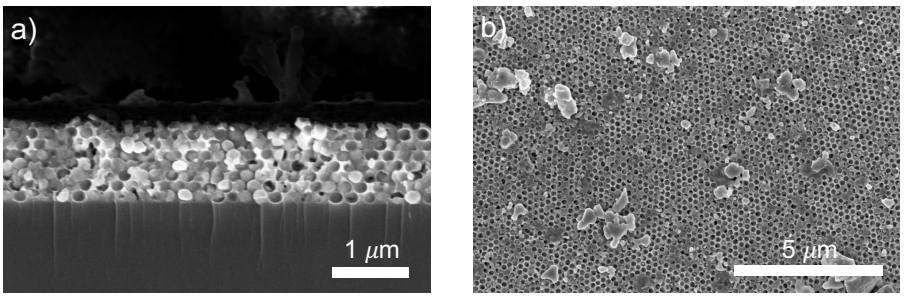


Figure 4.13: Cross section *a)* and top view *b)* of a SiO_2 inverse opal infiltrated with a 1.5M solution of $CH_3NH_3PbI_3$ in DMF/DMSO, spin coated at 2000rpm for 30 seconds. Inverse opal made by a one-step method.

The removal of anti-solvent as well as the decrease of the speed of spin coating greatly increases the filling of the inverse opal, but no over-layer is present anymore. As no anti-solvent is used, the film does not crystallise on top of the substrate due to the high boiling points of the used solvents, and most of the solution is ejected off the surface during the spin coating. However, due to the capillary forces inside the inverse opal, the infiltrated solution stays inside it. As no perovskite crystals seeds are present on the top of the sample, the crystallisation starts within the inverse opal, which keeps the precursors within the structure, and allows a good filling. However, as this method cannot provide a regular over-layer, it cannot be used to make solar cells.

4.3.5 Solvent retardation method

A high concentration is beneficial for a complete filling of the inverse opal, since more precursor is thereby loaded into the structure. However, a too high concentration increases the viscosity of the solution, which can prevent a proper infiltration. To overcome this effect, a deposition known as solvent retardation method is used[205]. In this deposition, initially made to produce extra thick perovskite films, a 1.5M concentrated solution is deposited on the sample, which is then briefly spun to remove excess solution. The sample is then left to dry for a certain time, to evaporate the solvent and so increase the concentration of the solution on the sample. The highly concentrated solution is then normally spin coated, with application of anti-solvent dripping.

The samples have been infiltrated with a 1.5M solution of $CH_3NH_3PbI_3$, by the side of the sample. The first spin coating time is three seconds with a speed of 1000 rpm, and the waiting time between 30 seconds and one minute. In order to favour the evaporation of the solvents, the spin coater chamber is opened during the waiting time to allow a good diffusion of the vapours. The samples made with this solvent retard method present a good absorption to the orange light, but are seen as greyish from the back.

The SEM analysis shows a flat and homogeneous surface, but pinholes are still visible (figures 4.14 *a)* and *b)* respectively). From the side, the top half of the sample is seen as strongly filled, with the presence of perovskite spheres close to the over-layer (figure 4.14 *c)*). The infiltration is stronger than the one previously observed with a standard deposition using a 1.5M solution.

Due to the strong concentration of the solution, the over-layer is quickly formed at the application of the anti-solvent, and is even self-maintained at the cracks area (figure 4.14 *d)*). However, in these areas, only a finite volume of solution is used to make the film, as it is limited by the over-layer on top. Because the amount of precursors within these volumes is insufficient to make a full film of the same volume, a highly porous film is created, as seen in figure 4.14 *d)*.

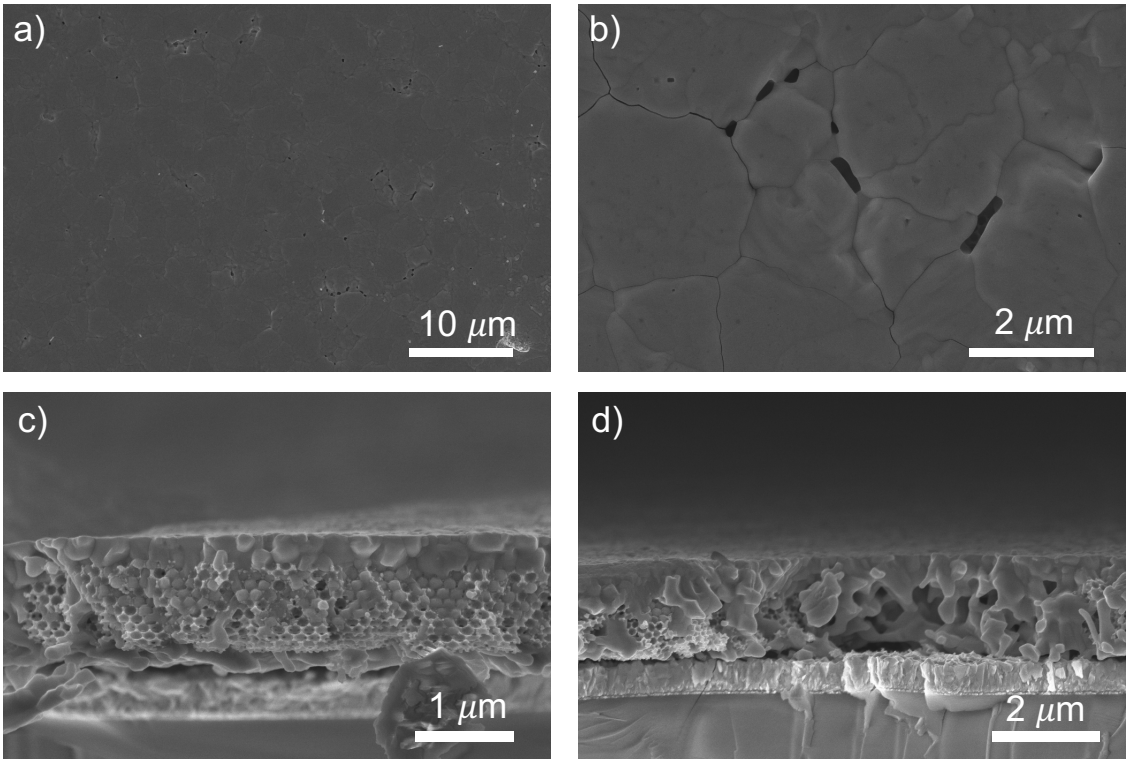


Figure 4.14: *a)* Top view of a FTO inverse opal infiltrated with a 1.5M solution of $CH_3NH_3PbI_3$ in DMF/DMSO. The sample is spin coated for one second, and is then rested for one minute to evaporate, and increase the precursor concentration. This is followed by a spin coating at 4000rpm for 30 seconds, with anti-solvent diethyl ether dripping at 7 seconds. *b)* Enhanced view of pinholes on top of the film. Cross section of the sample on a defect free part *c)* , and on a cracked part*d)*.

In spite of the higher concentration of precursors within the inverse opal,

the solvent retard method fails to provide a complete infiltration of the structure. The infiltration is mostly happening on the top of the structure, which is due to the perovskite crystal seeds present in the over-layer, as already hypothesised previously. However, this method provides an homogeneous over-layer, which does not follow the topology of the sample and stays flat even on top of the cracks, so can be used for the creation of solar cells.

4.3.6 Alternative crystallisation methods

The application of anti-solvent during the spin coating reduces the concentration of precursors within the inverse opal, which prevents a full coating of the structure, as previously seen. Instead of the deposition of anti-solvent to force the film crystallisation, it is possible to apply a strong nitrogen flow directly on the sample during the spin coating, which flush the evaporated solvent and decreases their partial pressure, which has the effect of suddenly increasing the evaporation rate of the solution [206, 207]. This evaporation quickly increases the concentration of the precursors, forcing the crystallisation of the perovskite.

In order to apply a strong and localised pressure on the sample, a nitrogen gun has been installed inside the glovebox. This gun is directly connected to an external nitrogen cylinder, whose pressure can be controlled. The samples are infiltrated with a 1.5M solution, and the pressure is applied after 7 seconds of spin coating, and is maintained until the end of it, after 30 seconds. The gun is directly vertically to the sample, with a distance of approximately 5cm between them. The pressure applied on the sample is limited because of the glovebox used. Indeed, for pressures of more than 3 bar applied during the whole time of spin coating, the glovebox pressure increases too much and cannot regulate, which could damage it. For this reasons, the pressure used in the experiments is limited to 3bar. Two speeds of 2000rpm and 4000rpm are tested, as well as three different pressure of 1, 2 and 3bars.

With visual tests, the samples made at 2000rpm, all appear quite transparent, for all tested pressures. It is hypothesised that due to the low spinning speed, the evaporation happening during the spin coating is very low, and so the solution does not reach a concentration which is high enough for the quenching to happen. Instead of creating a crystalline film, the nitrogen pressure pushes the solution out of the inverse opal, resulting in an extremely low infiltration.

At 4000rpm, the infiltrated perovskite shows a greater absorption, indicating better filling. The sample becomes more opaque when the pressure is increased, because of a better quenching of the solution. When the pressure is not high enough, only a few perovskite crystal seeds are formed on the surface of the inverse opal, and the crystals growth occur only from them, which results in a discontinuous film with material concentrated on the initially formed crystals. Because of the this, most of the film is uncovered, resulting in a low average absorption. With a higher pressure, more crystals are formed on the surface, giving a more homogeneous coverage.

At 3 bar, a film starts to get formed on top of the inverse opal (figure 4.15 *a)*), while keeping a large amount of infiltrated material (figure 4.15 *b)*). According to [206], a pressure of 6 bar is required to form a homogeneous film, but this pressure could not be reached because of technical reasons.

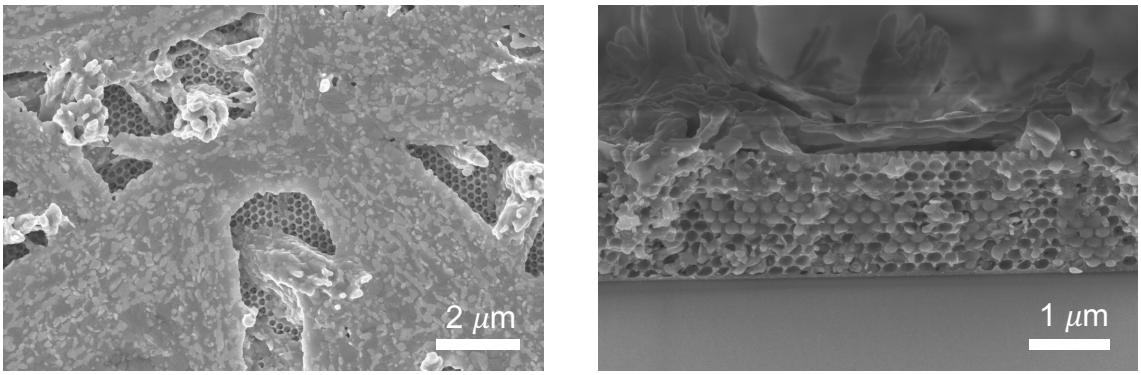


Figure 4.15: Top *a)* and cross section view *b)* of a FTO inverse opal infiltrated with a 1.2M solution of $CH_3NH_3PbI_3$ in DMF/DMSO spin coated at 4000rpm for 30 seconds, with a 3bar nitrogen pressure applied on the sample during spin coating, for 15 seconds. Inverse opal made with a one step nano-crystal infiltration method.

A second way of quenching the perovskite to form a flat film without the use of anti-solvent, is called flash vacuum. In this method, the freshly spin coated perovskite sample is put in a small chamber, where the pressure is quickly dropped at 20Pa [208]. The fast change of pressure provokes a forced evaporation of the solvent in a short time. As this evaporation primarily occurs on the surface of the film, the concentration is locally increased, resulting in a forced crystallisation of the material. In the same way as the high pressure method, this method does not remove precursor from within the inverse opal. Both methods can be combined, increasing the evaporation rate of the solvent even more[209].

This method have been tested for inverse opal infiltration, with the same solution concentration and spin coating parameter as previously specified. However, due to the absence of such a vacuum chamber within the glovebox where the samples are made, only the anti-chamber of the glovebox, used to take samples in or out, could provide vacuum. The vacuum in this chamber is reached slowly, in approximately 10 seconds, which is too slow to quench the film, resulting in a poor final homogeneity.

4.3.7 Two-step deposition

Prior to the development of the one-step method, directly synthesising $CH_3NH_3PbI_3$, perovskite solar cell could be made in a two step method. In this method, a lead iodide thin film is firstly made on the substrate, by spin coating a solution of PbI_2 in DMF, which is then annealed at a chosen temperature. The yellow film is them immersed into a solution of methyl-ammonium in IPA, where the film becomes black due to the infiltration of MAI in PbI_2, resulting in $CH_3NH_3PbI_3$ perovskite.

The two-step deposition presents two advantages compared to the mono step one. Firstly, due to a simpler deposition, the two-step method does not require any anti-solvent step, which makes the film deposition and material crystallisation easier to control. As only the lead iodide is initially dissolved and infiltrated in the inverse opal, the solution is less concentrated making it easier to infiltrate the structure. Secondly, when the film is immersed inside a methyl ammonium solution, it swells due to the infiltration of the MAI inside the structure, which adds more material within the inverse opal.

The chosen solvent is a mixture of DMF and DMSO, because of the propriety of DMSO to form a complex with lead iodide, so retaining more of the material in the final film. The amount of DMSO is chosen as being equimolar to the amount of PbI_2. The solution is made by dissolving 691 mg of lead iodide in 1ml of a DMF/DMSO solution, mixed in a 9:1.1 ratio.

A solution of MAI in isopropanol concentrated at 10mg/ml, is made by dissolving 50mg of MAI in 5 ml of IPA, then left to under stir for one hour prior to use. The dissolution is made inside a nitrogen glovebox. A small amount of IPA is introduced in the glovebox from a standard solution exposed at air, and is then let open for 2 hours while stirring, in order to release any oxygen or humidity.

After infiltration with the PbI_2 solution, the sample is spin coated at 2000rpm for 30 seconds, and is then annealed at $60°C$ for 30 minutes. The sample takes a strong yellow colour, and presents a good infiltration of the inverse opal, as barely no light scattering can be seen from the back of the sample. After the annealing, the sample is introduced for 10 minutes in the MAI solution. Shortly after the immersion, the sample takes a black colour, indicating the formation of $CH_3NH_3PbI_3$. After immersion, the sample is annealed at $100°C$ to finalise the crystallisation of the material and evaporate any residual solvent.

The final sample strongly absorbs light, as barely none of the orange light can be seen through it. Its top surface is black due to the presence of perovskite, and strongly scatters light, indicating a large roughness, as the crystallisation is less controlled compared to the previous methods. However, when seen from the back, an intense yellow colour is seen, which indicates the presence of lead iodide, meaning that not all of the initial material is converted.

An analysis by SEM shows the continuity of the film over the whole surface of the sample (figure 4.16 *a)*), as well as a strong roughness. The sample presents a large over-layer on top of the inverse opal, of approximately 7 µm (figure 4.16 *b)*). This large thickness is due to the low spin coating speed used, and the presence of DMSO in the solvent, which retains the lead iodide. A closer look at the surface of the sample reveals a different crystallisation compared to the bulk. It is hypothesised that the perovskite is only present on the first 800nm of the sample, which presents a different crystallisation, while the rest of the material is still lead iodide, as seen by the yellow colour of the back of the sample. In spite of this small amount of perovskite material, the infiltration of the inverse opal by the lead iodide is complete and reaches the bottom substrate (figure 4.16 *c)*).

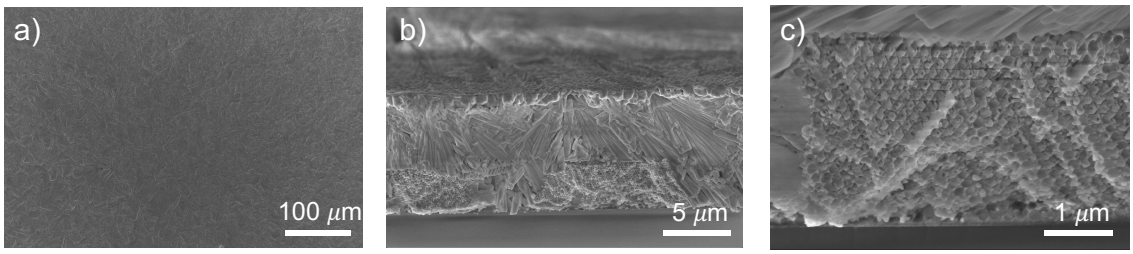


Figure 4.16: Top *a)*, cross section *b)* and magnified cross section view *c)* of a FTO inverse opal infiltrated with a 1.2M solution of PbI_2 in DMF/DMSO spin coated at 2000rpm for 30 seconds, annealed at $60°C$ for 10 minutes, followed by an immersion inside a 10mg/ml solution of methyl ammonium in IPA. The immersion is followed by an annealing at $100°C$ for 15 minutes. Inverse opal made with a one step nanocrystals infiltration method.

The small volume percentage of perovskite in the final film, and its presence only on the top of the sample, is due to the way the conversion from lead to perovskite happens in the two step method. The infiltration of methyl ammonium inside the lead iodide film occurs mostly from the top of the sample, which is where the conversion to perovskite firstly happens. Some of the isopropanol molecule does not stay on the immediate surface of the film, and diffuses deeper. When all the film of the surface is converted, then no more infiltration occurs, as the IPA cannot pass through the perovskite material which is already infiltrated.

In order to increase the percentage of conversion and fill the inverse opal with perovskite, the thickness of the over-layer has to be greatly reduced. However, as only 800nm of the film got converted, this alone cannot allow the full infiltration of the inverse opal, which is thicker. The concentration of the IPA solution also has to be reduced, to slow down the rate of conversion[189], so as to allow the diffusion of the molecules for a longer time, increasing the total amount of conversion.

4.4 Solar-cell power conversion efficienicy

In order to complete the solar cell, the hole transport layer and the top electrode are deposited on top of the perovskite. The hole transport layer deposition recipe is similar as the one used by our group to make standard devices. In brief, 2mg of poly (bis (4-phenyl) (2,4,6- trimethylphenyl)amine) (PTAA) are dissolved into 1ml of chlorobenzene, and left to stir for 30 minutes. The solution is spin coated on top of the perovskite sample at 3000 rpm, for 30 seconds. The gold electrode is deposited by thermal evaporation, in a vacuum chamber inside a glovebox. The samples are protected with masks, to deposit gold only on selected areas, which produces a pattern similar to what is schematised figure 4.2, with 6 electrodes. 50nm of gold is deposited with this method, at an average rate of 0.5 Å/s.

To measure the solar cell, the bottom electrode has to be contacted. To do so, a tissue lightly soaked with DMF is used to remove the PTAA layer and the perovskite from of the the side of the cell, as shown figure 4.2. The solar cells are

tested within a specific hermetic measurement cell, which automatically contacts the bottom and the six top electrodes. The analysed top electrode is selected with a mechanical switch. The measurement cell is placed inside a solar simulator, with an illumination of 1.5 sun. The solar cell is tested with a Source-meter Keithley 2400, used to sweep the voltage and measure the resulting current.

Due to short circuits between the FTO inverse opal and the gold top electrodes, almost all of the cells made in this thesis failed to produce any power, which results in an current area-voltage curve, also known as J-V curve, being a straight line and behaving like a standard resistance. These short circuits are due to an incomplete coverage of the FTO inverse opal by the perovskite material. The only cells possessing a sufficient overlayer to prevent short circuits are the cells made with the solvent retard method (figure 4.17). The cells made by two-step deposition appear to be thick enough to prevent a direct contact between the gold electrode and the FTO inverse opal, but due to lack of time these cells could not be tested.

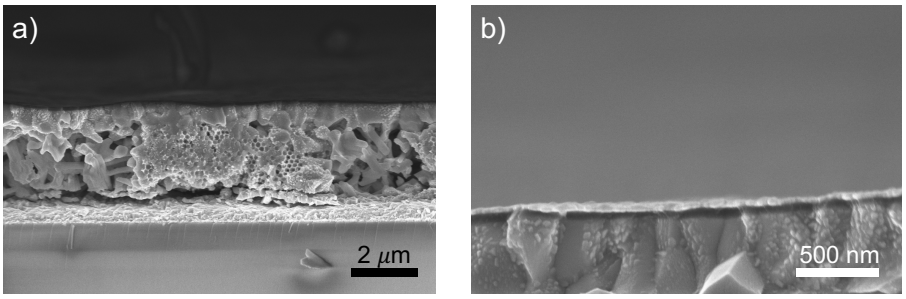


Figure 4.17: *a)* SEM cross section of a full solar cell with overlayer, made with the solvent-retard method. *b)* Magnified view of the top of the solar cell with, from bottom to top, the perovskite layer, the PTAA layer in dark, and the gold layer in white.

The tested solar cells which present a full overlayer of perovskite without any apparent FTO present a curve such as the one presented figure 4.18. On the bottom right of the curve, the solar cell has a negative current while being biased with a positive voltage, which means that it produces current, according to the generator convention. Only the main characteristics of the measurement are presented here, but more detailed information is found in the literature [88, 210].

Two of the main characteristics of a solar cell which can be extracted from an IV measurement, are the open circuit voltage (V_{oc}) and the short circuit current (J_{sc}), which represents the necessary voltage to cancel the current inside the cell and the current without any applied voltage respectively [88]. These two points are represented in figure 4.18, and the best measured device made with FTO inverse opal has value of 0.75V for the V_{oc}, and -0.233 mA/cm^2 for the J_{sc}, assuming a sample area of $4mm^2$. At these two points, the power produced by the solar cell is null. An ideal solar cell would generate a maximal power with a voltage V_{oc} and a current J_{sc}, which would make its IV curve follow the dotted lines on figure 4.18. However, the characteristics of a real solar cell are lower than an ideal one, and a factor named the fill factor (FF), represents this non-ideality and is calculated by comparing the areas in the bottom right quadrant between an ideal solar cell (blue rectangle), and the measured solar cell. The best FTO inverse opal solar cell made

in this thesis have a fill factor of 0.37. To finish, the most important value obtained from such a measurement is the photo-conversion efficiency (PCE), which represents the energy conversion between the incoming light and the produced electricity. The best device made presents a PCE of 6.46%.

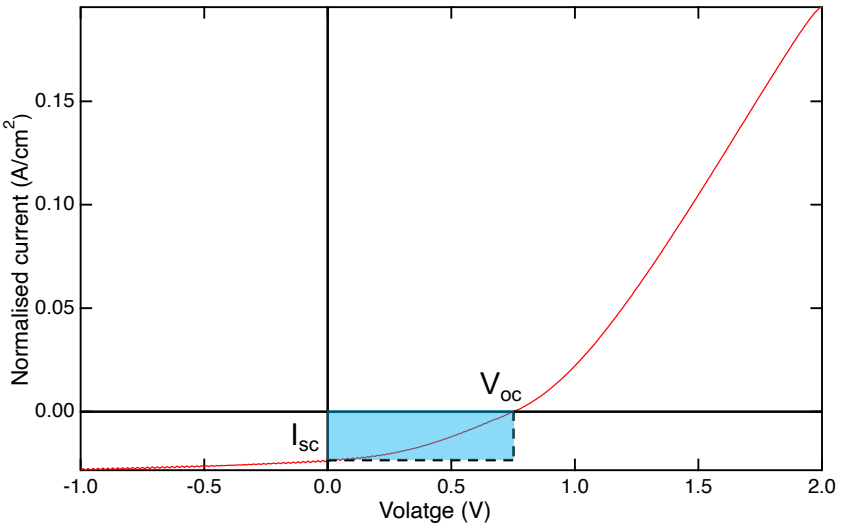


Figure 4.18: I-V curve of an FTO inverse opal base solar cell, under 1.5 Sun illumination. The open circuit voltage (V_{oc}) and the short circuit current (J_{sc}) are represented. The blue rectangle represents the behaviour of an ideal cell of the obtained V_{oc} and J_{sc}, and is used to calculate the fill factor.

The measured values of the best infiltrated solar cell are far below the best perovskite solar cells, which can achieve efficiencies up to 25.2%[176] .These low measured efficiencies are due to low V_{oc}, J_{sc} and fill factors, whose low values can be explained by the perovskite infiltration inside the FTO inverse opal. As it can be seen figure 4.17, the perovskite film is very porous in the areas where no inverse opal is present, which can lead to a large rate of recombination of the charges, and also a poor interface between the perovskite and the TiO_2. As previously reported, the perovskite crystallisation is a very sensitive step of the deposition, which has to be controlled to obtain the best performances. As the working solar cell deposition has been adapted to obtain a flat surface without any apparent FTO, irrespective of the perovskite crystallisation quality, the performances of the infiltrated perovskite is lower than a standard film. In addition, the infiltration of the perovskite inside the inverse opal is not complete, which can lead to a dye sensitisation of the solar cell, increasing the losses.

4.5 Conclusions

Fluorine tin oxide inverse opal have been made from polystyrene opal templates, made with nanoparticles of 250 nm. The infiltration is done by spin coating, and results in large areas of highly ordered structures without any over-layers. Many cracks are present in the final structures, due to the shrinking of both the PS

nanoparticles, and the crystallisation of amorphous precursors to crystalline structures. These structures are then covered with a conformal layer of titanium dioxide, deposited by atomic layer deposition with a 3 second holding time, to let the gaseous precursors infiltrate the structure. The homogeneity of the ALD deposition has been confirmed by SEM and TEM, for both cracked and crack-free structures.

The infiltration of $CH_3NH_3PbI_3$ inside the inverse opal is particularly delicate, due to the difficulties of controlling the perovskite crystallisation. The classical anti-solvent method, which consists in dropping a chosen solvent during the spin coating to promote a fast crystallisation of the perovskite, does not give good results for the inverse opal infiltration, because the anti-solvent ejects too many precursors from within the inverse opal, and thus prevents good infiltration. On the other hand, a deposition without anti-solvent gives better infiltration, with more material being present within the inverse opal, but the surface of the inverse opal is totally exposed.

Alternative ways of controlling the perovskite crystallisation, such as using a nitrogen gun during the deposition, have been tested. This method gives a better infiltration of the inverse opal, but which is still not totally full, due to the absence of material removed during the spin coating. Due to technical limitations, the pressure and duration of the use of the air gun had to be restricted, which limited the quality of the surface of the perovskite obtainable. To increase the filling of the inverse opal, the concentration of the perovskite solution has been increased with a method known as solvent retard. This method provides an homogeneous and thick over layer, due to the highly concentrated solution used, but failed to completely infiltrate the inverse opal. The reasons for the absence of total infiltration with a highly concentrated solution are not yet explained, but it is hypothesised that most of the material within the inverse opal are "absorbed" by the thick over-layer, where crystal growth occurs.

Due to the complex and hard to control mechanisms happening during the one-step deposition method, where both the methyl ammonium and the lead iodide are deposited simultaneously, the two step method has been tested, with the lead iodide being firstly deposited, and then impregnated by a methyl ammonium solution, to form $CH_3NH_3PbI_3$. This methods provides a good infiltration within the inverse opal, even though not all of the lead iodide is converted to perovskite. Due to lack of time, this method could not be optimised.

Almost all the infiltrated solar cells show a short circuit during the tests, due to the uncovered FTO inverse opal. Only the cells with a large overlayer could be measured, but show very poor characteristics, with only 6.46% PCE for the best device. The cracks present in the FTO inverse opal solar cell are a major concern for the creation of a performing solar cell, both because of the porosity of the film in the cracks and the need of an adapted deposition recipe to avoid short circuits. However, this adapted deposition can prevent good crystallisation of the perovskite layer, drastically reducing its performance. In order to make better solar cells with this architecture, it is thus very important to prevent the appearance of cracks inside the inverse opal, which is the goal of the next chapter.

Chapter 5

Crack-free FTO Inverse opal

The XRD measurements presented in this chapter have been done by Mr Bob Xu.

5.1 Fabrication process overview

Different methods are attempted in this chapter, in order to produce crack-free FTO inverse opal. A brief overview of these methods is shown figure 5.1.

The goal of the first method is to obtained a crack free opal, by using tin precursors as bindings agent to form covalent bounding between the PS-nanoparticles. To do so, PS-nanoparticles with COOH groups on their surface are mixed with a low amount of tin precursors (figure 5.1 *a*). When the nanoparticles are deposited on the substrate, the tin precursors start to react with the COOH groups, creating covalent bounding between the nanoparticles (figure 5.1 *b*). This prevent the apparition of cracks, which are due to the shrinking of the nanoparticles during drying.

The second method is the one-pot method, previously described in chapter 3. In this method, a suspension of PS-nanoparticles is mixed with tin precursors (figure 5.1 *c*). The tin precursors are introduced in a more important quantity compared to the previous method, as this time, the objective is to completely fill the space between the nanoparticles with precursors (figure 5.1 *d*).

The last method presented in this chapter consists in mixing PS-nanoparticles and FTO-nanocrystals (figure 5.1 *e*). When the nanoparticles are deposited, the nano-crystals occupy the space between them (figure 5.1 *f*). The self-assembly of the nanoparticles is not disturbed, if the size of the nano-crystals is small enough. This method is similar to the one-pot method, but due to the low reactivity of the nano-crystals compared to the dissolved precursors, a better stability is obtained using nano-crystals rather than precursors.

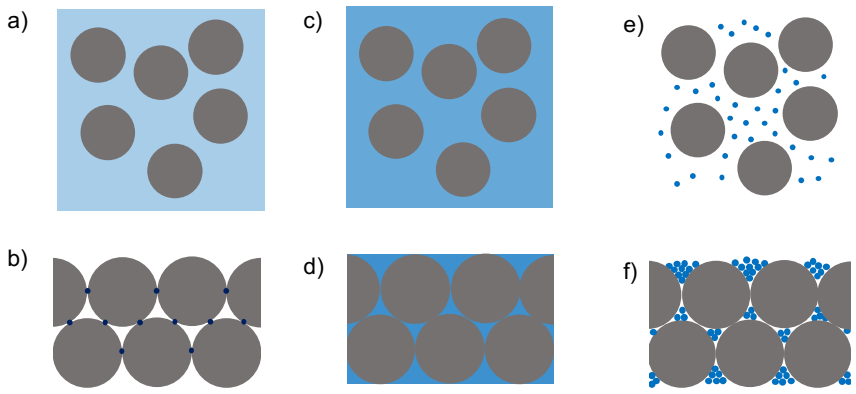


Figure 5.1: *a)* Mix of COOH-terminated PS-nanoparticles with a low amount of tin precursors, resulting in *b)* covalent bounds between the nanoparticles after the deposition. *c)* Mix of tin precursors with PS-nanoparticles, which produces *d)* an opal fully infiltrated with precursors. *e)* Mix of FTO-nanocrystals and PS-nanoparticles, resulting in an opal fully infiltrated with FTO-nanocrystals.

5.2 Crack-free polystyrene template

The cracks in inverse opal create light scattering in the structure, which is an unwanted effect for a photonic device, and is also undesirable when the inverse opal is used as an electrode, as it gives an irregular surface, preventing uniform coating. These cracks have two origins : the shrinking of polystyrene spheres after self assembly, giving a cracked opal, and the shrinking of the precursors from amorphous to crystalline, increasing the previously formed cracks. In order to reduce the amount of cracks in the inverse opal, the first task is to obtain a crack-free opal.

Different possibilities of crack-free opal are listed in section 1.3.5, but not all of these methods can be used in order to build an inverse opal afterward. One of the most promising methods is reported in a work from Shi *et al.* [79], where zirconium precursors creating covalent bounds between PS nanoparticles, terminated with COOH groups. In addition of creating covalent groups between particles, the zirconium precursors are expected to react with the rest of the surface of the nanoparticle, making it fully covered with zirconium.

If an inverse opal is made from this structure, it will also be covered of zirconium on its surface, as this material is resistant to high temperature annealing. Because the surface are extremely important in devices such as solar cells, this zirconium layer could reduce the cell performance. For this reason, it is decided to use a tin based cross linker to make covalent liaison between the particles.

The precursor used in the previous chapter, tin tetrachloride pentahydrate, is a good candidate for such a cross-linker, due its good solubility in water and its high reactivity. A small amount of precursors, 5 µl of a 0.05M solution of $SnCl_4$ in water, is added to a suspension PS-COOH nanoparticles, concentrated at 0.1%. This solution is kept at 60 $°C$ and 20 % RH, for 48 hours.

The opals formed with the addition of the tin precursor show a reduced

number of cracks (figure 5.2 *a)*), compared to a regular opal, and the cracks do not present any specific orientation. However, the nanoparticles packing present more defects, and contamination is observed between the particles and on top of them (figure 5.2 *b)*). This is attributed to the introduced precursors, which react between themselves instead of forming bounds between the particles. This is due to the high reactivity of tin tetrachloride, which can form aggregates with time. These aggregates can be seen on figure 5.2 *a)*, as white dots. It can also be observed on 5.2 *b)*, that some of the particles have a different apparent roughness than the others. Instead of being smooth as the regular nanoparticles, it appears that a rough shell is formed around them. A hypothesis for the appearance of these rough nanoparticles, is that when the precursor solution is added into the nanoparticles suspension, it is not immediately diluted. For a very short time, a part of the suspension is more concentrated than the rest of it. The PS-COOH nanoparticles in this region reacts quickly with the tin precursor, which form a shell around them. As the concentration of precursor is then decreased due to dilution, the formation of this shell is not observed for all nanoparticles. The nanoparticles which reacted with the tin precursor are then mixed with other ones, which results in an inhomogeneous suspension of nanoparticles with and without shells, giving an opal with a mix of these particles.

Due to the high reactivity of the tin precursor, the COOH groups on the surface of the nanoparticles react too quickly with it, or the precursors aggregate between themselves. To prevent this effect, ethanolamine C_2H_7NO is added to the solution, to stabilise the tin based molecule from reacting too quickly.[211] The same solution previously described is used, with the addition of $5\mu l$ of ethanolamine. The resulting opal present more cracks than the one without ethanolamine, and these cracks extend more along the close packed directions [110] than previously (figure 5.2 *c)*). The close range order is much better, very few defects are observed, as well as no aggregates due to precursors aggregation (figure 5.2 *d)*). The polystyrene nanoparticles also appear much closer and packed than for a conventional opal, which is due to the tin precursors creating strong bounds between the particles, forcing them to get as close as possible.

The cracks in the structure are not randomly organised (figure 5.2 *e)*). It can thus be supposed than a perfect crack free opal is primarily formed, but is then cracked during the drying of the sample. This time, the stabilised tin precursor do not react fast enough with the COOH groups to prevent the cracks from appearing. Instead, the reactions happen after the drying of the sample, resulting only in the nanoparticles getting closer after the crack formation. It can be confirmed that the nanoparticles are deformed and take a hexagonal shape due to the mechanical stress induced by the chemical boundings. Indeed, the particles located at the edge of a crack still present a spherical shape (figure 5.2 *f)*).

Both samples with and without the ethanolamine stabiliser posses cracks, but for different reasons. Without stabiliser, the tin precursor reacts too quickly and gets consumed by the COOH groups, while the addition of stabiliser makes the reaction too slow, making it happen only after the cracks have formed. The ideal condition would be to have the reaction between the tin and the carboxyl groups occurring at the exact time where the particles self-assemble, which requires a very

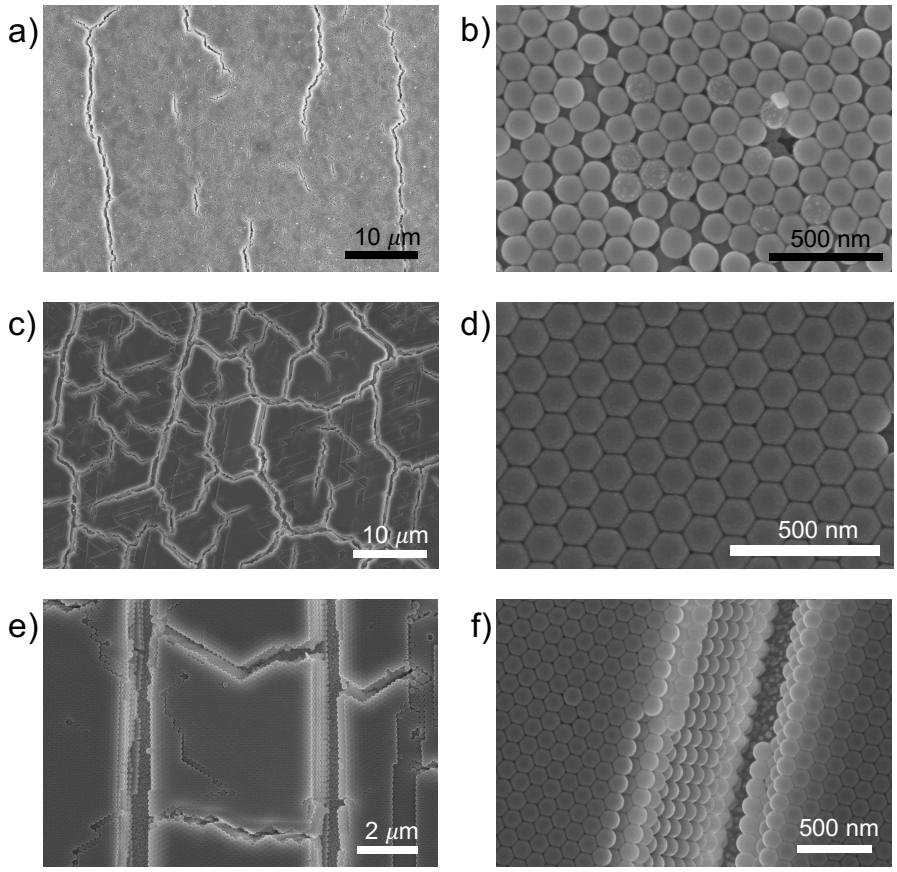


Figure 5.2: Large area (a) and magnified (b) SEM view of an opal made with a 5ml solution of PS-COOH particles (0.1% vol %) with 5μl of a 0.05M $SnCl_4$ solution as a cross-linker. Large area (c) and magnified (d) SEM view of an opal with the same solution as previously, where 5 μl of ethanolamine are added. Cracked structure obtained with stabilised tin cross linker (e), and enhanced view of the particles the the location of the cracks (f)

precise amount of stabiliser to precursor ratio.

In order to obtain the maximal amount of tin precursor which can be introduced in the opal suspension, while avoiding an excess of material which would lead to defects in the structure, the following experiment is performed. This is done by stabilising the solution with the addition of ethanolamine, and the amount of stabiliser in increased proportionally with the added precursors. Instead of the previous 5μl of 0.05M of $SnCl_4$ and 5μl of ethanolmaine, the volumes of these two compounds are increased to 7.5μl, 10μl, 12.5μl and 15μl.

The samples obtained have a similar crack pattern as previously observed on figure 5.2 *c)*, but differences appear at higher magnification. As observed on figure 5.3, for volumes of 10μl and more, visible precursor appears between the particles, meaning that the whole surface os the nanoparticles is covered by the precursor. It is then decided to use a volume of 7.5μl for the 0.05M precursor solution to obtain an optimal concentration of precursor.

The molar mass and the density of ethanolamine are 61.084$g.mol^{-1}$ and

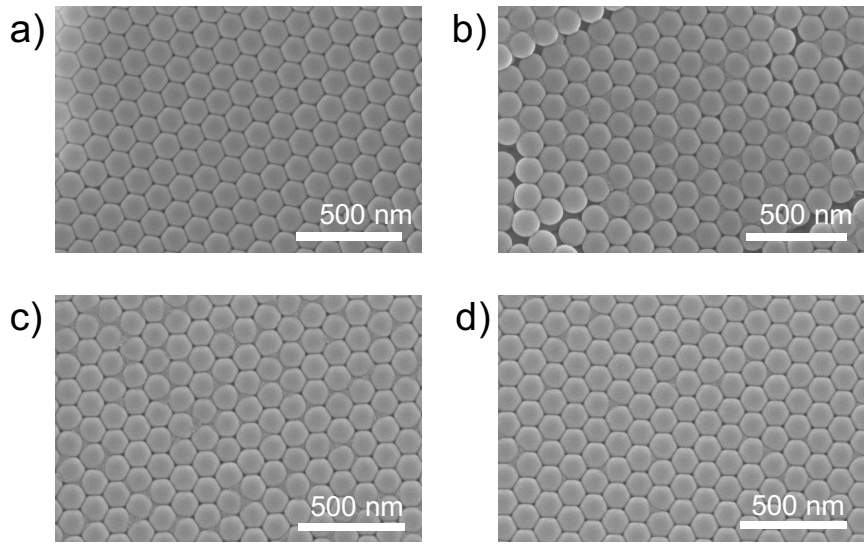


Figure 5.3: Magnified SEM view of opal samples made from a 5ml solution of PS-COOH particles (0.1% concentrated) with the addition of *a)*, 7.5μl of a 0.05M $SnCl_4$ and 7.5μl ethanolamine, *b)*, 10μl of a 0.05M $SnCl_4$ and 10μl ethanolamine, *c)*, 12.5μl of a 0.05M $SnCl_4$ and 12.5μl ethanolamine and *d,* 15μl of a 0.05M $SnCl_4$ and 15μl ethanolamine.

$1.0117 g/ml$ respectively. With these values, it can be calculated that the ratio of ethanolamine molecule to tin atom is approximately of 331:1, for all the solutions previously used. To reach a turning point of stability, it is decided to greatly decreases this ratio. Solutions with a 2:1 and 3:1 ratio are made, which consists of 7.5 μl of 0.05M of $SnCl_4$ solution stabilised with $0.045 \mu l$ and $0.068 \mu l$ of ethanolamine respectively.

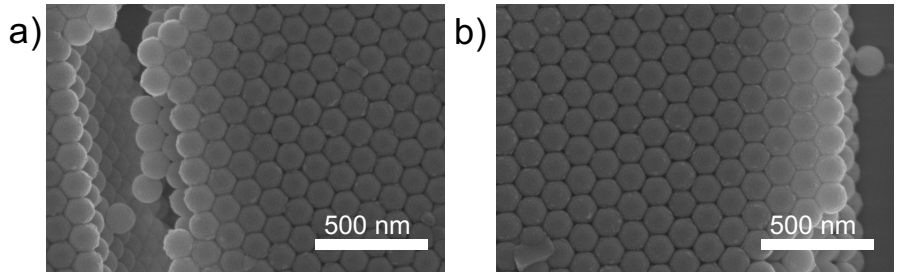


Figure 5.4: Magnified view of opal samples made from a 5ml solution of PS-COOH particles (0.1% concentrated), with 7.5 μl of a 0.05M solution of $SnCl_4$, stabilised by ethanolamine in a 2:1 (a) and a 3:1 ratio (b).

The resulting opals present more precursor aggregation than fully stabilised samples, but no particles with a shell can be seen, indicating that the ethanolamine still affects the precursor (figure 5.4).The surface of the nanoparticles presents a small homogeneous roughness, meaning that some of the precursors aggregate on the surface, and cracks are still present on both sample.

These results show an intermediate system lying between the completely stable precursor, which only reacts after the cracks are formed, and a less stabilised one, that react with particles immediately after being added to the suspension. With

a 2:1 and 3:1 ratio, the precursors reacts in a homogeneous way with the surface of the particles, but cracks are still formed, because either the reaction is too slow and occurs after cracks have formed, or it is too fast, and the precursors are already fully reacted with the particles surfaces, preventing addition bounding.

Because of the high sensitivity of this method, which required additional adjustment concerning the stabiliser to precursor ratio, as well as other parameters such as temperature, it is decided to work on an alternative method for the the fabrication of crack free inverse opal. In addition, because the boiling point of ethanolamine is 170 °C, its concentration in water increases during deposition, making the reaction more difficult to control.

5.3 One-pot method with tin oxide precursors

5.3.1 Zeta potential and solution stability

In order to make a crack-free inverse opal, a common method is to mix precursors of the wanted material of the inverse opal, directly in the nanoparticle suspension, as described in [82]. Because the entire structure has to be filled, the required amount of materials is much greater than in the previous part. As previously seen, the polystyrene nanoparticles with carboxyl groups on the surface, quickly react with the introduced tin precursors. Because of the greater amount of introduced precursors, it is expected that all the nanoparticles will be covered by precursors, which can disturb the good self-assembly of the structure. For this reason, the particles employed in this section are standard particles with SO_4^{2-} groups on the surface, which are not reactive.

The amount of required precursor can be estimated using the parameters used for the crack free inverse opal in silicon dioxide in [82]. By using the same molar amount of tin, a mass of 15.6mg of tin tetrachloride pentahydrate is found.

When tin tetrachloride is dissolved in water, a significant amount of hydrochloric acid is created, with makes the final solution highly acidic. The zeta potential of the used nanoparticles is negative, with a value of approximately -50mV. If these particles are in presence of an acidic solution, the zeta potential decreases (in absolute value), and can even reach 0mV in case of a highly acidic solution. This is because the highly mobile hydrogen cation, is attracted by the negative surface of the nanoparticle, and is then screening the negative value of the nanoparticles' zeta potential. With the addition of many ions, the charges composing the double layer totally cancel the ones of the nanoparticles surfaces, leading to a null zeta potential. Further addition of ions does not makes the zeta potential positive, as no charges are attracted by the particle.

It is commonly considered that a nanoparticle suspension with a zeta potential value between -30mV and +30mV is unstable, due to the weak repulsion between the nanoparticles, which leads to a quick aggregation, as explained by the

DLVO theory 1.3.2. Due to the large amount of precursor introduced to make the inverse opal, the solution becomes very acidic, leading to the aggregation of the nanoparticles, in some minutes. When this happens, no deposition occurs on the substrate, with the exception of randomly organised aggregates.

A solution to reduce the acidity due to the hydrochloric acid made from the precursor is to introduce a sufficient amount of base, such as ammonia or sodium hydroxide, to reach a pH value where the nanoparticle suspension is stable. However, as soon as any base solution is introduced into the 0.2M solution of tin tetrachloride, the solution becomes turby, indicating the reaction of the tin precursors with themselves, leading to the formation of nanoparticles. The dissolved tin precursor is only stable in highly acidic solution, otherwise it can become quickly hydrolysed (addition of an OH group), which makes it very reactive with other hydrolysed molecules or surfaces of the nanospheres.

The addition of surfactant, such as sodium dodecyl sulfate (SDS), can help to prevent the immediate aggregation of the nanoparticles, but a large amount of it is needed to have a noticeable effect. For the added amount of precursor, it is necessary to add at least 1ml of a 2% concentrated SDS solution, to avoid immediate aggregation. The aggregation eventually occur after several hours, but film can nevertheless be formed on the sample. However, this film is of poor quality (figure 5.5), due to both the aggregation between particles, and the amount of SDS introduced, which prevents a correct self-assembly.

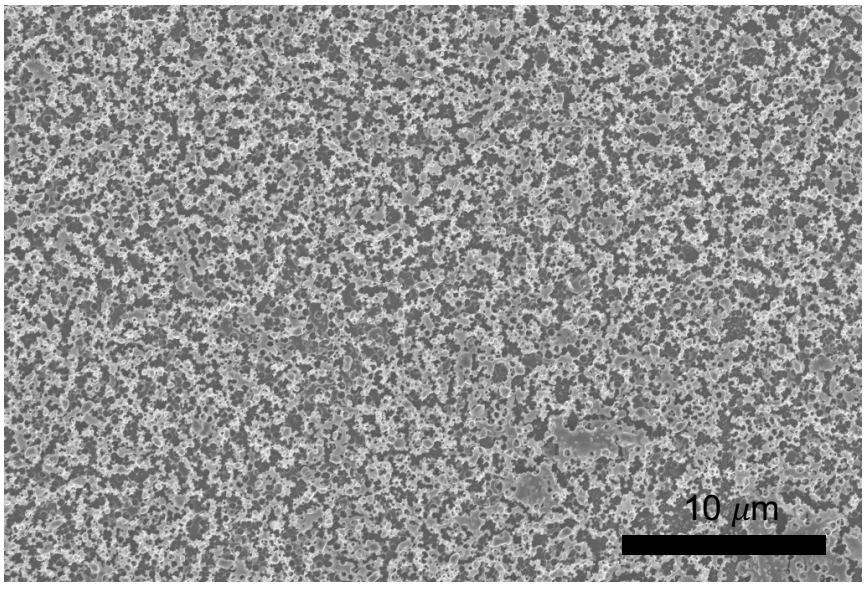


Figure 5.5: Inverse opal made with 5ml of 0.1% concentrated 200nm PS nanoparticles, with 15.6mg of tin tetrachloride pentahydrate. 1ml of a 2% solution of sodium dodecyl sulfate is added to the solution to prevent the aggregation of the nanoparticles.

5.3.2 Particles coating with positively charged polymer

The stability of the nanoparticle suspension is an important concern, in order to make a crack-free opal via a one-pot method. As previously seen, the acidity introduced by the tin precursor, reduces the zeta potential, which leads to a quick aggregation, and at best, a very poor film quality. The acidity shifts the zeta potential to higher values, due to the accumulation of positive ions around the negative particles. However, if positively charged nanoparticles were used, the acidity would not lead to any aggregation, as the positive ions would be repelled by the particles instead of being attracted by it.

A possible way to generate positively charged nanoparticles, is to coat the negatively charged particles which are normally used, with a positively charged polymer. A common polymer used for such coatings in poly-l-lysine, whose chemical structure is depicted figure 5.6. This polymer posses many branches terminated with amino groups, and is often provided already dissolved in water, with an equimolar amount of bromic acid, relative to the molar amount of branches on the polymer. The acid reacts with the basic amino group, giving a positive ammonium group at the end of most of the branches, and making the whole polymer positively charged.

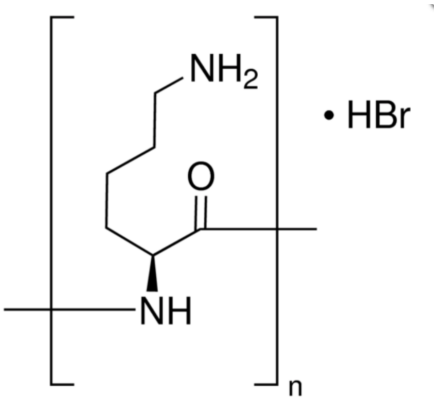


Figure 5.6: Chemical structure of a l-lysine monomer, protonated with bromic acid, in a 1:1 ratio.

Due to electrostatic forces, the positively charged polymer is attracted by the negatively charged nanoparticles, which leads to a coating of the nanoparticles by the polymer. Because of the large density of charges on the polymer, the charged double layer is composed of more positive than negative charge, giving the zeta potential a positive value. This is different from positive ions surrounding the nanoparticles, which can only bring the zeta potential to 0mV, as further positive ions are not attracted.

The solution of poly-l-lysine is concentrated at 0.1 vol% in water. The required amount of polymer necessary to coat all the nanoparticles is proportional to their total surface. As a rough approximation, it can be considered that both polystyrene and poly-l-lysine have the same density, and that the coating around the nanoparticles is uniform, with a thickness d. Under these conditions, the relative mass of the polystyrene nanoparticles compared to the polymer coating, is equal to the ratio between the volume of a nanoparticle, $\frac{4}{3}\pi R^3$, and the volume of the

coating, which can be approximated by the product of the sphere surface, $4\pi R^2$, and the coating thickness d. This ratio is equal to $\frac{3d}{R}$, and for a radius of 100nm, and an approximated coated thickness of 1nm, this ratio is equal to 0.03, meaning that the mass of poly-l-lysine has to be 3% of the polystyrene, to have a full coating. In other words, for the typical mass concentration of polystyrene suspension of 0.1%, a mass concentration of at least 0.003% of poly-l-lysine is needed.

To ensure a good coating of the nanoparticles, and because of the approximations used in the previous calculation, a larger amount of poly-l-lysine in introduced into the solution. It is chosen to use a mass concentration of 0.02% of poly-l-lysine, for a 0.1% concentrated suspension of 200nm polystyrene nanoparticle. This concentration is approximately 10 times greater than the calculated one, ensuring a complete coating. To obtain the desired concentrations, the solution consists of 1 ml of 0.1% concentrated poly-l-lysine, 4 ml of DI water, and 100 µl of 5% concentrated 200-nm polystyrene nanoparticles solution.

The way of mixing the different compounds follows a particular protocol. Indeed, if the concentrated negative particle solution is added to the solution of positively charged polymer, positively charged nanoparticles are formed, and they will quickly become attracted by the yet uncoated negatively charged nanoparticles. When this happens, aggregates can appear in the solution, and they are extremely difficult to break down due to the strong attraction between the particles. For this reason, the poly-l-lysine is slowly added to a diluted solution of polystyrene nanoparticles, and it progressively coats the nanoparticles. This coating is expected to be done in a homogeneous way, due to the fact that both species are diluted. However, because the nanoparticles pass from a negative zeta potential to a positive one, they have a null zeta potential for some time. To avoid any aggregation during this phase, the addition of poly-l-lysine in the polystyrene suspension, is done under sonication, which can break up the potential aggregates formed between weakly repelled nanoparticles. The solution is kept under sonication for one hour after the complete addition of the polymer.

Because the polymer is introduced in excess, the suspension is then centrifuged at 4000rpm, at 5°C, for one hour. After this, all the nanoparticles are sedimented on the bottom of the centrifugation tube, and the super natant is totally clear. The super natant, consisting of DI water and poly-l-lysine, is removed and replaced by DI water. The centrifugation tube is then sonicated for one hour, to allow a good dispersion of the sedimented nanoparticles. This whole process is repeated twice, to remove as much as polymer as possible.

The coated nanoparticles are well mono-dispersed, with an average value of $198.8nm \pm 25nm$, and have a positive zeta potential of $45.8mV \pm 5mV$, making them stable (figure 5.7). The good mono-dispersity indicates the absence of aggregates during the coating process. The suspension is stable for weeks at room temperature, and no sedimentation or aggregates have been seen even after a long time. For the fabrication of the inverse opal, a 5ml solution of 0.1% concentrated coated 200-nm nanoparticles is used, in which 15.6mg of tin tetrachloride and 0.165 mg of ammonium fluoride are added. A piranha treated FTO sample is vertically introduced into the solution, which is then let to evaporate at 60 °C and with 20%

RH, for 2 days. The samples are then calcined at 450 °C, for 4 hours, with a ramp rate of 1°C /min.

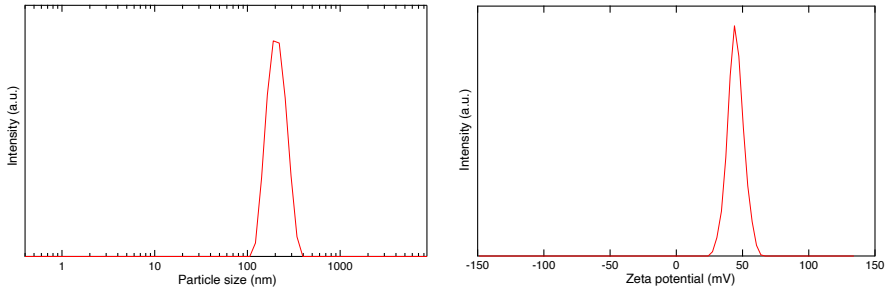


Figure 5.7: Size (*left*) and zeta-potential (*right*) of 200-nm polystyrene nanoparticles coated with poly-l-lysine.

The resulting samples present a homogeneous coating on the surface, have a white colour, due to a supposed strong scattering, and lack transparency. An analysis with SEM shows that many cracks are present at the surface of the sample, and little long range order can be seen (figure 5.8, *left*). In some isolated regions, short range order on the scale of one or 2 micrometers can be seen (figure 5.8, *right*). Even though these results are much better than those using uncoated nanoparticles, they cannot be used as an inverse opal due to the lack of order, leading to a total absence of optical effects.

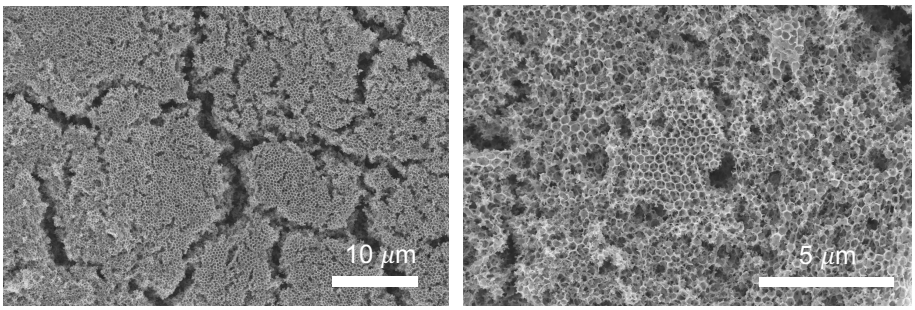


Figure 5.8: *Left :* One-step deposition of a 5ml suspension of 0.1% concentrated PLL-coated PS nanoparticles (200nm), blended with 15.6mg of tin tetrachloride and 0.165 mg of ammonium fluoride. *Right :* Isolated ordered structure.

The lack of order suggests an aggregation of the nanoparticles, even though they are positive in an acidic environment. To ensure this, 10 µl of 37% HCL is added to a 5 ml solution of 0.1% concentrated coated nanoparticles, and the suspension is let to rest at room temperature for several days. After two days, the bottom of the suspension starts to show a slightly more intense white colour, but the rest of it is still white, and no clear change is visible by eye. The increase of intensity in the white colour, is due to an increase of scattering, which itself is due to an increase in the density of polystyrene particles at the bottom of the vial, due to the onset of sedimentation. The difference in colour between the top and bottom part of the suspension is not obvious at first sight. By letting the solution rest for longer, the contrast becomes greater, but no complete sedimentation is observed, as the super natant remains cloudy.

It is hypothesised that the positive hydrogen ions added by the addition of acid, interfere with the coating of the nanoparticles, which results in a decrease of zeta potential, causing a decrease in the stability of the suspension. Even though the positive ions are repelled by the positively charged nanoparticles, some might pass the potential barrier due to their high mobility and small size, and reach the negative surface of the nanoparticle. When they do, they stay attracted by the surface of the particle, and thus might also repel some of the weakly bound poly-l-lysine polymer. In this way, an equilibrium between the ions and the coated polymer can be achieved, and some of the positive polymer are removed from the surface. Because of the low density of positive charges brought by the hydrogen ions compared to the polymers, the resulting total charge on the nanoparticle is decreased, which also reduces the zeta potential. If the zeta potential is significantly reduced, the nanoparticle suspension is no longer stable, and aggregation starts to occur.

The same effect is expected to appear for the solutions where the tin precursor is added, and should be even more important due to the temperature. With this effect, a particle coated with a positive polymer is still not stable because of the acid created by the tin precursor, and another solution has to be found.

5.3.3 Aminated Polystyrene nanoparticles

Instead of applying a coating which might be remove by external factors, the ideal solution is to use nanoparticles which are directly positive, due to their surface groups. Most of the commercially available nanoparticles have a negatively charged surface, but some particles can have amino group ($-NH_2$) on their surface, and these groups can take a proton due to the basic nature of amines, making them positively charged ($-NH_3^+$).

Such nanoparticles have to be sourced with care, since, even if the product number is the same, the vendor might not provide the same product. Particles with amino groups bought from Bangs Laboratories are made from nanoparticles with carboxyl groups, which are then chemically transformed. The surface of the nanoparticles under the name "amino", actually comprises a mixture of carboxyl and amino groups. Because of this, the zeta potential is negative, at around -30mV, which is less than for the standard nanoparticles, due to the removal of some of the negative groups.

On the other hand, amino functionnalised nanoparticles from the company Magsphere, present a positive zeta potential of 48.4mV (figure 5.9). These particles are also stable for days at room temperature, even when hydrochloric acid is introduced. The zeta potential of the particles is relatively stable with the addition of 10 µl of hydrochloric acid in a 5ml solution of 0.1% concentrated PS-NH2 nanoparticles, and has a value of 46.2mV (figure 5.9).

The nanoparticles used for this section are thus 200nm nanoparticles, with amino groups on the surface, from Magsphere.

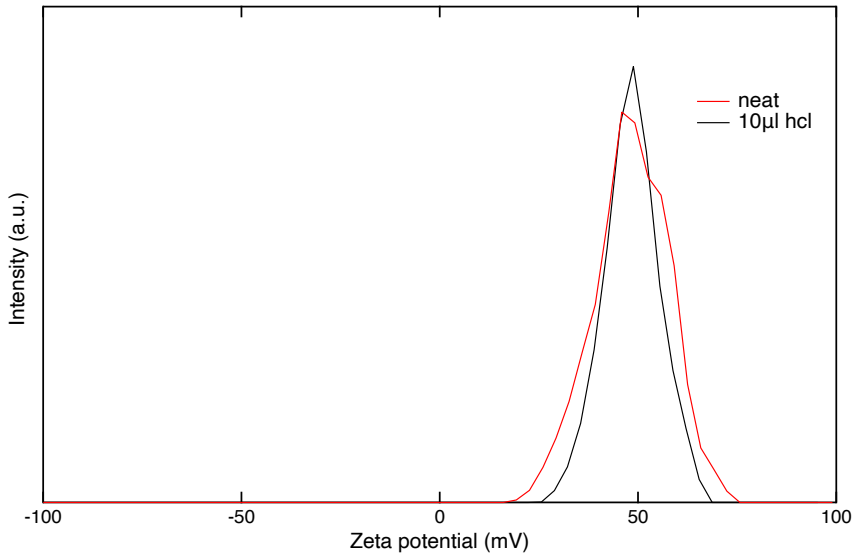


Figure 5.9: Zeta potential of $-NH_2$ terminated nanoparticles in pure DI water (red), and in a mixture of 5ml DI water with 10 µl concentrated hydrochloric acid (black).

The samples are made in the same way as normally, by placing a piranha-treated FTO sample vertically in a vial, filled with a suspension of 200-nm particles in DI water, concentrated at 0.1%, with 15.6 mg of tin tetrachloride and 0.165 mg of ammonium fluoride. The suspension is then let to evaporate at $60°C$ and 20 % RH for 2 days. The FTO sample is then calcined at 450 $°C$ for 4 hours, with a ramp rate of $1°/min$.

After calcination, the sample appears to be homogeneously coated, presents visible scattering, but is still transparent. As seen on SEM, the surface of the sample is very homogeneous, and only has a few cracks, which are not large, explaining the small amount of scattering visible (figure 5.10 *a)*). However, no order is present in the structure, even at small scale, as none of the pores of the inverse opal seem to have the same size (figure 5.10 *b)*).

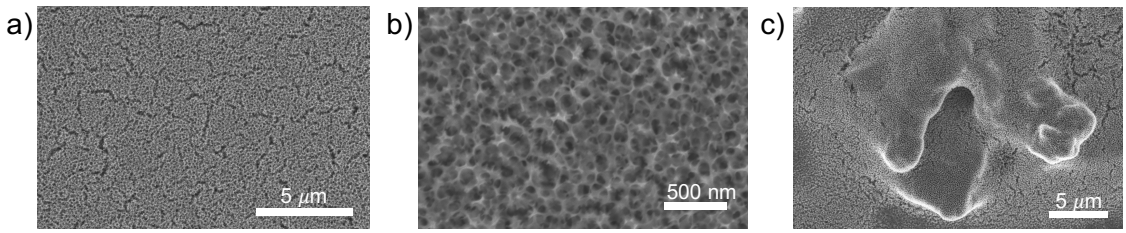


Figure 5.10: Low (a) and high (b) magnification of a FTO structure formed in a one-step procedure with amine-terminated nanoparticles. Three-dimensional defect on top of the structure (c).

This is explained by analysing the polystyrene nanoparticles under an electron microscope, where it is observed that they have a wide range of sizes, for particles which are nominally mono-dispersed (figure 5.11). The poor mono-dispersity of these nanoparticles is explained by the company as being a result of the synthesis

used to produce positively charged nanoparticles, which is less controlled than the one used to produce negative nanoparticles.

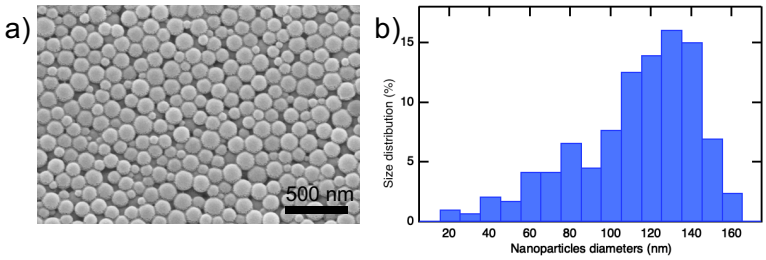


Figure 5.11: Opal formed by evaporation induced self assembly, with amine-terminated nanoparticles (a) and the measured diameters distribution (b).

Some parts of the sample are not flat and show a different topology, as seen figure 5.10 *c)*. Even if the global shape of these structures is irregular, they are still composed of connected pores, indicating that they are not aggregates of precursors, neither aggregates of nanoparticles, due to the similar shape of their inside compared to the rest of the structure. These shapes are also seen on the samples prior to calcination. It is believed that these exotic shapes are due to the self assembly of the particles being disturbed by the reaction of the tin precursors. The tin tetrachloride is stable in the solution, as this one is highly acidic, and no aggregates of only precursors are seen. However, in the meniscus, where the self-assembly takes place, the concentration of tin precursor is much greater due to water evaporation. Because of this, the precursors react, which can lead the self assembly in particular directions.

A possibility to increase the stability of the precursor is the addition of ethanolamine, as done in the previous part. However, because of the lack of uniformity of the $PS-NH_2$ nanoparticles, which cannot produce a regular inverse opal, this method was abandoned.

Different methods to produce crack free inverse opal in tin oxide have been tested, but unfortunately none of them produced a satisfying result. The acidity created by the tin tetrachloride dissolution makes the negatively charged nanoparticles aggregate, and the use of a positive coating on these same particles does not completely solve the problem, due to the weak bounding of the coating. On the other hand, naturally positive nanoparticles, obtained with amino groups on their surfaces, show poor mono-dispersity, and the high reactivity of the precursor creates irregular topologies on the film.

5.4 FTO crystalline nanoparticles

Due to the high instability of the precursors, and its release of acidic products, another possibility for the creation of crack-free inverse opal made of tin oxide, is to directly add crystalline materials, instead of precursors, during the formation of the opal. This technique is also known with the name “brick and mortar”, due to its

similarity with this classical building technique. The added crystals have to be of a small size, to prevent disturbing the self assembly of the polystyrene nanoparticles, and they have to be stable for a long time in aqueous solution.

5.4.1 Fabrication and characterisation

The procedure to make FTO nano-crystals is inspired by a work from Wu *et al.* [212]. There, a hydrothermal method is used to produce FTO nano-crystals of approximately 10nm, that display good electrical conductivity.

For this method, 6.67 g of $SnCl_4.5H_2O$ are dissolved at room temperature in 31 ml of DI water, giving a clear solution. A 3M $NaOH$ solution, made of 24 g of $NaOH$ pellets dissolved in 200 ml DI water, in then added drop-wise to the tin-chloride-based solution, until it reaches a pH of 8. A pH meter, permanently inserted into the solution, provides an accurate reading. The addition is done under constant stirring, and white aggregates appear with each drop of the 3M basic solution, due to the hydrolysis of the tin precursor, followed by its reaction with the other precursors. The solution becomes totally white and very viscous at around a pH of 5, and it is necessary to clean the sensor of the pH meter with DI water when too much of the viscous solution is stuck on it, to ensure a proper reading. An approximate volume of 28 ml of 3M $NaOH$ is required to reach a pH of 8.

The solution is now a mixture of different species, such as $Sn(OH)_4$ (upon complete hydrolysis), Na^+ and Cl^-. In order to eliminate the $NaCl$, the solution is filtered by vacuum filtration. The aggregated tin precursor, giving solution its viscosity, does not pass through the filter, in contrast to the sodium and chloride ions which remains dissolved in water. The filtration results in a clear and transparent liquid passing through the filter, while a white and dense powder stays on top. Large amounts of DI water are added during the filtration, to completely "wash" the salt from the $Sn(OH)_4$ aggregate.

The white residue, which is expected to be a pure aggregate of $Sn(OH)_4$, is then dissolved in 30ml of DI water, and under sonication for an hour, is broken up and dispersed. To this suspension, 1.41g of ammonium fluoride (NH_4F) is added, which results in a 2:1 ratio between tin and fluorine atoms. This ratio is expected to give the lowest sheet resistance for the synthesised nano-crystals [212]. After the sonication and the dissolution of NH_4F, the solution is not viscous but still white, indicating that tin precursors aggregates are still present, but much smaller than previously.

This solution is then put inside an autoclave "bomb" of 40 ml in volume, which is then tightly closed. The autoclave is placed inside an oven, and is heated at 180°C for 24 hours, with a ramp rate of 10°C/min. At the end of the heating time, the autoclave is cooled down naturally to room temperature.

In addition to the nanocrystals, many other materials are in the solution, such as unreacted precursors, NH_4^+ ions from the fluorine precursor. To remove these impurities, the solution inside the autoclave in centrifuged at 10000rpm, for

one hour, at 5°C. Each centrifugation tube is filled with 1ml of nano-crystals solution and 10ml of DI water. After centrifugation, the supernatant is removed, and replaced by DI water. The centrifugation tube is them sonicated for one hour, to allow a good dispersion of the nano-crystals. The centrifugation process is repeated three times.

The final solutions are made by mixing the contents of 4 centrifugation tubes, with a total volume of 44ml, with 156ml of DI water, resulting in a 200ml solution, with the 4ml of the initial solution dissolved in it, giving a dilution of 25 times. In spite of being diluted 25 times and passed under sonicator several times, these solutions are still cloudy, indicating the presence of aggregates.

In order to analyse the synthesised materials, the solution is left to dry in a petri dish, at room temperature, giving a fine white powder. This powder is then characterised for its mass loss and phase change with temperature, with TGA and DSC (figure 5.12 *a)*). The low mass loss observed on the sample purified by centrifugation, up to a maximum of 14% loss at 800 °C, indicates that a large fraction of the white powder is already in a crystalline state. In addition, no clear peak is observed on the DSC, indicating the absence of a phase change. In contrast, the same measurement is done on a sample where no centrifugation has been done, and a more important mass loss is observed, as well as a peak in the DSC graph at approximately 250 °C (figure 5.12 *b)*). This is probably due to unreacted precursors, which are still in solution after the annealing inside the autoclave, and which react together during the DSC measurement. From this observation, it can be speculated that the mass loss from the centrifuged sample could also come from unreacted precursors which were not removed by the centrifugation.

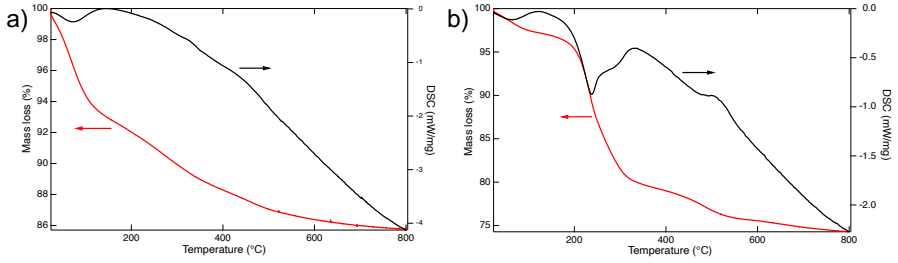


Figure 5.12: TGA/DSC of FTO nano-crystals made by hydrothermal method, centrifuged at 10000 rpm for one hour, at 5°C (a). For comparison, the nano-crystals from the same batch are measured without the centrifugation step (b). For both sample, a small amount of the suspension is left to dry naturally to obtain a FTO nano-crystal powder, which is measured by TGA/DSC.

To assess the crystallinity of the synthesised materials, the powder is deposited on carbon tape, which is itself stuck on glass. To remove the non-attached power from the carbon tape, the sample is shaked vigorously several times. The sample is then characterised by XRD, with angle varied from 5° to 55°. As neither the glass nor the carbon tape are crystalline, every peaks appearing from this measurement is due to the crystallinity of FTO nano-crystals. On the measured spectra (figure 5.13), three peaks are immediately identified and are fitted with a Gaussian function. The positions for these peaks are 26.72°, 33.58° and 52.04°. A fourth peak

can be identified at around 37.6°, on the edge of the peak at 33.58°, and because of its small size, this peak is not fitted, and its location is only approximated.

The peaks can be identified as being planes of tin(IV) oxide, by comparison with a crystallography reference database. From the low to the high angle, the peaks can be identified as the planes (110), (101), (200) and (211), as indicated in figure 5.13. The absence of others peaks, show that the synthesised material is entirely composed of tin(IV) oxide crystals. The very broad peaks are a clear indication of very small particle size.

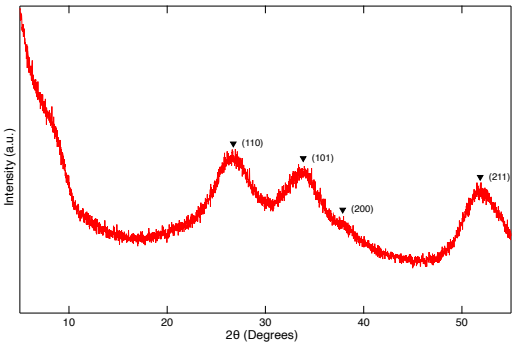


Figure 5.13: XRD of dried FTO nano-crystals. The FTO powder is held on a sample holder with double-sided sticky carbon tape.

In order to individually characterise the nanoparticles, a drop of the solution is deposited on a TEM grid coated with holey carbon. The drop is left to dry for an hour, and is then passed under the microscope, with an acceleration voltage of 200kV, without additional treatment. The particles appear to have a uniform spherical shape, as well as an average size of 6.4 ± 0.76 nm (figure 5.14 *a)*). All the observed nanoparticles appear to be crystalline, and even monocrystalline. A magnified view with HRTEM allows visualisation of the atomic plans, and especially the (110) and (101) plan are visible, as they are the ones with the most important d-spacing, of 0.35 nm and 0.28 nm respectively (figure 5.14 *b)*). To have a better characterisation of the d-spacing of the different atomic planes, SAED is done by selecting a large area of the sample. The resulting diffraction pattern is analysed by an FIJI plugin (*radial profile*), which plots the intensity of the pattern as a function of the distance to its centre (figures 5.14 *c)* and *d)* respectively). The rings can each be attributed to a diffraction plan, depending of the d-spacing measured. These planes and the measured d-spacing all correspond well to ones that characterise SnO_2, as already evidence by the XRD study.

Coming back to the original diluted suspension (with a dilution factor of 25), an analysis with DLS indicates that these suspensions have nanoparticles with an average diameter of either 191 or 73 nm, depending of how the data are normalised. In brief, 191 nm is the value obtained without normalisation, while 73 nm is obtained with a normalisation taking into account the fact that larger particles scatter more light than smaller ones. Both these numbers are much higher than the average particles size measured by TEM, indicating that aggregates between the particles occur in the solution. To break up and prevent the aggregates, the addition of tetramethylammonium hydroxide ($N(CH_3)_4^+OH^-$, or TMAOH) as a

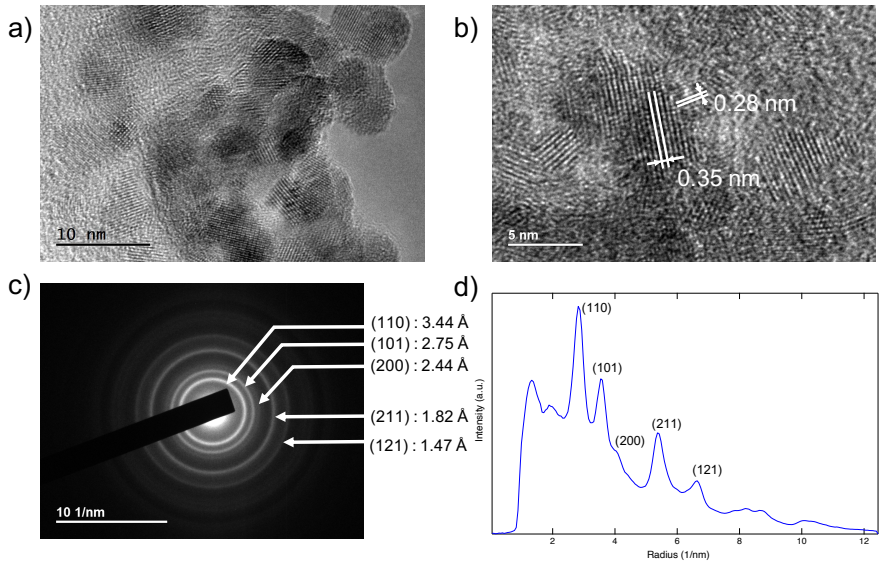


Figure 5.14: TEM (*a*) and HRTEM (*b*) of FTO nano-crystals, deposited on a holey carbon grid. Two different atomic planes are indicated on the HRTEM image. SAED on a large area (*c*), forming concentric rings due to the many different orientations of the measured crystals. (*d*) Radial intensity of the SAED.

surfactant/stabiliser, is a possible chemical way, as this compound is often used to prevent the aggregation of nanoparticles during synthesis. The used chemical is provided by Sigma Aldrich, and is concentrated at 25 wt%.

Different amounts of TMAOH are dropped in a 200 ml of FTO nano-crystals suspension under stirring, diluted 25 times from a fresh batch made the day before. One to two ml of the solution is then taken for a DLS and zeta potential analysis. The injected volumes of TMAOH add up to 600 µl, and a last solution have 1 ml of TMAOH, and is let to rest for 5 days before the measurement. The more TMAOH that is added to the solution, the more the particles decrease in size, as seen by figure 5.15 *a)*. This decrease of size appears to bottom out at 48nm for the measurement in intensity, with the curves for the solutions with 400 µl, 500 µl and 600 µl of TMAOH being extremely similar. The curves giving the size of the nanoparticles in number, also appear to saturate at 20nm (figure 5.15 *b)*), with the exception of the size distribution for the 600 µl curve, which is very different from the others, with an average size at 7 nm. It is believed that this is due to the small bump at around 10 nm, in the corresponding curve in intensity, whose appearance might be due to the TMAOH interfering with the measurement. The last curve, corresponding to 1 ml of TMAOH, let to rest 5 days prior to the measurement, indicates a size of particle of 20 nm, if measured in intensity, and 10 nm by number. The size obtained by the measurement in normalised DLS is extremely close to the ones obtained by TEM, giving a good confidence that aggregation is now suppressed.

The zeta potential measured from these suspensions passes from a sharp peak centred at -37 mV when no TMAOH is introduced, to an irregular smaller gaussian, centred approximately at the same location, for a volume of 300 µl and greater. This loss of accuracy can comes from two factors : firstly, due to the smaller size of the particles, measured by DLS, the measured Doppler effect used for zeta

potential can have a lower intensity, making it more difficult to measure. Secondly, the cuvettes used for zeta potential measurement, only support solution with pH between 3 and 10. Because of the introduction of a strong base in the suspension, it is possible that this limit is reached, and the electrodes on the zeta-potential cuvettes get damaged, reducing the accuracy of the technique. Because of this, the evolution of zeta potential with the reduction in the size of nanoparticles cannot be investigated.

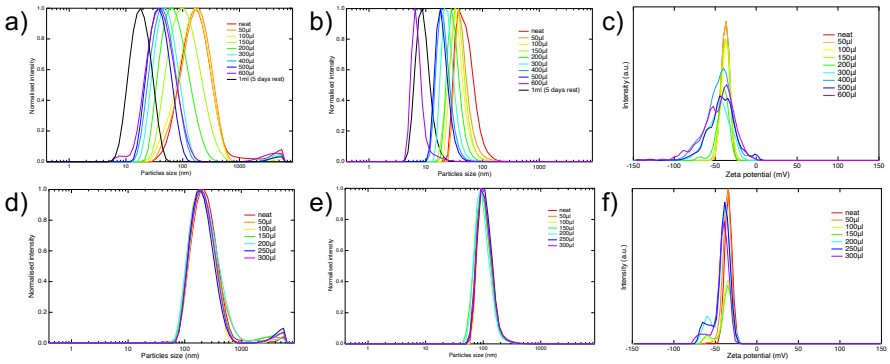


Figure 5.15: DLS intensity (*a*), DLS number (*b*) and zeta potential (*c*)results for a freshly made FTO nano-crystals suspension, stabilised with different amounts of TMAOH. (*a,b,c*) Same measurements, for a one week old FTO nano-crystals suspension, stabilised with the same amount of TMAOH.

An important point is that the stabilisation of the nanoparticles with TMAOH has to be done immediately after their synthesis, and their cleaning by centrifugation. If too long a time elapses between these, the nanoparticles will aggregates irreversibly, and the suspension become unusable. There is no effect from the addition of TMAOH on the size of the nanoparticles, for a one-week-old solution (figures 5.15 *d)* and *e)*). Both the measurement in intensity and in size are constant, with a peak centred at 240nm and 106nm respectively. These numbers are higher that the ones measured for a fresh solution without TMAOH, which indicates that bigger aggregates are formed over time. A second peak appears on the zeta potential graphs, on the left of the initial peak, at approximately -60mV. A possible explanation for these peaks is that because of the addition of TMAOH, more negative mobile charges are present in the solution, which can alter the measurement.

Solutions that become non-stabilised after one week do not appear to be recoverable, even with added TMAOH, after a long wait time and sonication. The reasons for the permanent binding are not fully understood, but are probably due to chemical reactions between the surface groups of the different nano-crystals, which are supposed to be OH groups.

The time required for the aggregates to break up after the introduction of the TMAOH in the suspension is extremely short. Pictures of a 500 µl drop of TMAOH in the 200 ml suspension have been taken, with $t = 0$ the time of the drops's application. The solution passes from cloudy at $t = 0$, to totally transparent at $t = 30$ s (figure 5.16). Because of their small sizes after the introduction of TMAOH, the nanoparticles scatter much less of the light, which makes the solution transparent. This transparency concerns the visible light, but may not be true for

the lower wavelengths, depending on the size of the nanoparticles.

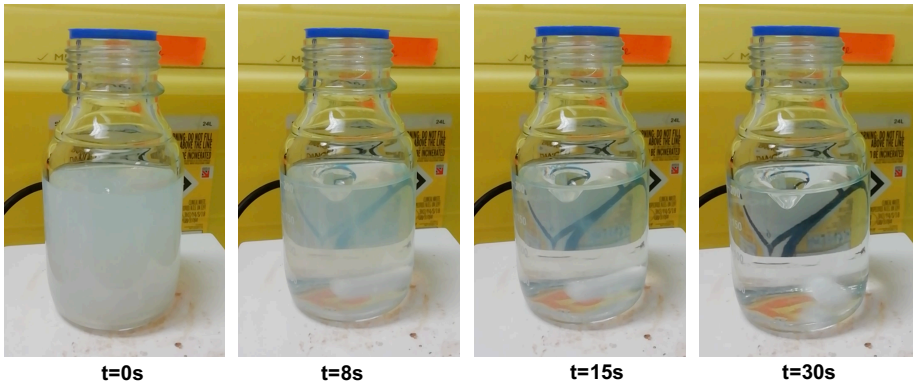


Figure 5.16: Transparency evolution of a 200 ml FTO nano-crystals suspension, after the addition of 500 µl of TMAOH. From left to right : suspension immediately after the addition of the stabiliser, after 8 seconds, 15 seconds and 30 seconds. The stabilised suspension is diluted 50 times from the original suspension, after its purification by centrifugation.

5.4.2 One-step co-infiltration

For this entire section, the parameters used for the inverse opal fabrication are the same, unless explicitly mentioned.

The FTO nano-crystal suspensions are diluted 25 times from the solution obtained after centrifugation. The dilute suspensions are made in 200-ml flasks, and are stabilised with a certain amount of tetramethylammonium hydroxide (TMAOH). The solutions for the evaporation-induced self assembly are made of 4 ml of DI water, 1 ml of the diluted FTO suspension and 100 µl of 5% concentrated 211-nm PS nanoparticles, from Microparticles Gmbh. These solutions are stirred for at least 2 hours, and are then sonicated for 30 minutes to break up any remaining aggregates. A piranha cleaned FTO sample, of approximately $2.5 \times 1\,\mathrm{cm}^2$, is vertically placed in the glass tube.

The solutions are evaporated in a humidity oven set to a temperature of 60 °C, and a relative humidity of 20%, for approximately 48 hours. The infiltrated opals are calcined at 400°C for four hours, with a ramp rate of 0.1°/min, then allowed to cool down naturally.

The SEM analyses are done without coating, as the structures and the substrates are conductive enough to avoid charging.

Stabilised nano-crystals

The addition of TMAOH to the suspension of FTO nano-crystals, eliminates its turbidity - at least to the naked eye. However, as seen in figure 5.15,

different amounts of stabiliser give different values of zeta potential, and thus different stabilities for the suspension, even if the all the solutions appear similar. As seen in chapter 3, the zeta potential value of polystyrene nanoparticles greatly influences the quality of the deposited opal. For that reason, solutions of FTO with different amounts of tetramethylammonium hydroxide are tested and compared.

Five different quantities of TMAOH are used in these experiments : 200 µl, 300 µl, 500 µl, 600 µl and 800 µl in 200-ml of diluted suspension. The samples are made following the recipe previously described, and the results are presented in figure 5.17. A clear improvement in the order of the inverse opal can be observed with the increase in the quantity of stabiliser added. For 200 µl, only a few cracks are present, but the long-range order of the structure is very bad, and only local order can be observed. When the quantity is increased to 300 µl of TMAOH, a better long range order appears, as well as oriented cracks. However, many individuals defects, as well as micro cracks, are present in the structure.

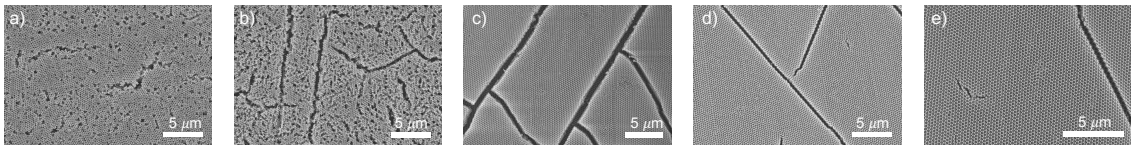


Figure 5.17: Order quality of inverse opals made from FTO suspensions with different amounts of TMAOH. The 200ml suspension are stabilised with *a)* 200 µl, *b)* 300 µl, *c)* 500 µl, *d)* 600 µl and *e)* 800 µl of TMAOH.

For an added volume of 500 µl of TMAOH and higher, the long-range order of the inverse opal is excellent, barely any defects are present and cracks are well oriented. The addition of more stabiliser also decreases the number of cracks, as a better filling of the opal is expected during the self assembly due to the high stability of the nanoparticles. This high-filling prevents an excessive shrinking of the structure during the calcination, hence the reduced number of cracks.

A larger view of a structure made with a well stabilised FTO suspension (600 µl of TMAOH), shows the good homogeneity of the structure as well as a mix between oriented and random cracks (figure 5.18 *a)*). At high magnification, the good connectivity between the top layer and the one just below it can be seen with the presence of three well defined mesopores within each of the majority of the pores (figure 5.18 *b)*). This indicates that the FTO nano-crystals do not prevent a good self-assembly of the polystyrene nanoparticles, with each nanoparticle having a good connection with its neighbours.

The structures made with weakly stabilised ($200\mu l$) and strongly stabilised ($800\mu l$) FTO suspension, have both a homogenous thickness over a large distance, and a good connectivity between the inverse opal and the substrate (figures 5.19 *a)* and *c)*). However, the cross section of the sample made with weakly stabilised suspension reveals internal defects, such as vacancies and disorder. These defects are due to the weak stability of the FTO nanoparticles, which prevents the good self assembly of the PS nanoparticles, causing many individual colloidal crystals to be formed. On the other hand, the strongly stabilised FTO suspension has a perfect internal organisation, with no breaking of the order of the structure.

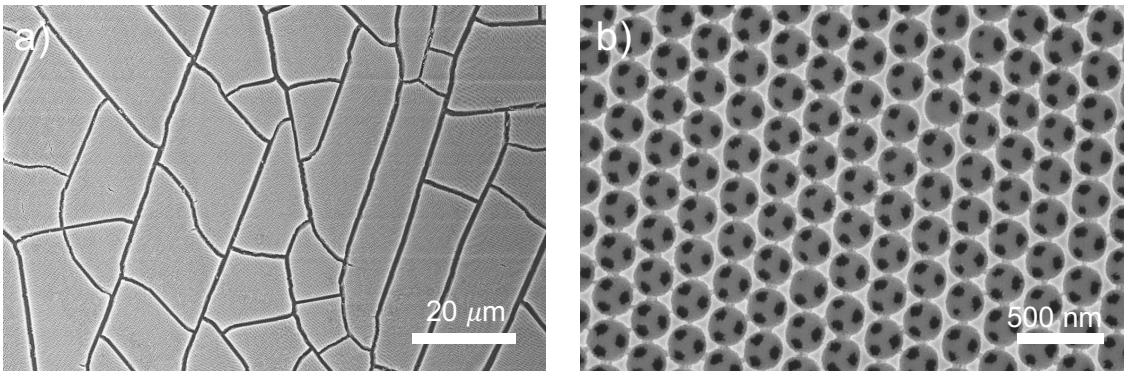


Figure 5.18: Low (*a*) and high (*b*) magnifications of an inverse opal made with a FTO suspension stabilised with 600 µl of TMAOH.

Defect appearance

The addition of TMAOH to stabilise the FTO suspension allows very good ordering of the inverse opal, as well a reduction of the total number of cracks. However, because this material is also deposited inside the opal during the self assembly, it can then re-crystallise and create some defects in the structure.

Very large area views of the inverse opals made with FTO nano-crystals show significant numbers of defects, for all the quantities of TMAOH added (figure 5.20). The inverse opals made with 200 µl and 300 µl of TMAOH, display many black dots on their surface (figure 5.20 *a)* and *b)*). At higher magnification, these dots appear to be some flower-shaped defects of approximately 5 µm, composed of individuals blocks (figure 5.20 *f)* and *g)*).

With higher amounts of TMAOH, the flower-shaped defects progressively disappear, and star defects starts to appear (figure 5.20 *c)*). These defects are much bigger, with dimensions which can go up to $100\mu m$. For the sample with $500\mu l$ of TMAOH, these defects are very regular, and always present 6 branches. At high magnification, it is observed that the branches of the stars defects follow the cracks of the inverse opal (figure 5.20 *h)*), and that the angle between the branches is always equal to 60°, due to the cracks being oriented on the [110] planes of the close-packed crystal.

At even higher volume of TMAOH, the stars defects look regular, and often have only 4 branches (figure 5.20 *d)* and *e)*). It is believed that this loss of regularity is due to the crack reduction previously mentioned, which prevents perfect stars being created. Other defects appear, which are very sharp and crystalline, and are created on top of the inverse opal (figure 5.20 *j)*). The previously mentioned defects are the ones which are the most present on the different samples, but others exist and are shown in appendix B. The mechanisms related to the formation of these defects are not fully understood.

All these defects create light scattering in the structure, and because most of them are above the surface of the inverse opal, they can prevent the creation of a multilayer device, as a short would be created. A simple way to reduce them,

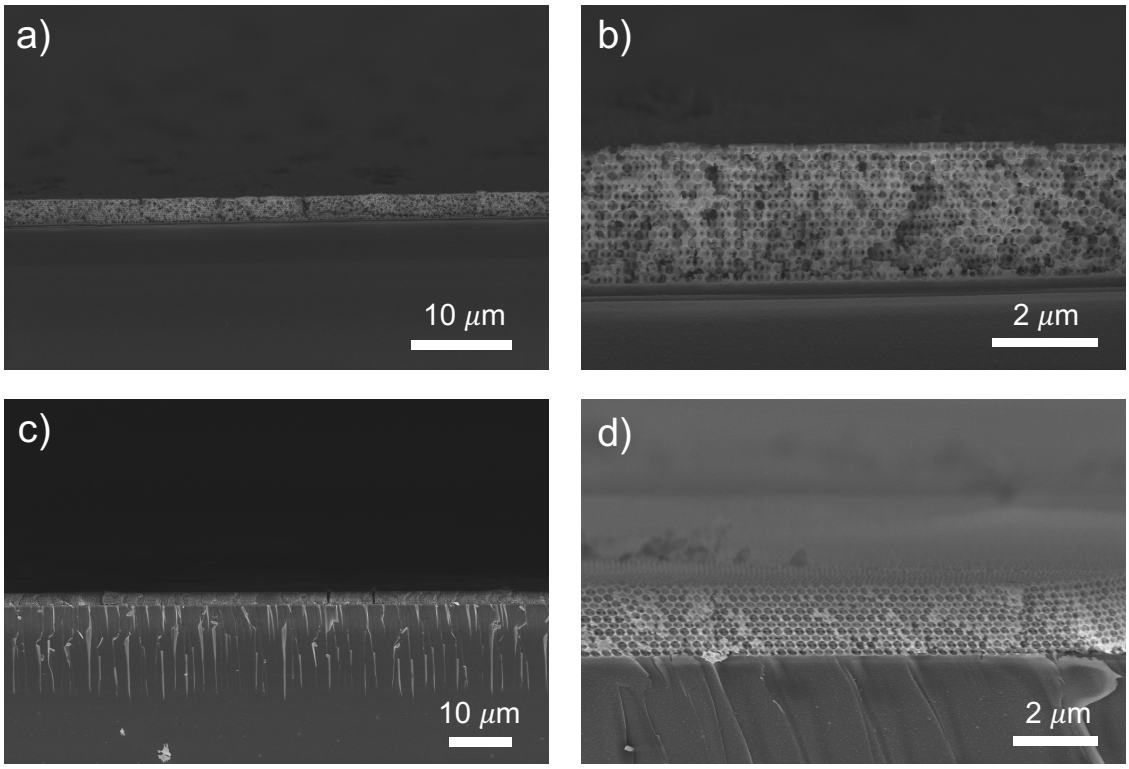


Figure 5.19: Cross sections at low and high magnification of a FTO inverse opal made with a FTO suspension stabilised with 200 µl of TMAOH (*a and b*), and with 800 µl of TMAOH (*c and d*)

is to reduce the volume of the FTO suspension added for the creation of the opal structure, which is 1ml by default in this chapter. To assess the effects of the volume of added suspension on the inverse opal quality, samples are made with 1.5 ml, 1 ml and 500 µl of FTO suspension stabilised with 1 ml of TMAOH. The same procedure is then applied for the creation of inverse opals.

As it can be expected, a greater added volume of the suspension creates more defects in the structure (figure 5.21). The defects for the sample with 1.5 ml and 1 ml of TMAOH, are mostly located on/beside a crack, but others defects on an area of regular surface are still present. The sample with only 500 µl of TMAOH still presents defects on its surface, despite the reduction of surfactant.

It could be thought that a greater added volume of suspension would completely remove the defects. However, as the amount of FTO nano-crystals is decreased, the filling of the space between the polystyrene nanoparticles is reduced, which impacts on the structure of the inverse opal. By comparing structures made with 1ml or 500μl of TMAOH, it is observed that the cracks are more oriented and the domains have a larger size, in the structure with a high loading of nanoparticles (figures 5.22 *a)* and *c)*). When looked at higher magnification, the structure appears denser and smoother for the highly loaded sample, compared to the sample with only 500μl of added suspension (figures 5.22 *b)* and *d)*).

An interesting feature is that the connections between the pores is larger for the sample with less added nano-crystal, which is attributed to the low-filling of

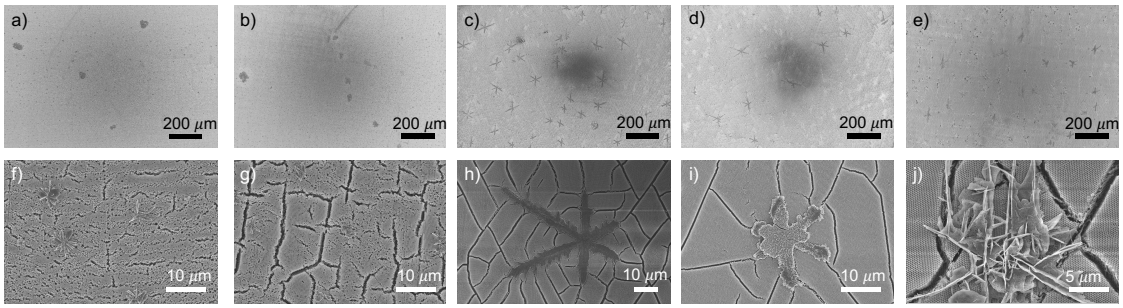


Figure 5.20: Large-area SEM views exhibiting the defects created on the inverse opal (top row), and high magnification on a characteristic defect of the structure. The inverse opals are made with a 200ml FTO suspension stabilised with 200μl (*a and f*), 300μl (*b and g*), 500μl (*c and h*), 600μl (*d and i*) and 800μl (*e and j*) of TMAOH.

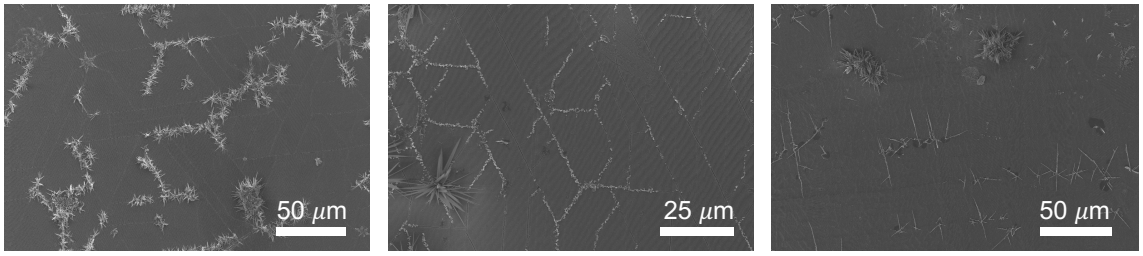


Figure 5.21: Opals made with 1.5ml (*a*), 1ml (*b*) and 500μl (*c*) of a 1ml TMAOH FTO suspension, diluted 50 times from the stock solution. The total volume used for the opal evaporation is maintained at 5ml, with a PS concentration of 0.1%.

this structure. By using this effect, the size of the connection between the pores can be controlled, allowing different properties for the structures.

Precursor infiltration

Even with high loading of FTO suspension and large quantities of stabiliser, cracks still appear on the structure. As the FTO nano-crystals filling the gaps between the PS nanoparticles do not immediately make covalent bonds between themselves, they do not prevent the shrinking of the opal, and thus cracks are created. To create covalent bonds and strengthen the structure, tin precursors are added, which react with themselves and with the FTO nano-crystals. This technique is known as "bricks and mortar", because of the mix of crystalline materials and their precursors.

As seen is previous sections, a known precursor of tin(IV) oxide, that is soluble in water is tin tetrachloride pentahydrate. This precursor creates a very acidic solution when it is dissolved, due to the hydrolysis of the molecule. It is stable if the solution stays acidic, but immediately reacts and forms aggregates when a basic solution is added. Because of this, if this precursor is added to the mix of PS nano-crystals and PS nanoparticles, two things happen : firstly, as the mix solution is basic, the precursor immediately hydrolyses and reacts, creating many aggregates.

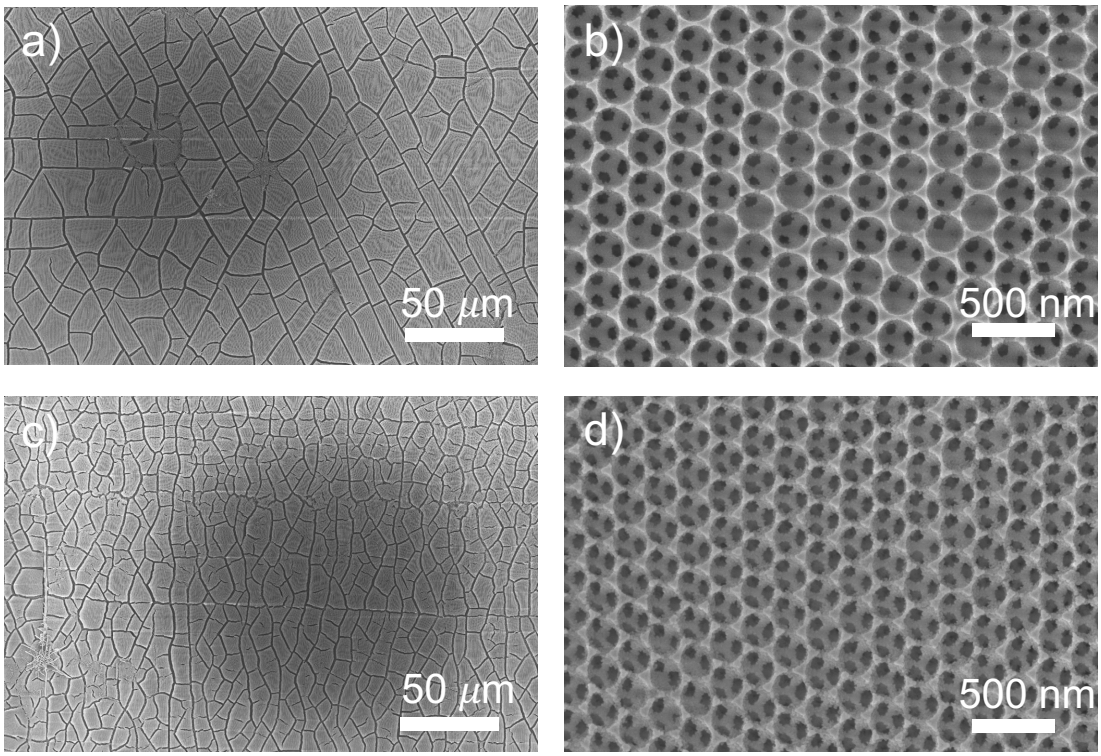


Figure 5.22: FTO inverse opals made with 1ml (a and b) and 500μl (c and d) of a 1ml TMAOH FTO suspension, diluted 50 times from the stock solution. The total volume used for the opal evaporation is maintained at 5ml, with a PS concentration of 0.1%.

Secondly, because of the acidity of the precursor, the zeta potentials of all the nanoparticles are changed, which can make them aggregate. Due to these effects, the precursor cannot be simply added to the FTO suspension, as one compound requires an acidic solution to stay stable, while the others need a basic solution.

In order to solve this problem, a possibility is to stabilise the precursor, to avoid any reaction even at basic pH. In a previous part, describing the work using $SnCl_4$ as a ligand between particles, ethanolamine is used to control the stability of this precursor. Even though ethanolamine is basic, due to its amine group, the solutions were stable, due to the small quantity of added stabiliser. However, when more bases are added to this solution and a neutral pH is reached, the precursors quickly aggregate. Adding more ethanolamine does not solve this problem, as this compound is also basic, and aggregates are created when its concentration is too high.

Another stabiliser is thus used, citric acid , which is known as a stabiliser for controlling tin reactions [213, 214]. This acid, when deprotonated, has a lot of negative charges on it, and is attracted to any positive ions in the solution. If citric acid is added to a solution of tin ions, the acid molecules form a shell around them, due to electrostatic forces (figure 5.23). This shell prevents any contact between the tin ions, and thus any reaction, due to steric hindrance. This process is called chelation, and citric acid is known as a chelating agent.

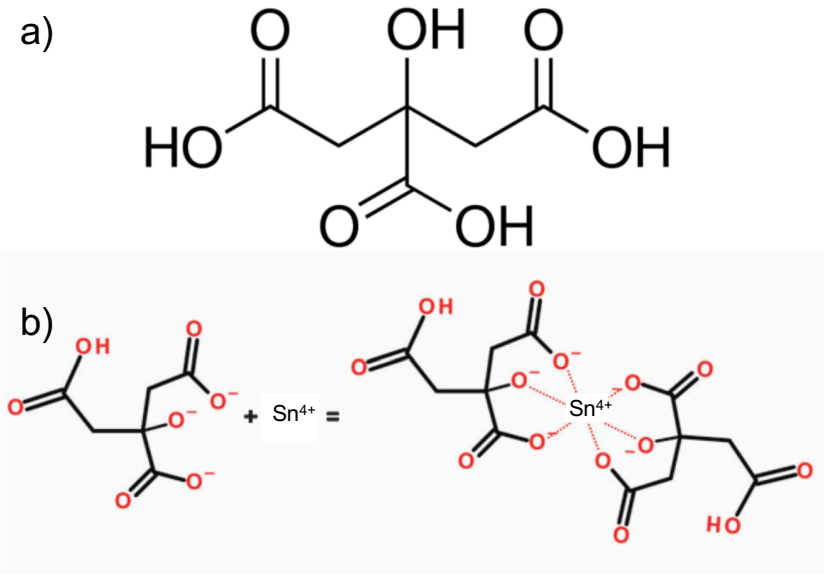


Figure 5.23: Molecule of citric acid (a), and deprotonated citric acid chelating a tin(IV) cation (b). Reproduced and adapted with permission from [15]

The procedure to stabilise the tin solution with citric acid is described hereafter. As citric acid is a solid compound, it is firstly dissolved in DI water, with a concentration of 5 g in 10 ml. 35 mg of $SnCl_4.5H_2O$ is dissolved in 1 ml of DI water, giving a concentration of 0.1M. When the tin tetrachloride is totally dissolved, the solution is completely transparent. The solution of citric acid is then slowly added drop-wise until a chosen concentration is reached. This solution turns slightly cloudy, probably due to the citric acid being in its protonated form, which does not dissolve well and form aggregates. Ammonia is then slowly added, to reach a pH of 7, which is checked with a pH paper. At the first drops of ammonia, the solution immediately turns transparent, as citric acid becomes deprotonated, and thus soluble. It is important to wait for the complete dissolution of $SnCl_4.5H_2O$ in DI water before the addition of citric acid, or else the chelating effect can prevent the total dissolution of the compound.

The final solutions, with a concentration of 0.1M of tin precursor, and a PH of 7 are transparent, which means that the precursors are stable. However, after a long time, the solution can turn cloudy, as the chelating agent does not totally prevent the reaction. A simple way to increase the stability of the solution, is to increase the amount of added chelating agent. In this way each tin ion is surrounded by more citric acid molecules, which prevents it from reacting in a more efficient way.

Two solutions of 0.1M tin oxide concentration are made with the procedure previously described, and are stabilised with 0.25M and 0.5M concentration of citric acid. The amount of ammonia is adjusted for both solutions to have a pH of 7. The solutions are then let to rest at room temperature for 48 hours. The solution stabilised with 0.25M citric acid becomes cloudy after 24 hours, while the one with 0.5M is still totally transparent after two days (figure 5.24). With 5 molecules of citric aid surrounding each tin ion, the second solution is extremely stable, and

because it is at neutral pH, it can be mixed with the FTO nano-crystals suspension, without changing the zeta potential.

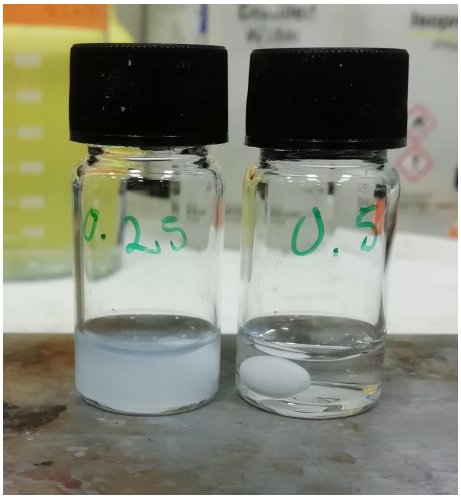


Figure 5.24: 0.1M solution of tin tetrachloride in methanol, stabilised with citric acid concentrated at 0.25M (*left*) and 0.5M (*right*), let to rest for 48 hours.

Adding more citric acid, makes the solution more stable, but it also requires more base to be added, to reach a neutral PH. These two compounds, citric acid and ammonia, are deposited inside the opal during the evaporation, and can create defects, just like tetra-methyl ammonium hydroxide. For this reason, they have to be minimised, and a optimum amount, giving stability and no defects in the final structure, has to be found. For this reason, the following experiments are done with 0.4M of citric acid, which gives a good stability for at least two days, and does not introduce as many "unwanted" molecules as other solutions.

New samples are made with this stabilised precursor, and the global composition of the solution is described hereafter. The initial solution is the same as in the previous part, with 1ml of a 25 diluted FTO suspension, stabilised with 800 µl of TMAOH (for a total volume of 200 ml), mixed with 4ml of DI water, and 100 µl of 5% concentrated 211-nm PS nanoparticles. To this solution is added 10 µl of a 0.1M tin tetrachloride solution, stabilised with 10 µl of 0.4M of citric acid, where 150 µl of ammonia is added to reach pH 7 (for 1ml solution). The others conditions for the evaporation and calcination are similar as the other samples.

The final samples are totally opaque and white, due to a poor organisation at both the long and the short range (figure 5.25). At low magnitude, large number of defects can be seen throughout the sample, and many areas, dark on the picture, are not covered by any material. On a closer scale, it can be seen that no order is present between the pores, and many cracks are present. In addition, areas of aggregated materials, which are supposed to be FTO nano-crystals, because of the small amount of tin precursors, are present.

Even though they are stable in the suspension, the FTO nano-crystals appears to aggregate on the substrate. In the meniscus where the evaporation and self assembly occurs, the condition of stability are different. It is supposed that in this area, the nano-crystals are not stable anymore, due to the difference of strength

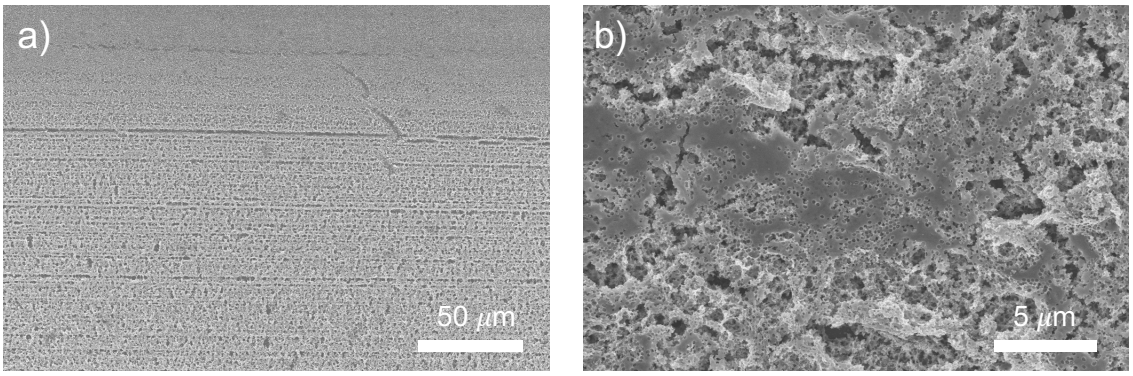


Figure 5.25: Low (*a*) and high magnification (*b*) of a FTO inverse opal made in a one step method, with 211nm PS particles concentrated at 0.1% in 5ml water, with 1ml of FTO suspension stabilised with 800 µl of TMAOH. 10 µl of a solution of 0.1M tetrachloride in methanol and 0.4M citric acid, neutralised at Ph 7 with ammonia, is added to the suspension.

between the hydrochloric acid and the ammonia. Indeed, hydrochloric acid is a strong acid while ammonia is a weak base. Even if the solution is neutral at the macroscale, the effect of HCl is supposed to be more important at the nanoscale, leading to some local areas with more acidity, which can result in the aggregation of the FTO nano-crystals. Another possibility is that the ammonia can evaporate faster than water due to its lower boiling point, resulting in a more acidic solution.

To test this hypothesis, a strong base, sodium hydroxide (NaOH), is used instead of ammonia in the previous solution. A 3M sodium hydroxide solution is made, by dissolving 24g of NaOH pellets in 200ml of DI water. 610 µl of this solution is used instead of the ammonia, to give the tin precursor solution a neutral PH. The rest of the procedure is done the same way.

The samples made with this composition are much better in terms of order, as seen in figures 5.26 *a)* and *b)*. The inverse opal presents randomly organised cracks, and has a good order. Interestingly, no defects due to the TMAOH are visible, but this effect has not been studied. Some small aggregates can still be seen at high magnification. This structure still has cracks, which could be due to an insufficient amount of added precursors. However, when 40 µl of the precursor solution is used (instead of 10 µl previously), many defects appear, at both the macro- and nano-scale (figures 5.26 *c)* and *d)*). These defects can be due to an instability of the FTO nano-crystals, because of all the compounds in the solution. Even though the amount of precursors is greater, the cracks are still present on the structure.

The goal of adding liquid precursor to the FTO nano-crystals solution is to eliminate the cracks of the inverse opal. However, because of the instability of the tin precursor, others materials have to be added, to stabilise both the precursor and the FTO nano-crystals. The best sample made with this method still shows cracks, and its global order is not as good as the samples made without liquid precursor. However, this method still provides a way of adding tin precursors in a stable way, and can possibly be improved in terms of precursors' stability and concentration, to

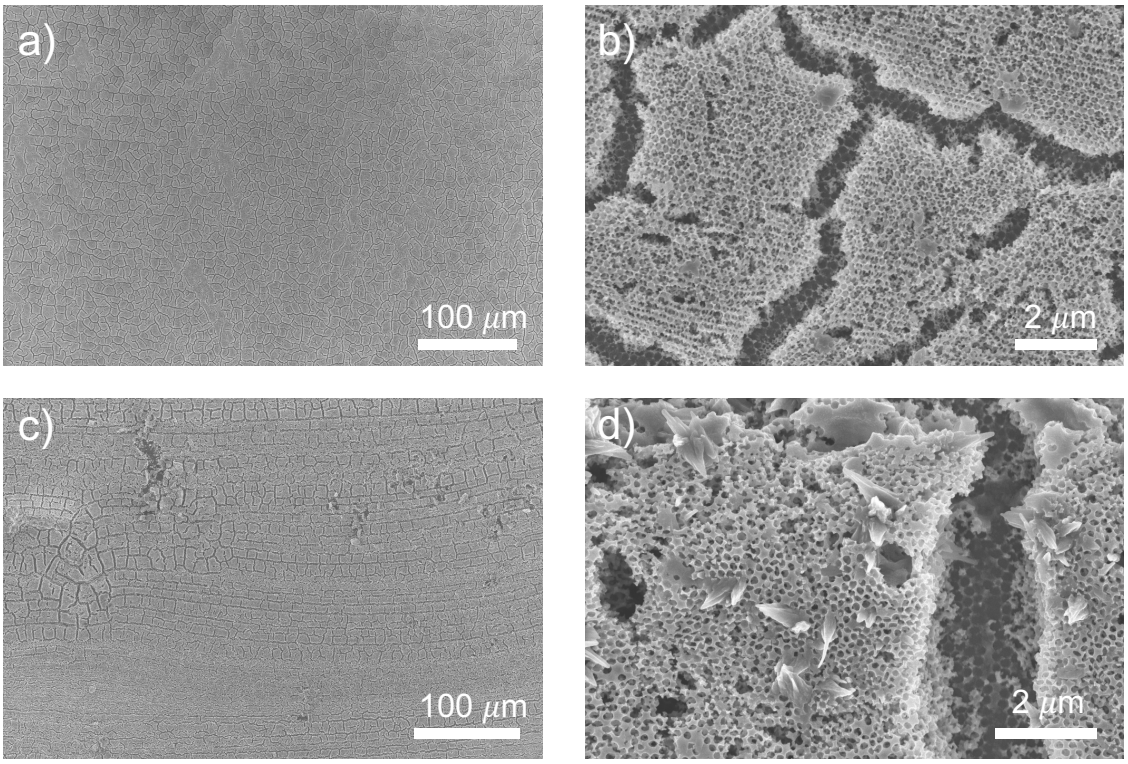


Figure 5.26: Low (left column) and high magnitude (right column) of a FTO inverse opal made in a one-step method, with 211-nm PS particles concentrated at 0.1% in 5 ml of water, with 1 ml of FTO suspension stabilised with 800 µl of TMAOH. 10 µl (*a and b*), and 40 µl (*c and d*) of a solution of 0.1M tetrachloride in methanol and 0.4M citric acid, neutralised at pH 7 with sodium hydroxide, is added to the suspension.

yield a better result.

Nano-crystal optimisation

The large amount of TMAOH introduced to the solution is responsible for the creation of defects within the inverse opal. High amounts are required to stabilise the FTO nano-crystals because of their low zeta potential, of approximately -37 mV. To decrease the added TMAOH, and thus the density of defects, a more stable FTO suspension should be used, as such a suspension would requires less stabiliser. Because of the complex processes occurring during the hydrothermal synthesis, and the lack of personal knowledge on this subject, it was decided not to try to optimise the conditions of the synthesis, to have a higher zeta potential. However, it is observed that by selecting only a part of the suspension obtained after the 24 hours annealing in the autoclave, better results are obtained for the formation of a crack-free inverse opal, without defects.

In detail, the autoclave is positionned vertically after it has cooled down to room temperature. It is supposed that there is a wide range of zeta potential amongst the formed nano-crystals. The nano-crystals with the less negative value

of zeta potential, which are less stable, form large aggregates, and sediments on the bottom of the autoclave, as summarised figure 5.27. The more stable particles, with highly negative zeta potential, either do not aggregate, or aggregate as smaller particles, and stay stable in solution, which makes them much more present at the top of the solution in the autoclave. Only the "liquid" part of the suspension is poured in a beaker, while the bottom of the suspension, more viscous and with a gelatine like texture, is rejected. The selected solution is then centrifuged three times, and is then diluted by a factor 25, in DI water.

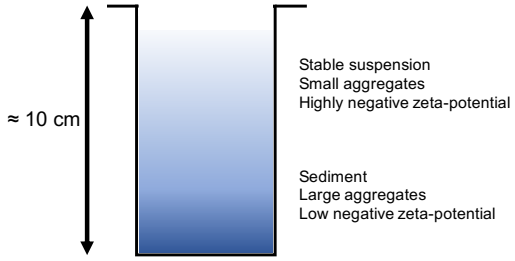


Figure 5.27: Schematic of the separation between the high and low zeta potential nanoparticles, in an autoclave placed vertically.

The resulting solution is still cloudy, due to the presence of aggregates. As in previous sections, the suspension is stabilised with TMAOH, immediately after centrifugation. However, the suspensions made with this new method require much less TMAOH to be stabilised, as only 50 µl of this chemical is introduced in a 200 ml solution to make it totally clear, compared to the 500 µl used in the previous section. The necessary amount of stabiliser is lower, because of: (i) the lower concentration of nanoparticles in the solution due to the initial selection depending on zeta potential, and also (ii) the use of a more stable suspension, due to the highly negative zeta potential. Due to time reasons, no detailed zeta potential and DLS analyses could be done on these samples.

To produce inverse opal, 1 ml of a stabilised solution of FTO nano-crystals is mixed with 4 ml of DI water, and 100 µl of a 5% concentrated suspension of 196-nm polystyrene nanoparticles, giving a final 0.1% concentration of polystyrene nanoparticles. A piranha treated FTO sample is placed vertically in the tube, and the solution is then let to evaporate at 60 °C and 20% RH. The samples are then annealed at 400 °C, for four hours, with a ramp rate of 1 °C per minute.

The resulting inverse opal presents no defects at all over a large area, as shown in figure 5.28 *a)*. The cracks that are present, which cover only a small fraction of the surface of the structure, are almost always oriented in regular directions, due to the good periodicity of the structure. The cracks follow some preferential directions of the inverse opal. This can be observed in figure 5.28 *b)*, where the directions of the cracks follow the orientations of the inverse opal. At a higher magnification (figure 5.28 *c)*), the good order and connectivity between the pores can be observed. Each pore has 3 mesopores, from the layer directly below it, and only a few of these connections appear to be blocked.

The method of selecting only stable FTO nano-crystals with high zeta

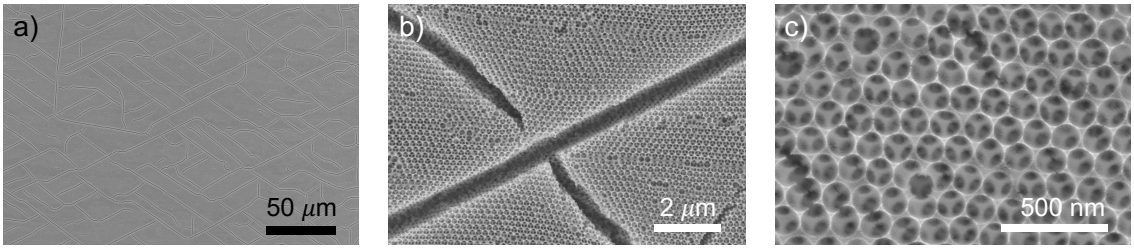


Figure 5.28: SEM images of a near-defect free FTO inverse opal, obtained by selection of high zeta potential nano-crystals, at *a)* high, *b)* medium and *c)* high magnification.

potential, shows very promising results, with the creation of a highly-ordered inverse opal, with oriented cracks and no surface defects. The absence of defects is due to the low amount of TMAOH introduced to stabilised the nanoparticles.

5.5 Conclusion

In this chapter, different methods for preparing crack-free FTO inverse opals have been investigated. It was found that a crack-free opal, which could be used as a template for a crack-free inverse opal, was hard to make with tin as a precursor, due to its instability. In the same way, the co-infiltration of dissolved tin precursors inside the gaps of the opal, did not provide the expected results, both because of the acidity of the solution, which makes standard PS nanoparticles aggregate, and again, because of the instability of the precursor.

The use of crystalline FTO nanoparticles for a co-infiltration method gives better results, because of the absence of acidity added by such a material. The FTO nano-crystals, made by a hydrothermal method, are stabilised with tetramethylammonium hydroxide, immediately after being synthesised. The amount of TMAOH added greatly improves the quality of the inverse opal, but creates many defects on its surface, due to the crystallisation of this material. Even when reducing the amount of FTO nano-crystals added to the solution, defects are still present.

A method was found for preventing the appearance of defects, by selecting only the most stable FTO nano-crystals after synthesis. The solution made with the selected nano-crystals required much less TMAOH to be stabilised, which prevents the creation of defects in the structure. Large scale highly ordered structures, with a reduced density of cracks, have been made with this method.

To totally prevent the appearance of cracks in the inverse opal, tin precursors are added in small quantities to the solution, to create covalent bounds between all the materials. However, due to the instability of this material and that of the FTO nano-crystals, the tin precursors have to be stabilised with citric acid, which plays the role of a chelating agent. The solutions made in this way are stable for a long time if a sufficient amount of citric acid is added. A strong base, sodium hydroxide, is used to give the solution a neutral pH, to avoid the aggregation of the

nanoparticles. The samples made with an optimised mix still present cracks, but are ordered on a large area, showing that this method is promising, but needs to be improved, to totally prevent the creation of cracks.

Chapter 6

OLEDs with Inverse Opal Structure

The XRD measurements presented in this chapter have been done by Miss Zhongyao Jiang, and the DSC measurements have been done by Mr Faisal Almana.

6.1 Motivation

Despite their many advantages for light-emitting devices, including high brightness, organic materials present a wide optical emission range. A narrower emission would allow a better contrast for emitting devices, and in an extreme case of a narrowed peak, a laser could be obtained. One of the main routes to narrowing the emission peak of an emissive device, is the creation of an optical cavity, which is done by carefully adjusting the thickness of each layer of the device, with the semiconductor device having approximately the thickness of half the emission wavelength. However, because of the poor electrical conductivity of organic materials, such a thickness for the semiconductor layer would greatly decrease their efficiency.

The search for an electrical organic laser has been on for a long time, because of the wide range of colours allowed by organic materials. Many advances in this field have been reported, but for now, no technology can create such a laser. The organic lasers currently used are optically pumped, meaning that their energy comes from the absorption of a light source, usually produced by another laser. Because of this, most of these lasers are only used in laboratories.

As reported in part 1.4.2, photonic crystal can be used as an optical cavity to produce laser effect with optical pumping. These lasers can have a very low threshold energy, depending of the quality of the cavity. The use of a photonic crystal with electrically pumped device have been demonstrated by Ozin *et al.*, and a sharpening of the emission peak of the organic compound have been observed. The 1D photonic crystal are made with the repetition of two layers : a low refractive index layer, made from conductive nanoparticles, and a high refractive index layer

made from a conductive transparent thin film. In this way, the photonic crystal can be conductive, and play the role of electrodes, while creating an optical cavity at the same time.

However, because the difference of refractive index between the two materials used is low, the crystal has to be thick to have a good reflectivity, which imply more defects, and potentially more losses. Contrary to a one dimensional photonic crystal, which is a succession of "solid" layers with similar (yet different) refractive index, an inverse opal has air as one of its materials, which results in a greater index contrast, and thus a better optical effect. For this reason, the use as an inverse opal as an optical cavity for an OLED could greatly enhance its performance.

In this chapter, we thus study the concept and possibility of an inverse opal-based OLED. In order to do so, a multilayer device, with an inverse-opal as its substrate is envisaged, as explained in figure 6.1. The traditional architecture of an emissive device, consisting of two electrodes, two transport layers, and one emissive layer is conserved, and transposed in three dimensions.

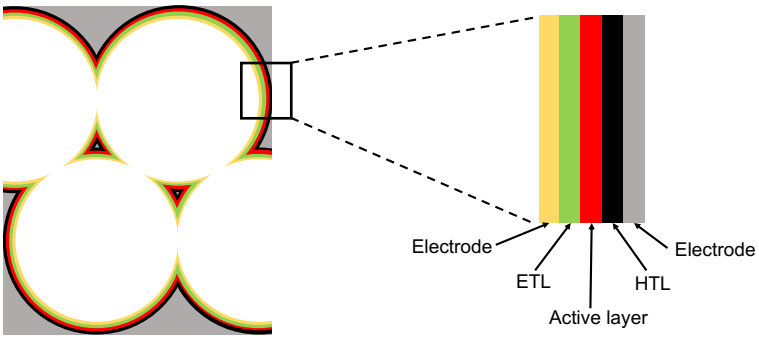


Figure 6.1: *Left :* Schematic of a multilayer device inside an inverse opal. *Right :* Magnification of the multilayer structure.

The inverse opal OLED structure would be designed to have its optical band-gap at the same wavelengths as the organic layer emission. However, this structure is different from an emissive layer which is sandwiched between two mirrors which makes a cavity. In this configuration, the light is freely emitted and is then reflected by the mirrors. In the case of a well designed inverse opal-OLED, the emission range is within the bandgap of the crystal, which prevents any light emission, due to the optical density of states which is zero. To allow light emission, a defect needs to be introduced in the structure, such as a layer with a different size of particles for instance. As this would be a complex architecture to build, this chapter only focus on a defect-free structure.

6.1.1 Materials

The inverse opal, which also plays the role of an electrode in this configuration, can be made in fluorine doped tin oxide because of the good conductivity and

transparency of this material, as discussed chapter 4. As seen in the previous chapters, atomic layer deposition is a very good technique for creating a conformal and regular layer inside inverse opal structures. The materials which can be deposited by the ALD in this laboratory, are titanium oxide, aluminium oxide, zinc oxide or any combination of them. Zinc oxide and titanium dioxide are two well-known electron conduction layers, and aluminium doped zinc oxide can be used as a transparent electrode[215]. In addition, a fine tuning of the electric properties of the material deposited by ALD is possible[216, 217], by varying the deposition temperature[218], or the ratio of doping for instance[219, 220]. With ALD, two layers can thus be deposited. Concerning the hole transport layer and emissive layer, another way of deposition is needed.

Sol-gel deposition can be used to coat the inside of inverse opal [221]. It is decided not to use a semiconducting polymer as the emissive layer, because the viscosity of a solution containing polymer could prevent the infiltration of the inverse opal. Instead, semiconducting small molecules are used to form the emissive layer.

Organic materials are frequently used as hole-transport layers, because of their good hole mobility. However, these materials can easily be dissolved, because of the weak interactions between organic molecules or polymers. This limits the possible solvent which can be used for the deposition of the emissive layer, as it could dissolve the hole transport layer. For this reason, a metal oxide material is preferred for this device, as it is more resistant against dissolution. It is decided to use nickel oxide, a well known hole transport material, which can also be used in solar cells.

In conclusion, it is decided to use a sol-gel method to deposit nickel oxide as a hole transport layer, and a semiconducting molecule as the emissive layer. For the electron transport layer and the outside electrode, zinc oxide and AZO are respectively used, and are deposited by ALD.

These combination of methods and materials are firstly tested on a planar cell, to test their validity. Then the coating of inverse opal with a solution method is tested with different methods, to produce optimal results. To finish, an optical simulation model is built, to asses the validity of the wanted structure.

A schematic of the envisaged process steps to build both the planar and the inverse opal OLED is presented in figure 6.2. The top row represents the fabrication of the planar cell, and the bottom one represents the fabrication of the inverse opal one. For these two architectures, the first step is to a FTO material, either as a thin film or as a 3D inverse opal (figures 6.2 *std-a* and *io-a* respectively) . The FTO is then homogeneously coated by nickel oxide, with a sol-gel method, such as spin coating (figure 6.2 *std-b* and *io-b*), and then, the active material is deposited in the same way (figure 6.2 *std-c* and *io-c*). Then zinc oxide, used as an electron transport layer, is homogeneously deposited via ALD (figure 6.2 *std-d* and *io-d*). To complete the device, the top electrode, here made of aluminium-doped zinc oxide, is also deposited by ALD (figure 6.2 *std-e* and *io-e*).

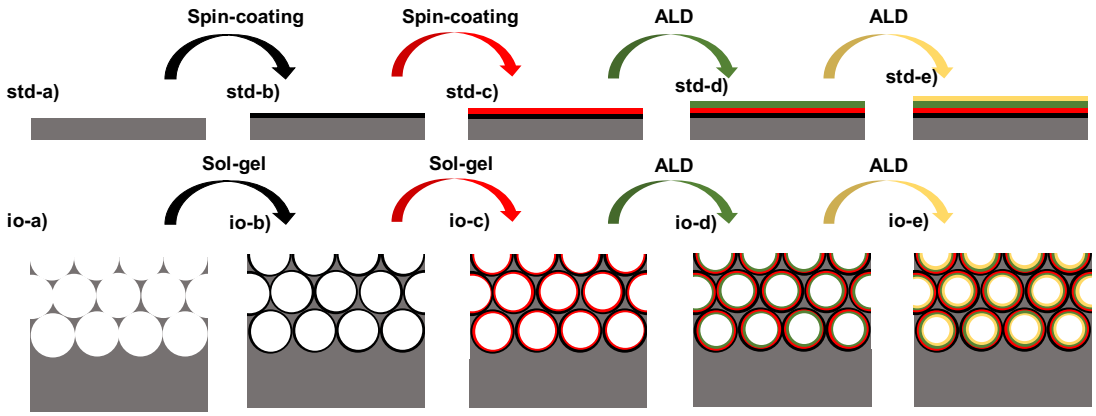


Figure 6.2: Fabrication process of a multilayer OLED for a standard substrate (*std-a)* to *std-e)*) and for an inverse opal substrate (*io-a)* to *io-e)*). From left to right, for both substrate : *a)* FTO substrate, *b)* deposition of nickel oxide by sol-gel, *c)* deposition of the active material by sol-gel, and deposition of zinc oxide and aluminium-doped zinc oxide, by ALD (*d)* and *e)* respectively).

6.2 Standard OLED fabrication

Prior to the fabrication of a three dimensional multilayer structure, a standard cell is fabricated, to test the compatibility between the chosen materials. The layers of this structure need to be made with the same materials as decided previously for an inverse opal multilayer, and deposited with the same methods. In the order of deposition, the hole transport layer and the active layer are firstly deposited by spin coating, followed by the electron transport layer and the outside electrode, deposited by Atomic layer deposition. Because of the extreme conformity of the ALD deposition, a cross section of a device made as previously described should look like the one schematically described on figure 6.3, *a)*. The electron transport layer and the electrode form a film not only on top of the structure, but all around it. Because of this, the AZO electrode is very close to the FTO electrode, as indicated with a red circle on figure 6.3, *a)*, and these two layers are only separated by a thin layer ($\approx 10nm$) of zinc oxide, which is not enough to prevent current to freely flow between the electrodes, creating a short circuit.

To prevent this, the FTO electrode can be etched on its side, in the same way as in chapter 4, with zinc powder and hydrochloric acid. A pattern such as the one represented on figure 6.3, *c)*, would give a device cross-section schematised figure 6.3, *b)*, where both electrodes are separated by a larger thickness of material. The represented schematics are not on scale; the layers thickness are in the order of the hundreds of nanometer, while the etching area has a millimetre size. A small FTO area that is not etched, is represented on the bottom of the schematic figure 6.3, *c)*, and its goal it to allow the contact between the bottom FTO electrode and an external testing device. This area is protected from the ALD deposition, by being covered by kapton tape, preventing any possible short circuits between the electrodes. This etched structure is used as the substrate throughout the work reported in this chapter.

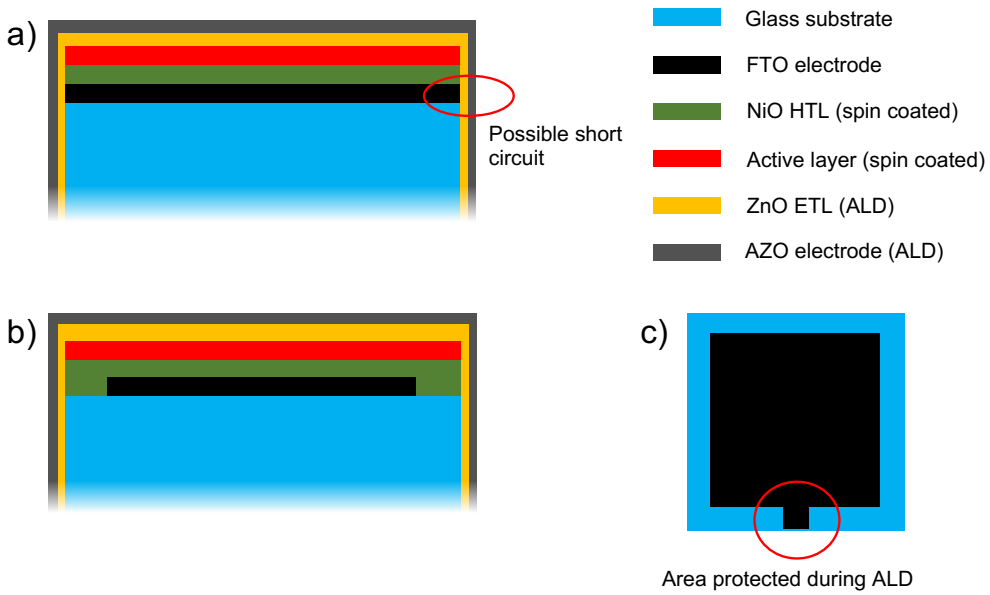


Figure 6.3: *a)* Cross-section schematic of a multilayer device, where the electron transport layer and the outside electrode are deposited by ALD. The red circle indicates the area where a short circuit between the two electrodes is possible. *b)* Cross section of the same device as *a)*, but with an etched FTO electrode on the sides, to prevent short circuit. *c)* Top view of the etched FTO on glass a substrate.

The nickel oxide layer is prepared from a nickel acetate tetra-hydrate precursor, whose chemical structure is represented in figure 6.4. This precursor is a well known compound to make NiO thin films. The recipe used in this thesis to produce a homogeneous thin film uses methoxy-ethanol as a solvent, and a 0.2 mol per litre concentration of nickel acetate [222, 223]. Ethanolamine is added to this solution, in a 1:1 molar ratio compared to the nickel precursor, to stabilise the solution and avoid a too-quick aggregation [211]. The mass and volume composition of a typical solution is given on table 6.1.

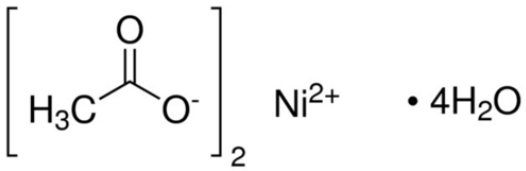


Figure 6.4: Chemical structure of nickel(II) acetate tetra-hydrate.

This solution is spin-coated at 4000 rpm for 40 seconds on an etched FTO substrate, after 10 minutes of UV-ozone treatment. The film is then annealed at 400 °C, for one hour, on a hot plate. The resulting films are visually homogeneous, with no visible defects, and have an average thickness of $15 \pm 4nm$, measured with profilometer.

The use of solution methods to make an active layer made of semiconducting molecules is not common in the literature, because evaporation methods give better results. Indeed, evaporation of molecule under vacuum, allows an accurate

Table 6.1: 0.2M nickel oxide solution composition

Material	Mass / Volume
Methoxyethanol	5 ml
Nickel acetate tetrahydrate	249 mg
Ethanolamine	60 µl

growth control, leading to a better crystallisation, and controllable physical properties. However, due to the goal of our device, which is to mimic the deposition method for an inverse opal coating, such an evaporation method is not suitable, and thus, the solution method is chosen.

A molecular active layer is composed of two different molecules : the host and the active molecule. If only active molecule were used to make a film, they would be too close to each other and interact too strongly, leading to a lower efficiency. For this reason, these molecules are often used in solution, or embedded in a matrix, which is known as the host. A standard host for a semiconducting molecule is CBP $(4,4' - Bis(9 - carbazolyl) - 1,1' - biphenyl)$, which can be blended with different active molecules. The active molecule chosen for this study is Ir(pic)2(acac) $(Bis(1{-}phenylisoquinoline)(acetylacetonate)iridium(III))$, which is a red emitter. The chemical structures of these two molecules are shown figure 6.5.

The mass ratio of host to active molecule is chosen to be 20:1, in accordance with studies found in literature[224, 225]. Two solvents have been tested with the same precursor concentration, chloroform and chlorobenzene, which both successfully dissolve CBP and Ir(pic)2(acac). For a spin coating speed of 4000 rpm for 40 seconds, on a nickel oxide thin film, chloroform gives homogeneous films of 150 ± 16 nm, while chlorobenzene do not give continuous film, because of its higher boiling point. For this reason, chloroform is chosen as a solvent, and the composition of the used solution is summarised table 6.2.

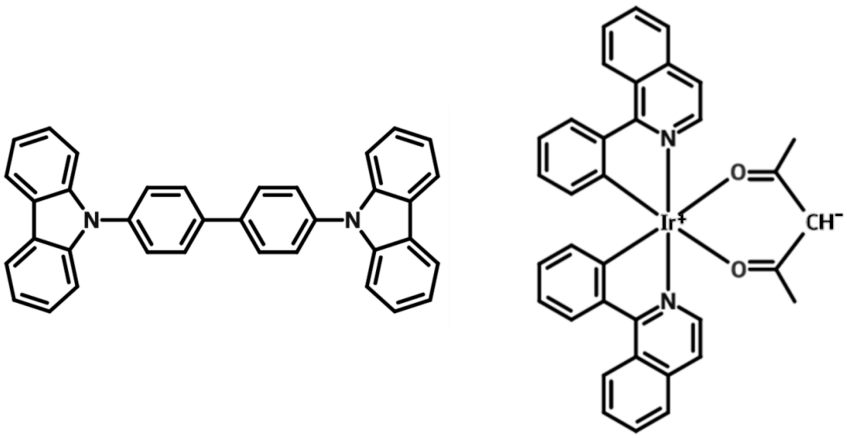


Figure 6.5: Chemical structure of 4,4'-Bis(9-carbazolyl)-1,1'-biphenyl (CBP) (left) and of Bis(1-phenylisoquinoline)(acetylacetonate)iridium(III) (Ir(pic)2(acac) (right). Reproduced with permission from Ossila [16].

The spin-coated films of CBP/Ir(piq)2(acac) in chloroform are homoge-

Table 6.2: CBP/Ir(piq)2(acac) solution composition

Material	Mass / Volume
Chloroform	1 ml
CBP	20 mg
Ir(piq)2(acac)	1mg

nous, and give an almost transparent and defect free layer. Such a film can be used as-cast, and gives a working OLED after deposition of the final layers. These other layers are deposited by evaporation, which do not require heating of the substrate. However, for the desired device, the two final layers are deposited by ALD, which requires annealing. As described in a next section, the sample is heated at up to 95°C, for the deposition of AZO. To ensure that such an annealing in the ALD does not damage the sample, a post deposition annealing at 95°C is done after the spin coating (i.e. prior to the ALD stage).

When annealed on a hot plate, some patterns which can be seen by eye starts to appear on the organic film, and grow over time. This effect starts to be visible at around 80°C, and becomes more noticable when the temperature increases. These patterns are observed with SEM for a sample annealed at 95°C (figure 6.6), and shows that discontinuities in the organic films are created, exposing the FTO/NiO layer under it. If the ZnO and AZO layers are deposited directly on top of the exposed area, a short circuit could be created, which would kill the device. In order to prevent this, the structure of the patterned area has to be understood.

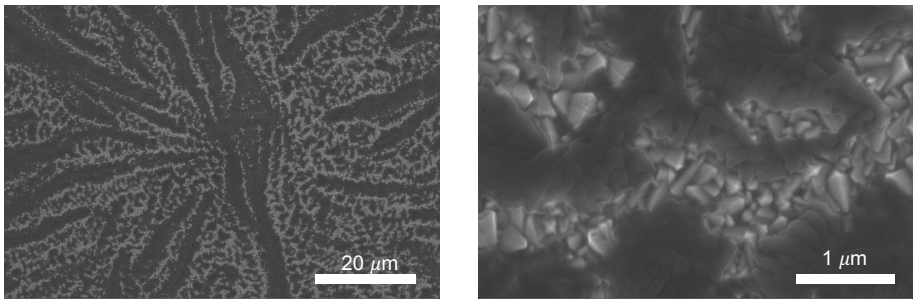


Figure 6.6: *Left :* SEM picture of defect on a CBP/Ir(piq)2(acac) thin film annealed at 95 °C. *Right :*Magnification of picture on *left*, showing the discontinuity of the organic film(in dark), and the exposition of the FTO(in light colour).

To understand this effect, differential scanning calorimetry is carried out on a powder sample, obtained by scratching thin film done with the solution described in table 6.2. In addition, XRD is measured on a FTO/NiO/(CBP-Ir(piq)2(acac)) sample, annealed at two different temperatures. The results of these analyses are shown on the left and right of figure 6.7 respectively. The DSC scan is composed of two heating-cooling cycles, which show differences, due to the melting of the sample and the evaporation of gas during the first cycle. No clear feature appears on the first scan in the temperature range where the pattern occurs on the thin film. On the second cycle, an increase of the heat flow occurs at 100°C, but this feature does not correspond to a classical phase change, which is a sharp peak.

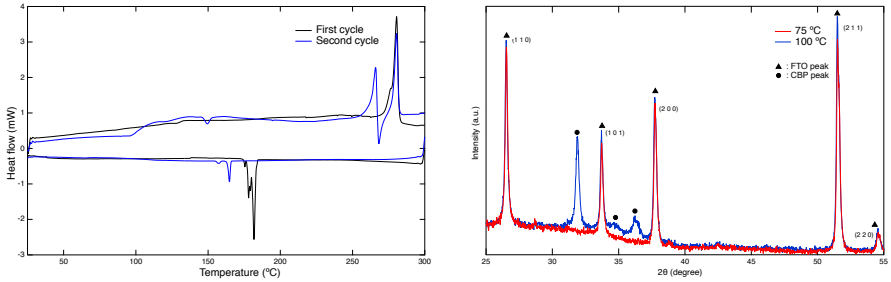


Figure 6.7: *Left :* DSC scan of a CBP/Ir(piq)2(acac) blend in a 20:1 mass ratio. The heating and cooling rate are 10 °C/min. *Right :* XRD on a FTO/NiO(10nm)/CBP-Ir(piq)2(acac)(100nm) device, after annealing at 75 °C (blue curve) and 100 °C (red curve).

The XRD of the device annealed at 75 °C shows peaks that we can identify as being FTO. The absence of peaks attributed to nickel oxide, which is supposed to be crystalline after its calcination, is explained by the small thickness of this layer ($\approx$ 15nm). With the annealing at 100 °C, new peaks appear, which we attribute to the crystallisation of the CBP/Ir(piq)2(acac) layer, because of the stability of the FTO and NiO at these temperatures. These new crystal planes indicates that the organic layer crystallises when annealed at 100 °C, which can be the origin of the crack pattern observed on visually and on figure 6.6. It can be supposed that this crystallisation starts before 100 °C, as it can be observed by eye.

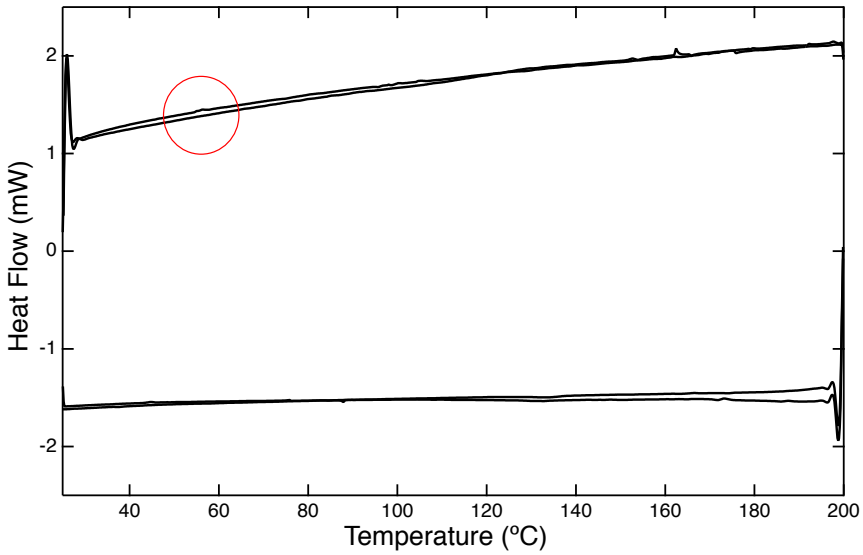


Figure 6.8: DSC of CBP powder, annealing and cooling at 10 °C/min, under nitrogen.

Because of the complexity of the blending between CBP and Ir(piq)2(acac), the complete understanding of the DSC can be challenging. For this reason, a DSC of the CBP alone is done (figure 6.8). A small peak can be observed at 58 °C, which we suppose of being the glass transition temperature of this material, which is similar to the values found in the literature. When the sample temperature is above the glass transition temperature, the molecules composing the film can move more freely, and can re-arrange their position, due to the weak Van der Wals forces between them.

Molecular crystal seeds are formed within the film, and crystal growth occurs around them. Because of the increased spatial mobility of the molecules after the glass transition, the molecules can move over large distances to participate in the crystal growth. Because of these movements, molecule-depleted regions appear between the crystals, creating the pattern seen on figure 6.6.

Due to the low temperature glass transition of CBP, another molecule compatible with the active compound and the solvent is selected. The host BCzPH (9,9'-Diphenyl-9H,9'H-3,3'-bicarbazole), whose chemical structure is shown figure 6.9, has a glass transition temperature of 100 °C, according to the supplier (Ossila), and is soluble in chloroform. A solution with the same mass concentration as previously (table 6.2) is prepared, by replacing the CBP with BCzPH. The solution is spin coated at 4000 rpm, for 40 seconds, on the FTO/NiO thin film. The sample is then annealed at 95 °C, for 30 min, on a hot plate.

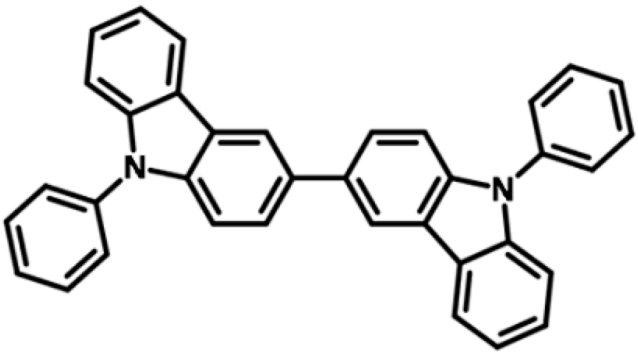


Figure 6.9: Chemical structure of 9,9'-Diphenyl-9H,9'H-3,3'-bicarbazole (BCzPH). Reproduced with permission from Ossila [16].

With the new host, the film is still homogeneous after annealing, and no crystal formation is visible by eye. A more accurate analysis on SEM still shows no defects or exposed FTO areas, as we can see on figure 6.10, *left*. At high magnification, the edges of some FTO crystals can be seen (figure 6.10, *right*), due to electron signal coming from a substantial depth below the surface, but the surface is only composed of the BCzPH/Ir(piq)2(acac) layer.

The structure FTO/NiO/(BCzPH/Ir(piq)2(acac)) is coated by ALD, with two successive steps, without sample removal from the ALD chamber. Prior to the depositions, a piece of kapton tape is deposited on the area indicated on figure 6.3, *c)*, to avoid a direct contact of the new layers with the FTO. The first step deposits the electron transport layer, made of zinc oxide. This deposition is done at 75 °C, and has 100 cycles of zinc-oxygen precursors, to have an expected thickness of 10 nm. The low temperature used for this deposition ensure a semiconducting effect for this layer. The second layer is made of aluminium doped zinc oxide, with a aluminium and zinc an a ratio of 1:15. This deposition is done at 95 °C, and has 63 super cycles, composed of 15 cycles of zinc, for one cycle of aluminium, giving a total of 1008 cycles, and an expected thickness of approximately 100 nm. The doping of aluminium at this ratio, with the increased temperature of deposition,

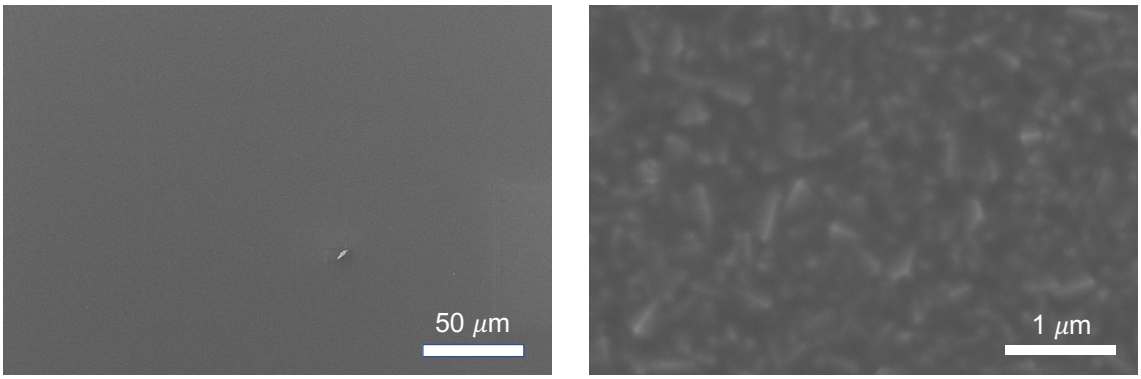


Figure 6.10: Large (*left*) and close view (*right*) of a spin coated BCzPH/Ir(piq)2(acac) layer (20:1 mass ratio), after annealing at 95 °C. The molecules are dissolved in chloroform, and spin coated at 4000 rpm for 40 seconds, on a FTO/NiO substrate.

gives a material which is more a conductor than a semiconductor. To increase even more the conductivity, the deposition temperature could be increase, but this is not possible with the organic layer in our device.

The completed device is highly transparent, and does not present any visible defects. A SEM cross section of the device is shown on figure 6.11, *left*, and all the layers can be distinguished, with the exception of the zinc oxide and the AZO, which have a too similar morphology and composition. A careful study on different region of the device, indicates that there is no direct contact between the FTO and the ALD layers, showing that the BCzPH host did not change morphology during the annealing. However, there is a poor adhesion between the organic layer, and the electron and hole transport layer, which can be seen in many areas where these layers are detached from each other.

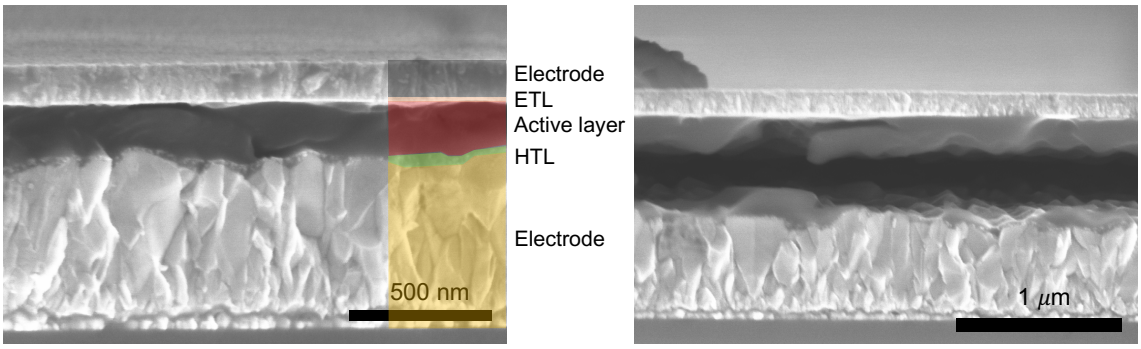


Figure 6.11: *Left :* Cross section of FTO/NiO/(BCzPH/Ir(piq)2(acac))/ZnO/AZO device. The layers are highlighted in different colours : golden, green, red, yellow and grey, for the bottom electrode, hole transport layer, active layer, electron transport layer and top electrode respectively. *Right :* Delamination of the active layer, on both the electron and hole transport layer.

Unfortunately, the completed device could not be electrically tested, due to time and equipment reasons. Nevertheless, a clear device structure have been demonstrated, with no defects that could lead to a short circuit. A complete study would require a STEM/EDX analysis, to be sure that no precursors of the ALD go

into the organic layer, as it can be observed with some polymers.

In conclusion, it has been shown that with a careful choice of the organic compounds, a multilayer device can be obtained, with the two final layers deposited by atomic layer deposition. This structure could be very interesting to study deeply, due to the two transparent electrodes, which would make it a transparent OLED.

6.3 Coating challenges

In this part, polystyrene nanoparticles of 488 nm are used, and the opals are formed on fluorine tin oxide substrate, treated with piranha solution, by evaporation induced self assembly, at 60 °C, and at 20 % RH. The opals are then infiltrated with a 0.2M solution of fluorine doped tin oxide in methanol, with a ratio fluorine:tin of 1:10. The infiltration is done on the side of the opal, and is followed by a spin coating of 40 seconds, at 2000 rpm. The sample is left to dry for 15 minutes at room temperature, and is then annealed at 60 °C for 15 minutes, to evaporate solvent residuals. Due to the infiltration of precursors, the optical properties of the opals change, and thus, the reflected colour is shifted. The infiltration process is then repeated, until no more colour change is observed, meaning that no more infiltration can be achieved. The infiltrated opal is finally heated at 450 °C for four hours, with a temperature ramp of 1 °C/min, and a natural cooling.

As previously explained, the only materials which can be deposited with the ALD system in our laboratory are zinc oxide, aluminium oxide, titanium dioxide and combinations between them. In order to deposit other materials, nickel oxide and BCzPH in our case, a sol-gel method is decided. It should be noted that because of the conductive structure used (FTO), electrodeposition could be used to deposit nickel oxide on the surface of the inverse opal, in a regular way. However, to the best of our knowledge, the deposition of molecule with this method is challenging, and thus, a sol gel method would still need to be used to deposit BCzPH. To avoid optimising two different methods to coat materials inside an inverse opal, it is decided to use a sol-gel method for both the nickel oxide and the BCzPH.

As an initial try for making a nickel-oxide coating, the same solution concentration (table 6.1) and the same spin coating parameters as the flat cell, are used for the inverse opal. The solution is dropped on the side of the sample, to allow a better infiltration, and a colour change, from green to pink-reddish is observed, confirming a good infiltration. After the spin-coating, the sample is let to dry at room temperature for 15 minutes, and then annealed at 400 °C for 30 minutes.

From a top view, a homogenous coating of the inverse opal is observed (figure 6.12). However, no coating is visible on the inside of the structure, as can be seen on a tilted sample, where the contrast between the top and the inside of the inverse opal is clear.

The apparent absence of a nickel oxide coating on the inside of the inverse opal can be explained by considering how films are formed during spin coating.

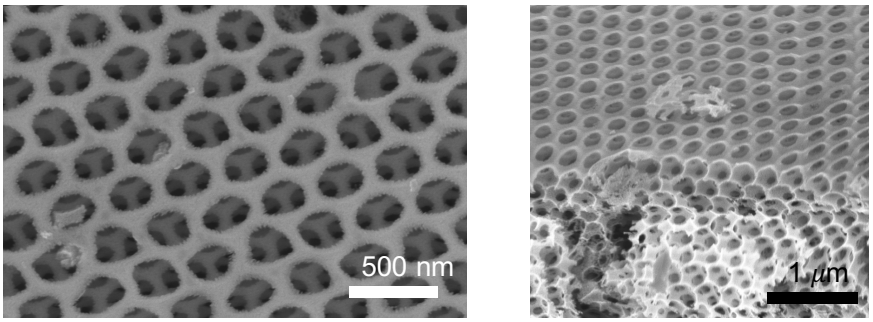


Figure 6.12: Top (*left*) and 45° inclined view (*right*) of a 0.2M nickel acetate solution spin coated at 4000 rpm on a FTO inverse opal. The sample is calcined at 400 °C for 30 minutes after deposition.

The schematics *a)*, *b)* and *c)* of figure 6.13, represent the three main steps of film formation on a flat substrate. The rotation of the substrate ejects large fraction of the solution on the top of the sample, which becomes so thin that evaporation occurs quickly on it, compared to its volume. Due to the solvent's evaporation, the precursors' concentration increases, and agglomerates start to form. These agglomerates then sediment on the substrate, which gives a flat and homogeneous thin film. The precursors forming the final film come from the solution drop, whose volume is bigger than the film itself.

In the case of an inverse opal, depicted on schemes *d)*, *e)* and *f)*, the film formation on the top of the structure is similar to the film formation of a standard film, with the materials coming from the whole drop on top of the sample. However, for the coating of the inside of the inverse opal, the precursor forming the film can only come from the inside of the inverse opal, which is a much smaller volume than that of the drop, leading to a much smaller coating thickness.

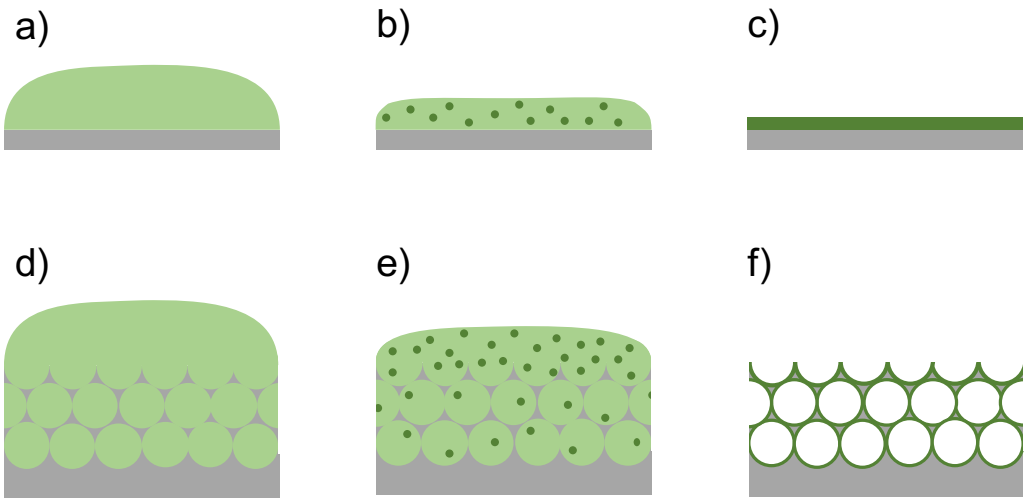


Figure 6.13: Comparison between spin coating done on a flat substrate (*top row*) and on a three dimensional inverse opal (*bottom row*). Deposition of the solution on the substrate (*a and d*), spin coating and evaporation of the solution (*b and e*) and film formation on the substrate (*c and f*)

As a first approximation, we make the assumption that the precursors used

to form a thin film inside a sphere of the inverse opal, only come from the inside of the sphere. With this hypothesis, the required concentration of precursor to form a film of a certain thickness, can be calculated. The thickness of the wanted nickel oxide film is named h, and the radius of the empty sphere of the inverse opal is named R_1. Using these notations, the radius $R_2 = R_1 - h$ can be defined, and is the radius of the air sphere, taking into account the nickel oxide layer thickness. With these notations, the volume of the nickel oxide film, V_{NiO}, is the difference of the volume V_1 and V_2, which are the volume of the air sphere without and with the oxide layer respectively. This volume is expressed in function of R_1 and R_2 in equation 6.1.

$$V_{NiO} = \frac{4}{3}\pi(R_1^3 - R_2^3) \approx 4\pi R_2^2 h \tag{6.1}$$

The mass of NiO composing this volume can be calculated from two different ways. Firstly, by the multiplication of the NiO film volume V_{NiO}, by the density of nickel oxide, $d_{NiO} = 6.67 g/cm^3$. Secondly, if we define n_{NiO}, the amount of moles of the NiO compound in the thin film, and M_{NiO} its molar mass, the mass of the film is simply $n_{NiO}M_{NiO}$. Due to its composition, we can of course calculate M_{NiO} as the sum of the molar mass of its compounds, M_{Ni} and M_O. These two ways of calculating the mass of the film, are summarised in equation 6.2.

$$m_{NiO} = V_{NiO}d_{NiO} = n_{NiO}(M_{Ni} + M_O) \tag{6.2}$$

The mass of nickel acetate tetra-hydrate inside one sphere of the inverse opal can be calculated by using the formula, $m_{Ni-acetate} = n_{Ni-acetate}M_{Ni-acetate}$. Because only one atom of nickel is present in the nickel acetate tetra-hydrate molecule (figure 6.4), the molar amount of this precursor is similar as the one of nickel, i.e., $n_{Ni} = n_{Ni-acetate}$. In addition, due to the presence of only one atom of nickel in the NiO compound, we have $n_{Ni} = n_{NiO}$. With these different equalities, $n_{Ni-acetate}(= n_{NiO})$ can be calculated, by isolating n_{NiO} i.e. equation 6.2, which leads to equation 6.3, expressing the mass of nickel acetate tetra-hydrate inside one inverse opal sphere, needed to have a nickel oxide thin film with a thickness h.

$$m_{Ni-acetate} = M_{Ni-acetate}\frac{V_{NiO}d_{NiO}}{M_{Ni} + M_O} \tag{6.3}$$

The required concentration of nickel precursor can now be calculated, by dividing its mass, by the volume of the sphere where the solution is, which is V_1 in this case. With this final calculation, the equation 6.4, expressing the required concentration of nickel precursor in a solvent, to have a specific thickness of nickel oxide thin film, which also depends on the size of the inverse opal spheres.

$$C_{Ni-acetate} = \frac{M_{Ni-acetate}V_{NiO}d_{NiO}}{(M_{Ni} + M_O)V_1} \tag{6.4}$$

In order to visualise the mass concentration of precursor required to form a film of a certain thickness, this equation is plotted on figure 6.14, for different pore sizes of inverse opal. It can be seen that the required concentration increases for smaller pore size, for the same coating thickness. This is due to the higher surface area, and so the greater amount of material required for a coating, of smaller pore size structures. It is thus easier to coat a large pore, because of the lower required concentration. The required concentration to obtain a thin film, is extremely high, even for a film less than 5 nm. The values obtained by this calculation, which are very often higher than 1 g/ml, can be compared with the concentration used for the standard device made in the previous part, which is 50 mg/ml.

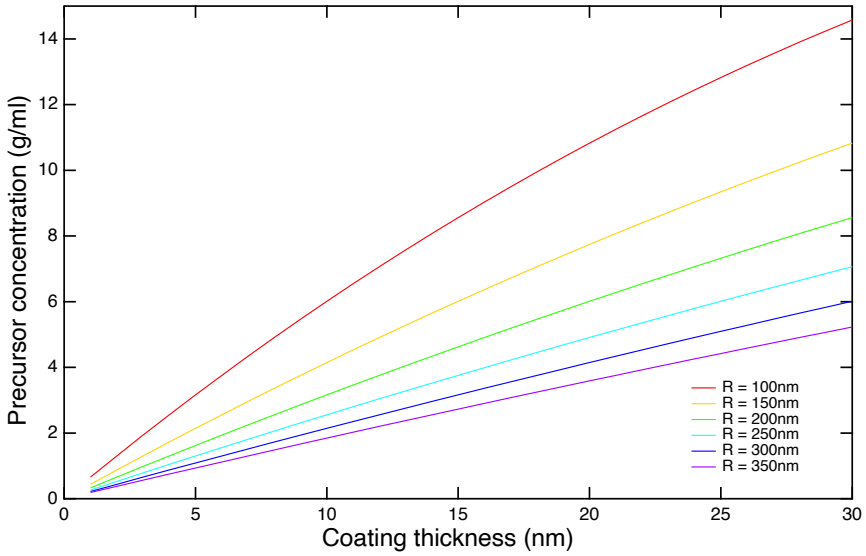


Figure 6.14: Calculated required concentration of nickel acetate precursor to coat the inverse opal with a specified thickness of crystalline nickel oxide, for different inverse opal pore sizes.

An improvement to this calculation can be done, by taking into account the connections between the pores. As these areas do not need to be coated, the required amount of precursor per pore is decreasing. Each sphere in a fcc structure is connected to 12 others spheres (figure 1.18). To deduct the volume corresponding to these areas from V_{NiO}, we make the approximation that these volumes are cylindrical, instead of a more complex geometrical form. A new parameter needs to be introduced to this calculation, corresponding to the size of the connection between two pores, which is supposed to be a circle. As seen in the previous sections, the inverse opal pores can be more-or-less connected from each other, mostly depending on the opal formation. To stay general with the different size of pores, it is supposed that the radius of the circle connecting two pores is a fraction of the pores radius R_1, and can thus be expressed as $r = R_1/k$. With this radius, the volume which needed to be deducted from V_{NiO}, can be expressed as $12\pi(R_1/k)^2h$, the volume of 12 cylinders of height h, and radius R_1/k. By integrating this volume in equation 6.4, the equation 6.5 is obtained.

$$C_{Ni-acetate} = \frac{M_{Ni-acetate} d_{NiO} (V_{NiO} - 12\pi(R_1/k)^2 h)}{(M_{Ni} + M_O) V_1} \tag{6.5}$$

This equation, which depicts a more accurate required concentration, is plotted on figure 6.15, for a pore radius of 300 nm, and for different sizes of connection between the pores. As expected, a bigger connection reduces the amount of precursor needed, and thus the concentration. The values obtained for the maximal sintering between the pores, with a radius of $R_1/2$, are very small in comparison of the other curves, which might be due to the limit of the approximation considering the volumes to subtract as cylinders. For a large radius, the difference between a cylinder of a portion of sphere becomes important, and the cylinder over estimates the real volume.

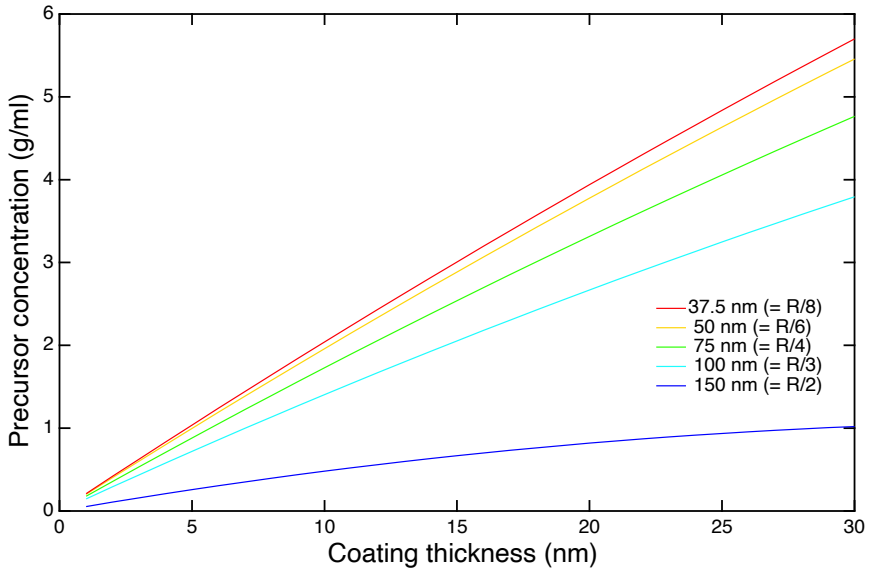


Figure 6.15: Calculated required concentration of nickel acetate precursor to coat the inverse opal with a specified thickness of crystalline nickel oxide for an inverse opal with a pore size of 300 nm, corrected with different pore connections sizes.

The rest of the curves still show a decrease of the precursor concentration, compared to figure 6.14, and a coating with a thickness of 10nm requires approximately a precursor concentration of 1.2 to 1.5 g/ml (for the considered pore size). These values are still large compared to the concentration of solution used for a standard thin film. However, the coating can be done in multiple times, with an annealing between each coating, to avoid the dissolution of the already deposited species. Doing so can create a good coating for the inside of in inverse opal, but the surface of the structure needs to be taken care of, as too many depositions could create an over-layer on it, preventing any further infiltration. The coating thus needs to be homogeneous, both inside the opal, and on its surface.

The large amount of precursor material needed to make even an extremely thin film can be explained for two reasons. Firstly, the final material is crystalline, where the atoms are packed, which requires a large number of atoms to make even a thin film. Secondly, the "useful" part of the precursor is only the nickel atom, while the rest of the compound (acetate groups and water molecules) do not participate in the film creation. These groups are used for the dissolution and the stability of the nickel ion, but also increase the total mass of required precursor.

The dissolution of nickel acetate tetra-hydrate in methoxy-ethanol, can also reach a saturation point at these high mass concentrations. As in the previous section, the solutions are made with an equi-molar amount of nickel precursors and of ethanolamine. A solution with a concentration of 150 mg/ml of nickel precursor, which is three times more concentrated than the flat film recipe, shows an intense green colour, and is stable for days under stirring, as no aggregates is seen. A much more concentrated solution of 500 mg/ml has a very dark green colour, and cannot be fully dissolved at room temperature. When heated and stirred at 80 ° C, all the precursors are dissolved, but, on return to room temperature, the solution precipitates.

As highly concentrated solutions are not stable at room temperature, it is decided to use a solution with only 150 mg/ml as a starting point for the study of coating inverse opal. While this concentration is not enough to make a good thin film, according to our calculations, it can be a good way to test deposition methods, while still providing enough materials to be detected.

At this concentration, the spin coating deposition always gives an over-layer on top of the material, even at high speed (tested until 10000 rpm). To avoid the formation of an over-layer, a sandwiched method is tried, where the inverse opal is pressed by a piece of glass, which is firmly maintained to the sample with a clip. This method is adapted from the infiltration of opal with precursors. The highly concentrated solution is then infiltrated on the side of the sample, and quickly spreads through it, owing to capillary effects. The sample is then directly annealed at 300 °C, on a hot plate for 30 minutes, while still being pressed against the piece of glass.

The samples made with this method, show an apparently good coating, both on top and on the side of the structure (figures 6.16, *a)* and *b)* respectively). Many aggregates are present on the surface of the substrate due to the sedimentation of the precursors, or lurk in the cracks. The coating which can be seen on the inverse opal, might also be due to the precursors which are present in the cracked area of the inverse opal, and which agglomerate on the inverse opal, forming a film. Unfortunately, no cross section of these samples could be taken, so this hypothesis could not be checked, but it is highly unlikely that such a thick coating would permeate throughout the structure.

It can be supposed that for a structure without any cracks, the coating would be much more homogeneous inside the inverse opal, but the top part would still present a thick layer. In addition, there are inhomogeneities on the top of the structure, and some parts of it are covered by a substantial over-layer (figures 6.16, *c)* and *d)*). The over-layers are randomly distributed all over the sample, preventing any further deposition. It is supposed that these defects appear, even though the sandwich method should prevent it, because of the irregular thickness of the inverse opal. Because of this irregularity, the contact between the flat protection and the inverse opal is not perfect, a large volume of solution can be trapped on top of the structure. In these areas, an over-layer is then formed due to the sedimentation of the precursors.

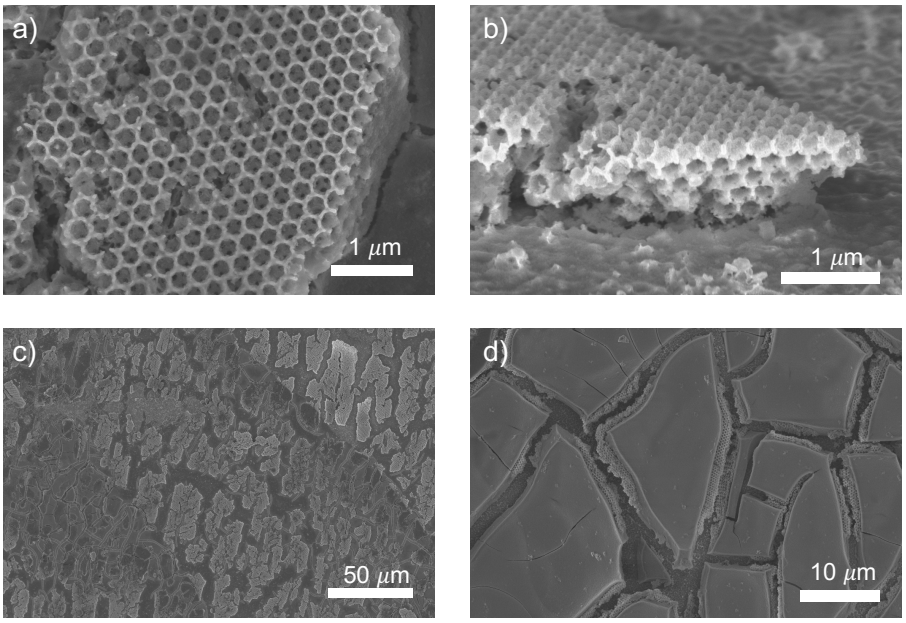


Figure 6.16: FTO inverse opal with 488-nm pores, coated by a sandwiched infiltration of a 150mg/ml nickel acetate solution, immediately followed by an annealing at $300°C$. Top (a) and side (b) views of a coated structure without overlayer. (c) Large view of the structure, indicating irregular areas with over-layer (darker areas) and (d) magnification on inverse opals with overlayer.

In order to prevent defects of the coating with irregular samples, the same method of protection of the top surface is employed, but this time, no annealing is done, and the solution is let to dry at room temperature for some days. In this way, because of the diffusion of the precursors in the solution, a more homogeneous coating, due to a better repartition of the precursors, is anticipated. After the natural drying of the solvent, the samples are annealed on a hot plate at 300 °C for 30 minutes.

This methods gives a very different result from that of fast annealing. Large aggregates can be seen on top of the sample, however no homogeneous over-layer is seen (figure 6.17 *a)*). Due to the low temperature at which the evaporation of the solvent occurs, it is supposed that the precursors aggregate between each other, but stay in suspension. When the aggregates are too big, or the solvent is evaporated, it sediments on the surface of the inverse opal. The top of the inverse opal is coated with a thick layer of nickel oxide, and aggregates inside the structure are visible (figure 6.17 *b)*). On a 45 degree tilted view, the difference between the top and the inside of the structure is clear, as no obvious coating can be seen on the inside while a thick layer, which is also quite porous, is present on the top of the inverse opal (figure 6.17 *c)*). A closer look on the porous layer, and the aggregates which are inside the inverse opal, reveals that these aggregates can take the shape of a ball inside the opal itself (*d)*)

With these observations, it it hypothesised that because of the low temperature, the nickel precursors do not aggregate immediately, and stay in solution on an initial stage. As the solvent evaporates, and thus its volume decreases, it

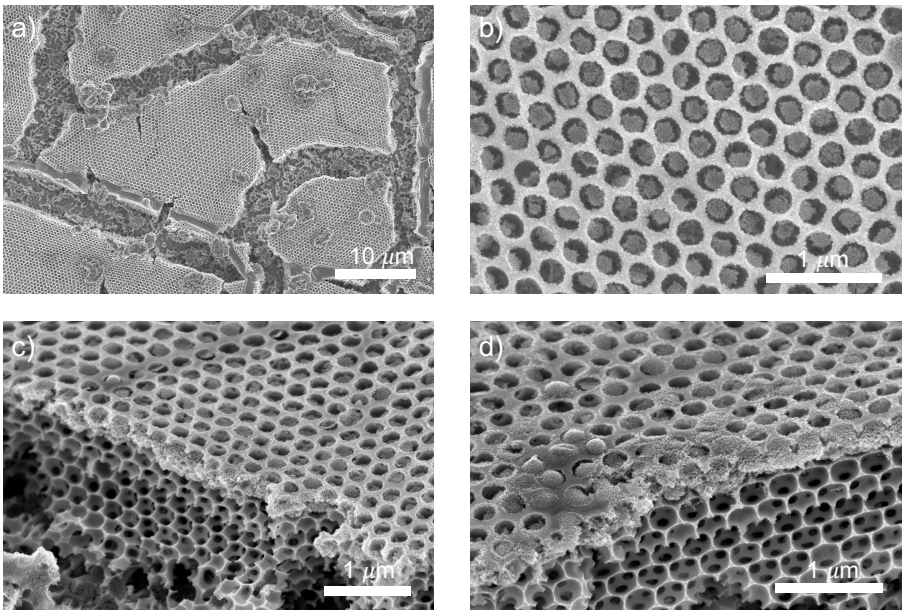


Figure 6.17: FTO inverse opal with 488-nm pores, coated by a sandwiched infiltration of a 150 mg/ml nickel acetate solution, let to dry at room temperature for two days, followed by an annealing at $300°C$. (a) Medium and (b) high magnification of the structure after annealing. (c) Side view of the structure, and (d) observation of ball shaped nickel oxide deposition within the inverse opal.

no longer fills the space between the substrate and the glass slide on top of the sample. Due to the difference of surface energy between these two surfaces, the solvent preferentially stays on only one of these surfaces, which we suppose to be the glass one in our case, confirmed by SEM images. Due to evaporation of the solvent, the concentration of the precursor increases, until it reaches saturation point, and the precursors starts to aggregate. When this saturation point occurs, the solvent which is still not evaporated is located on the top part of the inverse opal, where the glass slide is located. Because of this, all the precursors aggregates on the top of the structure, which leads to a very thick coating, which is porous due to the slow aggregation of precursors, which forms nanoparticles instead of films. Due to the saturated concentration of the solution, the precursors inside the opal can aggregate in the form of a sphere.

The inverse opal coating methods using a top flat substrate to prevent an over-layer do not provide the expected results, because of the imperfections of the opal, or because of the influence of the covering layer. The ideal repartition of solution on the inverse opal, would consist of a perfect infiltration inside the structure, as well as a small wet layer on top of it, with the dimension of the size of the opal pores. This situation requires a volume of solvent equal to $V = S * h * 0.74$, where S is the surface of the sample, h is the height of the inverse opal, and 0.74 represents the fraction of the inverse opal occupied by air. For a sample of $1\,\mathrm{cm}^2$ with a height of 1 µm, this volume is equal to 0.074 µl. This amount is far too small to be deposited in an homogeneous way on a sample, both because of the difficulty of spreading such a small amount, and because of the fast evaporation of this amount of solvent.

To overcome this problem, the solution is dropped on a sample which is placed in a vertical position (figure 6.18 *a)*) instead of a horizontal one. Due to gravity forces, the solution is naturally dragged in the bottom direction. However, a part of the solution stays inside the structure and on top of it, due to capillary forces (figure 6.18 *b)*). As the volume of dropped solution is greater than the theoretical value to fill the inverse opal (V = 0.074 µl), an excess of solution is present at the propagation front of the solution. When the solution reaches the end of sample, a large part of the excess can stay on the bottom of the sample, due to surface tension (figure 6.18 *c)*). Indeed it is not energetically favourable for the solvent to create more surfaces in contact air, which is the only material after the sample, in the same way as a drop of water can stay at the edge of a glass slide. If there is still an excess solution at the bottom of the sample, it will spread homogeneously on the sample as soon as it goes back to a horizontal position, giving an over-layer on the sample.

To prevent this excess of solution, another substrate with the same thickness and surface energy is placed immediately after the inverse opal. In this way, the solution can keep spreading to the second substrate, due to similar surface energies, leaving no excess on the sample. For samples made with this method, a solution of 150 mg/ml of nickel precursors in methoxy-ethanol have been used. 5 µl of solution is dropped directly on the edge of a 1 cm^2 FTO inverse opal sample, with a FTO substrate directly placed on the bottom of it. The 5 µl are dropped as homogeneously as possible over the edge of the sample, to cover the maximum of surface. A clear colour change can be observed after the spreading of the solution into the sample. The reflected colour is similar from the front on the back of the sample, indicating a good infiltration. The samples are then annealed up to 300 °C, for one hour, in a tube furnace with a ramp rate of 1 °C/min.

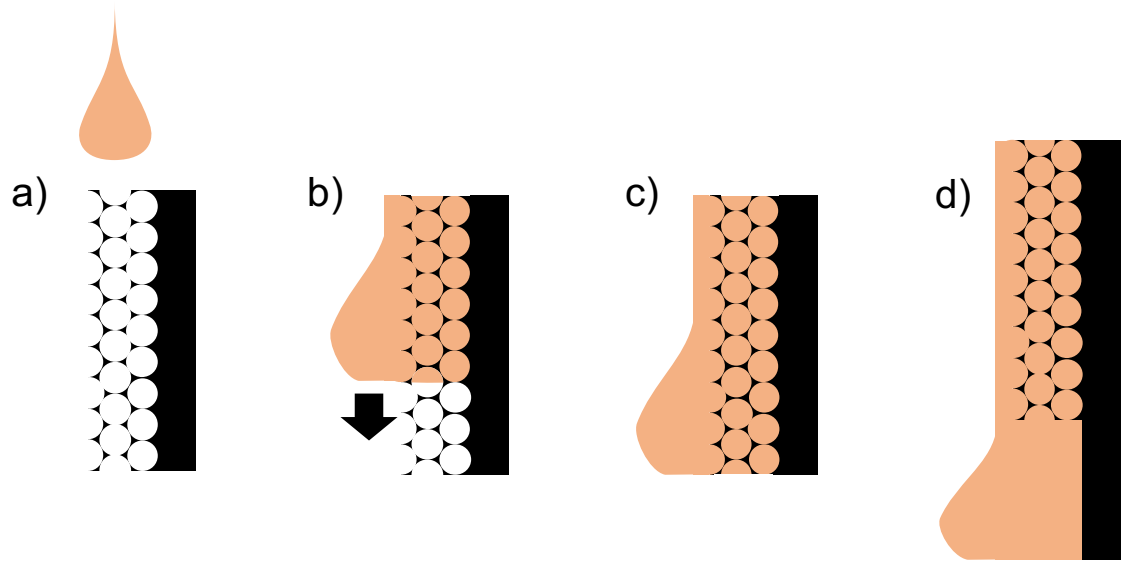


Figure 6.18: Schematic of the homemade vertical drop deposition method. (*a*) Vertically placed sample, and solution dropped on top of it. (*b*) Spreading of the solution inside the structure driven by gravity and capillarity. (*c*) Formation of an excess of solution at the bottom of the sample, due to the surface tension of the solution. (*d*) Addition of a substrate directly in contact with the bottom of the sample, preventing the an excess of solution on the inverse opal.

The samples made in this way present no over-layer, and a close look on the surface does not show any aggregates or excess of precursors (figures 6.19 *a)* and *b)*). A cross section of the sample reveals an homogeneous infiltration over the whole thickness, which can be seen with the "granular" aspect of the inverse opal (figures 6.19 *c)*). At an extreme magnification, it can be observed that the deposited layer consists in islands of materials, giving it the previously seen granular aspect. This deposition is constant with the calculations concerning the mass concentration and the resulting layer thickness : at the used concentration $150mg/ml$, an extremely small layer of approximately 1nm should be formed. However, the growth of a material is not a conformal layer by layer, but is by islands. Instead of a continuous thin layer, many isolated islands are formed, as there is not enough precursor to form a continuous film.

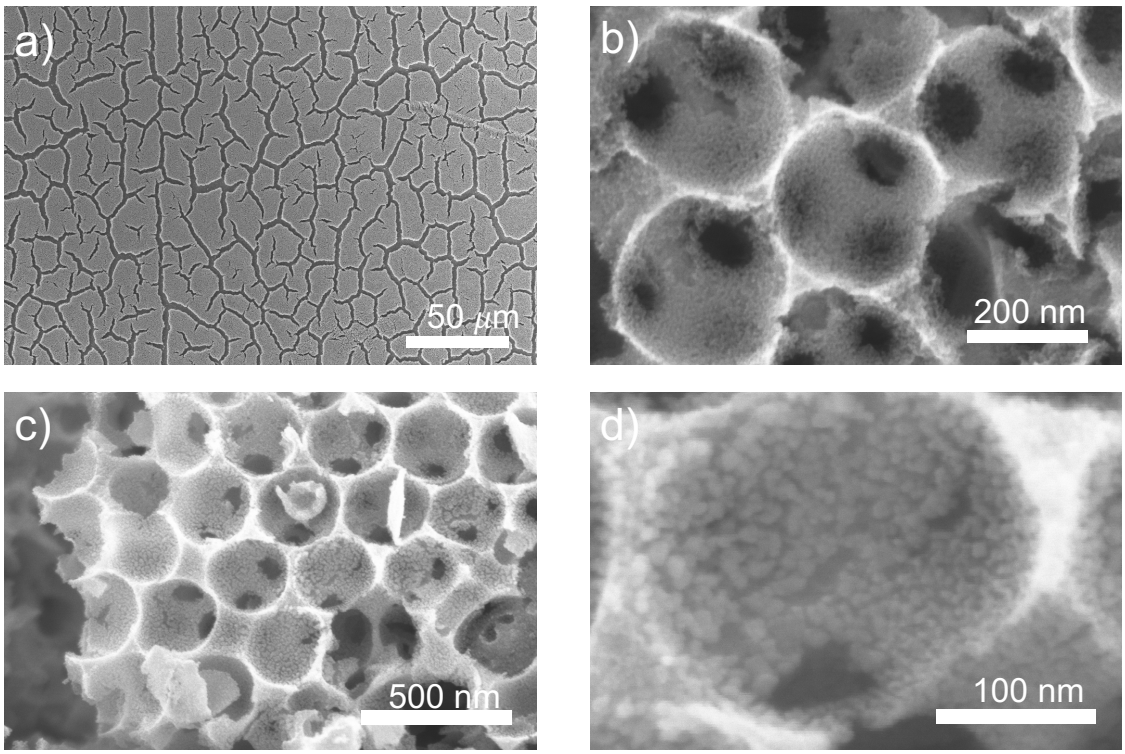


Figure 6.19: 488-nm FTO inverse opal, infiltrated with a 150 mg/ml nickel acetate solution in methanol, by vertical drop method. Top view at low (a) and high (b) magnification of the coated structure after annealing at 300 °C. Cross section of the coated inverse opal (c) and ultra high magnification on one coated pore in cross section (d), showing the rough surface due to the NIO coating.

The observations on SEM gives good indication of the quality of the deposition, but are extremely local. To verify if the inverse opal is coated homogeneously on a large scale, in the order of a square millimetre, optical measurements are done, with a tilt-able Uv-Vis. The sizes of the pores of the inverse opal do not change due to the coating, but the average refractive index does, due to the presence of the coating material with $n > 1$ where air was previously. As the average refractive index increases, the coated sample is expected to have red-shifted reflection peaks, compared to the uncoated one. This is confirmed by the figure 6.20 (*left*), where the same sample is measured for reflection, before and after coating, at different an-

gles. All the peaks corresponding to the coated sample (dotted lines) are at longer wavelength than the ones for the uncoated samples, and this is summarised on 6.20 (*right*).

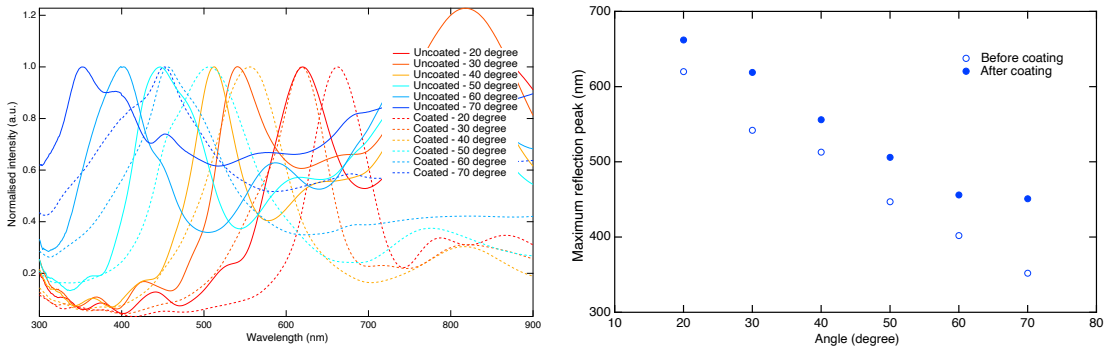


Figure 6.20: *Left :* Reflectance Uv-Vis at different angles for a 488-nm FTO inverse opal prior (plain lines), and after (dashed lines) NiO deposition by vertical drop method. *Right :* Maximum peak position for the coated and uncoated structures.

To confirm the fact that the coating on the inside of the inverse opal is made of nickel oxide, TEM and STEM imaging are useful techniques. The samples are prepared by crushing the coated inverse opal sample, in a vial filled with ethanol, which is then sonicated. A drop of the ethanol solution with inverse opal parts in it, is then deposited on a TEM copper grid with holey carbon. The imaging is done at 200kV, due to the good resistance of metal oxide materials to electron damage.

To quantify chemically the atoms present in this structure, STEM and EDX are used. STEM is done with a probe of 1nm, and the selected area is scanned 3 times pixel by pixel, in order to reduce the noise. The distribution of nickel, oxygen and tin, as well as their superposition, are represented figure 6.21. A clear correlation is present between the distribution of oxygen and tin in the imaged sample, as these species compose the core of the inverse opal. The nickel signal is only present at the perimeter of the visible pores of the inverse opal, because of the projection effect already discussed in 4.2.2. This signal is very strong on most of the visible pores, but is absent from the one located on the bottom right of the sample, indicating an incomplete coating. This defect could come from an isolated pore, badly connected to its neighbours, or a bad infiltration of the solution, either due to its viscosity or due to too small pores, preventing its flow. This analysis made with STEM/EDX have been repeated on 10 samples on the grid, and they all present the same strong nickel signal corresponding to a good inverse opal coating.

In conclusion, a regular and thin coating of a FTO inverse opal has been obtained with nickel oxide, with a homemade method, consisting of a vertical sample where a drop of concentrated solution is deposited. This method provides no over layer, and a consistent coating result on a large area. The coating does not form a continuous film, because of the lack of introduced precursors, but additional coatings in the same conditions can be done to obtain a continuous and regular film. However, it appears that not all the inside of the inverse opal is coated, as some of the pores do not present any nickel signal. This is attributed to the defects in the inverse opal, where not all of the pores are well connected, resulting in isolated pores, which are

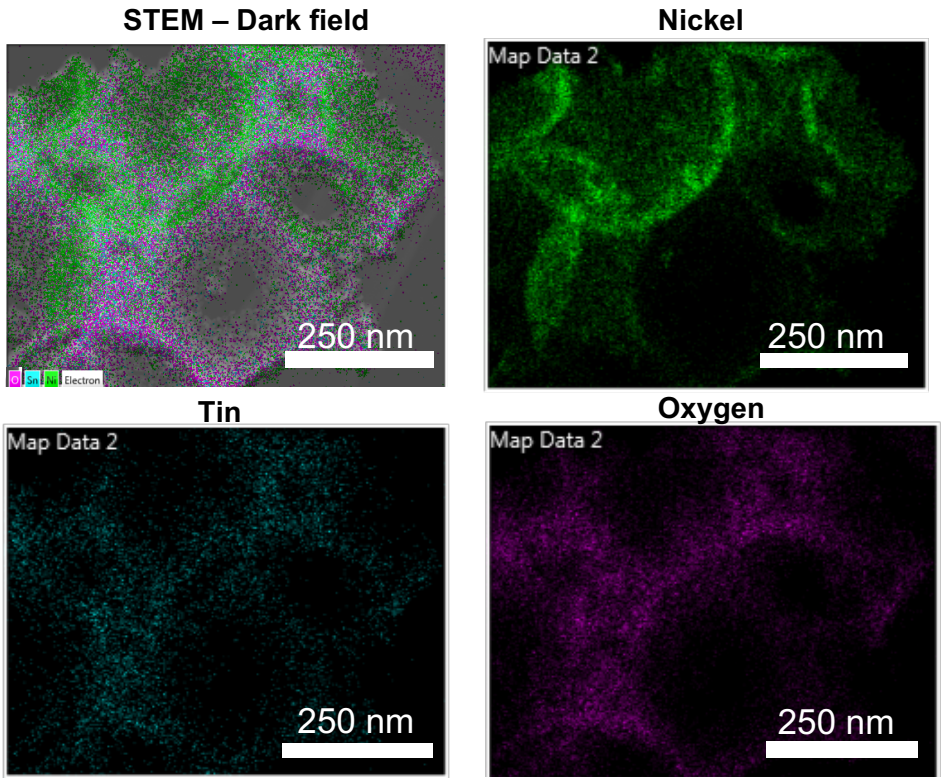


Figure 6.21: STEM/EDX of a 488-nm FTO inverse opal coated with NiO by vertical drop method. Clock-wise, from the top right picture, Nickel, Oxygen, Tin, and the dark field image with the superposition of the three elements.

difficult to be infiltrated. This problem could be tackled with a crack free inverse opal, which presents better and more regular connections, as seen in chapter 5.

The coating with semiconducting molecules could not be done because of time constraints, but with the same reasoning leading to equation 6.5, it can be shown that for the same thickness of coating, the necessary concentration of molecules is lower. This is due to two main effects : firstly, the deposited material is amorphous, which results in a lower density, and secondly, because the molecules are dissolved directly in their final forms, without any additional groups to stabilise them. By taking into account these differences, and by reusing the same notations as previously, equation 6.6 is obtained, where the density of CBP, d_{cbp}, is taken to equal $1.2\,\mathrm{g\,cm^{-3}}$. For simplicity, the volume due to the connections between the pores are neglected in this equation.

$$C_{cbp} = \frac{d_{cbp} V_{cbp}}{V_1} \tag{6.6}$$

The values obtained with this equation are plotted in figure 6.22, for different pore radii. The necessary mass concentration for the molecule is much small than the one for the nickel precursors, due to the effects cited above. It is still large, as a layer of 10 nm theoretically requires 0.1-0.3 g/ml depending on the inverse opal. In addition, contrary to the nickel oxide where the atoms are covalently linked and

cannot be re-dissolved, multiple coatings with a molecule can be problematic, as the solution will dissolve the previously made coating.

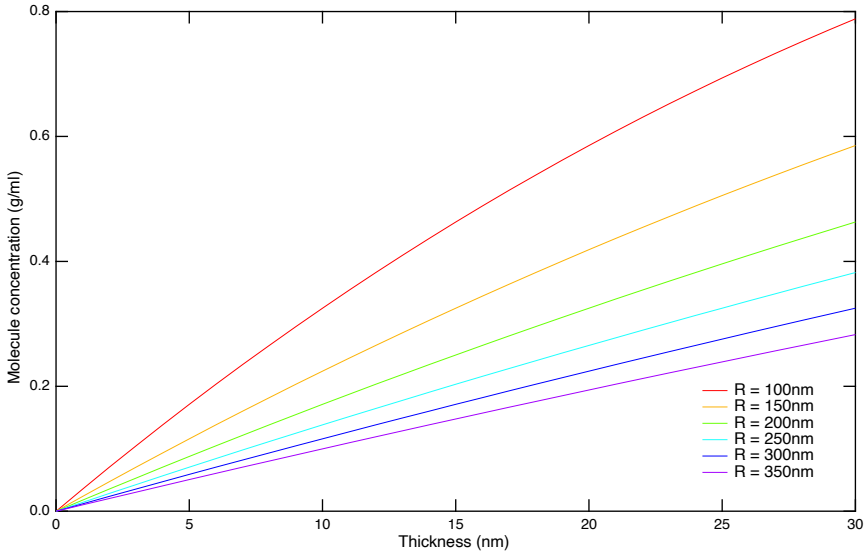


Figure 6.22: Calculated required concentration of CBP to coat the inverse opal to a specified thickness of crystalline CBP, for different inverse opal pore sizes.

6.4 Structure simulation

As a three-dimensional device can be extremely difficult to fabricate, a convenient way to study and design such a device is to use a simulation. As Maxwell's equations are well known, very accurate simulations can be done using specialised software. In this part, two different softwares are used to simulate different features of the wanted device.

6.4.1 Simulation model

Before defining the size of the simulated structure, preliminary work was done to study the fabrication limits of a three dimensional device, in an inverse opal structure. The goal of this work is to calculate the theoretical thickness limits for the films in a three dimensional multilayer structure. Indeed, the film thickness for a conventional device is not limited, as nothing prevents it to be large; however, confined within an inverse opal, space is limited for the films coated on it.

A simple model for opal structure (and the associated inverse opal), is a model using hard spheres, which are non-deformable. In this model, the contacts between the spheres are punctual (single point). The associated inverse opal model is thus composed of air sphere, contacting each other in a punctual way, and so, we can consider them isolated from each other. In this configuration, it is impossible to deposit layers inside the air spheres after the inverse opal formation, and even it it was done by another way, these layers would not be connected to each other.

As we can observe in the opal and inverse opal previously made, the spheres do not behave as in the hard sphere model, and can be deformed. This deformation gives a higher contact area between adjacent spheres, resulting in an inverse opal with connected air spheres. In such a configuration, it is possible to coat the inside of the inverse opal, with a continuous film.

However, the amount of deformation of the polystyrene nanoparticles, creating the connections between of the inverse opal, can vary between samples, depending of the annealing temperature, the size or the materials of the particles. For the wanted calculation, it is then decided to use an extreme case, where the particles are strongly connected, as schematised on figure 6.23, which represents such a structure, with a different cross-section. The scheme on the left of figure 6.23 represents the view of a cutting plane passing by the centre of all the nanoparticles, showing the maximum possible contact between them. In this plan, the particles form a perfect succession of hexagons, with no space between them. If we look at this structure from a slightly higher plane, the contacts decrease, the particles decrease, and space appears between them, until the contact is reduced to a single point between the particles, as shown in the right of the figure.

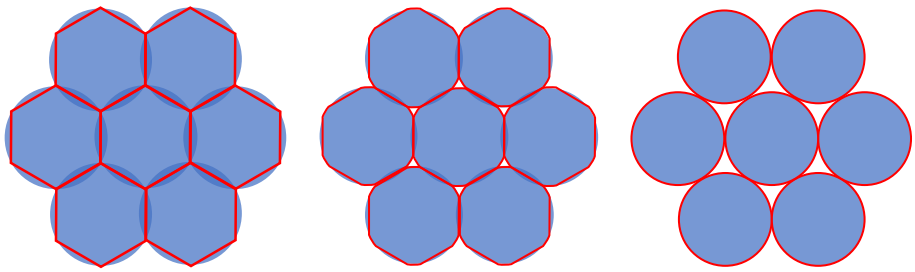


Figure 6.23: Maximum contact model between nanoparticles. Only one layer with seven nanoparticles is represented. *Left :*Plane passing through the centre of the particles. *Middle:* Intermediate plane, showing space between the particles, *Right:* Minimal contact between the particles. The initial spherical form of the nanoparticles is represented, by superposition of colours, and the particles' limits are shown with red lines.

The volume occupied by the spheres in this model is calculated, and is equal to 87.6%, higher than the normal 74% is a standard fcc model with hard spheres. It can be deduced that the corresponding inverse opal occupies only 12.4% of space. It should also be noted that such an inverse opal could not be done in reality for two reasons. Firstly, the infiltration of the precursors can not happen in the structure, as some planes shows no void where the precursor could pass. Secondly, even if such a structure was formed, it would collapse immediately, as some parts of the structure would have a thickness of zero (because of the absence of void between the particles). So we consider this model as an extreme limiting case.

We now calculate the thickness limit of a coating inside this inverse opal. We make the hypothesis that the coating is homogeneous and conformal, meaning that any shape or angles of the inverse opal can be repeated on the coating. Such a coating is represented on the left of figure 6.24, with the inverse opal in grey, and the conformal coating in red. It should be noted that this schematic is represented at an intermediate plane (see figure 6.23) and not at the plane with maximum contact

between the spheres, or else no inverse opal would be seen. The limit thickness for an inverse opal coating can be defined at the thickness for which the air spheres are isolated from each other. When the air spheres become isolated, no further addition of material is possible, as there is no way for the precursors to reach the isolated volumes.

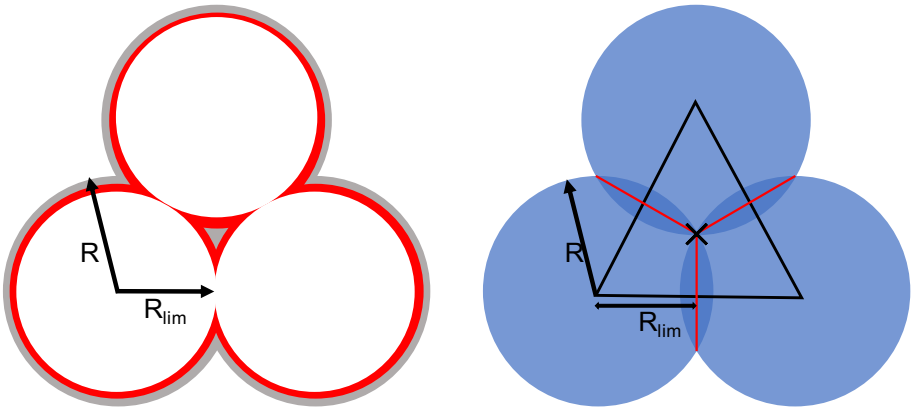


Figure 6.24: *Left:* Inverse opal schematic, associated with a compact opal model. In grey, the inverse opal and in red, a coated layer. *Right:* Packed opal, with an equilateral triangle linking the centres of the spheres, as well as the triangles' centre, at the point where the 3 spheres contact. R is the radius of the initial nanoparticle, and R_{lim} is the radius of the air sphere inside the inverse opal, in the limiting case where the air spheres contacts are punctual.

The coating in red in figure 6.24 is represented with the maximal limit thickness, because the air spheres are only contacting in a punctual way. The radius of the air sphere at this limit is named R_{lim}, while the radius of the air sphere without coating is R. We also define h, as the thickness of the coating, which is equal to $h = R - R_{lim}$. An opal with the same notation is represented on the right of figure 6.24. For this structure, R is simply the initial radius of the nanoparticles, while R_{lim} is half the distance between the centres of two nanoparticles. Because this structure is periodic, the three centres of the particles are equidistant from each other, forming an equilateral triangle, and the contact point between the three particles occurs at the centre of this equilateral triangle.

Each side of the previously defined equilateral triangle measures $2R_{lim}$. With trigonometric consideration, we know that the distance D between any summit of the triangle and its centre, is equal to : $D = \frac{2R_{lim}}{\sqrt{3}}$. However, the distance D is also equal to the radius R of the sphere, as it can be seen on figure 6.24, right. We thus have the equation 6.7.

$$R = \frac{2R_{lim}}{\sqrt{3}} \tag{6.7}$$

The limit of thickness h_{lim} for the coating of this inverse opal is simply given by $R - R_{lim}$, and so, we can now calculate this limit, expressed in equation 6.8.

$$h_{lim} = R(1 - \frac{\sqrt{3}}{2}) \approx R * 0.134 \tag{6.8}$$

This relation can be used to calculate the required radius for the polystyrene nanoparticles, for a desired thickness of device (multilayer coating). For instance, if a device thickness of 60 nm is needed, the required radius for the nanoparticles is around 450 nm, by application of equation 6.8. This formula only gives a rough idea of the connection between the size of the particles and the maximum thickness of the devices, because of the used approximations : ideal compact opal, no change of size during the fabrication of the inverse opal, and an extremely conformal coating of the inverse opal.

However, with this initial approximation, we can notice that relatively big nanoparticles are needed even for small device thickness. With these large particles, the corresponding optical band-gap for an inverse opal is outside of the visible light range, as it can be calculated using equation 1.4. To use this equation, we suppose that a coating with the maximum thickness is applied on the inverse opal, which gives a standard inverse opal with isolated air sphere. The inverse opal matrix and the coating are supposed to have the same refractive index, and so, can be considered as the same material. In these conditions, the part occupied by the air represents 74%, while the part occupied by the high refractive index material is 26%.

Table 6.3: Calculated size of nanoparticles, and spectral location of the bandgap of the corresponding inverse opal, for different coating thickness. The theoretical diameter of the nanoparticles and the location of the optical band-gap are calculated through equation 6.8 and 1.4 respectively. The calculations use an inverse opal made of materials of refractive index n=1 and n=1.9, in an fcc structure.

Coating thickness (nm)	Nanoparticle diameter (nm)	Predicted band gap location (nm)
20	298	629
40	597	1258
60	896	1886
80	1194	2515
100	1493	3144

Calculated values of the needed nanoparticles size and the corresponding band gaps of the inverse opal, depending of the required coated thickness, are indicated table 6.3. It can be seen that with the exception of a device of 20 nm, with band-gap around 629 nm, any thickness more important than this has a band-gap in the infrared. A solution could be to use an extra thin device of 20 nm or less, but where the device is composed of many layers. Each of these layers would be so thin that parasitic effects, such as quantum tunnelling, might appear.

6.4.2 Band-gap analysis

Instead of using the first band-gap of the inverse opal, it is more convenient to use the effect of a band-gap with a higher order, which interacts with high frequency, and thus, lower wavelengths. As the formula derived from the Bragg law is only an approximation, the higher order band-gaps are calculated with the MIT photonic band-gap (MPB) software package. The required parameters for the software are briefly described hereafter, and the full code is given in appendix D.

MPB requires the description of the unit cell, as well as the crystal vectors, in order to fully describe the crystal. For our simulation, we suppose that the inverse opal is coated with the maximum thickness possible, with the same material as the matrix, which actually makes this structure a standard fcc inverse opal, with isolated air spheres. A face centred cubic structure can be defined with a single element, which is then repeated on the three following vectors, $(1,1,0),(1,0,1)$ and $(0,1,1)$ (the coordinates are expressed from an orthonormal system). We thus define our structure with a unit cell composed of a block of material, with an air sphere inside of it, and by the three vectors previously described. By convention an analogy with crystallography, the three vectors are given a size of $\frac{1}{\sqrt{2}}$, to give a size of one to the elementary cell.

The MPB software solves the master equation 1.10 for selected k values, and for a defined number of modes. The k values are interpolated on some selected axes of the Brillouin zone, XU, UL, $L\Gamma$, ΓX, XW and WK, with 12 points per axis. To detect the position of the high-order band-gaps, 15 modes are calculated for each point.

The result of the simulation is presented in figure 6.25, where the horizontal axis represents the considered axes of the Brillouin zone, while the vertical one represents the frequency of the modes, in a dimensionless unit. Each one of the red curves represents a mode, going from 1 to 15, from bottom to top.

The main axis of interest for this work is the ΓL axis, which represents the normal direction to the [111] plane. The partial band-gaps on this axis are highlighted in blue in figure 6.25. Over the fifteen calculated modes, three band-gaps are detected, with the first one, at the lowest frequency, corresponding to the band-gaps previously calculated in table 6.3.

Two band gaps of higher order are detected at higher frequencies, on the $L\Gamma$ axis. The corresponding wavelengths, for an inverse opal with a pore size of 597 nm and a refractive index of 1.9, are summarised in table 6.4. The first band-gap, from 1141nm to 1308nm, is corresponding well with the value obtained with the modified Bragg law (1258nm). The two other band gaps are within the optical range, and can thus be used for creating optical cavities for an OLED. However, these band gaps have an extremely small width, of 4nm and 7nm for the second and third order respectively, limiting their efficiency.

To have a more accurate idea of the optical properties of the coated inverse opal, another simulation is performed on MPB, using a simplified model with only

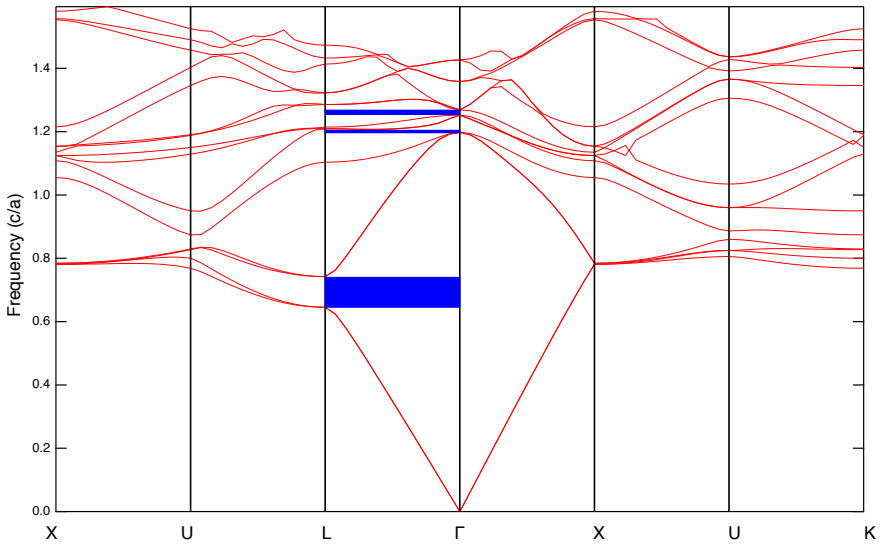


Figure 6.25: Optical band diagram of an inverse opal, made of air (n=1) and a material with refractive index n=1.9, simulated with MPB. The 15 first bands are represented. The partial band-gaps on the ΓL direction are highlighted in blue.

Table 6.4: Optical band-gap frequencies measured from figure 6.24, and their corresponding wavelengths, for an inverse opal whose pores are 597 nm in diameter.

Band-gap	Dimensionless frequencies	Optical band-gap (nm)
First band-gap	0.646 to 0.740	1308 to 1141
Second band-gap	1.197 to 1.204	705 to 701
Third band-gap	1.255 to 1.268	673 to 666

one coating layer. This new layer is chosen to have a high refractive index of 2.5, to represent the active layer. In this new model, the FTO inverse opal is supposed to be made from fully connected nanoparticles, as described section 6.4.1. The coating thickness is the one calculated by equation 6.8, to have the maximal thickness possible. The final diameter of the air sphere is 597nm, the same as the previous simulation.

The optical properties of the coated inverse opal are extremely similar to the ones of the standard inverse opal, for the same pore size (figure 6.26 and table 6.5). The very similar properties between the two structures can be explained by the small thickness of the coating (40nm), compared to the pore diameter of 597nm. Secondly, for the frequencies close to the band-gap, the fields are concentrated either inside the high or inside the low refractive index material. For this reason, the coating layer which acts as the frontier between these two materials, does not greatly affect the band-gap's position.

The previous simulations show that both for the uncoated and the coated inverse opal, the high-order optical band gaps have a very small spectral width, and thus cannot be used for an optical cavity. In order to have better optical effects, the contrast between the high- and the low-refractive-index materials has to be

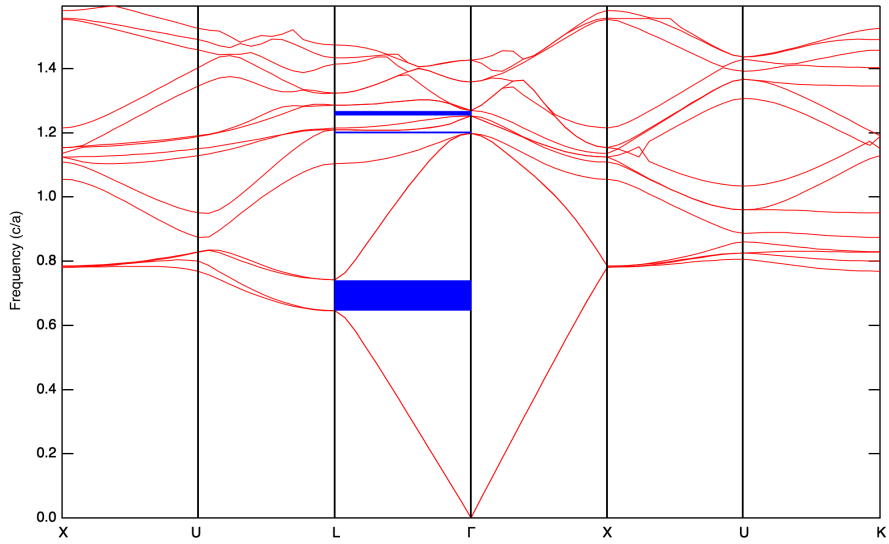


Figure 6.26: Optical band diagram of an inverse opal made of air (n=1), with a core material with a refractive index n=1.9, coated with a material with refractive index n=2.5, simulated with MPB. The coating's thickness is calculated according to equation 6.8. The first 15 bands are represented. The partial band-gaps on the ΓL direction are highlighted in blue

Table 6.5: Optical band-gap frequencies measured from figure 6.26, and their corresponding wavelengths, for a coated inverse opal with a pore size of 597 nm.

Band-gap	Dimensionless frequencies	Optical band-gap (nm)
First band-gap	0.647 to 0.739	1305 to 1142
Second band-gap	1.199 to 1.203	704 to 702
Third band-gap	1.255 to 1.266	673 to 667

increased. The only way to do so is to increase the refractive index of the material composing the inverse opal. The optical characteristics of a coated structure, with a coating material having a refractive index of 2.2, are presented in figure 6.27, and the corresponding band-gaps in table 6.6.

Table 6.6: Optical band-gap frequencies measured from figure 6.27, and their corresponding wavelengths, for a 597nm diameter pore size inverse opal.

Band-gap	Dimensionless frequencies	Optical band-gap (nm)
First band-gap	0.550 to 0.662	1535 to 1275
Second band-gap	0.972 to 0.998	869 to 846
Third band-gap	1.036 to 1.105	815 to 764

Due to the increase in the effective refractive index of the inverse opal, the band gap positions are red-shifted, which is consistent with the modified Bragg equation 1.4. The frequency width of the second and third optical band gap is greatly increased, from 4nm to 43nm for the former, and from 7nm to 51nm for the latter. Due to the red shifting, the second optical band gap now lies in the infrared,

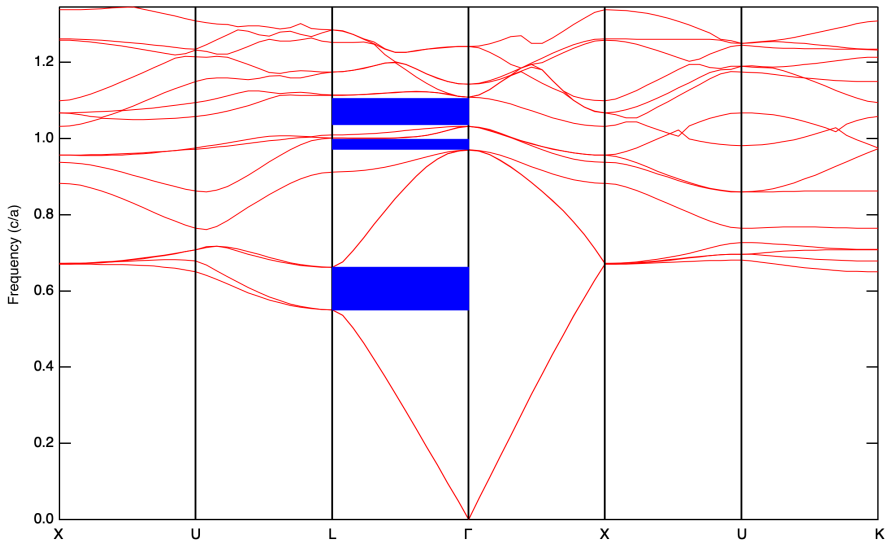


Figure 6.27: Optical band diagram of an inverse opal made of air (n=1), with a core material whose refractive index n=2.2, simulated with MPB. The 15 first bands are represented. The partial band-gaps on the ΓL direction are highlighted in blue.

but a substantial fraction of the third one still covers the visible range.

In conclusion for this section, due to the limitations of the possible coating thickness inside an inverse opal, the size of the pores used in this thesis need to be increased to allow a coating of at least 40nm, which is defined as the minimum device thickness. This increase in the size of the inverse opal red-shifts the position of the first optical band-gap into the infrared, and thus higher order optical band-gaps need to be used for visible light. Both for coated and uncoated structures, the second and third optical band-gap of a 597nm pores FTO ($n = 1.9$) inverse opal, are in the visible range. However, the width of these band-gaps is extremely small, limiting their utility real-world devices, due to possible irregularities in the structure. In addition, a very thick structure is needed to create an optical cavity.

One way to increase the width of the higher-order optical band-gaps is to increase the refractive index of the inverse opal's material. When a material with n=2.2 is used, the width of the OBGs are greatly increased, allowing the possible creation of an optical cavity in a device. However, only a few chemical systems provide transparent conductive oxides with high refractive indices, and a compromise needs to be found between the required refractive index, and the other required properties of the material.

6.4.3 FDTD model

The simulations made with MPB gives information about the band-gap position of the inverse opal depending on the size of the pores, for an infinite structure. However, it does not predict the degree of extinction of the waves inside the structure, or other information related to finite, real-life devices. To do so, finite

difference time domain (FTDT) is employed, with the MEEP software.

Just like MPB, the user needs to give information to the software, concerning the device structure, and also the experimental conditions. MPB only requires a unit cell description as well as the "crystal" vectors, as it considers only infinite periodic structures. The definition of a structure with MEEP consists in the definition of all the individuals elements of the structure, one by one. In other words, the refractive index for every point in a three dimensional space has to be specified. Standard geometric forms, such as a sphere or a block are used to define the structure. In addition, as the structure is finite, boundary conditions have to be defined on the edges of the simulated structure. The details of the choices for the boundaries and the structured parameters chosen for this work are given below.

The simulation is made within a three-dimensional volume, which is a rectangular cuboid (a cube where each dimension can be different), where the three dimensions can be freely choose. The origin of coordinates $(0, 0, 0)$ is defined as the centre of the cuboid. During the definition of the structure, some points outside of the volume can de described with a certain refractive index, but they are ignored for the simulation. For instance, a sphere whose centre is located on one of the faces of the cuboid, has half of its volume inside the simulated domain, and the other half outside.

The starting point for building the previous FTO inverse opal is a substrate made of glass, with a thin layer of FTO on top. This is replicated in the simulation by the creation of a thick block of material with a refractive index of 1.5 with a thin block of 100nm of a material with refractive index 1.9. These two blocks represents glass and FTO respectively. As previously said, only simple elements can be used to describe the structure, and because an inverse opal is made of complex shapes, it cannot be described in one step. However, a useful feature of MEEP's structural description is that, if a point has different values of refractive index attributed to it, only the last one is used, i.e. the last given information supersedes all the others.

Exploiting this feature, the inverse opal is described by firstly defining a block of material with $n = 1.9$, followed by the addition of spheres with $n = 1$, at the coordinates corresponding to an fcc crystal, as represented in figure 6.28. The structure is then finalised by defining a block of material with $n = 1$ on top of the structure, representing air. All the parameters chosen for the simulation can be modified, such as the diameter of the air sphere, the number of layers, or the refractive index of any particular volume. The thickness of the FTO block where the air spheres are located, is chosen so that the top layer is "cut" in half, as in figure 6.28.

The positions of the spheres with $n = 1$, have to be carefully chosen to be in an fcc configuration. It is considered for simplicity that the air spheres only touch each other in a punctual way. With this assumption and trigonometric considerations, the coordinates of the spheres can be calculated, layer by layer. A schematic of a hexagonal packing is represented in figure 6.29 *a)*, with the coordinates of the centre of each sphere described in part *c)* of the same figure. With these coordinates, and by using the spatial periodicity and symmetry of the fcc structure, the

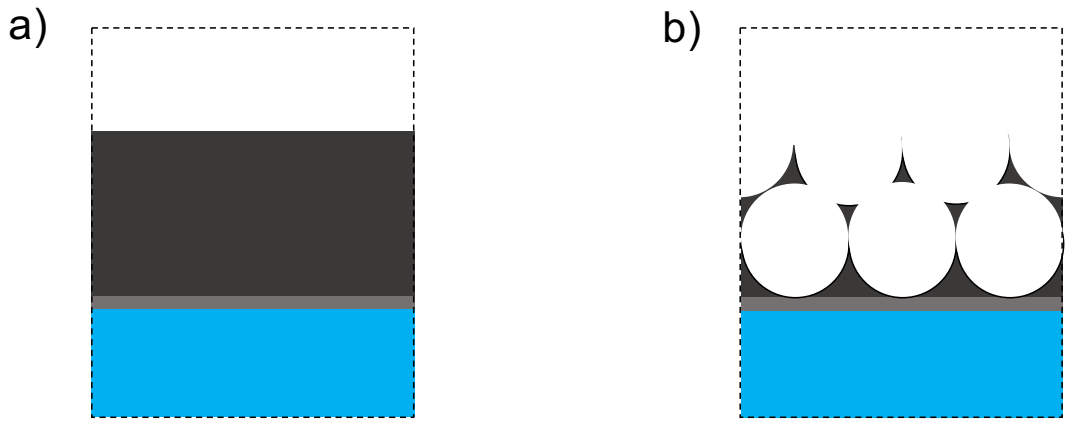


Figure 6.28: (*a*) Initial step for the inverse-opal model's creation, from bottom to top: a block of glass (blue), a block of FTO representing the initial thin film (light grey) and a second block of FTO representing the inverse opal. (*b*) Addition of air spheres within the second layer of FTO.

position of all spheres can be calculated. The second layer of the structure is also in a hexagonal organisation, but shifted compared to the first one. This shift can occur in several directions, but is chosen to be on the X axis for this model, as represented 6.29 *a)*, where the red dots represent the centres of the second layer spheres. In this configuration, the centres of the spheres shift at $D\frac{-1}{\sqrt{3}}$ on the X axis. The distance between two planes of particles is calculated as being $D\frac{\sqrt{2}}{\sqrt{3}}$, with D the diameter of the spheres. The coordinates of the second plane of nanoparticles can thus be deduced from the first one, by doing a translation of vector $(D\frac{-1}{\sqrt{3}}, 0, D\frac{\sqrt{2}}{\sqrt{3}})$, which is represented in figure 6.29 *d)*. For the same reasons, every layer of coordinates can be deduced from the previous one.

Concerning the boundaries conditions, MEEP allows three choices : a perfect metal layer, with a perfect reflection for all wavelengths, a perfectly matched layer (PML) which is an ideal material absorbing all incoming waves with zero reflection, and Bloch conditions, described hereafter. If Bloch conditions are chosen for one face of the simulated volume, the opposite face must also have Bloch conditions, i.e. periodic boundary conditions. In this configuration, the values of the two faces are identical, which creates a continuity in the structure. For instance, if a wave is going to the $+X$ face, and Bloch conditions are applied, the wave pass through the $+X$ face and re-appears at the $-X$ face. The Bloch conditions do not "terminate" the structure, contrary to the metal and PML layer, but instead creates an infinite periodicity in the chosen directions.

As an ideal inverse opal film is periodic in two directions, it is thus decided to use Bloch conditions for the X and Y directions. This choice requires a well chosen size for the simulation volume, to avoid discontinuities from one face to another. With a structure oriented as in figure 6.29, the size of the structure has to be $k_1 D\sqrt{3}$ for the X direction, and $k_2 D$ for the Y direction, with k_1 and k_2 two integers which can be different.

The electromagnetic waves going to the top of the simulation are equivalent

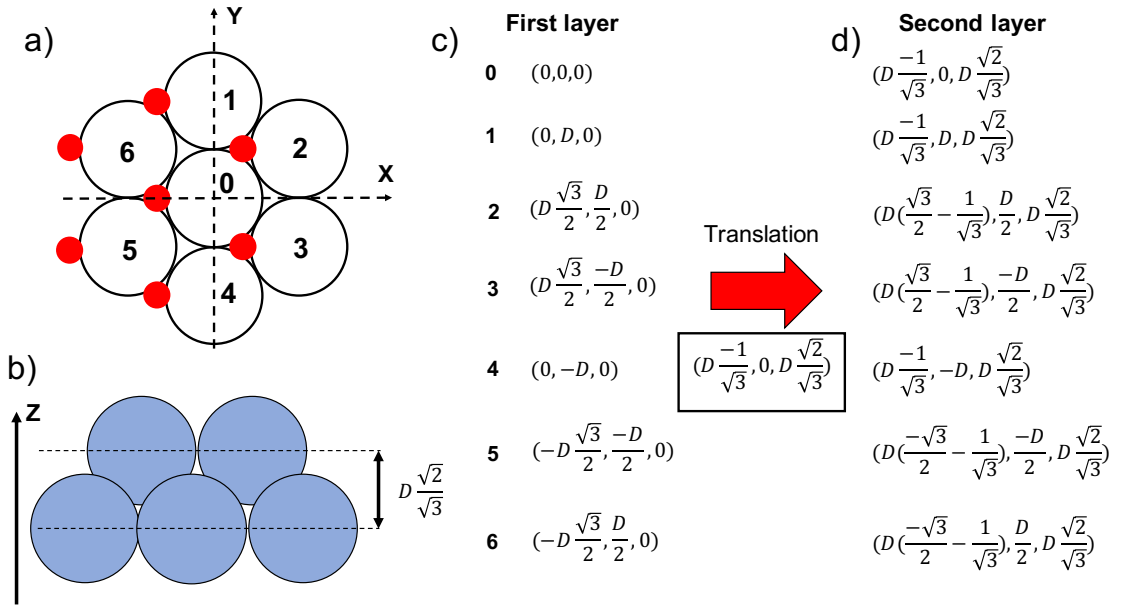


Figure 6.29: (a) Hexagonal packing of seven particles, with an orthogonal axis centred on the middle particle. The red dots represents the position of the nanoparticles of the second layer. (b) Vertical distance between the centres of the nanoparticles from two different levels. (c) Coordinates of the nanoparticles represented in (a), depending of their diameter D. (d) Coordinates of the second layer of nanoparticles, obtained by a translation from the first layer coordinates.

to waves leaving the device, and not interacting anymore with it. The same is true for waves going to the bottom of the structure, which are waves going to the thick glass substrate, and not coming back, if we neglect the reflections from the other side of the substrate. For these reasons, PML layers are chosen for the top and bottom part of the simulation, to absorb all the electromagnetic waves coming out of the simulated structure.

To study the optical characteristics of a structure, two possibles excitations are possible with MEEP. The first possibility is to use a monochromatic wave, emitted from either a point, a line, or a surface. The wave is emitted for an infinite duration, and its progression through the structure can be analysed, by looking at the value of the electric field inside the structure. The other possibility is to simulate a whole set of wavelengths, by the emission of a pulse of a finite duration. As the Fourier transformation of a pulse contains different frequencies, many of them can be analysed at one time with a well chosen pulse. The pulse energy can be analysed, with the calculation of a Poynting vector on a surface specified by the user. By measuring the energy of the pulse with and without the structure, one can see the impact of the structure on a wide range of frequencies. A summary of the simulated inverse opal, where the various boundaries and the locations of the waves' source and detector, are represented figure 6.30.

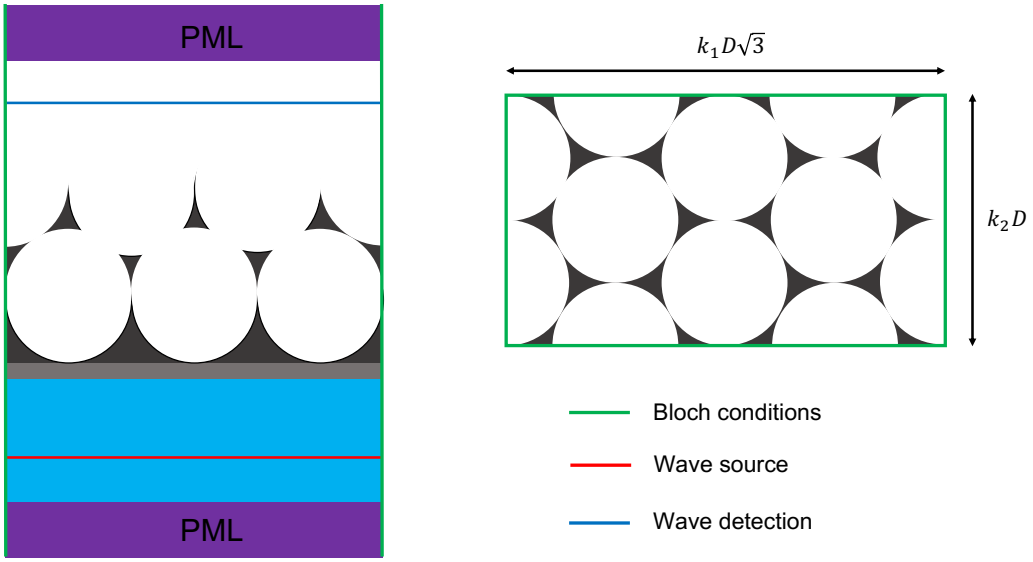


Figure 6.30: *Left :* Schematic of the as-developed inverse opal model. Periodic Bloch boundary conditions are applied for the lateral faces, while perfectly matched layers (PML) are used for the bottom and top faces. The wave source is below the inverse opal (red line) and the wave detector is above it (blue line). *Right :* Model seen from top, with the size requirements for the x and y faces. k_1 and $_2$ are positive integers, which can be different.

6.4.4 FDTD results

The three-dimensional FDTD model code is presented in Appendix E. A common way to assess the validity of the model, is to extract the three-dimensional dielectric constant. A common way to visualise a three-dimensional structure is to slice it into dimensional planes, at different locations. Three slices on the x , y and z axis, and passing through the centres of the pores, are presented in figures 6.31, *a)* , *b)* and *c)*, respectively. In comparison, slices not passing through the pores' centres are also presented (figure 6.31, *d)* , *e)* and *f)*). The colours on the figures represent different values of the refractive index.

As it can be seen, the structure of an ideal inverse opal with punctual contact between the pores is well represented. A clear contact is present between the glass and the FTO layer, and a thin film of FTO is present on the glass, to represented the FTO pre deposited on the glass substrate. The size of the simulation cell makes the structure perfectly periodic, which allows the simulation of an infinite inverse opal, in the xy plan. Different colours, i.e. different refractive indices, are visible within the inverse opal, particularly figure 6.31 *f)*. These variations of refractive index are due to the discretisation of the structure, which implies an averaging of the refractive index for the lattices at the frontier between two different materials. The blue layer on the bottom of the structure, is the PML, which has a refractive index of 1 for this representation. A top PML is also present, but cannot be seen at it has the same refractive index as air.

As previously described, the simulation is done by sending a pulse of waves

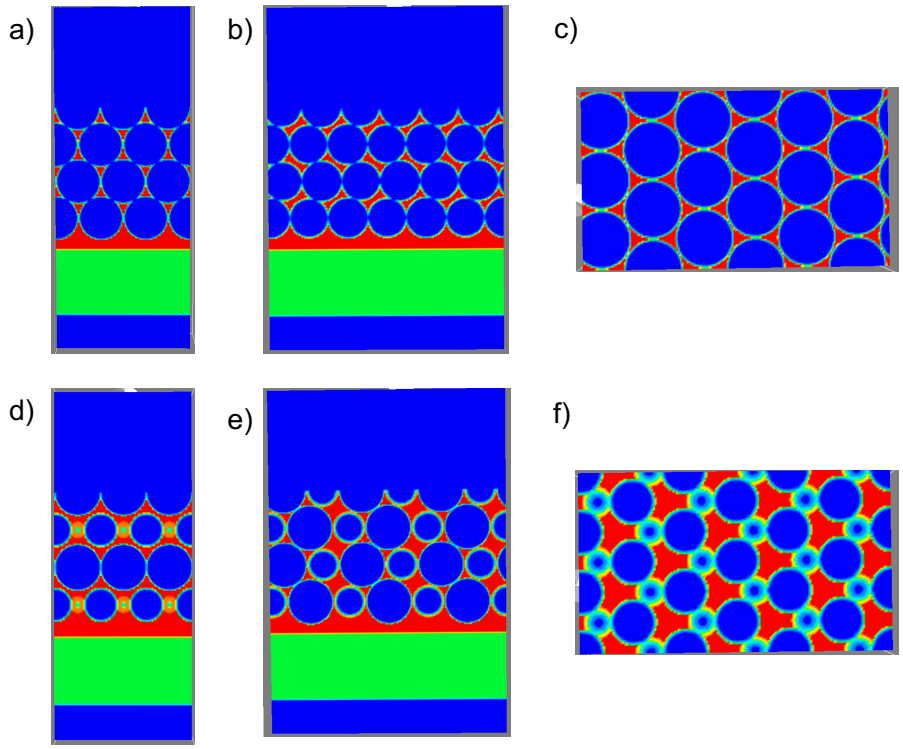


Figure 6.31: Slices of the three-dimensional dielectric constant model, passing by the centre of the pores (top row) and off-centre of the pores (bottom row). The slices are through the x axis (*a* and *d*), the y axis (*b* and *e*) and the z axis (*c* and *e*).

to the structure, and to measure their intensity after they have passed through it. By applying a Fourier transform to decompose the frequencies of the received pulse, the interaction of the structure within a certain range of wavelengths can be deduced. Different criteria can be used to end the simulation. With this pulse analysis, a well chosen criterion is to stop the simulation when the measured intensity of the pulse becomes very small, meaning that most of the pulse passed through the structure. More precisely, the simulation stops when the ratio of the current measured intensity divided by the highest one, becomes smaller than a chosen threshold, chosen at 10^{-9} in our case.

An intriguing effect is observed when the previously described ratio is measured. On the first phase of the simulation, the ratio is normally decreasing in a regular way. However, when a certain time is reached, the ratio does not decrease anymore, but increases instead, until it reaches the value of one (figure 6.32 *a*). In this case, the simulation stops when the time limit of 72 hours is reached. The stagnation at one of the ratio is due to the fact that the measured intensity is also the highest one at that moment. A more insightful way to figure out what happens in the simulation, is to plot the absolute measured intensity, represented in figure 6.32 *b*. After an initial decrease, the intensity exponentially grows with the iterations, reaching very large values at the end of the simulation. This continual increase of the intensity, long after the initial pulse source has been turned off, reveals a problem with the simulation and the established model.

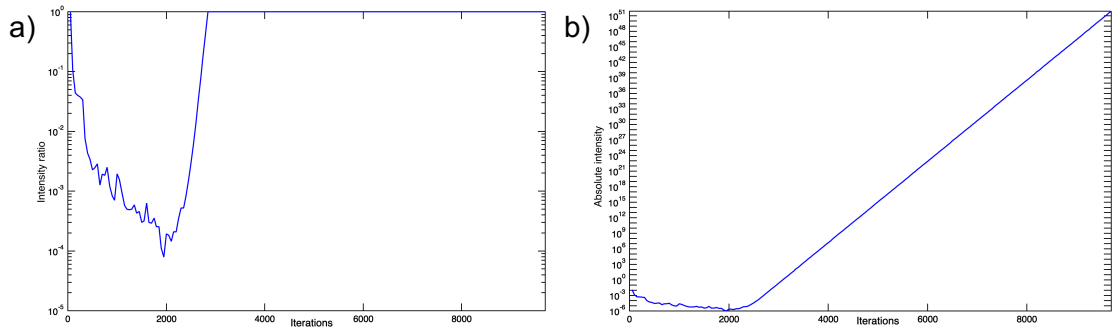


Figure 6.32: *a)* Ratio of measured intensity on maximal intensity, and *b)* measured intensity only, for each step of a non-converging simulation.

To solve this problem, many parameters of the simulations has been changed, and are listed hereafter.

- Increase of the 3D model resolution. A decrease of each lattice individual size reduces the error due to the discretisation. However, an increase by two of the resolution, increasing the simulation time by 16 (factor two for each of the dimension, plus a factor two for the time step, linked to the spatial resolution).
- Decrease of the Courant factor. As previously said, the time step is calculated from the spatial resolution, and both are linked with the Courant factor. This factor, initially at 0.5, should not be increased to avoid the simulation becoming unstable, but can be reduced to improve its accuracy, at the cost of a longer required simulation time.
- Increase of the PML layer. To avoid any non-absorbed light which would parasite the simulations, the absorbing layers can be increased, as the cost of an increased required computing power.
- Use of a supercell. Increase of the k_1 and $_2$ integers described figure 6.30
- Change of the time for the pulse source emission. A slower emission prevents the apparition of unwanted high frequencies, but increases the time of the simulation.
- Increases of the distance between the source and the inverse opal, and same with the detector. A source (or detector) too close from a structure, can be influenced by the optical density of states.

Although these modifications impact the results of the simulation, none of them, individually or in combination with others, succeed to provide a converging simulation. To explain the continual increase of the measured intensity, it is hypothesised that not all the energy from the initial emitted pulse is absorbed by the PML layers. As explained on the MEEP website, the absorption of the PML is not perfect when the beams are not perpendicular to it. In an extreme case, there is no absorption when the electromagnetic fields propagate in a parallel direction to the PML. Due to the large size of the pores of the inverse opal, a diffraction phenomenon

appears for the transmitted light, as well as for the light within the structure. A small portion of the light is hypothesised to be diffracted at angles of approximately 90°, parallel to the PML.

This phenomenon would appear for a real design as well. However, due to the Bloch boundary conditions used in the model, the waves diffracted at 90° in one direction (right or left), re-appear on the opposite side of the model. Because these waves are not absorbed by the PML, they are permanently existing in the model, and their energy is counted at every step, increasing the measured intensity. In addition, the Bloch boundaries conditions can create a phase problem for the waves travelling in the parallel directions. The phase of the waves has to be exactly the same for the opposites faces of the model, but taking into account the wavelength, the refractive index and the size of the cell, this condition can only be achieved for a small number of frequencies. For the other frequencies, the simulation might not be stable, leading to un-physical fields with large values. This effect increases even more the accumulation of energy, preventing a convergence of the simulation.

In order to absorb the parallel waves, another boundary condition is used, with an absorber layer instead of a perfectly matched layer. Despite possible reflections at the interface, this layer provides a greater absorption for all kind of incoming electromagnetic fields. By using this layer, with the same thickness as the PML, the ratio of measured intensity appears to slowly decrease, until it reaches the wanted target (10^{-9} in the given example) 6.33. The small increase of the measured intensity at approximately 1500 iterations is attributed to the slow light effect, with lights at precise frequencies, takes longer to pass through the structure, and are thus detected later.

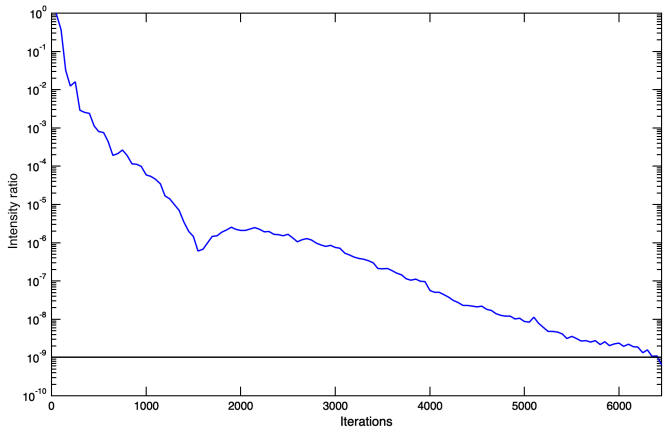


Figure 6.33: Ratio of measured intensity on maximal intensity for a converging simulation, stopped when it reaches the specified target of 10^{-9} (indicated with a horizontal line).

To characterise different sizes of inverse-opal structures, a set of 8 simulations are made each time, with the pore size of the structure going from 270 nm to 340 nm, by step of 10 nm. A inverse opal with 5 layers is used, made with a material with a refractive index of 2.2. A single unit cell is used, with $k_1 = 1$ and $k_2 = 1$ according to figure 6.30, to reduce the size of the simulation. A range of wavelengths from 600 nm to 1000 nm is used, to cover the two expected partial

band-gaps. The target for this set of simulation is 10^{-7}, to allow a fast convergence (taking approximately one day) for all the different structures.

As previously discussed, a wide range of wavelengths are analysed by sending a pulse inside the structure, and performing a Fourier transform on the result. However, the obtained results do not have the same intensities for all the frequencies, as can be seen in figure 6.34 *a)*, which is obtained by sending a pulse through air, with no structures present, and figure 6.34 *b)*, obtained with an inverse opal with a pore size of 270 nm. The resulting intensities are much smaller on the extremities of the considered range of wavelengths. In order to have comparable intensities over the whole range of wavelengths, the measured intensities have to be normalised, which is done by diving the intensities obtained in a simulation of the wanted configuration, by the intensities obtained in a simulation of a configuration with exactly the same dimensions, but without any structure. In other words, the intensities shown figure 6.34 *b)* are divided by the ones of figure 6.34 *a)*. The result of this normalisation is shown 6.34 *c)*, and a more homogeneous intensity for the whole range of wavelengths is observed. This normalisation is repeated for all the obtained spectra.

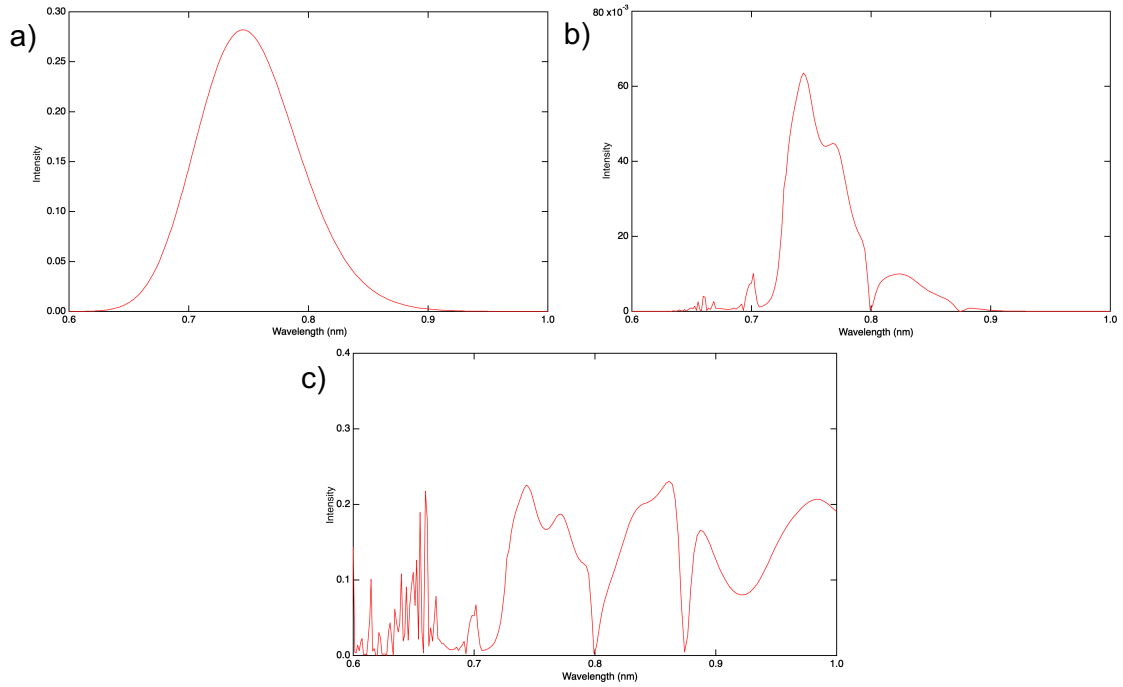


Figure 6.34: Spectral intensity of the transmitted waves for a simulation (a) without any structure and (b) with the presence of an inverse opal cell. *c)* Normalisation of the spectra measured with the presence of the inverse opal, by the one obtained with an empty cell.

The normalised spectra obtained by varying the inverse opal pore size are presented figure 6.35, with the pore size increasing from top to bottom. The first observation that can be made is that the left of the spectra are noisier than the rest, and the range of the noisy part increases with increasing size of the pores. As this effect appears to be dominant for smaller wavelength and large pore sizes, it is hypothesised that it is due to diffraction within the inverse opal. Due to the many layers present in the structure, the shorter wavelengths are diffracted into many different directions, making their interpretation difficult.

On the other side of the figure some dips in the curves can be observed, and vary with the pore size, as indicated by the dashed lines. According to the study made on MPB for an inverse opal made with material with refractive index 2.2, two of the observed dips can be identified as being due to optical band-gaps. These two dips are indicated on figure 6.35 with black dashed lines. According to figure 6.27 and table 6.6, the first dip at shorter wavelengths is identified as being the third optical band-gap in the [111] direction, while the second dip is the second optical band-gap in the same direction. As anticipated by the mode solver MPB, the third bandgap has a larger range than the second one, which is confirmed by the analysis with MEEP. A third dip, indicated with a green dashed line, is observed at higher wavelength for the inverse opals with pore sizes radius inferior to 300nm. This dip cannot be identified as an optical bandgap in the [111] direction. It is hypothesised that it is due to a bandgap in another direction, but whose effect is visible due to diffraction within the inverse opal. According to figure 6.27, a possible band-gap could be the one in the XU direction, whose frequency is just below the one of the second bandgap. However, no formal investigation has been made to prove this hypothesis.

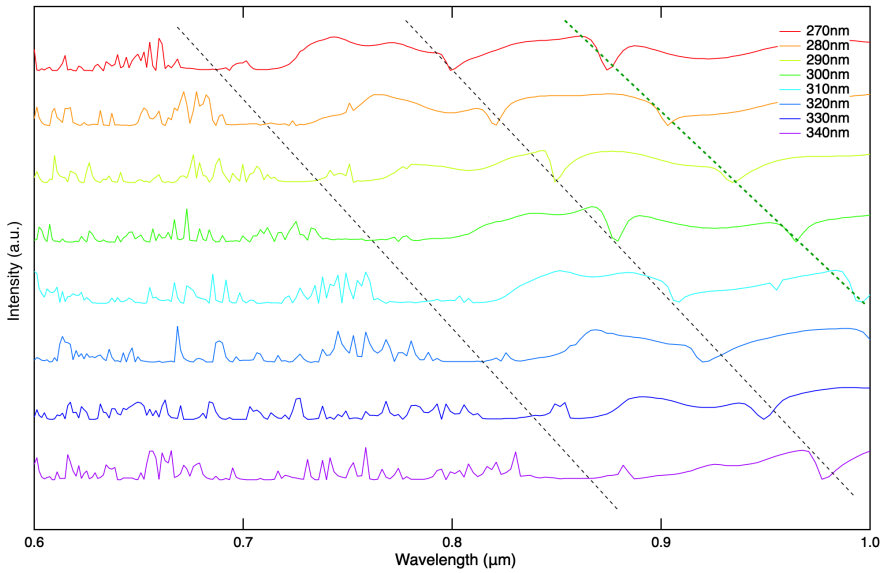


Figure 6.35: Normalised transmitted spectrum for a 5 layers inverse opal made of a n=2.2 dielectric material, for 8 different pore sizes, ranging from 270 nm (*top*) to 340 nm (*bottom*) in steps of 10 nm. The two band-gaps predicted by the mode solver are indicated with black dashed lines, and a third non-identified dip in the transmission spectra is indicated with a green dashed line.

To confirm the origin of the observed artefacts in the measurements, new calculations are done with a different target, increasing the accuracy but also the required computing time. The new target is 10^{-9}, a hundred times smaller that the one previously used. The comparison between the transmitted spectrum of a structure with a pores size of 340nm and a target of 10^{-7}, and one with a target of 10^{-9} is presented figure 6.36. As observed, both spectra are perfectly similar, even for the noisy part, indicating that the sharp peaks do not come from a lack of accuracy in the simulation.

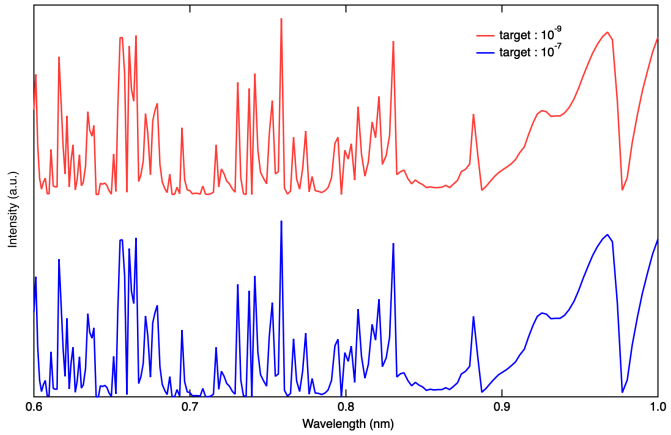


Figure 6.36: Normalised transmitted spectrum for an inverse opal with pore sizes of 340nm, with a convergence target of 10^{-9} (*top*) and of 10^{-7} (*bottom*).

The increase of accuracy indicates that the origin of the sharp peaks are due to an incomplete model. To fully understand their origins, the reflectance spectrum should also be measured, to assess that the sum of reflectance and transmittance is equal to one. The measure of the reflectance spectrum should be taken with care, as the source can interfere with this measurement. Additional experiments can include the variation of the distance between the inverse opal and the measurement plan, and the reduction of the reflection by the absorber layer, what requires a more in-depth study of its mechanism.

As previously seen, the optical characteristics of an inverse opal with large pores have been computed, although its interpretation can be delicate, both due to the large amount of diffraction within the structure, and the multiple optical band-gaps in different directions. In spite of these difficulties, the two expected high order band-gaps could be detected for different pore sizes of inverse opals.

6.4.5 Three-dimensional multilayer coating model

To finish this chapter, the protocol to make a multicoated inverse opal model is explained. The model of inverse opal with maximal connection between the pores is used, just like in part 6.4.1. As previously calculated, the theoretical limit for the coating of such of model is described with equation 6.8, and at this limit the air spheres composing the coated inverse are isolated.

To create multiple coatings, the fact that during the model definition, new refractive indices replace old ones is used, in the same way the inverse opal is defined, by adding air spheres inside a block of FTO material. This time, after the creation of an FTO block, spheres corresponding to the first coating are firstly added to the model. These spheres overlap each other due to their greater diameters than those of the air spheres. After this, slightly smaller spheres representing the second coating, centred on the same points as the previous ones, are added to the model. This procedure is repeated with as many spheres as needed, and is terminated with the addition of air spheres to the model, whose radius is chosen to only have a punctual

contact between the pores. This whole procedure is described in figure 6.37, for a single coating layer. Due to the model used for the inverse opal, with a maximal connection between the initial pores, its core is barely visible on this model.

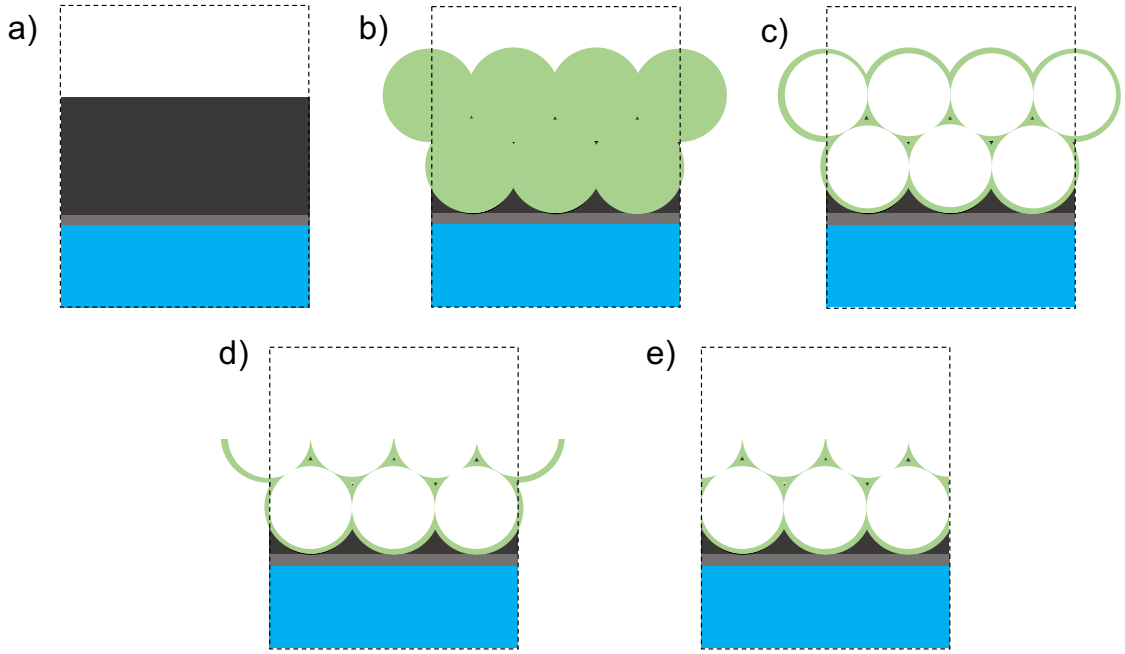


Figure 6.37: Bilayer inverse opal model creation. (a) Initial configuration, with a block of glass (in blue) a block of FTO representing the initial thin film (in light grey) and a second block of FTO (in dark grey). (b) Addition of nickel oxide spheres, centred on the standard coordinates, with greater radii than the final those of the pores, making the spheres overlap. (c) Addition of air spheres, placed within each of the nickel oxide spheres, with a radius corresponding to the final pore size. (d) Creation of open hemisphere on top of the inverse opal, with the addition of a block of air. (d) Final model, as the features outside the defined cell are removed by the simulations' boundary conditions.

Due to time constrains and convergence problems, no successful simulations could be obtained for the inverse opal with multilayer coatings. In order to simulate the stimulated emission, a material with a negative absorption is envisaged, which would increase the fields amplitude passing through it.

6.5 Conclusions

In this chapter the idea and concept of a three dimensional OLED are discussed. The goal for such a structure is to create an optical cavity within the device itself to sharpen the emission spectrum. The organisation of the layers is chosen in the same way as a conventional emissive device, with an active layer sandwiched between an electron and a hole transport layer, and two electrodes at the extremities of the device. Because all the layers will strongly interact with light, they all have to be transparent, including the electrodes. For fabrication purposes, the following architecture is chosen, from the core of the inverse opal to the air : fluorine tin

oxide (electrode), nickel oxide (hole transport layer), host molecule/Ir(piq)2(acac) (active layer), zinc oxide (electron transport layer) and aluminium doped zinc oxide (electrode).

Prior to the three dimensional device fabrication, a standard flat device is made with the previously described architecture in order to check the compatibility of the materials and the deposition methods. Because of the annealing done during the ALD steps, the organic layer can crystallise if its glass transition temperature is too low, leading to the creation of holes in the layer. To avoid this effect, the molecule BcZPH is used as a host for the organic layer. Due to its higher glass transition temperature of 100 °C, the film stays continuous after an annealing at 95 °C. No penetration of the organic layer by the ALD deposited materials is observed, assuring a good layer formation on top of the active layer. However, the adhesion of the active layer on both the hole and the electron transport layer is weak, as delamination of these layers is readily observed. Due to time constraints these devices could not be electrically or optically tested.

In order to conformally deposit materials which cannot be deposited by ALD inside the inverse opal, a solution method has been established. The challenges for this deposition are the absence of an overlayer on top of the structure, and a homogeneous deposition within the inverse opal. The major difference with a standard sol-gel deposition is that, to coat the inside of the inverse opal, all the necessary precursors needs to be already inside the structure, which requires a very high concentration. The developed method consists of dropping a small amount of a highly concentrated solution on a vertically oriented sample. To avoid the accumulation of solution at the bottom of the sample, another substrate is directly stuck to the inverse opal, to ease the removal of solution. This method provides a homogenous coating within the inverse opal, without any overlayer. However, due to the high required concentration, only a non-continuous layer could be obtained with this method.

Simulations have been carried to assess the optical properties of a three-dimensional coated structure. Preliminary calculations lead to the establishment of a relation between the coating size in the inverse opal and the dimensions of the pores. This formula shows that a large pore size is required for a minimal OLED multilayer device to be coated. Due to this size, the primary optical band-gap is red-shifted to the infrared, but the second and third OBG located in the visible region, as confirmed with simulation. However, these band-gaps have very small spectral widths, and cannot be used as an optical cavity, even with the help of a coated layer. A solution to increase the size of these band-gaps, is to use a core material with a higher refractive index.

To assess the properties of a finite-sized device, a 3D-FDTD model has been made, and time simulation done with the MEEP software. Due to the complexity of the structure, high spatial resolution, as well as the imposition of particular boundary conditions are required to get the simulation to converge. Even with these adjustments, the measured transmitted spectrum exhibits a lot of sharp peaks, which are attributed to diffraction effects within the inverse opal, and which cannot be reduced with increasing accuracy. Nevertheless, the band-gaps predicted by MPB

are detected for different pore sizes, confirming the validity of the model and its use for three-dimensional OLED simulation.

In order to improve the accuracy of the model, reflectance spectra need to be acquired, to confirm or not if the sum of the transmitted and reflected waves is equal to one, as one might expect since no material is absorbing. If it is not the case, it indicates that some waves are not measured, and are probably trapped within the structure. In addition, the reflection of the "absorber" boundaries layers has to be decreased as much as possible to avoid mistakes in the measurement. To do so, a better understanding of the total effect of this layer is required.

Chapter 7

Large-scale processing

The work presented in this chapter has been made during a two weeks secondment at the Holst Centre, in Eindhoven, Netherlands. The slot die coater was operated by Arjan Langen, the Uv-Vis by Vittal Thanjavurprakasam, and the SEM by a technician from an external company.

7.1 Motivation for upscaling

The samples made during this thesis are done with laboratory dimensions, of approximately 1-2cm^2, and the time to make them is approximately 2 days. With the technique used in this thesis, multiple samples can be made at the same time due to the large volume of the humidity chamber, but the size of the samples remains limited. This small size and long process time are not a problem for experimental work, due do the relatively small amount of samples needed. However, these parameters would be a major problem for industrial-scale production, where bigger samples made in smaller amounts of time are required.

The normal way of production in the microelectronics industry is to work batch to batch, with all the devices on circular silicon substrates, called wafers. The wafer size is regularly increasing, to process more devices in the same amount of time. However, in the recent field of flexible electronics, the idea of printing electronics emerged, with the ultimate goal of printing electronic devices in the same way newspapers are currently printed. With this method, the substrate can be any flexible material, enabling a non-interrupted printing process.

One of the most well-known techniques for printed electronics is roll to roll (R2R) printing, where a flexible substrate is put in movement and is guided by moving rolls. A common way to deposit thin films in R2R is to use die coating, where a wet films is deposited on the substrate, and is then dried while moving. The drying can be done naturally at room temperature, but other units and processes can be added on the R2R production line, such as a heating area, infrared or ultraviolet exposure zones, and also cooling units. With this method, many devices such as

organic solar cells[226], organic light emitting diode[227] and photodetectors [228] have been successfully printed.

The deposition on a flexible roll is the ultimate goal of this field, however, it is also the most complicated one. The initial work to deposit a material by slot die coating is not done directly on flexible substrate with R2R, but is tested on hard substrates like glass, in a process known as sheet to sheet slot die coating. When the parameters are optimised for sheet to sheet deposition, one can begin to work on the equivalent R2R process.

A limited number of studies trying to upscale ordered nanoparticles deposition have been reported. Most of the work involves heterogeneous solution, such as suspensions of nanoparticles or nanowires, and these works reports a non-ordered deposition [228] [229] with no optical effects. Blade-coating has been reported as a good method to deposit thick and ordered nanoparticle layers [230, 231], but this deposition method requires an extremely low speed, in the order of one micrometer per second. The so called floating method, where a single monolayer of nanoparticles floats on the surface of water and self-assembles into a compact structure, can be used for large area deposition. The floating monolayer is then transferred to a substrate, which can be done by placing the substrate below the monolayer, and slowly lowering the level of water [232], or by using a continuous transfer method such as a modified roll to roll method [233, 234]. The major limitation of this technique is the formation of a floating monolayer, which requires a slow speed of formation, in order for the particles to stay on the surface of the water. Spray coating can also be employed to cover large areas with nanoparticles [235], and in this case the drying and packing of the nanoparticles occurs in air, not on the surface on the sample. This technique allows fast coating over large areas on many different substrates, however a low quality packing is obtained on the final film.

In a recent work, Zhao *et al.* [236] developed a method to deposit large area opal, exhibiting good optical bandgap, using a shear processing method. To obtain good results, modified nanoparticles are used, consisting of a polystyrene core and a shell of poly(ethyl acrylate) (PEA) and poly(methyl methacrylate) (PMMA). The shell's role is to melt during the deposition, and ensure a good adhesion between the spheres. The films obtained with this method are tens of micrometers thick, are well ordered on the top and more disordered on the bottom. The main limitation of this method is that the final structure is already filled with polymer (PEA and PMMA), and so cannot easily be extended to create inverse-opal structures.

In this work, we present the deposition of opal photonic structures with sheet to sheet slot die coating, with the objective of scaling up and reducing the processing times to those of the methods used in the previous chapters.

7.2 Slot die coating

7.2.1 Working principle

As discussed previously, a slot die coater will deposit a wet film with a precise thickness, which will form a thin film upon drying. The quality and the thickness of the film will depend on many parameters, such as the hydrophilicity/-surface energy of the substrates's surface, the coating speed, the flow rate of the solution dispensed, its viscosity, and the temperature. The schematic figure 7.1 represents the deposition area between the sample and the bottom of the die. The coating gap and the die gap (B and C respectively on figure 7.1) are chosen by the operator.

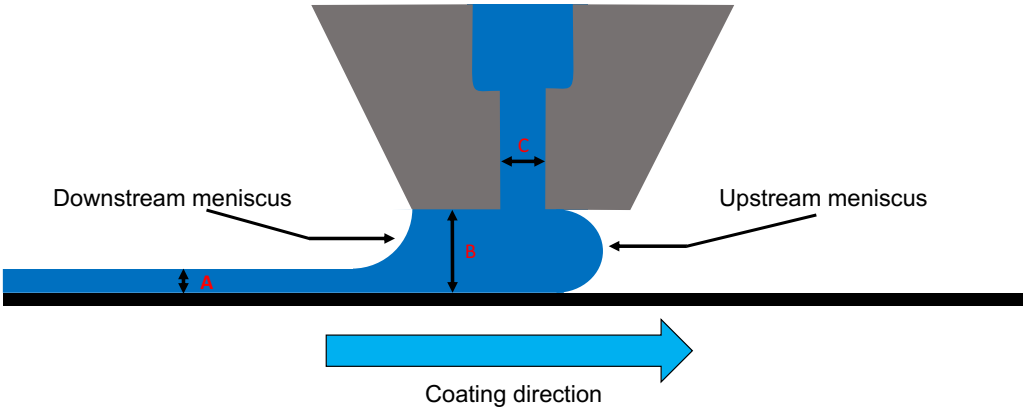


Figure 7.1: Sketch of a slot die coater. A: Wet thickness. B: Coating gap. C: Die gap.

After the deposition of a wet film, the sample is dried either in an oven or on a hot plate. Both methods can give different results, as a hot plate create convection current within the wet layer, due to the difference of temperature between the hot plate and the air, while this effect does not occur within the oven.

7.2.2 Equipment

The equipment used for the deposition is an nTact, located in a cleanroom and can be seen in figure 7.2. Prior to the deposition, a preparation of the die is necessary.

In addition of an extreme cleanliness of the inside of the die, the critical step for the preparation is the uniformity of the gap between the two parts of the

die. Any difference of distance could lead to an uneven delivery of solution, which would create variation in the final film thickness. To obtain a uniform spacing, a kapton film of a specific thickness (65µm in our case) is inserted between the two parts of the die. These parts are then linked together with screws all over the surface of the die. The screws are tightened with a torque wrench, to ensure exactly the same force across all of them. The screws can be seen on 7.3 left picture, where the dispensing area can also be seen on top of the die.

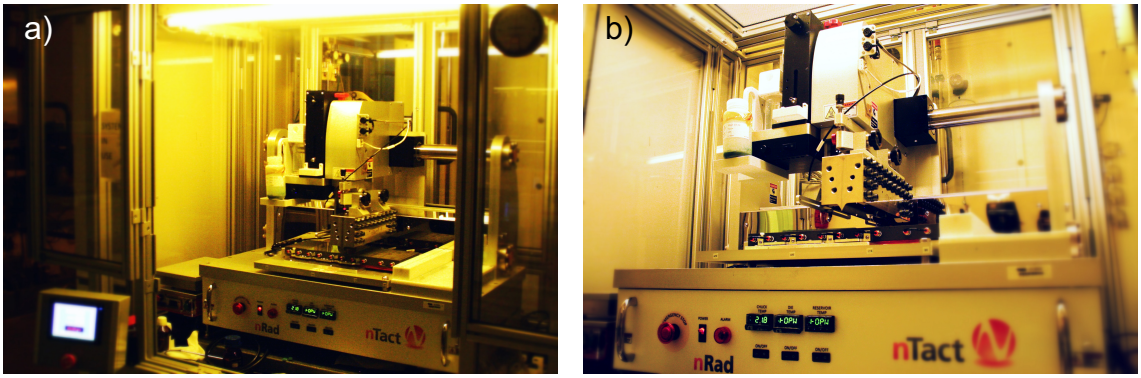


Figure 7.2: Slot die coater from (a) above and (b) from below.

The prepared die in then mounted on the machine, where an adjustment to obtain perfect horizontality of the die is done. If required for the experiments, the die can be heated at a specific temperature, by insertion of heating elements inside it. The holes where these elements are inserted can be seen on 7.3, right picture.

The die is then filled with solution, which is stored in a small reservoir inside it. The transfer of solution from the bottles to the die is done with a system shown in 7.4, where a syringe controlled by the machine, pumps the solution, and thereby sends it to the die. This system is not present in figure 7.2. The filling of the die requires approximately 30mL of solution, this is why at least 50mL of solution is needed for every experiment.

During the coating, the delivery of the solution is controlled by the system shown in figure 7.4. The syringe's plunger is controlled by a motor, enabling a delivery accuracy down to one microliter. The volume of the standard syringe is 2mL, which limits the total amount of solution that can be coated to this amount. However, bigger syringes can be adapted on this equipment, to overcome this limit.

7.3 Experimental

The experimental section presents two different deposition techniques carried out by slot die coating, which will be detailed hereafter. Ideally, the same particles sizes should be used for the two deposition techniques, to allow an accurate comparison between them. Unfortunately, due to the large amount of solution consumed by the machine, and because of logistic problems, different sizes of particles had to be used for the experiments. In section 7.3.1, particles with sizes of

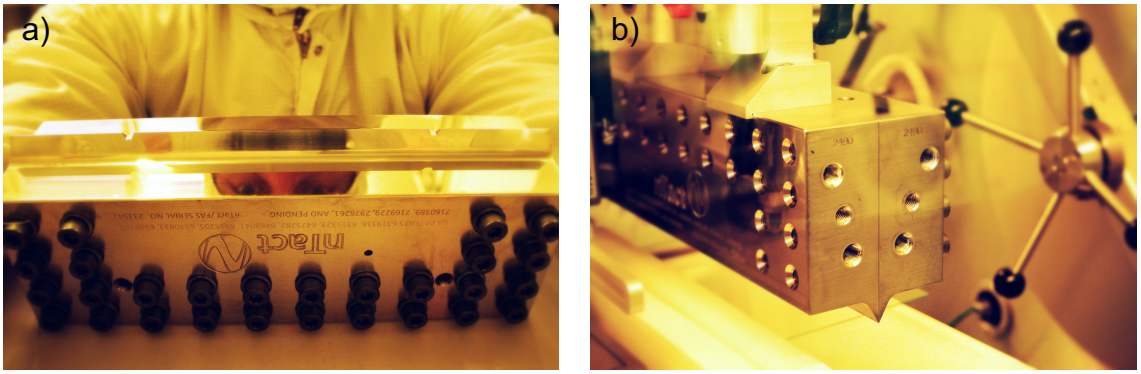


Figure 7.3: Die seen from bottom (a) and mounted on the equipment (b).

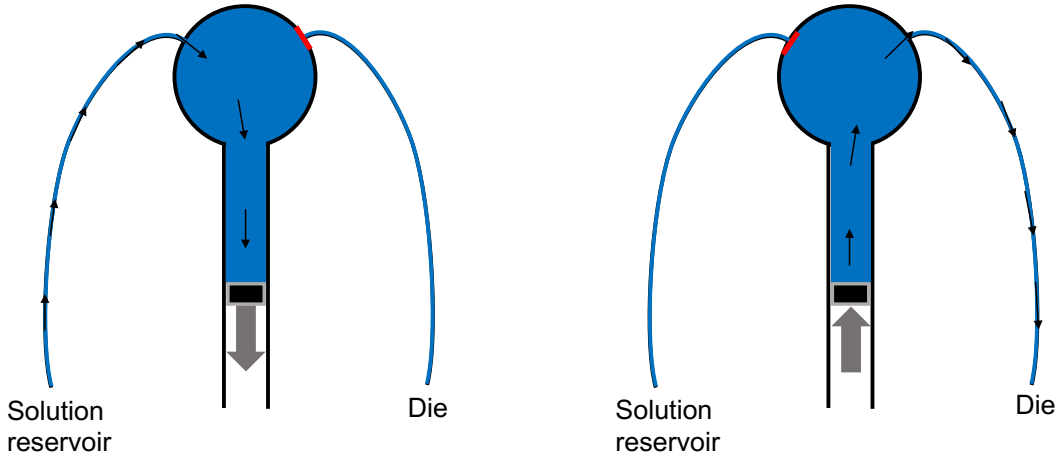


Figure 7.4: *Left :* Loading of the solution from the main reservoir. *Right :* Dispense of the solution to the die.

1.28 μm and 800 nm have been used, while in section 7.3.2 sizes of 488 nm and 250 nm have been used. These differences have to be taken into account for an accurate comparison between the 2 techniques, as the final thicknesses were different. However, the major differences observed between the 2 techniques cannot only be due to the particles size differences, which are still of the same order of magnitude.

7.3.1 Classical coating

As explained in the section 7.2.1, a classical slot die coating is depositing a wet film of solution, which is then dried either on a hot plate or inside an oven. This method of deposition gives good quality films for polymers, molecules or inorganic materials.

There are two main differences between a thin film deposition and the opal deposition we want to achieve: the first one is the behaviour of the wet film upon drying, the second one is the thickness of the target wet film.

For standard film drying, we can consider the wet film as being a homogeneous solution with diluted materials in it. When dried, the solute will aggregate and form a homogeneous film on the substrate. However, a solution of nanoparticles cannot be consider as homogeneous, as the size of particles is above 100 nanometers (for the particles used in this thesis). In this case, the drying of the wet film could lead to inhomogeneity in the final film.

The second difference concerns the thickness of the films, and the amount of required materials, which is far larger in the case of an opal film. We only focus on the fabrication of monolayer structures, because this requires less material.

To know the required wet thickness to form a monolayer opal film, we first calculate the thickness of an ideal film formed with the same amount of material used to make a monolayer of polystyrene nanoparticles. In order to obtain this thickness, we calculate the ratio of the volume occupied by a sphere, to the volume occupied by a cube with the same diameter, as quantifies by equation 7.1. This ratio, approximately equal to 52%, indicates that a monolayer of nanoparticles of diameter D, possesses the same amount of material as a thin film with a thickness of $t = fD$.

$$f = SphereVolume/CubeVolume$$

$$f = \frac{\frac{1}{6}\pi D^3}{D^3} = \frac{\pi}{6} \tag{7.1}$$

As an approximation, we consider that during the formation of a thin film by slot die coating, all the materials dissolved in solution are used to form an ideal film upon evaporation. If we consider that the amount of materials dissolved in the wet film is the same as the final thin-film, we can consider the equality 7.2, where T_w is the wet thickness, C is the concentration of solution, in mass per volume, t and ρ the thickness and density of the thin film respectively.

$$T_w C = t\rho \tag{7.2}$$

Combining equations 7.1 and 7.2, and the fact that $t = fD$, we obtain equation 7.3, giving the wet thickness needed to make a monolayer of nanoparticles of diameter D, knowing the concentration of the solution, and the density of the material.

$$T_w = \frac{fD\rho}{C} = \frac{\pi D\rho}{6C} \tag{7.3}$$

The theoretical wet thickness required given by equation 7.3 is represented on the figure 7.7, for polystyrene nanoparticles, at 3 different concentrations. As can be observed on this figure, for a concentration of 1% per weight, the required

wet thickness can quickly rise to tens of micrometers, which is far thicker than a conventional slot die coating.

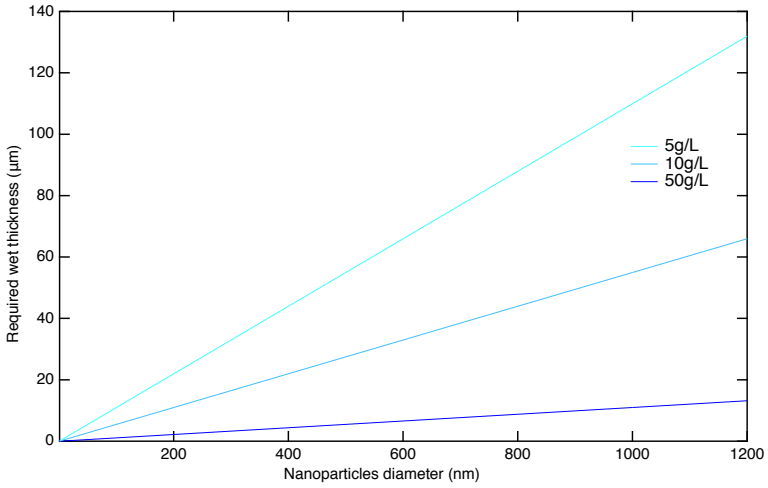


Figure 7.5: Required wet thickness for a monolayer of polystyrene nanoparticles. Different concentrations of solutions are represented.

Table 7.1: 1.28um nanoparticles coating, concentration of 1% per weight

Name	Die speed	dispense rate	T°C chuck	Observations
1.28-1	50 mm/s	50 uL/s	RT	no optical effects
1.28-2	50 mm/s	100 uL/s	RT	no optical effects
1.28-3	10 mm/s	200 uL/s	60	liquid stuck to downstream

Table 7.2: 800nm nanoparticles coating, concentration of 0.8% per weight

Name	Die speed	dispense rate	T°C chuck	Observations
800-1	25 mm/s	250 uL/s	RT	no optical effects
800-2	10 mm/s	100 uL/s	RT	liquid stuck to downstream
800-3	25 mm/s	250 uL/s	65	weak optical effects

The initials coatings, made with 1.28 µm and 800 nm nanoparticles diluted 1% and 0.8% by weight respectively, are summarised in tables 7.1 and 7.2. In these coatings, it can be observed that a large amount of solvent is still present on the substrate at the end of the coating. This is both due to the large volume spread on the substrate, due to the high required wet thickness, and to the amount of energy required to make water evaporate. In addition, the solvent is not uniformly spread, and the majority of it is located at the end of the coating area. Due to the large surface tension of water, the downstream meniscus (figure 7.1) is also in contact with the die itself, leading to a low amount of solvent being deposited. Instead, we observe an accumulation of solvent on the back of the die, which is released at the end of the coating when the die leaves the sample, leading to a non-uniform coating across the substrate.

The substrate with the deposited solvent is then put in an oven at 80 °C, to allow a uniform evaporation of the solvent. Due to the low amount of material

deposited on the first part of the substrate, this area appears transparent after evaporation. As can be seen on figures 7.6 and 7.8, the particles are uniformly dispersed on the substrate. With a higher magnification, it can be observed that the particles are forming chains and starts to stick to each other, but because of the insufficient amount of material, no hexagonal close packing can be observed.

In order to increase the amount of nanoparticles deposited, the chuck (and the substrate on it) can be heated. By doing so, the water is evaporating in a faster way, which can increase the amount of particles deposited on the substrate. However, by comparing samples $800-1$ and $800-3$ in table 7.2, which have the same deposition parameters except for the chuck temperature, one finds extremely similar depositions. The heating of the chuck, with these coating parameters, does not impact much on the deposition and the amount of material deposited. Because of the small amount of time given for water evaporation, the additional energy brought by the hot chuck, is not sufficient to make a significant difference.

Another method to improve the amount of material deposited on the sample, is to increase the total amount of solvent which is dispensed on the substrate, by reducing the die speed and increasing the dispense rate, as for sample $1.28-3$, in table 7.1. However, this method does not deposit more material, as most of the solvent is still caught by the downstream meniscus.

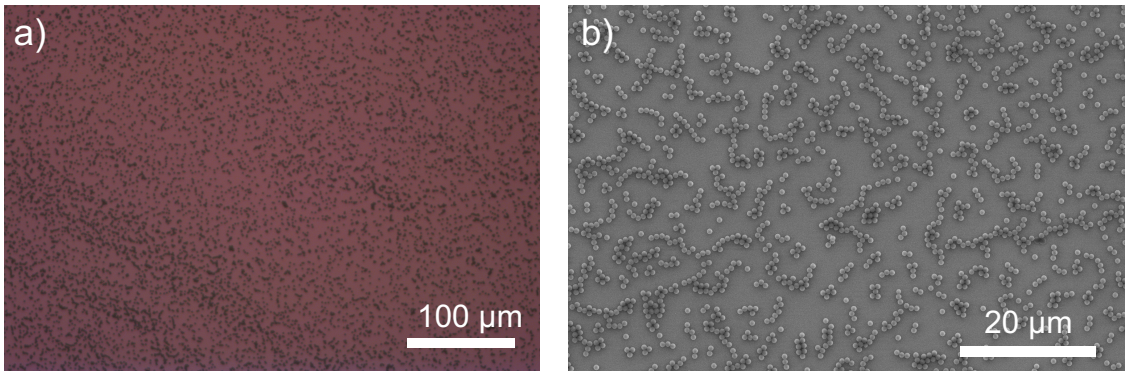


Figure 7.6: Optical microscope (a) and SEM (b) of slot die coated glass sample with 1.28 μm nanoparticles (sample 1.28-2 from table 7.1)

At the other side of the substrate, where the water accumulated on the die is released, more polystyrene particles are present to form a compact layer, and optical effects can start to occur, as can be seen on figure 7.9. Hexagonal packing can be observed under a microscope, but due to the poor control on the self-assembly, many close-packed domains exhibit small size and random orientation. Cubic packing can also be found in this area, as non-ordered phases.

Due to the many different sphere-organisation types, small and non-oriented domains, as well as a possible multi-layered structure, the optical properties of this sample do not show a typical optical band gap, indicated by a clear dip in the transmission spectrum, but more a succession of peaks that cannot be identified (figure 7.10). These many peaks can be due to optical bandgaps of the hexagonal and the cubic packing, as well as Fabry-Perot interferences. The transmission spectrum of the weakly-coated side of the substrate does not exhibit any specific features,

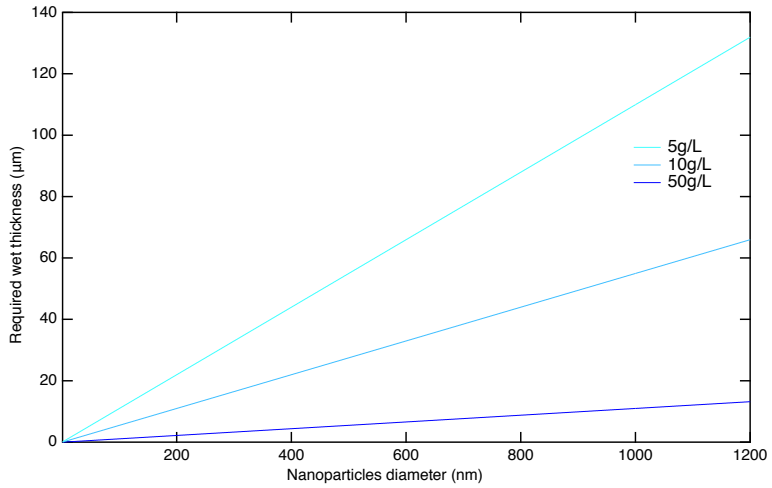


Figure 7.7: Required wet thickness for a monolayer of polystyrene nanoparticles. Different concentrations of solutions are represented.

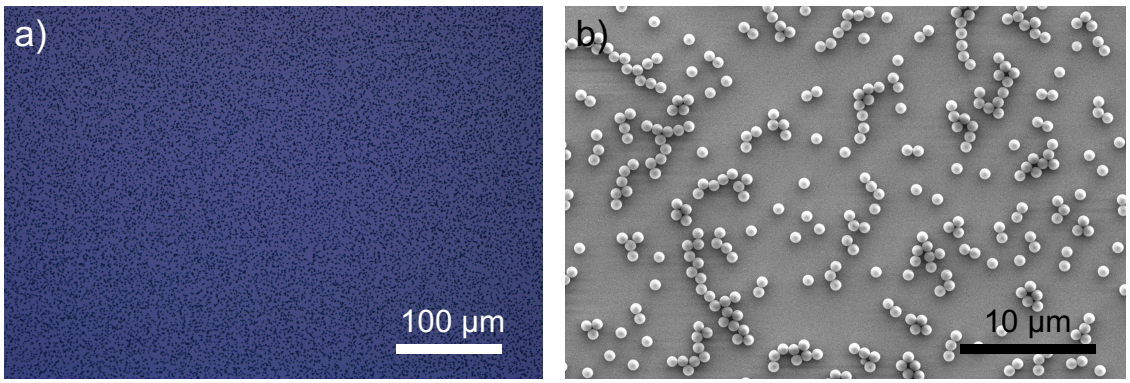


Figure 7.8: Optical microscope (a) and SEM (b) of slot die coated glass sample with 800 nm nanoparticles (sample 800-1 from table 7.2)

because of the absence of close-packing between the nanoparticles.

Different methods have been tested to allow a more uniform wet thickness across the substrate, where the main objective is to avoid the water accumulation on the die, at the downstream meniscus.

An intuitive approach is to increase the speed of the die, to prevent the water meniscus from catching up with the die. If one uses this technique, the delivery rate has to be increased too, in order to deliver the same total amount of solution on the substrate (sample "Fast", in table 7.3). In spite of increasing the die speed, the same problem of non-uniform coating is observed, probably because the higher delivery rate cancels out the benefit from increasing the speed.

Another way of approaching this problem is to change the gap distance between the die and the substrate, indicated as B on figure 7.1. By doing so, gravity should prevent the water staying on the die, and force it to go on the substrate (sample "Curtain", in table 7.3). In our case, a gap of 3 mm is used for this deposition, instead of the usual 300 μm. This coating looks more like a technique

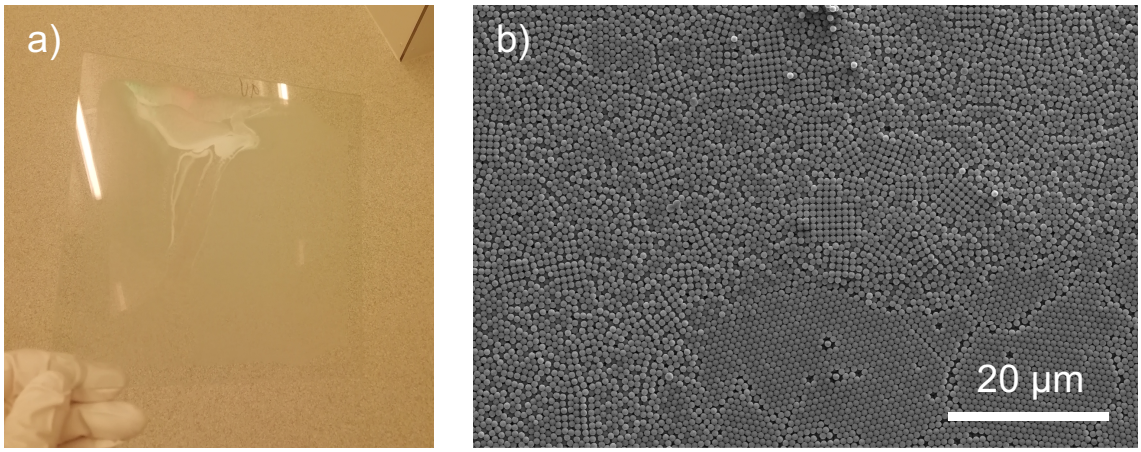


Figure 7.9: (a) Optical effects due to a large aggregation during the solvent drying. (b) SEM analysis of the thick deposition area.

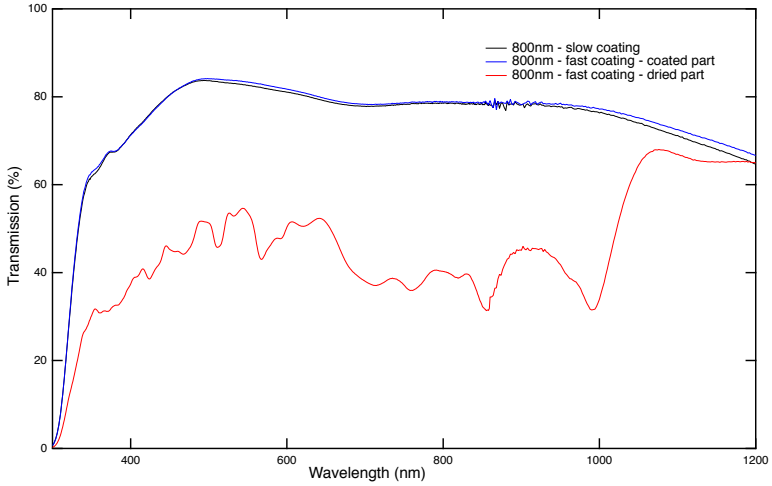


Figure 7.10: Uv-Vis transmission spectra of slot die coated 800nm particles, in thin and thick area.

Table 7.3: 800nm special coatings, concentration of 0.8% per weight

Name	Die speed	dispense rate	T°C chuck	Observations
Fast	40 mm/s	400 uL/s	RT	no optical effects
Curtain	10 mm/s	100 uL/s	RT	gap at 3000 um
Blade	40 mm/s	400 uL/s	RT	better homogeneity

called curtain coating, where the solution is ejected from the die head far from the substrate. This technique is mostly used for viscous material, that can maintain a stable film when "free falling" between the die and the substrate. In the case of water, even if its surface tension is really high, its viscosity is quite low. For this reason, the curtain formed by the solution is not stable and can be easily broken if the coating gap is too large. It is worth saying that when a defect appears in the curtain, it cannot be self-repaired and only gets worse. If the coating happens in a good way, this method gives a more uniform film than the standard one, but it is still not good enough for a correct packing between the nanoparticles to occur.

The last method tested to create a more uniform coating implied the modification of the solution dispensed onto the substrate. Instead of a regular dispense during the die movement, all the solution is dispensed at the beginning of the substrate (sample "Blade", in table 7.3). The die then starts its displacement, and the solution is carried by the surface tension. This methods more looks like blade coating, where a solution is deposited on a substrate by being spread by a blade movement, rather than slot die coating. Due to the large surface tension, and the large amounts of water involved, most of the solution is carried until the end of the coating creating a non-uniform wet thickness.

It can be seen through these different coating methods, that a uniformly thick wet layer of water is extremely hard to obtain by slot die coating. In addition, when a sufficient amount of material is present to form a compact layer of nanoparticles, the formation of periodic structures is poorly controlled, and gives small and non oriented domains, as well as some random packings of nanoparticles.

7.3.2 Slow coating

The classical slot die coating did not give good depositions, mostly because of the large required wet-thickness, which cannot be obtained with water as a solvent. To overcome this limit, another deposition method which mimics the evaporation-induced self-assembly deposition, has been tried. To the best of our knowledge, this is the first time this method have been tried on slot-die coating.

In a classical deposition, the film is formed upon drying of the wet layer previously deposited. In this new deposition method, the films is formed with the drying of the meniscus, in the same way as the EISA deposition. For this evaporation to happen and to be significant enough for a film to be deposited, the substrate temperature must be high, and the die speed has to be slow. For this last reason, we choose to call this type of deposition : "slow-coating".

Table 7.4: 800nm slow coating, concentration of 0.8% by weight

Name	Die speed	dispense rate	T° chuck	Observations
S800-1	0.5 mm/s	$10\,\mu l\,s^{-1}$	40 °C	Faded stripes, 1 mm distance
S800-2	0.5 mm/s	$20\,\mu l\,s^{-1}$	65 °C	Visible stripes, 1 mm distance
S800-3	0.5 mm/s	$40\,\mu l\,s^{-1}$	70 °C	Visible stripes, half a millimeter distance

For this new technique of coating, the die speed is strongly reduced, to reach 0.5 mm/s as indicated in table 7.4. At this speed, the complete coating takes around 5 minutes, for a 15x15cm^2 substrate. The dispense rate is adjusted to a lower value than the previous coatings, to obtain a similar amount of solution deposited.

The first remarkable feature is the appearance of stripes, parallel to the coating direction. These stripes become more visible and close to each other with a higher substrate temperature and an increase of the dispensing rate. An increase of temperature has a direct impact on the evaporation rate of the water, leading to the

deposition of more material on the substrate, which explains the stripes becoming more visible as temperature increases.

As can be seen on figures 7.11 and 7.12, the stripes consist in denser regions of nanoparticles, where a hexagonal packing starts to form. This effect, which is the previously described stick slip effect, occurs if the meniscus movement is too fast or if there are not enough nanoparticles in the solution. To obtain this effect with this deposition method indicates a good similarity with the evaporation induced self assembly deposition.

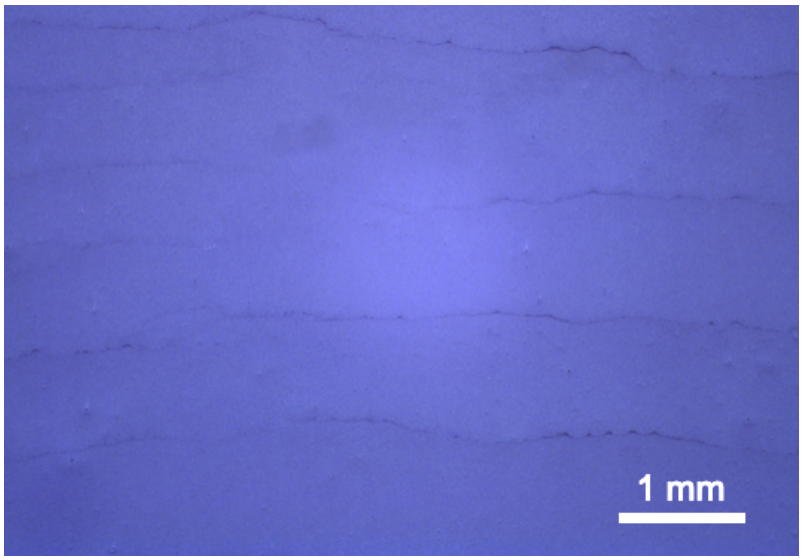


Figure 7.11: Microscope view of a slow-coating of 800nm nanoparticles, exhibiting stick slip effect. The deposition is in the vertical direction.

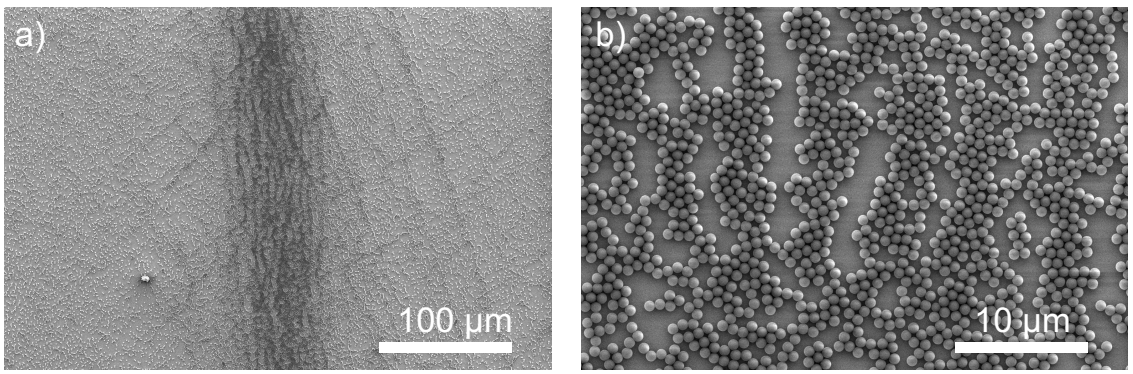


Figure 7.12: Low (a) and high magnification (b) SEM view of a stripe of slow-coated 800nm nanoparticles.

The amount of water dragged with the downstream meniscus and then staying on the substrate is less important than with the previous coatings techniques, but is still significant. This problem comes from the very high specific heat capacity and heat of vaporisation of water, $4.1814 J/(g.K)$ and $2257 kJ/kg$ respectively. These values imply that if some water at room temperature is deposited on a heated surface, it takes a long time for it to reach a high temperature, and then evaporate, due to the large amount of energy required.

To overcome this problem, the solvent can be deposited at a higher temperature. To do so, one can heat the die to a certain temperature, with the insertion of heating elements inside it. The solution inside the die will take the same temperature, and less energy will be required to evaporate the solution after deposition, leading to a faster evaporation on the substrate.

From now on, both the substrate and the chuck will be heated at specific temperatures to allow a faster evaporation of the solvent, and thus a greater amount of material to be deposited.

The solution used for this series of deposition consists of 488 nanometer particles, concentrated at 1.2%.

Table 7.5: 488nm slow coating, concentration of 1.2% by weight

Name	Die speed	dispense rate	T° chuck	T° die	Observations
S488-1	1 mm/s	$10\,\mu l\,s^{-1}$	60 °C	60 °C	Optical effect on edges
S488-2	0.5 mm/s	$3.6\,\mu l\,s^{-1}$	60 °C	60 °C	Weak optical effects
S488-3	0.5 mm/s	$5\,\mu l\,s^{-1}$	70 °C	70 °C	Good optical effects

The chuck and the die are heated at the same temperature for these depositions, at 60 °C for two of them and 70 °C for the last one, as detailed in table 7.5. It can be observed on figures 7.13 and 7.14 that an increase of the die and chuck temperature, as well as in reduction of the die speed, creates a better coverage of the substrate. The temperature increase creates a faster rate of evaporation for the solvent, and the slower deposition speed allows more time for the solvent evaporation, both effects leading to more material deposited. It can also be observed that the residual solvent on the substrate is drastically reduced compared to initials coatings.

Increasing the amount of deposited nanoparticles makes the film passing from isolated islands, to a continuous films with many voids, to finally a full films covering totally the substrate, as seen in figure 7.13. Interestingly, even for the sample with a film formed with isolated islands, hexagonal packing can be observed (figure 7.14). The size of the domains is greater than for the non-controlled growth observed in figure 7.9, and their orientation is more regular. Compared to an opal formed by evaporation induced self assembly, more defects are present, due to a faster formation.

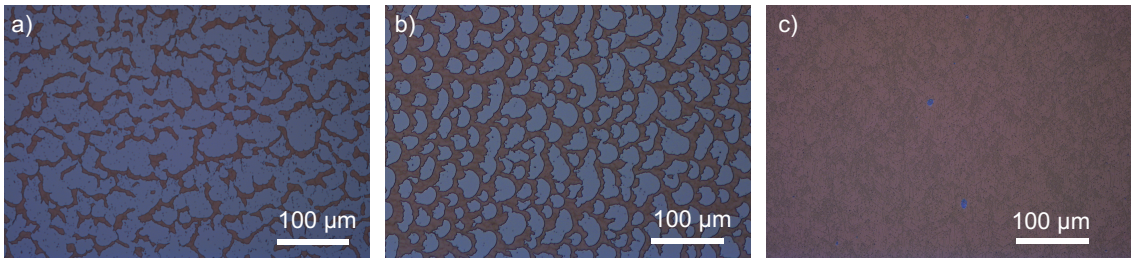


Figure 7.13: Optical microscopy of samples S488-1 (a), S488-2 (b) and S488-3 (c) according to table 7.5.

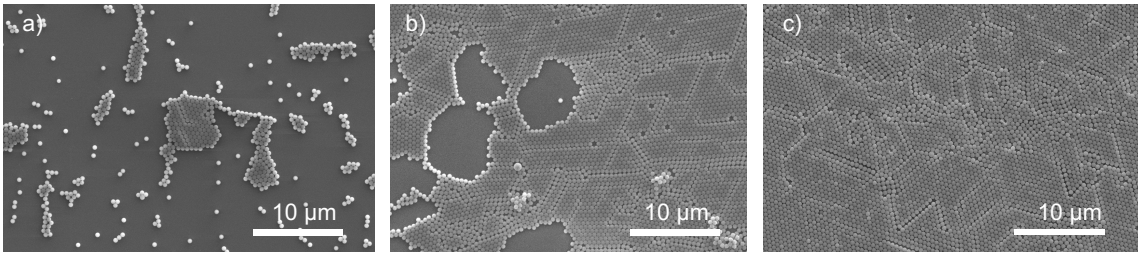


Figure 7.14: SEM of samples S488-1 (a), S488-2 (b) and S488-3 (c) according to table 7.5.

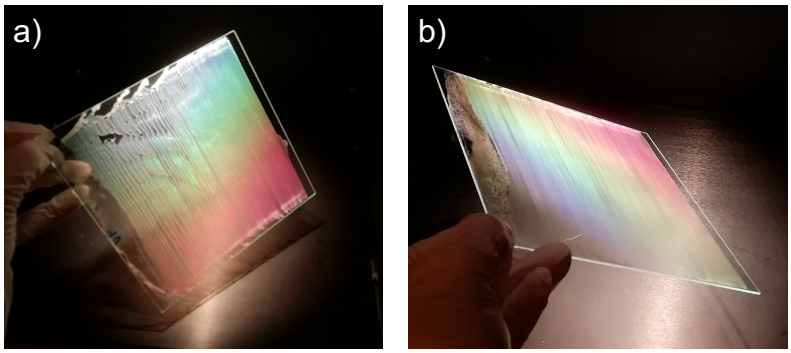


Figure 7.15: Sample S488-3 under white light illumination, with a low (a) and a high incidence angle (b).

For the two samples with the best coverage, optical effects can be seen (figure 7.15), which are due to diffraction for these samples. These effects indicate good long range order and well-orientated domains. Horizontal lines, perpendicular to the coating directions are still visible with this technique, and are probably due to the stick slip effect. This effect occurs because of the relatively high speed of the coating compared to the evaporation induced self assembly, which prevents the meniscus from smoothly following the same speed as the die. However as more material is deposited, this effect tends to reduce, as it can be observed in figure 7.15, where the stripes begin to fade for the last sample.

To ensure the presence of a photonic bandgap, Uv-Vis reflection spectra, taken with an integrating sphere, have been measured (Figure 7.16). The interferences observed around 900nm are due to a change of lamp in the equipment, and is not due to the sample. The sample with the lowest amount of material deposited (S488-1) does not exhibit any specific features, and presents a reflection only from the glass substrate. Although the nanoparticles are assembled in a hexagonal pattern, the coverage of the substrate is not sufficient to obtain a clear photonic effect.

For the samples S488-2 and S488-3, clear photonic effects can be seen, which can be separated depending on where they are on the optical spectrum. From the region above 700 nanometers, the reflection intensity firstly decreases, and then increases to reach above its original value, and then decreases again. This pattern looks like a wave, and can be interpreted as optical interference due to a Fabry-Perot etalon effect, the deposited nanoparticle layer acting as a thin film for photons at high wavelengths.

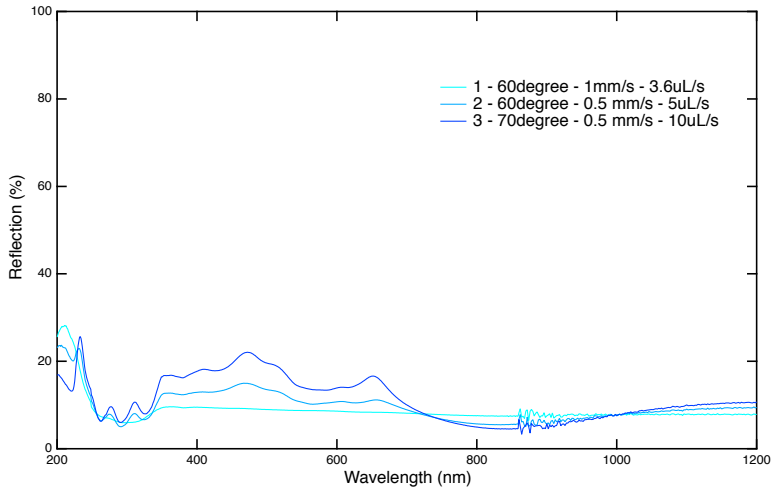


Figure 7.16: Uv-Vis reflection of slow-coated 488-nm particles, with different deposition parameters.

Peaks are observed below 700 nm, with their intensity being proportional to the coverage of the sample. These peaks are attributed to various partial bandgaps of the layer, which are weak due to the layers' small thickness. This effect confirms the good organisation of the polystyrene nanoparticles by slot die coating.

Table 7.6: 250nm slow coating

Name	Die speed	dispense rate	° chuck	° die	Observations
S250-1	0.5 mm/s	$10\,\mu l\,s^{-1}$	70 °C	60 °C	good green colour
S250-2	1 mm/s	$10\,\mu l\,s^{-1}$	60 °C	60 °C	average optical effects
S250-3	1.5 mm/s	$5\,\mu l\,s^{-1}$	70 °C	70 °C	weak effect

A similar behaviour is observed for the 3 samples made with 250nm nanoparticles, whose deposition parameters are provided table 7.6. As expected from previous observations, the lower the speed of deposition, the higher the coverage of the sample, as seen in figure 7.17. The organisation of the nanoparticles in close-packed crystal also gets better as the deposition speed is reduced (figure 7.18). The sample made with the highest speed (S250-1) only presents a small portion of organised nanoparticles and an incomplete coverage of the surface. The sample S250-5 covers most of the surface, but only approximately 50 % of it is organised into compact structures. The sample made with the slowest deposition (S250-3), has a surface fully covered, and all of the nanoparticles are organised into a hexagonal pattern.

The reflectance Uv-Vis measurements of these three samples (figure 7.19) show a good agreement with the SEM observations, with peaks increasing intensities with increasing surface coverage and order between the nanoparticles. Sample S250-3 exhibits a light green colour visible by eye, which is seen on Uv-Vis as the 600nm peak.

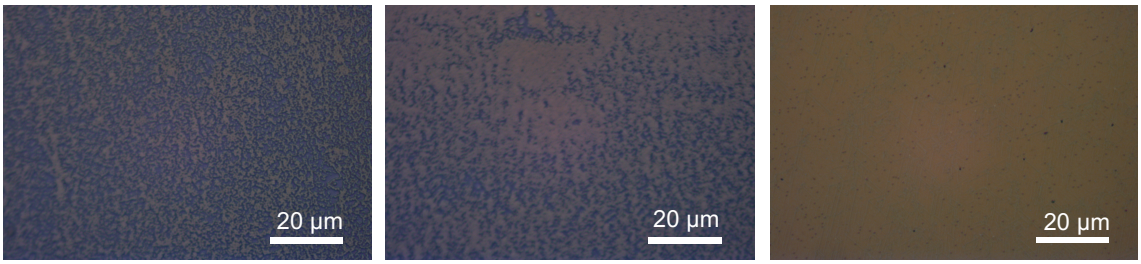


Figure 7.17: Optical microscopy of samples S250-1 (a), S250-2 (b) and S250-3 (c) according to table 7.6.

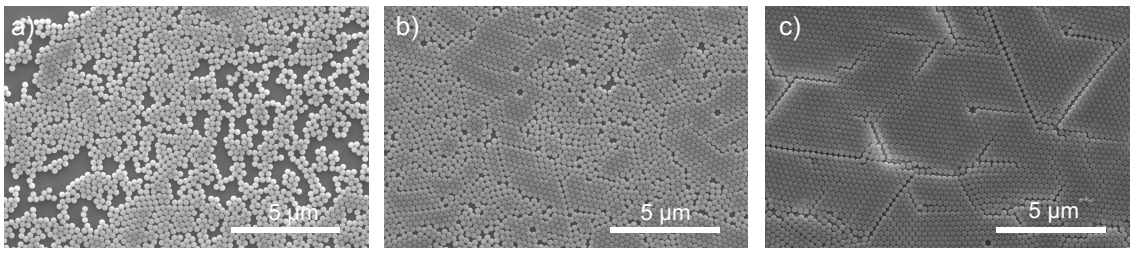


Figure 7.18: SEM of samples S250-1 (a), S250-2 (b) and S250-3 (c) according to table 7.6.

7.3.3 Flexible substrate

Sheet-to-sheet slot die coating allows a much faster and larger area deposition compared to the previously used evaporation induced self assembly. However, this method only works sample per sample, and not in a continuous way. A well known method to obtain a continuous coating (R2R) is the roll-to-roll coating, which deposits materials on a flexible substrate, in the same way as a newspaper-printing machine does. In order to assess the possibility of using R2R for opal deposition, we make some preliminary depositions using sheet to sheet slot die coating on flexible substrates, using Polyethylene Terephthalate (PET).

The main difference between PET and glass which is relevant for our deposition is the surface energy, which has a value of 83.4 mJ/m^2 for glass, and 44.6 mJ/m^2 for PET. This difference impacts the wetting of the solvent on the PET, which does not spread as nicely as on the glass. For this reason, with similar conditions as the previous depositions (table 7.7) most of the solvent stays on the downstream, and no deposition is observed. This effect can be reduced with plasma treatment, increasing the hydrophilicity of the PET and the amount of deposited nanoparticles. However this treatment could not be improved enough during the time of the secondment, and although deposition of nanoparticles occurred, no clear optical effect was observed (figure 7.20). The observed interferences are due to Fabry Perot effect, due to the small thickness of the PET.

Table 7.7: Flexible substrate coating

Die speed	dispense rate	chuck temperature	die temperature
3	10	70 °C	70 °C

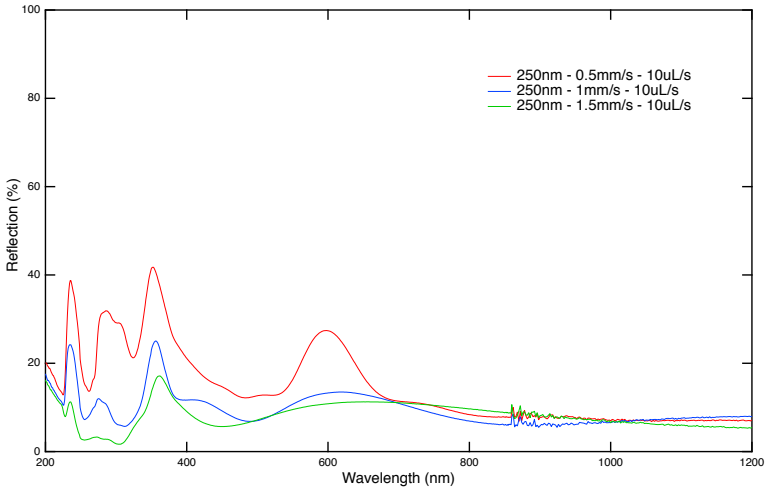


Figure 7.19: Uv-Vis reflection of slow-coated 250-nm particles, at three different speed.

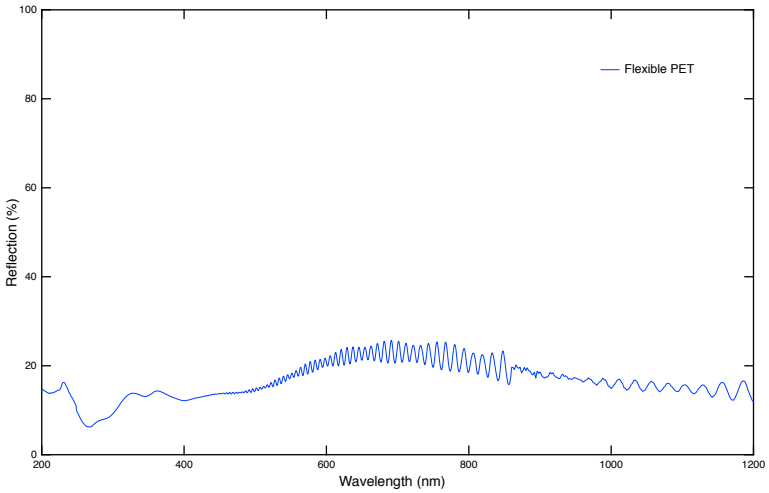


Figure 7.20: Uv-Vis reflectance of slow-coated 250-nm particles, on a flexible plasma treated PET substrate.

7.3.4 Conclusions

Large-area deposition of opal have been tested on a sheet-to-sheet slot die coater. The classical deposition with this method, consisting of a wet layer deposition which is then dried to form a film, did not give good results for opal structures, especially because of the thick wet film required. In addition, water takes a long time to evaporate, and so, most of the solvent was still on the substrate after the deposition.

To overcome these problems, we implemented another deposition method, which uses the same principle as the evaporation induces self assembly. Instead of evaporating a wet film already deposited on the substrate, the drying and the self assembly of the nanoparticles occurs directly on the meniscus, in the same way as the method used in the rest of this thesis. For this deposition, a slow speed of around 1-2mm/s is used for the die, allowing a coating of the substrate in approximately 3

minutes. In addition, both the substrate and the die are heated, to allow a faster evaporation of the water. Ideally, the evaporation of water should match the speed of the die, to avoid any solvent residuals.

With this new method, layers of good quality have been deposited, with continuous film on approximately one third of the substrate. These structures exhibit clear photonics effect, which can be seen with naked eye, and photonic band gaps have been observed with uv-vis measurements. However, at the temperatures used, the solution can dry inside the die, leading to a partial or total blockage of the dispenser which prevents correct deposition (figure 7.21).

For these experiments, the concentration of the solutions were approximately 1% by mass. This concentration was chosen due to the limited amount of available nanospheres for the experiments, in conjunction with the large total volume needed by the machine. To increase the quality of the deposition and avoid the die-clogging problem, one could increase the concentration of the solution. Indeed, with a more concentrated solution, one could dispense less solution to deliver the same amount of material. With less solvent on the substrate, the amount of evaporation required would be reduced, which would allow a faster deposition speed, or the use of a lower temperature for both the die and the substrate.

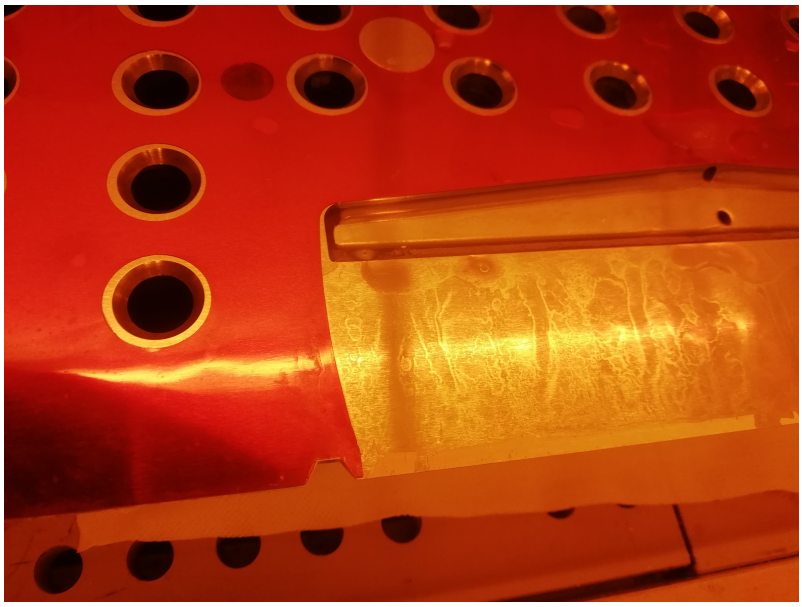


Figure 7.21: Polystyrene nanoparticles drying and aggregating at the bottom of the die.

Chapter 8

Conclusions

This thesis presented the fabrication of inverse opals in fluorine tin oxide, and their implementation in devices, for potential enhanced properties.

The fabrication of these structures is initially done in two steps, firstly with the creation of an opal structure made of polystyrene nanoparticles, which is then infiltrated with a precursor solution. The nanoparticles are deposited by evaporation induced self-assembly, giving a highly ordered structure over a large area of approximately $1 \times 2.5\,\mathrm{cm}^2$. The parameters used for the deposition, giving a repeatable thickness and organisation, are a temperature of $60°C$ and a relative humidity of 20%. The treatment of the glass substrate with piranha solution prior to the deposition, greatly enhances the hydrophilicity of its surface, and improves the packing of the nanoparticles due to their greater mobility on the surface of the sample.

The fabricated opals have been optically tested to assess their periodicity over large areas. A clear optical band-gap can be seen both in reflection and transmission Uv-Vis, as well as with naked eye, showing the good three dimensional periodicity of the photonic crystals. However, a clear difference in intensity is seen between the specular and the total reflection (transmission), which is due to the cracks present on the structures, creating an important scattering effect. To further assess the quality of the PhC, the structures are measured by a tilt-able Uv-Vis, used in specular reflection. A clear variation of the optical band-gap, due to the [111] of the opal, is observed, in accordance with the modified Bragg law. Some fundamental characteristics of the structures, such as the size of the particles and the refractive index, can be extracted from these measurements. A second band-gap can be observed in these measurements, which is attributed to the [200] plane. In the fcc structure, this plane is not perpendicular to the surface, and the ability to show the corresponding OBG reveals a very good periodicity. A protocol has been established for the opals' infiltration, which consists in successive spin coating, with visual controls based on optical properties of the structure.

The infiltration protocol has been used to infiltrate a 0.2M solution of $Sn(Cl_4).5H_2O$ in methanol inside a 1 µm opal, made of 250 nm nanoparticles. After calcination, a cracked structure made of crystalline FTO is obtained, with a similar

periodicity to the original opal. Visually, this structure is transparent due to the small pore sized of the inverse opal, but is cloudy because of the cracks. Atomic layer deposition is used to coat homogeneously the whole inside of the inverse opal with TiO_2, with a thickness of 10nm. A hold time is used during the ALD deposition, to allow the precursors to fully penetrate the structure before being evacuated. The regularity of the coating thickness across the structure is assessed with high resolution SEM, using back scattered electrons, as well as STEM/EDX.

Many different methods have been used to infiltrate the coated FTO inverse opal with $MAPbI_3$ perovskite. A major difference between a standard film deposition and one inside an inverse opal, is that only the precursors already inside the inverse opal can participate in the perovskite formation inside the structure, while a standard film can be formed with precursors from a larger volume. This limitation implies that the solution concentration needs to be very high, for a complete filling of the inverse opal. It has been observed that the standard deposition using anti-solvent dripping to force the crystallisation of the material, reduces the concentration of precursor within the inverse opal, leading to an incomplete filling. In addition, when a crystalline overlayer is formed on top of the structure, by forced crystallisation, the precursors within the inverse opal aggregates on this overlayer, resulting in an infiltration only on the top of the structure. It is hypothesised that this aggregation is because there are no or just a few crystal seeds inside the inverse opal, and so the precursors are reacting faster with the already formed crystals in the overlayer.

The increase of the solution concentration is performed after its infiltration inside the inverse opal, by a solvent retarded evaporation method. Even thought this method increases the global filling of the inverse opal, the application of anti-solvent still limits the filling. To avoid this, the quenching of the perovskite solution is performed with the application of a strong nitrogen flow directly on the sample during the spin coating. Doing so provides a very good filling of the inverse opal, but due to technical limitations, the pressure delivered by the nitrogen gun could not be as high as needed, resulting in a poor surface quality. Another tested method uses a two step deposition, with firstly the infiltration of the lead iodide, followed by its conversion to perovskite, by dipping in a methyl ammonium solution. This methods provides a very good infiltration of the material, due to the more controllable crystallisation of lead iodide, but its conversion to perovskite only occurs on the surface, due to the high thickness of deposited lead iodide.

Working solar cells have been made with this architecture, using the solvent retard method to have a continuous overlayer, preventing the exposure of the FTO inverse opal, which would lead to short circuits. The maximum measured efficiency for this solar cells architecture is 6.46% with a fill factor of 0.37. These low parameters are explained by the incomplete filling of the inverse opal, as well as the porous perovskite present in the cracks of the structures. In addition, lead halide perovskite is an extremely delicate material to deposit in order to obtain good solar cells performances. Due to the particular deposition used to infiltrate the inverse opal, the lead halide perovskite might not present good parameters to obtain a good solar cell.

Different methods have been tested in order to create crack-free inverse opal in FTO, in order to facilitate the infiltration of this structure, and enhance the optical effects. To do so, FTO nano-crystals have been synthesised by hydrothermal methods. Immediately after the synthesis, the suspension is stabilised with the addition of a certain amount of tetra-methyl ammonium hydroxide, which prevent the nano-crystals from aggregating. The TEM and DLS analysis reveal a small dispersity of these nano-crystals, with an average size of 7nm. The quality and organisation of the opal formed by the one-step infiltration of the nano-crystals increases with the amount of added stabiliser. However, large defects are formed on top of the structure because of the recrystallisation of the stabiliser. The density of cracks after calcination is greatly reduced compared to the standard method, and spatially organised cracks following the [100] directions are visible, indicating the good order of the structure. A careful selection of the nanoparticles after their synthesis, to only take the ones with a high zeta potential, reduces the amount of stabiliser needed, and thus reduces the density of defects on the final structure while keeping a good organisation (packing).

To completely suppress the cracks in the inverse opal, the addition of dissolved precursors is necessary to ensure the cohesion of the structure after the initial evaporation. To stabilise the the highly reactive tin precursor, citric acid is successfully used as a chelating agent. However, as both tin tetrachloride and citric acid are acidic compounds, a certain amount of base has to be added to this solution, to prevent the destabilisation of the PS and FTO suspension, which have negative zeta potential. An optimal balance in the ratio of these components has been found to produce a regular inverse opal, but with an increased amount of cracks compared to the standard recipe. Further work on the stability of the precursor is needed to completely suppress the cracks from these structures.

A novel architecture for a three-dimensional organic light emitting display has been proposed in this thesis, with the objective of using the inverse opal as an optical cavity, to sharpen the emission spectrum of the active layer. This new architecture consists in a multilayer coated inverse opal, with the same succession of layers as a standard OLED. Firstly, a multilayer device has been made on a standard flat surface, but with the materials and methods envisaged for the three-dimensional architecture. It was observed that the active layer, made with a blend of host and active materials, is very sensitive to annealing, due to the low glass transition temperature of the emissive organic material used. When annealed above this temperature, the organic material crystallises, which leads to the exposure of the layer underneath. To avoid this, a host molecule with a high glass transition of 100 $°C$, BCzPH, is used. The atomic layer deposition forms a conformal layer on top of the organic material, without any obvious unwanted infiltration.

As not all material needed for the fabrication of this new architecture could be deposited by atomic layer deposition, sol gel techniques have been developed to homogeneously coat the inside of the inverse opal. Similarly to the perovskite infiltration, a high concentration is needed to coat the inverse opal, as only precursors which are inside it are used for the coating. The difference with the previous depositions, is that no over-layer is wanted for this structure. The most optimal coating is obtained with a solution concentrated at 150 mg/ml, in a homemade vertical depo-

sition method. A non-continuous thin layer, made of isolated islands of nickel oxide, is observed on both SEM and TEM. The confirmation of the deposition is also done by optical characterisation, with an observed shift of the effective refractive index.

Due to the particular structure of the inverse opal, not all thicknesses of coating can be achieved. Through theoretical geometric considerations, a relation between the maximum coating thickness and the size of the inverse opal pores has been established. By considering an average device thickness, it is shown that a large opal pore size is needed, which leads to the utilisation of high-order optical band-gaps to create an optical cavity in the visible range of wavelengths. The high order band-gaps have smaller spectral widths, however. It is shown that a material with a high refractive index has to be used for the core of the inverse opal in order to provide wide enough band-gaps for use as optical cavities. A three-dimensional model of the inverse opal has been made to simulate its interaction with light. This model initially showed difficulties to converge over a stable measurement, what is attributed to diffraction within the inverse opal deviating the light in multiple directions. Due to the perfectly matched layers chosen as the upper and lower boundary conditions, some of the waves, especially the waves propagating orthogonally to the layers, are not absorbed and lead to simulation instabilities. When replaced by absorbing layers, i.e. different boundary conditions, the waves are more absorbed and a converging simulation is obtained, but increased reflections are expected. The resulting transmitted spectra exhibits the expected optical band-gaps, but a certain amount of noise is still present. More simulations and improved choices of parameters are required to fully characterise the coated structure.

To conclude this work, large scale depositions of polystyrene nanoparticles has been performed by slot die coating, to prove the possible scaling up of the work initiated in this thesis. The deposition have been made with a suspension concentrated at approximately 1%, on UV-ozone treated glass substrates of $15 \times 15\,\mathrm{cm}^2$. A thin deposition of one to two layers of nanoparticles could be achieved over the whole substrate, by heating both the suspension and the substrate during the deposition, and by using a low speed of 0.5mm/s to 1.5mm/s. The samples made by this deposition process exhibit light reflection in the visible range, due to Fabry-Perot interferences rather than a photonic crystal effect, due to their extremely small thickness. These results are promising for the fabrication of homogenous opals on large scale substrates.

Chapter 9

Future work

Most of the work initiated in the course of this thesis project has the potential to be continued and optimised, due to the small amount of research made in certain area.

It has been observed during the work on the creation of a FTO crack free inverse opal that the zeta potential of the synthesised FTO nano-crystals was a critical factor for the quality of the structure. If the zeta potential is not high enough, additional stabilisers have to be introduced, but these compounds create defects due to their recrystallisation. To avoid this, additional work on the synthesis of the FTO nano-crystals has to be done, in order to maximise their zeta potential, so as to enhance the quality of the inverse opals. Similarly, on crack-free FTO inverse opal, the stabilisation of the added precursors still need to be improved, to completely remove cracks from the final structure.

Once a repeatable method for the creation of crack free FTO inverse opal is found, the fabrication of a three-dimensional solar cell becomes easier, due to the reduced risk of exposing the FTO electrode after the perovskite infiltration. However, the methods for a complete infiltration of the perovskite still need optimisation. Amongst the tested methods, the two steps infiltration needs to be improved for the methyl ammonium infiltration, to allow a full conversion of the material. The solvent retarded method can still be improved, both to have a better infiltration, and a deposited material of better quality. In addition, deposition techniques coming from work on mesoscopic perovskite solar cells, which also uses a thick scaffold, could be adapted for an inverse opal solar cell.

In the future, the materials used to make the solar cell could be changed, to make a full use of the inverse opal electrode structure. It is well known that by varying the composition of the perovskite, its band-gap and the position of the conduction and valance band can be tuned. However, this can also affect its electronic properties, such as the charge mobility. With the use of an inverse opal as an electrode, there is a greater tolerance to the charge mobility reduction, because of the short distance between the charge excitation and the electrode. Other parameters, such as the bands' position, can thus be optimised to improve the performances of the solar cell.

The use of ferroelectric materials as a coating for the inverse opal can be envisaged, to make use of a permanent internal field within the structure, which could greatly enhance charge separation. In a standard device, the electron transport layer is only in contact with the active layer on a small surface, and a permanent internal field from this layer would only affect a small volume of the active layer. On the other hand, due to the large surface area provided by a 3D structure, the field would affect most of the active layer, greatly enhancing its effect. Due to the complex composition of ferroelectric materials, research on their ALD deposition has to be conducted, to ensure a continuous layer inside the structure. If this method of deposition is not possible, a sol-gel deposition could be attempted, as shown with the deposition of nickel oxide in chapter 6.

The fabrication of a multilayer inverse opal structure for optical effects, needs to be performed on a crack free structure, to minimise the scattering losses. As seen with the deposition of nickel oxide inside the inverse opal, the sol-gel method can be used as a coating method, but the homogeneity of the coating is not controlled. For this reason, the thickness of layer deposited by this method has to be minimised, to decrease the amount of defects inside the structure. Research has to be done on the deposition by ALD of hole transport layers such as nickel oxide. Molecular layer deposition can also be a possibility for the deposition of emitting molecules within the structure. Another possibility for the homogeneous coating of the FTO inverse opal, is to use electrodeposition, because of the conductive nature of the structure. Such deposition can be used to fill opal and make inverse opal, but a limiting factor is the difficulty for the precursor to travel within the structure. This effect has to be taken into account, to avoid an inhomogeneous coating between the top and the bottom of the inverse opal.

Last but not least, for the work initiated in this chapter, the flat OLED made with atomic layer deposition for the top electrode can be optimised, with the potential of making a fully transparent OLED. Accurate measurement of the impact of the temperature and the composition of the films deposited by ALD has to be performed, to have a clear separation between the electron transport layer and the electrode.

The initiated FDTD model for the simulation of multilayer coated inverse opal still has room for improvement. Work to decrease the reflections created by the boundaries layers which interfere with the wanted measurement has to be performed. To do so, the parameters of the simulation such as the different lengths used in it, and the position of the measurement plane, have to be optimised. When this step is achieved, multilayer structures can be accurately simulated. To simulate the stimulated emission occurring inside the excited active layer, a positive gain material corresponding to the emission spectrum can be used, which will amplify the intensity of the waves inside the inverse opal. As a first approximation, the source of the emission can be considered as being homogeneous over the whole structure, and a volume source can be used on the whole inverse opal.

The work started on large-scale photonic crystals can be greatly improved, building upon to the observations already made. With a more concentrated solution, and an adapted deposition, monolayers of polystyrene nanoparticles can be ob-

tained. The next stage of this work, would be to deposit another layer of polystyrene nanoparticles on top of the previous one, which could allow the creation of opals with controllable thickness, on large lateral scale. The infiltration of these structures, to create inverse opal, has to be adapted due to their large scale. Slot die coating or dip coating can be envisaged to obtain a large scale homogeneous infiltration.

When both the deposition of a monolayer by slot die coating, and the one-step infiltration of opal with FTO nano-crystals are stable and optimised, the combination of these two techniques allow the fabrication of large scale FTO inverse opal, which could open new possibilities for device implementation.

Acknowledgements

I really want to thank people who helped me, either for my work, or simply for moral support. My supervisor, Dr Martyn McLachlan, for accepting me into his group, and for his constant support through these 4 years. Mahmoud Ardakani and Ecaterina Ware for their constant support and training in electron microscopy. Prof. Andrew Horsfield and Dr. Anna Regoutz for giving me the chance to get involved with tutoring, which is one of the activity I enjoyed the most during my time here. Also a big thank you to Dr. Manjula, for her help for the AFHEA application, and anything related to teaching in general. A particular thanks to Dr. Andreas Kafizas, for all his help concerning electrodeposition and photocatalysis in general. Even if none of the work done with him is presented in this thesis, I really thank him for how much he helped me, and for the permanent positive energy that he gave. A very big thank you to Dr. Xuha Wang, for all her help concerning metal evaporation, impedance spectroscopy and much useful advice on things related to science. Thank you so much for all your help and support, especially during my first year when my only wish was to stop everything. Finally I want to thank all the team of HPC Imperial, for their help with software installation and help with questions concerning the use of the supercomputer.

The secondments I made outside Imperial were several of my best memories related to my work. For my secondment in Technion, in Israel, I really thank Prof. Gitti Frey for accepting me in her team for two weeks, and I thank my friend, Artem Levitsky for his help, day and night, for ALD deposition and high resolution SEM imaging. Concerning my secondment in the Holst Center, in Eindhoven, I deeply thank Dr. Robert Abbel, for organising my stay here, and for being more than kind in accepting a change of date for the secondment at the last minute. I really thank Dr. Arjan Langen for his long help with the slot-die coater, and the opal deposition. I also thank Dr. Daniel Tordera and Vittal for their help and support in my two-week stay in Eindhoven.

I also want to thank all my group for all the nice time we spent, inside and outside Imperial. I want to thank and salute my very good friend Jonathan, for all the wonderful time trying restaurants and other activities in London, and for all the nice time we spent. A big thank you to the rest of the people in Imperial, for all the memorable moments we spent : Dr. Bob Xu (Mister Bob), Dr Francesco Reale (the real one), Yohan, Faisal, Birsen, Dean, Becky, Shengyang, Jaspreet... to cite only a few.

A big thank you to the ITN INFORM people, with who I made many travels across Europe, with a big particular mention to my good friends, Jongmin and Nikos.

To my parents, Franck & Solange, for all your support, merci infiniment. I hope you will still be proud of me, even after I left France and spent years in London, for not much in the end.

And finally, to you Anna, $\alpha\gamma\alpha\pi\eta\ \mu o\upsilon$. I would not have finished it if was not thanks to your support, and I will never be able to thank you enough for it. Mmma.

Appendix A

Bragg law for tilted opal

The Bragg diffraction due to an inclined plane inside an opal, requires more calculation compared to a standard horizontal plane. The plane on which the diffraction occurs in supposed to be at an angle α measured to the horizontal, as indicated by figure A.1. The incident beam is at an angle θ with respect to the normal of the structure. The same notation established in section 1.2 is used here, including equation 1.2, and Snell's law, 1.3.

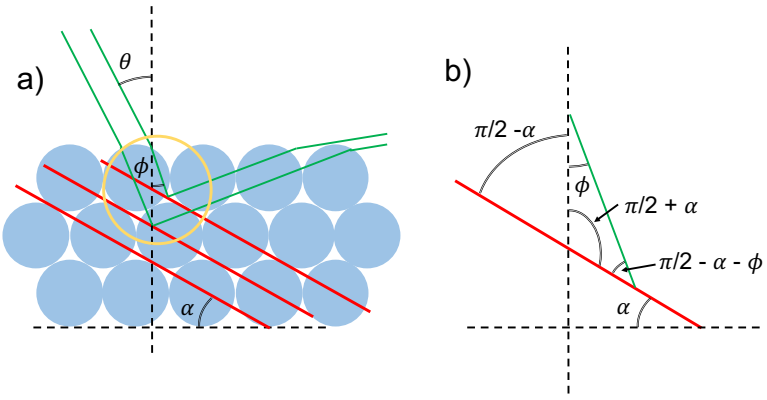


Figure A.1: *a)* Schematic of beam interaction with an inclined plane in an opal, and *b)* enlargement of the area and description of the used angles within the yellow circle in *a)*.

The waves are firstly refracted at the interface between the air and the opal, according to Snell's law. The diffraction effect occurs when the waves reach the inclined plan, in the same way as the standard Bragg law. In order to calculate the angle of interaction between the refracted wave and the inclined plane, trigonometric calculations are used, which are represented in figure A.1 *b)*. The angle of interaction is found to be $\frac{\pi}{2} - \alpha - \phi$. Considering this angle, the Bragg law can be applied for the waves diffracted between the inclined plane and equation A.1 can be established, with d_α the distance between two inclined planes, which is immediately simplified with classical trigonometric rules.

$$\begin{aligned} k\lambda_{opal} &= 2d_\alpha \sin(\frac{\pi}{2} - \alpha - \phi) \\ k\lambda_{opal} &= 2d_\alpha \cos(\alpha + \phi) \end{aligned} \tag{A.1}$$

The sum within the cosine can be expanded with the well-known relation $\cos(\alpha+\phi) = \cos(\alpha)\cos(\phi) - \sin(\alpha)\sin(\phi)$. Applying this to equation A.1 allows the extraction of $\cos(\phi)$ and $\sin(\phi)$, which can be transformed with Snell's law to make θ appear, as summarised equations A.2

$$\begin{aligned} k\lambda_{opal} &= 2d_\alpha \cos(\alpha + \phi) \\ k\lambda_{opal} &= 2d_\alpha(\cos(\alpha)\cos(\phi) - \sin(\alpha)\sin(\phi)) \\ k\lambda_{opal} &= 2d_\alpha(\cos(\alpha)\sqrt{1 - \sin(\phi)^2} - \sin(\alpha)\sin(\phi)) \\ k\frac{\lambda_{air}}{n_{eff}} &= 2d_\alpha(\cos(\alpha)\sqrt{1 - \frac{\sin(\theta)^2}{n_{eff}^2}} - \sin(\alpha)\frac{\sin(\theta)}{n_{eff}}) \end{aligned} \tag{A.2}$$

After simplification, the modified Bragg-Snell law for an inclined plan can be found and is shown in equation A.3.

$$k\lambda_{air} = 2d_\alpha(\cos(\alpha)\sqrt{n_{eff}^2 - \sin^2(\theta)} - \sin(\alpha)\sin(\theta)) \tag{A.3}$$

Appendix B

Inverse-opal defects

In chapter 5, different strategies have been tested to reduce the amount of cracks within the inverse opal. One of them uses the addition of FTO nano-crystals with the polystyrene nanoparticles suspension, and is then evaporated by evaporation induced self assembly. It has been observed that a certain amount of stabiliser is required to prevent the aggregation of the FTO nano-crystals. Tetra methyl ammonium hydroxide (TMAOH) is used in this study as a stabiliser.

However, if too-large important amount of stabiliser is added to the suspension, defects start to appear on top of the opal upon drying of the solution still containing stabiliser, and these defects stay on the structure after calcination. The most prevalent defects are already discussed in chapter 5, but others have been detected, and are shown hereafter. The SEM pictures presented in figures B.1 and B.2 have been made on the same sample prior and after annealing respectively. The sample have been made with 250-nm nanoparticles, concentrated at 0.1%, with the addition of 1ml of FTO nano-crystals suspension, from a 200-ml stock solution stabilised with 800 µl of TMAOH.

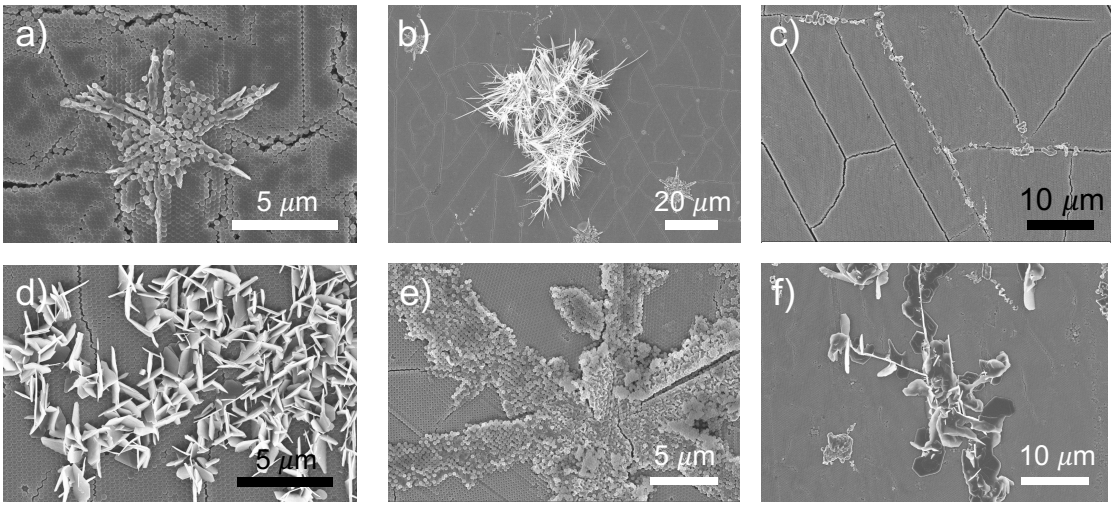


Figure B.1: Defects present on an opal made with the addition of FTO nano-crystals, stabilised with $800\mu l$ of TMAOH.

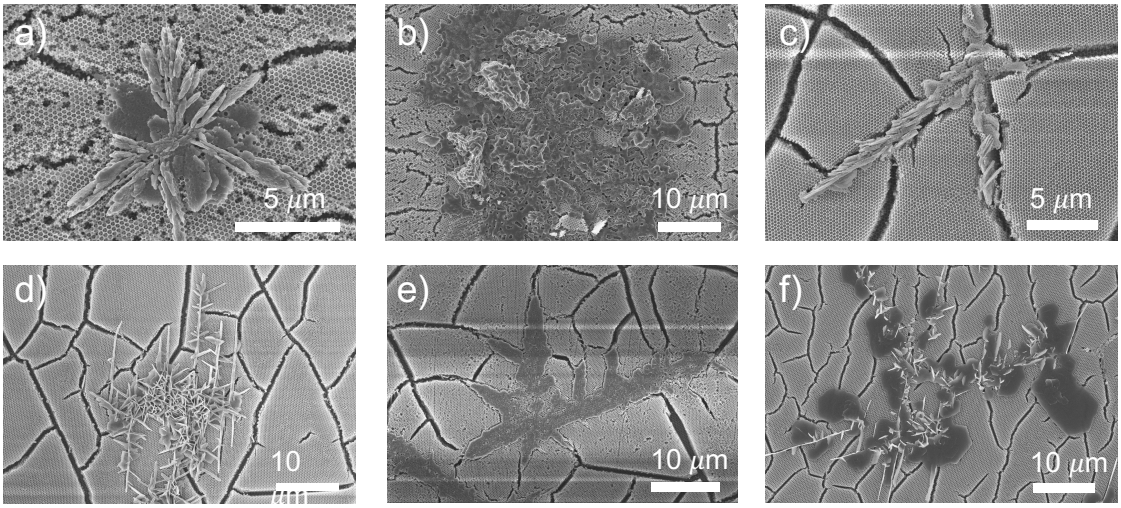


Figure B.2: Defects present on an inverse opal after annealing, made with the addition of FTO nano-crystals stabilised with $800\mu l$ of TMAOH.

Appendix C

Inverse-opal square packing

During the work made in chapter 5 for the creation of crack free FTO inverse opal, particles disposed in a square period have been observed. These particular structures have been observed mostly for structures made with FTO nano-crystals which are weakly stabilised, with $200\mu l$ and $300\mu l$ of TMAOH. The observed square packings are not stable over long range, and are isolated within larger hexagonal packings. SEM pictures of the same sample stabilised with $200\mu l$ of TMAOH, prior and after annealing, are presented figure C.1.

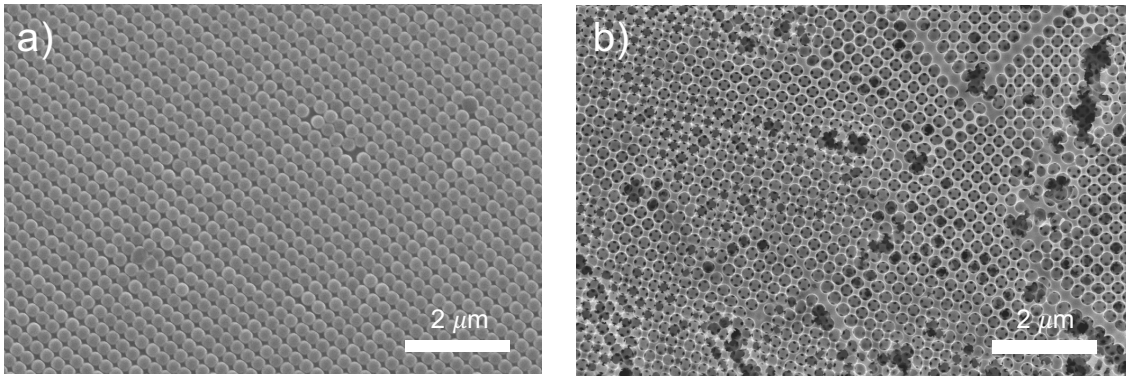


Figure C.1: [100] plan of a fcc crystal on top of the sample, prior *a)* and *b)* after annealing. Sample made with the addition of FTO nano-crystals, stabilised with $200\mu l$ of TMAOH.

It is hypothesised that the observed square periods are views of the [100] planes of the face centre cubic crystal, and not a cubic packing. The normal orientation of the colloidal crystal expose the [111] plan to the surface, due to its higher density. However, due to the presence of weakly stabilised FTO nano-crystals, defects due to aggregation are created on the substrate. These defects might act as nucleation areas, and because their orientation is not always parallel to the substrate, some of them can induce a different orientation of the colloidal crystal, and expose the [100] planes on the top of the structure.

Appendix D

MPB

```
(set! geometry-lattice (make lattice
                  (basis-size (sqrt 0.5) (sqrt 0.5) (sqrt 0.5))
                  (basis1 0 1 1)
                  (basis2 1 0 1)
                  (basis3 1 1 0)))

; Corners of the irreducible Brillouin zone for the fcc lattice

 (set! k-points (interpolate 12 (list
                              (vector3 0 0.5 0.5)    ; X
                              (vector3 0 0.625 0.375)   ; U
                              (vector3 0 0.5 0)    ; L
                              (vector3 0 0 0)     ; Gamma
                              (vector3 0 0.5 0.5)    ; X
                              (vector3 0.25 0.75 0.5)   ; W
                              (vector3 0.375 0.75 0.375))))
; K

 ; parameters

 (define-param radair (/ 1 (* 2 (sqrt 2))))
  ; the radius of air sphere

(define air (make dielectric (epsilon (* 1 1))))
(define fto (make dielectric (epsilon (* 1.9 1.9))))


; Unit cell of fcc latice : an air sphere inside a block of material

(set! geometry (list (make block (center 0 0 0)
(size 1 1 1) (material fto))

                     (make sphere (center 0 0 0) (radius radair)
```

```
                              (material air))
                                             ))

;simulation parameters

 (set-param! resolution 64) ; use a 64x64x64 grid
 (set-param! mesh-size 8)
 (set-param! num-bands 15)

; run calculation
 (run)
```

Appendix E

MEEP - standard inverse opal

```
(set! eps-averaging? false)
(set-param! resolution 50)


(define-param rad 0.31) ; radius internal spheres

(define-param fto-thick 0.1) ; bottom layer fro
(define-param glass-thick 2)

(define-param air-thick 5) ; air layer on top

(define-param pmlt 2)

(define-param layers 9) ; amount of inverse opal layer
(define-param excite 2) ; from top, level where is the excitation

(define-param perio 2) ; for repeated units

(set-param! k-point (vector3 0 0 0))


; calculated values

(define dist (* 2 rad)) ; dist between spheres centre

(define-param centre-dist (* dist (/ (sqrt 2) (sqrt 3))))
; vertical distance between 2 spheres centres.
(define io-thick (+ rad (* centre-dist (- layers 1))))
; distance between bottom of the IO and the top (half sphere)



(define sx (* perio dist (sqrt 3)))
```

```
(define sy (* perio dist))
(define sz (+ (* pmlt 2) glass-thick fto-thick io-thick air-thick))

(set! geometry-lattice (make lattice (size sx sy sz)))

(define glass-centre (+ pmlt (/ glass-thick 2) (/ sz -2)))
; centre of glass
(define fto-centre (+ glass-centre (/ glass-thick 2) (/ fto-thick 2)))
; centre FTO
(define io-centre (+ fto-centre (/ fto-thick 2) (/ io-thick 2)))
; centre IO
(define air-centre ( - (/ sz 2) pmlt (/ air-thick 2)))
; centre air

(define first-layer (+ fto-centre (/ fto-thick 2) radius-nio))
; first layer coordinate

(define excite-level (+ fto-centre (/ fto-thick 2)
                        (+ radius-nio (* centre-dist (- layers excite)

(define k 0) ; test variable
; materials

(define air (make dielectric (epsilon (* 1 1))))
(define fto (make dielectric (epsilon (* 2.5 2.5)))

(define glass (make dielectric (epsilon (* 1.5 1.5)))


;obj-list test



(set! geometry
          (list
           (make block
             (center 0 0 glass-centre)
             (size sx sy glass-thick)
             (material glass))
           (make block
             (center 0 0 fto-centre)
             (size sx sy fto-thick)
             (material fto))
           (make block
             (center 0 0 io-centre)
             (size sx sy io-thick)
             (material fto))
           )
```

```
)



(map (lambda (z)
(map (lambda (y)
(map (lambda (x)
(if (even? z) (set! k 0) (set! k 1))
(set! geometry
     (append geometry
     (list (make sphere
    (center (+ (* y dist (/ (sqrt 3) 2)) (* k (* dist (/ -1 (sqrt 3)))))
    (+ (* x dist) (* y (/ dist 2))) (+ first-layer (* z centre-dist)) )
            (radius rad)
            (material air))  )))
)
(arith-sequence -5 1 10)))
(arith-sequence -5 1 10)))
(arith-sequence 0 1 layers))


(set! geometry
     (append geometry
        (list
         (make block
             (center 0 0 air-centre)
             (size sx sy air-thick)
             (material air)
         )
        )
     )
)



(define-param lam 0.65)
(define-param lam-range 0.15)

(define-param lam-min (- lam lam-range))
(define-param lam-max (+ lam lam-range))

(define-param fmin (/ 1 lam-max))
(define-param fmax (/ 1 lam-min))

(define-param fcen (/ (+ fmin fmax) 2))

(define-param df (- fmax fmin))
```

```
(set! sources (list
     (make source
         (src (make gaussian-src (frequency fcen) (fwidth df)))
         (component Ex)
         (center 0 0 (+ (/ sz -2) pmlt 0.5))
         (size sx sy 0))))

(set! pml-layers (list(make absorber (thickness pmlt) (direction Z))))

(define-param nfreq 200)
; number of frequencies at which to compute flux


(define trans ; trans flux
      (add-flux fcen df nfreq
                (make flux-region
                  (center 0 0 (- (/ sz 2) pmlt 2)) (size sx sy 0))))




(run-sources+
(stop-when-fields-decayed
50 Ex (vector3 0 0 (- (/ sz 2) pmlt 0.1)) 1e-9)
)



(display-fluxes trans)
```

Appendix F

MEEP - multilayer inverse opal

```
(set! eps-averaging? false)
(set-param! resolution 50)


(define-param rad 0.32) ; radius internal spheres
(define-param nio_thick 0.010) ; thickness NiO
(define-param active_thick 0.015)
(define-param zno_thick 0.010)
(define-param azo_thick 0.011)

(define-param fto_thick 0.1) ; bottom layer fro
(define-param glass_thick 2)

(define-param air_thick 5) ; air layer on top

(define-param pmlt 2)

(define-param layers 9) ; amount of inverse opal layer
(define-param excite 2) ; from top, level where is the excitation

(define-param perio 2) ; for repeated units

(set-param! k-point (vector3 0 0 0))


; calculated values

(define dist (* 2 rad)) ; dist between spheres centre
(define tot_layers (+ nio_thick active_thick zno_thick azo_thick))
 ; total thickness of all layers
(define radius_nio (+ rad tot_layers))
; radius of initial void inside IO, use to build NiO layer
(define radius_active (- radius_nio nio_thick))
```

```
; radius sphere for active layer
(define radius_zno (- radius_active active_thick))
 ; radius sphere ZnO
(define radius_azo (- radius_zno zno_thick))
; radius AZO sphere
(define radius_void (- radius_azo azo_thick))
; radius AZO

(define-param centre_dist (* dist (/ (sqrt 2) (sqrt 3))))
 ; vertical distance between 2 spheres centres.
(define io_thick (+ radius_nio (* centre_dist (- layers 1))))
 ; distance between bottom of the IO and the top (half sphere)



(define sx (* perio dist (sqrt 3)))
(define sy (* perio dist))
(define sz (+ (* pmlt 2) glass_thick fto_thick io_thick air_thick))

(set! geometry-lattice (make lattice (size sx sy sz)))

(define glass_centre (+ pmlt (/ glass_thick 2) (/ sz -2)))
; centre of glass
(define fto_centre (+ glass_centre (/ glass_thick 2) (/ fto_thick 2)))
; centre FTO
(define io_centre (+ fto_centre (/ fto_thick 2) (/ io_thick 2)))
; centre IO
(define air_centre ( - (/ sz 2) pmlt (/ air_thick 2)))
 ; centre air layer

(define first_layer (+ fto_centre (/ fto_thick 2) radius_nio))
; first layer coordinate

(define excite_level (+ fto_centre (/ fto_thick 2)
            (+ radius_nio (* centre_dist (- layers excite)))))

(define k 0) ; test variable
; materials

(define air (make dielectric (epsilon (* 1 1))))
(define fto (make dielectric (epsilon (* 2.5 2.5))))
(define nio (make dielectric (epsilon (* 1.8 1.8))))
(define zno (make dielectric (epsilon (* 1.8 1.8))))
(define azo (make dielectric (epsilon (* 2 2))))
(define active (make dielectric (epsilon (* 2.5 2.5))))

(define glass (make dielectric (epsilon (* 1.5 1.5))))
```

```
;obj-list test



(set! geometry
          (list
           (make block
             (center 0 0 glass_centre)
             (size sx sy glass_thick)
             (material glass))
           (make block
             (center 0 0 fto_centre)
             (size sx sy fto_thick)
             (material fto))
           (make block
             (center 0 0 io_centre)
             (size sx sy io_thick)
             (material fto))
           )
)

;nio spheres

(map (lambda (z)
(map (lambda (y)
(map (lambda (x)
(if (even? z) (set! k 0) (set! k 1))
(set! geometry
     (append geometry
     (list (make sphere
       (center (+ (* y dist (/ (sqrt 3) 2)) (* k (* dist (/ -1 (sqrt 3)))))
           (+ (* x dist) (* y (/ dist 2))) (+ first_layer (* z centre_dist)
       (radius radius_nio)
       (material nio))  )))
)
(arith-sequence -5 1 10)))
(arith-sequence -5 1 10)))
(arith-sequence 0 1 layers))


;active spheres

(map (lambda (z)
(map (lambda (y)
(map (lambda (x)
(if (even? z) (set! k 0) (set! k 1))
(set! geometry
```

```
      (append geometry
      (list (make sphere
        (center (+ (* y dist (/ (sqrt 3) 2)) (* k (* dist (/ -1 (sqrt 3
            (+ (* x dist) (* y (/ dist 2))) (+ first_layer (* z centre_
        (radius radius_active)
        (material active))  )))
)
(arith-sequence -5 1 10)))
(arith-sequence -5 1 10)))
(arith-sequence 0 1 layers))


;zno sphere

(map (lambda (z)
(map (lambda (y)
(map (lambda (x)
(if (even? z) (set! k 0) (set! k 1))
(set! geometry
      (append geometry
      (list (make sphere
        (center (+ (* y dist (/ (sqrt 3) 2)) (* k (* dist (/ -1 (sqrt 3
            (+ (* x dist) (* y (/ dist 2))) (+ first_layer (* z centre_
        (radius radius_zno)
        (material zno))  )))
)
(arith-sequence -5 1 10)))
(arith-sequence -5 1 10)))
(arith-sequence 0 1 layers))


; azo layer

(map (lambda (z)
(map (lambda (y)
(map (lambda (x)
(if (even? z) (set! k 0) (set! k 1))
(set! geometry
      (append geometry
      (list (make sphere
        (center (+ (* y dist (/ (sqrt 3) 2)) (* k (* dist (/ -1 (sqrt 3
            (+ (* x dist) (* y (/ dist 2))) (+ first_layer (* z centre_
        (radius radius_azo)
        (material azo))  )))
)
(arith-sequence -5 1 10)))
(arith-sequence -5 1 10)))
(arith-sequence 0 1 layers))
```

```
;air layer

(map (lambda (z)
(map (lambda (y)
(map (lambda (x)
(if (even? z) (set! k 0) (set! k 1))
(set! geometry
     (append geometry
     (list (make sphere
       (center (+ (* y dist (/ (sqrt 3) 2)) (* k (* dist (/ -1 (sqrt 3)))))
           (+ (* x dist) (* y (/ dist 2))) (+ first_layer (* z centre_dist)
       (radius radius_void)
       (material air))  )))
)
(arith-sequence -5 1 10)))
(arith-sequence -5 1 10)))
(arith-sequence 0 1 layers))

(set! geometry
     (append geometry
        (list
         (make block
             (center 0 0 air_centre)
             (size sx sy air_thick)
             (material air)
         )
        )
     )
)



(define-param lam 0.65)
(define-param lam_range 0.15)

(define-param lam_min (- lam lam_range))
(define-param lam_max (+ lam lam_range))

(define-param fmin (/ 1 lam_max))
(define-param fmax (/ 1 lam_min))

(define-param fcen (/ (+ fmin fmax) 2))

(define-param df (- fmax fmin))


(set! sources (list
```

```
      (make source
      (src (make gaussian-src (frequency fcen) (fwidth df)))
      (component Ex)
      (center 0 0 (+ (/ sz -2) pmlt 0.5))
      (size sx sy 0))))

(set! pml-layers (list (make absorber (thickness pmlt) (direction Z) )

(define-param nfreq 200)
 ; number of frequencies at which to compute flux


(define trans ; trans flux
      (add-flux fcen df nfreq
                (make flux-region
                  (center 0 0 (- (/ sz 2) pmlt 2)) (size sx sy 0))))




(run-sources+
(stop-when-fields-decayed 50 Ex
        (vector3 0 0 (- (/ sz 2) pmlt 0.1)) 1e-9)
)



(display-fluxes trans)
```

Appendix G

Permission documents

Authorisation for the use of an image from the book "Photonic crystals : Molding the flow of light", Princeton Press [3] .

Dear David –
Thank you for your online permissions request.
Please note that permission is not needed to reproduce Princeton University Press content within a PhD thesis/dissertation. Please be sure to credit the material appropriately. Permission is only granted for internal publication of your work (i.e., library binding, UMI, class assignment), with no external distribution permitted of any kind. If you publish your dissertation, thesis, or translation in the future in any form and include PUP material you must request formal permission. Please note that this is applicable only for material for which Princeton University Press holds the copyright. For images and illustrations, please check the credit line. If the material is copyrighted by another institution or individual, you will need to contact the appropriate party for permission. It is the requestor's responsibility to ascertain copyright.
Best,
PUP Permissions Department
Princeton University Press

Authorisation for the use of chemical structures pictures from Ossila :

Dear David,
I hope that you are doing well today.
I can confirm that we are happy for you to use the following pictures, so long as a linkback is given to the original Ossila page in the figure caption (not the end captions). Please read the below link with further information on the permission:
`https://www.ossila.com/pages/reprinting-permissions?_pos=1&_sid=59b75922a&_ss=r`
If you need anything further then please do let me know.
Kind regards,
Rosie
Customer Care and Logistics Manager

Ossila Ltd, Solpro Business Park, Windsor St, Sheffield, S4 7WB.

Request sent for the authorisation for the use of an image from the thesis "Investigation of multiferroic and photocatalytic properties of Li doped BiFeO3 nanoparticles prepared by ultrasonication" [12] .

Dear Sir, Madam,

My name is David Poussin, I am a PhD student at Imperial College London. I would like to ask you permission to use a figure from the following PhD thesis, made in your university, for my own thesis (it is a scheme describing a technique).
Investigation of multiferroic and photocatalytic properties of Li doped BiFeO3 nanoparticles prepared by ultrasonication
Areef Billah, A. H. M.
URI: http://lib.buet.ac.bd:8080/xmlui/handle/123456789/4495
Date: 2016-05
Would I be possible for me to reuse it?
Thank you very much by advance,
David Poussin

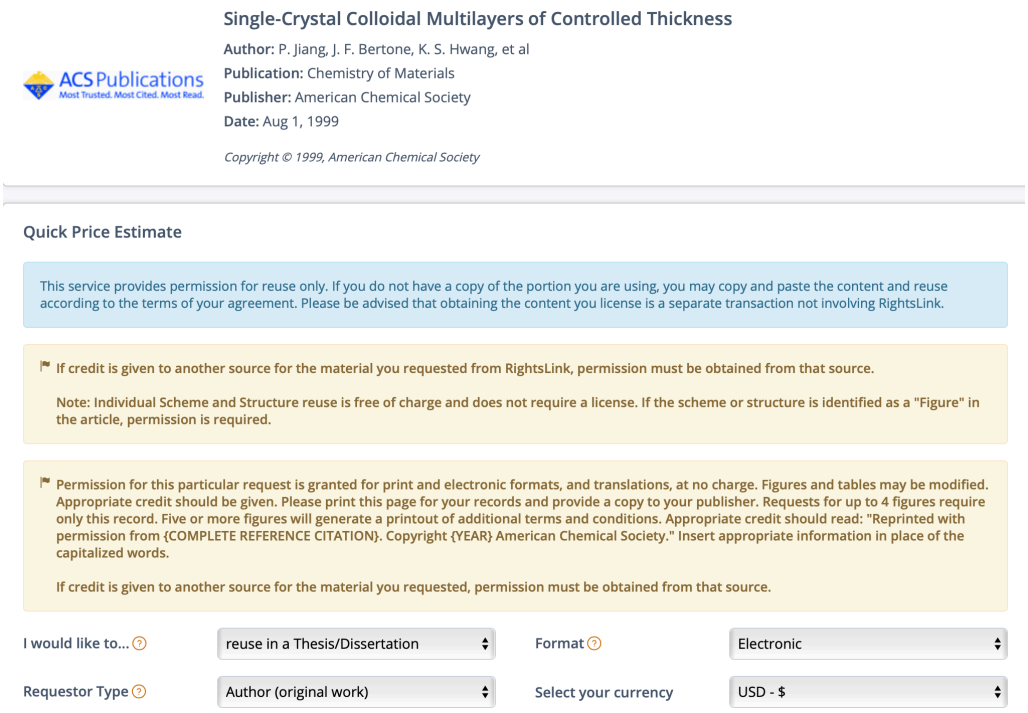


Figure G.1: Authorisation for the use of an image from [5].



Particulate pattern formation and its morphology control by convective self-assembly

Author: Satoshi Watanabe,Minoru T. Miyahara
Publication: Advanced Powder Technology
Publisher: Elsevier
Date: November 2013

Copyright © 2013 The Society of Powder Technology Japan. Published by Elsevier B.V. All rights reserved.

Order Completed

Thank you for your order.

This Agreement between Mr. David Poussin ("You") and Elsevier ("Elsevier") consists of your license details and the terms and conditions provided by Elsevier and Copyright Clearance Center.

Your confirmation email will contain your order number for future reference.

License Number	4802140708888	Printable Details
License date	Apr 04, 2020	

Licensed Content

Licensed Content Publisher	Elsevier
Licensed Content Publication	Advanced Powder Technology

Order Details

Type of Use	reuse in a thesis/dissertation
Portion	figures/tables/illustrations
Number of figures/tables/illustrations	1

Figure G.2: Authorisation for the use of an image from [6].



Microscopy evidence of the face-centered cubic arrangement of monodisperse polystyrene nanospheres

Author: Hui Zhang,Ren-guan Duan,Fan Li,Qing Tang,Wen-chao Li
Publication: Materials & Design
Publisher: Elsevier
Date: 2007

Copyright © 2005 Elsevier Ltd. All rights reserved.

Order Completed

Thank you for your order.

This Agreement between Mr. David Poussin ("You") and Elsevier ("Elsevier") consists of your license details and the terms and conditions provided by Elsevier and Copyright Clearance Center.

Your confirmation email will contain your order number for future reference.

License Number	4802140983952	Printable Details
License date	Apr 04, 2020	

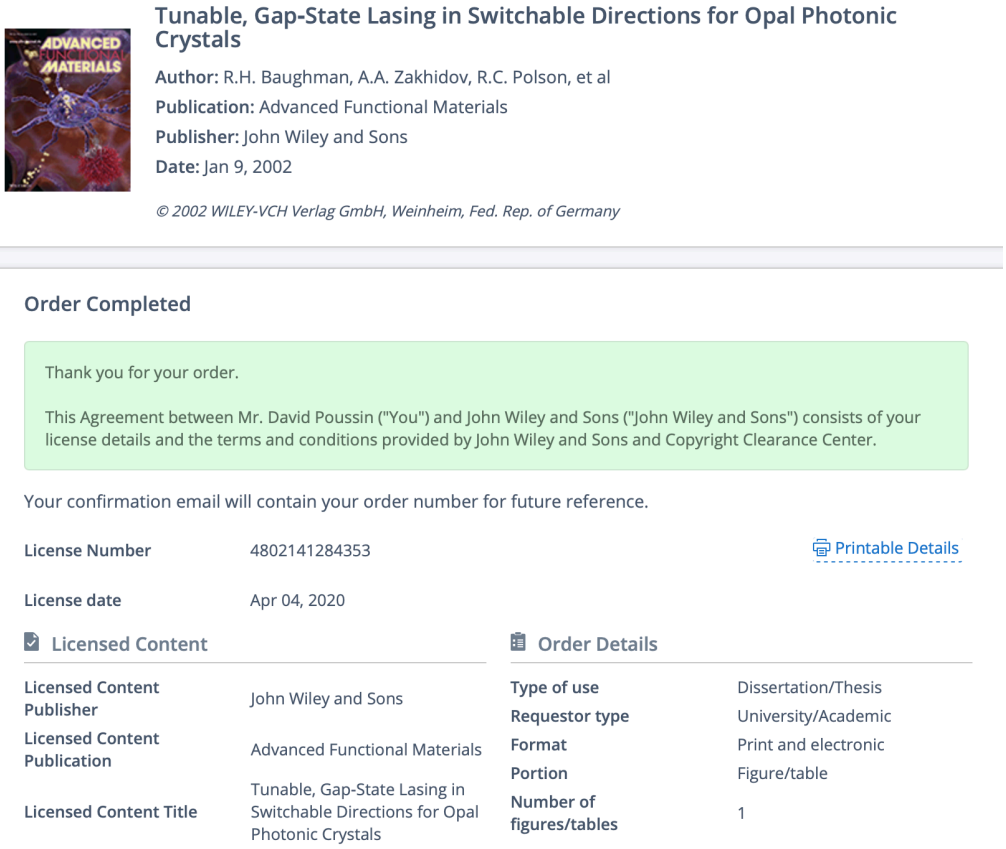
Licensed Content

Licensed Content Publisher	Elsevier
Licensed Content Publication	Materials & Design

Order Details

Type of Use	reuse in a thesis/dissertation
Portion	figures/tables/illustrations
Number of figures/tables/illustrations	1

Figure G.3: Authorisation for the use of an image from [7].



Tunable, Gap-State Lasing in Switchable Directions for Opal Photonic Crystals

Author: R.H. Baughman, A.A. Zakhidov, R.C. Polson, et al
Publication: Advanced Functional Materials
Publisher: John Wiley and Sons
Date: Jan 9, 2002

© 2002 WILEY-VCH Verlag GmbH, Weinheim, Fed. Rep. of Germany

Order Completed

Thank you for your order.

This Agreement between Mr. David Poussin ("You") and John Wiley and Sons ("John Wiley and Sons") consists of your license details and the terms and conditions provided by John Wiley and Sons and Copyright Clearance Center.

Your confirmation email will contain your order number for future reference.

License Number	4802141284353
License date	Apr 04, 2020

Printable Details

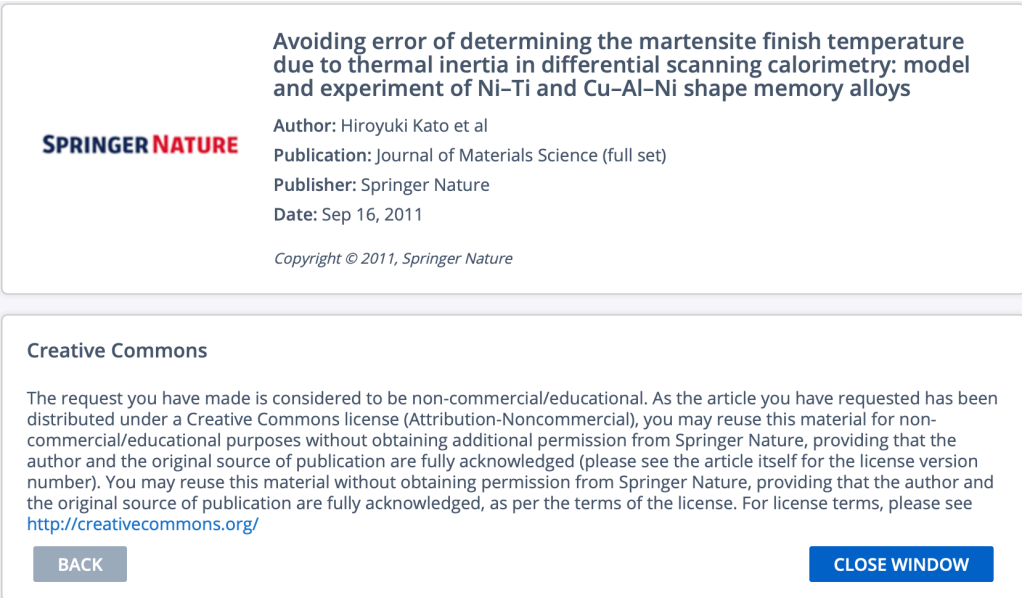
Licensed Content

Licensed Content Publisher	John Wiley and Sons
Licensed Content Publication	Advanced Functional Materials
Licensed Content Title	Tunable, Gap-State Lasing in Switchable Directions for Opal Photonic Crystals

Order Details

Type of use	Dissertation/Thesis
Requestor type	University/Academic
Format	Print and electronic
Portion	Figure/table
Number of figures/tables	1

Figure G.4: Authorisation for the use of an image from [9] .



Avoiding error of determining the martensite finish temperature due to thermal inertia in differential scanning calorimetry: model and experiment of Ni–Ti and Cu–Al–Ni shape memory alloys

Author: Hiroyuki Kato et al
Publication: Journal of Materials Science (full set)
Publisher: Springer Nature
Date: Sep 16, 2011

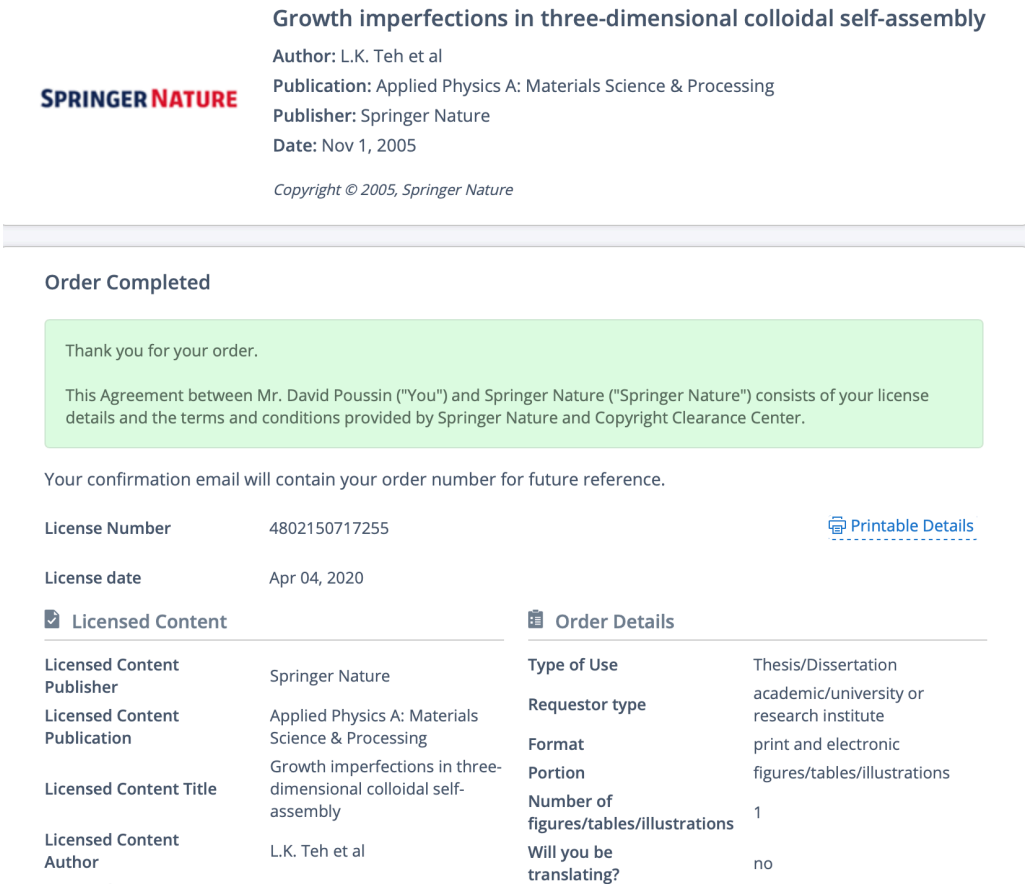
Copyright © 2011, Springer Nature

Creative Commons

The request you have made is considered to be non-commercial/educational. As the article you have requested has been distributed under a Creative Commons license (Attribution-Noncommercial), you may reuse this material for non-commercial/educational purposes without obtaining additional permission from Springer Nature, providing that the author and the original source of publication are fully acknowledged (please see the article itself for the license version number). You may reuse this material without obtaining permission from Springer Nature, providing that the author and the original source of publication are fully acknowledged, as per the terms of the license. For license terms, please see http://creativecommons.org/

BACK CLOSE WINDOW

Figure G.5: Authorisation for the use of an image from [13] .



Growth imperfections in three-dimensional colloidal self-assembly

Author: L.K. Teh et al
Publication: Applied Physics A: Materials Science & Processing
Publisher: Springer Nature
Date: Nov 1, 2005

Copyright © 2005, Springer Nature

Order Completed

Thank you for your order.

This Agreement between Mr. David Poussin ("You") and Springer Nature ("Springer Nature") consists of your license details and the terms and conditions provided by Springer Nature and Copyright Clearance Center.

Your confirmation email will contain your order number for future reference.

License Number	4802150717255
License date	Apr 04, 2020

Printable Details

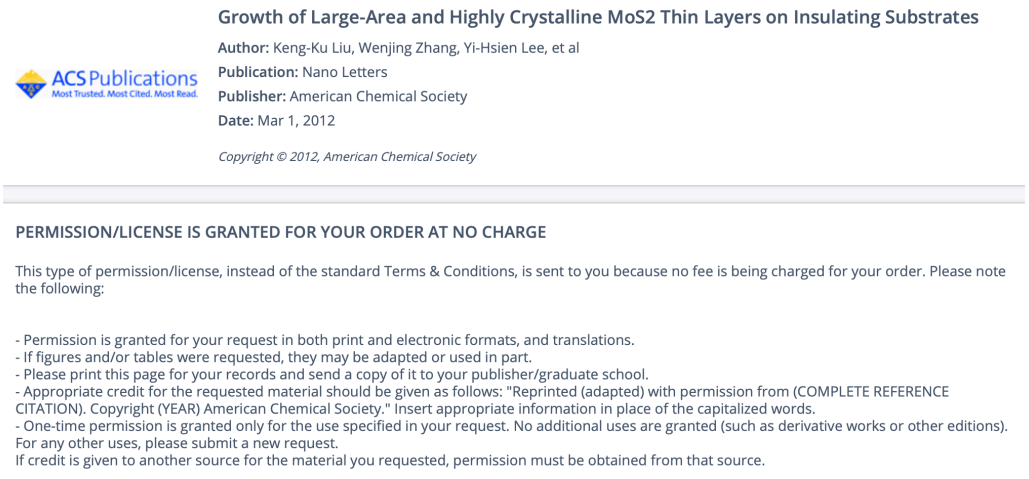
Licensed Content

Licensed Content Publisher	Springer Nature
Licensed Content Publication	Applied Physics A: Materials Science & Processing
Licensed Content Title	Growth imperfections in three-dimensional colloidal self-assembly
Licensed Content Author	L.K. Teh et al

Order Details

Type of Use	Thesis/Dissertation
Requestor type	academic/university or research institute
Format	print and electronic
Portion	figures/tables/illustrations
Number of figures/tables/illustrations	1
Will you be translating?	no

Figure G.6: Authorisation for the use of an image from [14].



Growth of Large-Area and Highly Crystalline MoS2 Thin Layers on Insulating Substrates

Author: Keng-Ku Liu, Wenjing Zhang, Yi-Hsien Lee, et al
Publication: Nano Letters
Publisher: American Chemical Society
Date: Mar 1, 2012

Copyright © 2012, American Chemical Society

PERMISSION/LICENSE IS GRANTED FOR YOUR ORDER AT NO CHARGE

This type of permission/license, instead of the standard Terms & Conditions, is sent to you because no fee is being charged for your order. Please note the following:

- Permission is granted for your request in both print and electronic formats, and translations.
- If figures and/or tables were requested, they may be adapted or used in part.
- Please print this page for your records and send a copy of it to your publisher/graduate school.
- Appropriate credit for the requested material should be given as follows: "Reprinted (adapted) with permission from (COMPLETE REFERENCE CITATION). Copyright (YEAR) American Chemical Society." Insert appropriate information in place of the capitalized words.
- One-time permission is granted only for the use specified in your request. No additional uses are granted (such as derivative works or other editions). For any other uses, please submit a new request.

If credit is given to another source for the material you requested, permission must be obtained from that source.

Figure G.7: Authorisation for the use of an image from [10].

Bibliography

[1] T. Klein, "The 'fire' of opals," *Europhysics News*, vol. 46, no. 2, pp. 15–16, 2015.

[2] J. Sanders, "Structure of opals," *Journal de Physique Colloques*, vol. 46, 1985.

[3] J. D. Joannopoulos, S. G. Johnson, J. N. Winn, and R. D. Meade, *Photonic crystals : Molding the flow of light*.

[4] Inductiveload, "Brillouin zone."

[5] P. Jiang, J. F. Bertone, K. S. Hwang, V. L. Colvin, P. Jiang, J. F. Bertone, K. S. Hwang, and V. L. Colvin, "Single-Crystal Colloidal Multilayers of Controlled Thickness Single-Crystal Colloidal Multilayers of Controlled Thickness," *Chem. Mater*, vol. 11, pp. 2132–2140, 1999.

[6] S. Watanabe and M. T. Miyahara, "Particulate pattern formation and its morphology control by convective self-assembly," *Advanced Powder Technology*, vol. 24, no. 6, pp. 897–907, 2013.

[7] H. Zhang, R. guan Duan, F. Li, Q. Tang, and W. chao Li, "Microscopy evidence of the face-centered cubic arrangement of monodisperse polystyrene nanospheres," *Materials and Design*, vol. 28, no. 3, pp. 1045–1049, 2007.

[8] X. Chen, S. Yang, Y. C. Zheng, Y. Chen, Y. Hou, X. H. Yang, and H. G. Yang, "Multifunctional Inverse Opal-Like TiO2Electron Transport Layer for Efficient Hybrid Perovskite Solar Cells," *Advanced Science*, vol. 2, no. 9, pp. 1–6, 2015.

[9] M. N. Shkunov, Z. V. Vardeny, M. C. DeLong, R. C. Polson, A. A. Zakhidov, and R. H. Baughman, "Tunable, gap-state lasing in switchable directions for opal photonic crystals," *Advanced Functional Materials*, vol. 12, no. 1, pp. 21–26, 2002.

[10] K. K. Liu, W. Zhang, Y. H. Lee, Y. C. Lin, M. T. Chang, C. Y. Su, C. S. Chang, H. Li, Y. Shi, H. Zhang, C. S. Lai, and L. J. Li, "Growth of large-area and highly crystalline MoS 2 thin layers on insulating substrates," *Nano Letters*, vol. 12, no. 3, pp. 1538–1544, 2012.

[11] Hydrargyrum, "XRD-scheme."

[12] A. Billah, *Investigation of multiferroic and photocatalytic properties of Li doped BiFeO3 nanoparticles prepared by ultrasonication*. PhD thesis, 2017.

[13] H. Kato and K. Sasaki, "Avoiding error of determining the martensite finish temperature due to thermal inertia in differential scanning calorimetry: Model and experiment of Ni-Ti and Cu-Al-Ni shape memory alloys," *Journal of Materials Science*, vol. 47, no. 3, pp. 1399–1410, 2012.

[14] L. K. Teh, N. K. Tan, C. C. Wong, and S. Li, "Growth imperfections in three-dimensional colloidal self-assembly," *Applied Physics A: Materials Science and Processing*, vol. 81, no. 7, pp. 1399–1404, 2005.

[15] D. Yoon, Q. Su, H. Wang, and A. Manthiram, "Superior power density solid oxide fuel cells by enlarging the three-phase boundary region of a NiO-Ce0.8Gd0.2O1.9 composite anode through optimized surface structure," *Physical Chemistry Chemical Physics*, vol. 15, no. 36, pp. 14966–14972, 2013.

[16] "Ossila."

[17] R. Feynman, "There's plenty of room at the bottom."

[18] C. Kittel, *Introduction to Solid State Physics*. 1996.

[19] L. Rayleigh, " XVII. On the maintenance of vibrations by forces of double frequency, and on the propagation of waves through a medium endowed with a periodic structure ," 1887.

[20] H. Shen, Z. Wang, Y. Wu, and B. Yang, "One-dimensional photonic crystals: Fabrication, responsiveness and emerging applications in 3D construction," *RSC Advances*, vol. 6, no. 6, pp. 4505–4520, 2016.

[21] P. Lalanne, C. Sauvan, and J. P. Hugonin, "Photon confinement in photonic crystal nanocavities," *Laser and Photonics Reviews*, vol. 2, no. 6, pp. 514–526, 2008.

[22] C. Zhang, R. Elafandy, and J. Han, "Distributed Bragg Reflectors for GaN-Based VCSELs," *Applied Sciences*, vol. 9, no. 8, p. 1593., 2019.

[23] Laseroptik, "Laseroptik - High refelection."

[24] R. D. Meade, K. D. Brommer, A. M. Rappe, and J. D. Joannopoulos, "Existence of a photonic band gap in two dimensions," *Applied Physics Letters*, vol. 61, no. 4, pp. 495–497, 1992.

[25] H. Ye, Y. Liu, and Z. Yu, "Optical Diode Based on Two-Dimensional Photonic Crystal," *IntechOpen*, vol. Chapter 9, 2018.

[26] H. Benisty, C. Weisbuch, D. Labilloy, M. Rattier, C. J. Smith, T. F. Krauss, R. M. De La Rue, R. Houdré, U. Oesterle, C. Jouanin, and D. Cassagne, "Optical and confinement properties of two-dimensional photonic crystals," *Journal of Lightwave Technology*, vol. 17, no. 11, pp. 2063–2077, 1999.

[27] P. Russel, "Photonic Crystal Fibers," *Science*, vol. 299, p. 358, 2003.

[28] K. Tajima, J. Zhou, N. Nakajima, and K. Sato, "Ultralow Loss and Long Length Photonic," *Lightwave*, vol. 22, no. 1, pp. 7–10, 2004.

[29] E. Yablonovitch, "Inhibited Spontaneous Emission in Solid-State Physics and Electronics," *Physical Review Letters*, vol. 58, no. 20, 1987.

[30] E. Yablonovitch, T. J. Gmitter, and K. M. Leung, "Photonic band structure: The face-centered-cubic case employing nonspherical atoms," *Physical Review Letters*, vol. 67, no. 17, pp. 2295–2298, 1991.

[31] W. L. Vos, R. Sprik, A. van Blaaderen, A. Imhof, A. Lagendijk, and G. H. Wegdam, "Strong effects of photonic band structures on the diffraction of colloidal crystals," *Physical Review B - Condensed Matter and Materials Physics*, vol. 53, no. 24, pp. 16231–16235, 1996.

[32] A. Blanco, E. Chomski, S. Grabtchak, M. Ibisate, S. John, S. W. Leonard, C. Lopez, F. Meseguer, H. Miguez, J. P. Mondla, G. A. Ozin, O. Toader, and H. M. Van Driel, "Large-scale synthesis of a silicon photonic crystal with a complete three-dimensional bandgap near 1.5 micrometres," *Nature*, vol. 405, no. 6785, pp. 437–440, 2000.

[33] H. Li, J. Wang, Z. Pan, L. Cui, L. Xu, R. Wang, Y. Song, and L. Jiang, "Amplifying fluorescence sensing based on inverse opal photonic crystal toward trace TNT detection," *Journal of Materials Chemistry*, vol. 21, no. 6, pp. 1730–1735, 2011.

[34] J. E. G. J. Wijnhoven and W. L. Vos, "Preparation of Photonic Crystals Made of Air Spheres in Titania," *Science*, vol. 281, no. 5378, pp. 802–804, 1998.

[35] R. W. Scott, S. M. Yang, G. Chabanis, N. Coombs, D. E. Williams, and G. A. Ozin, "Tin dioxide opals and inverted opals: Near-ideal microstructures for gas sensors," *Advanced Materials*, vol. 13, no. 19, pp. 1468–1472, 2001.

[36] M. Sadakane, T. Horiuchi, N. Kato, C. Takahashi, and W. Ueda, "Facile preparation of three-dimensionally ordered macroporous alumina, iron oxide, chromium oxide, manganese oxide, and their mixed-metal oxides with high porosity," *Chemistry of Materials*, vol. 19, no. 23, pp. 5779–5785, 2007.

[37] A. A. Zakhidov, R. H. Baughman, Z. Iqbal, C. Cui, I. Khayrullin, S. O. Dantas, J. Marti, V. G. Ralchenko, J. Marti, and V. G. Ralchenko, "Carbon Structures with Three-Dimensional Periodicity at Optical Wavelengths," *Science*, vol. 282, no. 5390, pp. 897–901, 1998.

[38] B. H. Juárez, C. López, and C. Alonso, "Formation of zinc inverted opals on indium tin oxide and silicon substrates by electrochemical deposition," *Journal of Physical Chemistry B*, vol. 108, no. 43, pp. 16708–16712, 2004.

[39] Y. C. Lee, T. J. Kuo, C. J. Hsu, Y. W. Su, and C. C. Chen, "Fabrication of 3D macroporous structures of II-VI and III-V semiconductors using electrochemical deposition," *Langmuir*, vol. 18, no. 25, pp. 9942–9946, 2002.

[40] Y.-J. Lee and P. Braun, "Tunable Inverse Opal Hydrogel pH Sensors," *Advanced Materials*, vol. 15, no. 78, pp. 563–566, 2003.

[41] J. Lu, F. Zheng, Y. Cheng, H. Ding, Y. Zhao, and Z. Gu, "Hybrid inverse opals for regulating cell adhesion and orientation," *Nanoscale*, vol. 6, no. 18, pp. 10650–10656, 2014.

[42] K. Min, S. Kim, and S. Kim, "Deformable and conformal silk hydrogel inverse opal," *Proceedings of the National Academy of Sciences of the United States of America*, vol. 114, no. 24, pp. 6185–6190, 2017.

[43] S. Y. Lin, J. G. Fleming, D. L. Hetherington, B. K. Smith, R. Biswas, K. M. Ho, M. M. Sigalas, W. Zubrzycki, S. R. Kurtz, J. Bur, and J. J., "A three-dimensional photonic crystal operating at infrared wavelengths," *Nature*, vol. 394, no. 6690, pp. 251–253, 1998.

[44] S. Ogawa, M. Imada, S. Yoshimoto, M. Okano, and S. Noda, "Control of Light Emission by 3D Photonic Crystals," *Science*, vol. 305, no. 5681, pp. 227–229, 2004.

[45] L.-J. Chen, X.-Z. Dong, Y.-Y. Zhao, Y.-L. Zhang, J. Liu, M.-L. Zheng, X.-M. Duan, and Z.-S. Zhao, "Fabrication and optical transmission characteristics of polymers woodpile photonic crystal structures with different crystal planes," *AOPC 2015: Advances in Laser Technology and Applications*, vol. 9671, no. October 2015, p. 967127, 2015.

[46] O. Deparis, S. R. Mouchet, and B. L. Su, "Light harvesting in photonic crystals revisited: why do slow photons at the blue edge enhance absorption?," *Physical Chemistry Chemical Physics*, vol. 17, no. 45, pp. 30525–30532, 2015.

[47] B. Corcoran, C. Monat, C. Grillet, D. J. Moss, B. J. Eggleton, T. P. White, L. O'Faolain, and T. F. Krauss, "Green light emission in silicon through slow-light enhanced third-harmonic generation in photonic-crystal waveguides," *Nature Photonics*, vol. 3, no. 4, pp. 206–210, 2009.

[48] T. Baba, "Slow light in photonic crystals," *Nature Photonics*, vol. 2, no. 8, pp. 465–473, 2008.

[49] Https://microparticles.de/en/product-palette.html, "Microparticles Gmbh."

[50] H. microspheres/non-functionalized polystyrene, "Bangs laboratories."

[51] S. T. Ha, O. O. Park, and S. H. Im, "Size control of highly monodisperse polystyrene particles by modified dispersion polymerization," *Macromolecular Research*, vol. 18, no. 10, pp. 935–943, 2010.

[52] G. Tuin, A. Peters, A. Van Diemens, and H. Stein, "Preparation large monodisperse polystyrene particles," *Journal of Colloid and Interface Science*, no. 158, pp. 508–510, 1993.

[53] Y. Yan and Q. M. Chen, "Rapid synthesis of monodispere polystyrene microspheres and self-assembly of colloidal crystal on mica," *Journal of Dispersion Science and Technology*, vol. 30, no. 4, pp. 575–580, 2009.

[54] W. Stober and A. Fink, "Controlled Growth of Monodisperse Silica Spheres in the Micron Size Range," *JOURNAL OF COLLOID AND INTERFACE SCIENCE*, vol. 26, pp. 62–69, 1968.

[55] B. Derjaguin and L. Landau, "Theory of the stability of strongly charged lyophobic sols and of the adhesion of strongly charged particles in solutions of electrolytes," *Progress in Surface Science*, vol. 43, no. 1-4, pp. 30–59, 1993.

[56] H. Zheng and S. Ravaine, "Bottom-Up Assembly and Applications of Photonic Materials," *Crystals*, vol. 6, no. 54, 2016.

[57] H. Bodiguel, F. Doumenc, and B. Guerrier, "Stick-slip patterning at low capillary numbers for an evaporating colloidal suspension," *Langmuir*, vol. 26, no. 13, pp. 10758–10763, 2010.

[58] L. V. Woodcock, "Entropy difference between the face-centred cubic and hexagonal close- packed crystal structures," *Nature*, vol. 385, no. 6612, pp. 141–143, 1997.

[59] A. D. Bruce, N. B. Wilding, and G. J. Ackland, "Free Energy of Crystalline Solids : A Lattice-Switch Monte Carlo Method," *Physical Review Letters*, vol. 79, no. 16, pp. 14–17, 1997.

[60] A. You, M. A. Y. Be, and I. In, "Can stacking faults in hard-sphere crystals anneal out spontaneously ?," *J.Chem. Phys.*, vol. 110, no. 4589, 1999.

[61] H. Cong and W. Cao, "Colloidal Crystallization Induced by Capillary Force," *Langmuir*, vol. 19, pp. 8177–8181, 2003.

[62] B. Li, D. Zhou, and Y. Han, "Assembly and phase transitions of colloidal crystals," *Nature reviews materials*, vol. 1, no. February, pp. 1–13, 2016.

[63] E. Velasco, L. Mederos, and G. Navascue, "Phase Diagram of Colloidal Systems," *Langmuir*, vol. 7463, no. 5, pp. 5652–5655, 1998.

[64] A. Yethiraj and A. Van Blaaderen, "A colloidal model system with an interaction tunable from hard sphere to soft and dipolar," *Nature*, vol. 421, no. 6922, pp. 513–517, 2003.

[65] P. Jiang and M. J. McFarland, "Large-scale fabrication of wafer-size colloidal crystals, macroporous polymers and nanocomposites by spin-coating," *Journal of the American Chemical Society*, vol. 126, no. 42, pp. 13778–13786, 2004.

[66] Z. Z. Gu, A. Fujishima, and O. Sato, "Fabrication of high-quality opal films with controllable thickness," *Chemistry of Materials*, vol. 14, no. 2, pp. 760–765, 2002.

[67] H. Yang and P. Jiang, "Large-scale colloidal self-assembly by doctor blade coating," *Langmuir*, vol. 26, no. 16, pp. 13173–13182, 2010.

[68] Y. Xu, G. J. Schneider, E. D. Wetzel, and D. W. Prather, "Centrifugation and spin-coating method for fabrication of three-dimensional opal and inverse-opal structures as photonic crystal devices," *Journal of Microlithography, Microfabrication and Microsystems*, vol. 3, no. 1, pp. 168–173, 2004.

[69] D. D. Van Beek, P. B. Radstake, A. V. Petukhov, and H. N. Lekkerkerker, "Fast formation of opal-like columnar colloidal crystals," *Langmuir*, vol. 23, no. 23, pp. 11343–11346, 2007.

[70] M. Holgado, F. García-Santamaría, A. Blanco, M. Ibisate, A. Cintas, H. Míguez, C. J. Serna, C. Molpeceres, J. Requena, A. Mifsud, F. Meseguer, and C. López, "Electrophoretic deposition to control artificial opal growth," *Langmuir*, vol. 15, no. 14, pp. 4701–4704, 1999.

[71] X. Ye, J. Huang, Y. Zeng, L.-X. Sun, F. Geng, H.-J. Liu, F.-R. Wang, X.-D. Jiang, W.-D. Wu, and W.-G. Zheng, "Monolayer Colloidal Crystals by Modified Air-Water Interface Self-Assembly Approach," *Nanomaterials*, vol. 7, no. 10, p. 291, 2017.

[72] P. Colson, C. Henrist, and R. Cloots, "Nanosphere lithography: A powerful method for the controlled manufacturing of nanomaterials," *Journal of Nanomaterials*, vol. 2013, 2013.

[73] F. Meseguer, A. Blanco, and H. Miguez, "Synthesis of inverse opals," *Colloids and Surfaces A: Physicochemical and Engineering Aspects*, vol. 202, pp. 281–290, 2002.

[74] X. Li, M. Puttaswamy, Z. Wang, C. Kei Tan, A. C. Grimsdale, N. P. Kherani, and A. I. Y. Tok, "A pressure tuned stop-flow atomic layer deposition process for MoS 2 on high porous nanostructure and fabrication of TiO 2 /MoS 2 core/shell inverse opal structure," *Applied Surface Science*, vol. 422, pp. 536–543, 2017.

[75] E. A. Gaulding, G. Liu, C. T. Chen, L. Löbbert, A. Li, G. Segev, J. Eichhorn, S. Aloni, A. M. Schwartzberg, I. D. Sharp, and F. M. Toma, "Fabrication and optical characterization of polystyrene opal templates for the synthesis of scalable, nanoporous (photo)electrocatalytic materials by electrodeposition," *Journal of Materials Chemistry A*, vol. 5, no. 23, pp. 11601–11614, 2017.

[76] Q. N. Pham, M. T. Barako, J. Tice, and Y. Won, "Microscale Liquid Transport in Polycrystalline Inverse Opals across Grain Boundaries," *Scientific Reports*, vol. 7, no. 1, pp. 1–9, 2017.

[77] M. A. McLachlan, C. C. A. Barron, N. P. Johnson, R. M. De La Rue, and D. W. McComb, "Preparation of large area three-dimensionally ordered macroporous thin films by confined infiltration and crystallisation," *Journal of Crystal Growth*, vol. 310, no. 10, pp. 2644–2648, 2008.

[78] M. Curti, G. López Robledo, P. C. dos Santos Claro, J. H. Ubogui, and C. B. Mendive, "Characterization of titania inverse opals prepared by two distinct infiltration approaches," *Materials Research Bulletin*, vol. 101, no. August 2017, pp. 12–19, 2018.

[79] X. D. Shi, W. Y. Liu, D. Zhao, X. T. Li, R. M. Dou, K. J. Shea, and X. H. Lu, "Coordination-bond-driven fabrication of crack-free photonic crystals," *Journal of Materials Chemistry C*, vol. 4, no. 30, pp. 7208–7214, 2016.

[80] B. Yi and H. Shen, "Facile fabrication of crack-free photonic crystals with enhanced color contrast and low angle dependence," *Journal of Materials Chemistry C*, vol. 5, no. 32, pp. 8194–8200, 2017.

[81] Y. Huang, J. Zhou, B. Su, L. Shi, J. Wang, S. Chen, L. Wang, J. Zi, Y. Song, and L. Jiang, "Colloidal photonic crystals with narrow stopbands assembled from low-adhesive superhydrophobic substrates," *Journal of the American Chemical Society*, vol. 134, no. 41, pp. 17053–17058, 2012.

[82] B. Hatton, L. Mishchenko, S. Davis, K. H. Sandhage, and J. Aizenberg, "Assembly of large-area, highly ordered, crack-free inverse opal films," *Proceedings of the National Academy of Sciences of the United States of America*, vol. 107, no. 23, pp. 10354–10359, 2010.

[83] A. Richel, N. P. Johnson, and D. W. McComb, "Observation of Bragg reflection in photonic crystals synthesized from air spheres in a titania matrix," *Applied Physics Letters*, vol. 76, pp. 1816–1818, apr 2000.

[84] K. R. Phillips, T. Shirman, E. Shirman, A. V. Shneidman, T. M. Kay, and J. Aizenberg, "Nanocrystalline Precursors for the Co-Assembly of Crack-Free Metal Oxide Inverse Opals," *Advanced Materials*, vol. 30, no. 19, pp. 1–7, 2018.

[85] J. Zhou, J. Wang, Y. Huang, G. Liu, L. Wang, S. Chen, X. Li, D. Wang, Y. Song, and L. Jiang, "Large-area crack-free single-crystal photonic crystals via combined effects of polymerization-assisted assembly and flexible substrate," *NPG Asia Materials*, vol. 4, no. 8, pp. e21–7, 2012.

[86] L. Wang and X. S. Zhao, "Fabrication of crack-free colloidal crystals using a modified vertical deposition method," *Journal of Physical Chemistry C*, vol. 111, no. 24, pp. 8538–8542, 2007.

[87] "Thegreenage."

[88] J. Nelson, *The Physics of Solar Cells*. 2003.

[89] W. Shockley and H. J. Queisser, "Detailed balance limit of efficiency of p-n junction solar cells," *Journal of Applied Physics*, vol. 32, no. 3, pp. 510–519, 1961.

[90] S. Khosroabadi and S. H. Keshmiri, "Design of a high efficiency ultrathin CdS/CdTe solar cell using back surface field and backside distributed Bragg reflector," *Optics Express*, vol. 22, no. S3, p. A921, 2014.

[91] Y. Peng, L. Zhang, N. Cheng, and T. L. Andrew, "ITO-free transparent organic solar cell with distributed bragg reflector for solar harvesting windows," *Energies*, vol. 10, no. 5, 2017.

[92] L. Zeng, Y. Yi, C. Hong, J. Liu, N. Feng, X. Duan, L. C. Kimerling, and B. A. Alamariu, "Efficiency enhancement in Si solar cells by textured photonic crystal back reflector," *Applied Physics Letters*, vol. 89, no. 11, pp. 17–20, 2006.

[93] R. B. Wehrspohn and J. Ůpping, "3D photonic crystals for photon management in solar cells," *Journal of Optics*, vol. 14, no. 2, 2012.

[94] A. Bielawny, J. Üpping, P. T. Miclea, R. B. Wehrspohn, C. Rockstuhl, F. Lederer, M. Peters, L. Steidl, R. Zentel, S. M. Lee, M. Knez, A. Lambertz, and R. Carius, "3D photonic crystal intermediate reflector for micromorph thin-film tandem solar cell," *Physica Status Solidi (A) Applications and Materials Science*, vol. 205, no. 12, pp. 2796–2810, 2008.

[95] P. Bermel, C. Luo, L. Zeng, L. C. Kimerling, and J. D. Joannopoulos, "Improving thin-film crystalline silicon solar cell efficiencies with photonic crystals," *Optics Express*, vol. 15, no. 25, p. 16986, 2007.

[96] S. Guldin, S. Hüttner, M. Kolle, M. E. Welland, P. Müller-Buschbaum, R. H. Friend, U. Steiner, and N. Tétreault, "Dye-sensitized solar cell based on a three-dimensional photonic crystal," *Nano Letters*, vol. 10, no. 7, pp. 2303–2309, 2010.

[97] A. Mihi, M. E. Calvo, J. A. Anta, and H. Míguez, "Spectral response of opal-based dye-sensitized solar cells," *Journal of Physical Chemistry C*, vol. 112, no. 1, pp. 13–17, 2008.

[98] A. Mihi, F. J. López-Alcaraz, and H. Míguez, "Full spectrum enhancement of the light harvesting efficiency of dye sensitized solar cells by including colloidal photonic crystal multilayers," *Applied Physics Letters*, vol. 88, no. 19, 2006.

[99] O. Deparis and O. El Daif, "Optimization of slow light one-dimensional Bragg structures forphotocurrent enhancement in solar cells," *Optics Letters*, vol. 37, no. 20, p. 4230, 2012.

[100] N. J. Thompson, D. N. Congreve, D. Goldberg, V. M. Menon, and M. A. Baldo, "Slow light enhanced singlet exciton fission solar cells with a 126% yield of electrons per photon," *Applied Physics Letters*, vol. 103, no. 26, pp. 1–4, 2013.

[101] S. Zhou, R. Tang, and L. Yin, "Slow-Photon-Effect-Induced Photoelectrical-Conversion Efficiency Enhancement for Carbon-Quantum-Dot-Sensitized Inorganic CsPbBr3Inverse Opal Perovskite Solar Cells," *Advanced Materials*, vol. 29, no. 43, pp. 1–9, 2017.

[102] N. Yantara, T. T. T. Pham, P. P. Boix, and N. Mathews, "Modulating light propagation in ZnO–Cu2O-inverse opal solar cells for enhanced photocurrents," *Phys.Chem.Chem.Phys*, vol. 17, pp. 21694–21701, 2015.

[103] S. J. Ha, J. H. Heo, S. H. Im, and J. H. Moon, "Mesoscopic CH3NH3PbI3perovskite solar cells using TiO2inverse opal electron-conducting scaffolds," *Journal of Materials Chemistry A*, vol. 5, no. 5, pp. 1972–1977, 2017.

[104] J. W. Lee, J. Lee, C. Kim, C.-Y. Cho, and J. H. Moon, "Facile fabrication of sub 100 nm mesoscale inverse opal films and their application in dye-sensitized solar cell electrodes," *Scientific Reports*, vol. 4, no. 1, p. 6804, 2015.

[105] J.-H. Shin and J. H. Moon, "Bilayer Inverse Opal TiO ₂ Electrodes for Dye-Sensitized Solar Cells via Post-Treatment," *Langmuir*, vol. 27, no. 10, pp. 6311–6315, 2011.

[106] L. Liu, S. K. Karuturi, L. T. Su, and A. I. Y. Tok, "TiO2inverse-opal electrode fabricated by atomic layer deposition for dye-sensitized solar cell applications," *Energy and Environmental Science*, vol. 4, no. 1, pp. 209–215, 2011.

[107] S. Yuan, H. Huang, Z. Wang, Y. Zhao, L. Shi, C. Cai, and D. Li, "Improved electron-collection performance of dye sensitized solar cell based on three-dimensional conductive grid," *Journal of Photochemistry and Photobiology A: Chemistry*, vol. 259, pp. 10–16, 2013.

[108] H. Round, "A note on carborundum," *Electrical World*, vol. 49, 1907.

[109] A. Bernanose and P. Vouaux, "Électroluminescence organique : étude du mode d'émission," *J. Chim. Phys.*, vol. 50, pp. 261 – 263, 1953.

[110] A. Bernanose, "Sur le mécanisme de l'électroluminescence organique," *J. Chim. Phys.*, vol. 52, pp. 396 – 400, 1955.

[111] A. Bernanose, M. Comte, and P. Vouaux, "Sur un nouveau mode d'émission lumineuse chez certains composés organiques," *J. Chim. Phys.*, vol. 50, pp. 64 – 68, 1953.

[112] J. H. Burroughes, D. D. Bradley, A. R. Brown, R. N. Marks, K. Mackay, R. H. Friend, P. L. Burns, and A. B. Holmes, "Light-emitting diodes based on conjugated polymers," *Nature*, vol. 347, no. 6293, pp. 539–541, 1990.

[113] R. Feynman, *The Feynman Lectures on Physics Vol II Electromagnetism and Matte*. 1963.

[114] S. Wu, H. Xia, J. Xu, X. Sun, and X. Liu, "Manipulating Luminescence of Light Emitters by Photonic Crystals," *Advances Materials*, vol. 30, pp. 1–26, 2018.

[115] F. Jin, C.-F. Li, X.-Z. Dong, W.-Q. Chen, and X.-M. Duan, "Laser emission from dye-doped polymer film in opal photonic crystal cavity," *Applied Physics Letters*, vol. 89, no. 24, p. 241101, 2006.

[116] F. Jin, Y. Song, X. Z. Dong, W. Q. Chen, and X. M. Duan, "Amplified spontaneous emission from dye-doped polymer film sandwiched by two opal photonic crystals," *Applied Physics Letters*, vol. 91, no. 3, pp. 1998–2001, 2007.

[117] F. Jin, L. T. Shi, M. L. Zheng, X. Z. Dong, S. Chen, Z. S. Zhao, and X. M. Duan, "Lasing and amplified spontaneous emission in a polymeric inverse opal photonic crystal resonating cavity," *Journal of Physical Chemistry C*, vol. 117, no. 18, pp. 9463–9468, 2013.

[118] L. Bechger, P. Lodahl, and W. L. Vos, "Directional fluorescence spectra of laser dye in opal and inverse opal photonic crystals," *Journal of Physical Chemistry B*, vol. 109, no. 20, pp. 9980–9988, 2005.

[119] H. Yamada, T. Nakamura, Y. Yamada, and K. Yano, "Colloidal-crystal laser using monodispersed mesoporous silica spheres," *Advanced Materials*, vol. 21, no. 41, pp. 4134–4138, 2009.

[120] Y. Nishijima and S. Juodkazis, "Optical characterization and lasing in three-dimensional opal-structures," *Frontiers in Materials*, vol. 2, no. June, pp. 1–10, 2015.

[121] S. Furumi, T. Kanai, and T. Sawada, "Widely tunable lasing in a colloidal crystal gel film permanently stabilized by an ionic liquid," *Advanced Materials*, vol. 23, no. 33, pp. 3815–3820, 2011.

[122] M. Scharrer, A. Yamilov, X. Wu, H. Cao, and R. P. H. Chang, "Ultraviolet lasing in high-order bands of three-dimensional ZnO photonic crystals," *Applied Physics Letters*, vol. 88, no. 20, pp. 2004–2007, 2006.

[123] S. Schunemann, S. Brittman, K. Chen, E. C. Garnett, and H. Tuysuz, "Halide Perovskite 3D Photonic Crystals for Distributed Feedback Lasers," *American Chemical Society*, vol. 4, no. 2, pp. 2522–2528, 2017.

[124] D. P. Puzzo, M. G. Helander, P. G. Obrien, Z. Wang, N. Soheilnia, N. Kherani, Z. Lu, and G. A. Ozin, "Organic light-emitting diode microcavities from transparent conducting metal oxide photonic crystals," *Nano Letters*, vol. 11, no. 4, pp. 1457–1462, 2011.

[125] J. Schneider, M. Matsuoka, M. Takeuchi, J. Zhang, Y. Horiuchi, M. Anpo, and D. W. Bahnemann, "Understanding TiO 2 Photocatalysis : Mechanisms and Materials," *Chemical Reviews*, vol. 114, pp. 9919–9986, 2014.

[126] A. Kudo and Y. Miseki, "Heterogeneous photocatalyst materials for water splitting," *Chemical Society reviews*, vol. 38, no. 1, pp. 253–278, 2009.

[127] T. Jafari, E. Moharreri, A. S. Amin, R. Miao, W. Song, and S. L. Suib, "Photocatalytic water splitting - The untamed dream: A review of recent advances," *Molecules*, vol. 21, no. 7, 2016.

[128] H. Hirakawa, M. Hashimoto, Y. Shiraishi, and T. Hirai, "Photocatalytic Conversion of Nitrogen to Ammonia with Water on Surface Oxygen Vacancies of Titanium Dioxide," *Journal of the American Chemical Society*, vol. 139, no. 31, pp. 10929–10936, 2017.

[129] M. Ren, R. Ravikrishna, and K. T. Valsaraj, "Photocatalytic degradation of gaseous organic species on photonic band-gap titania," *Environmental Science and Technology*, vol. 40, no. 22, pp. 7029–7033, 2006.

[130] K. Nakata and A. Fujishima, "TiO 2 photocatalysis: Design and applications," *Journal of Photochemistry and Photobiology C: Photochemistry Reviews*, vol. 13, no. 3, pp. 169–189, 2012.

[131] A. Fujishima, X. Zhang, and D. A. Tryk, "TiO 2 photocatalysis and related surface phenomena," *Surface Science Reports*, vol. 63, pp. 515–582, 2008.

[132] K. Kim, P. Thiyagarajan, H. J. Ahn, S. I. Kim, and J. H. Jang, "Optimization for visible light photocatalytic water splitting: Gold-coated and surface-textured TiO2 inverse opal nano-networks," *Nanoscale*, vol. 5, no. 14, pp. 6254–6260, 2013.

[133] H. Zhao, M. Wu, J. Liu, Z. Deng, Y. Li, and B. L. Su, "Synergistic promotion of solar-driven H2generation bythree-dimensionally ordered macroporous structured TiO2-Au-CdS ternary photocatalyst," *Applied Catalysis B: Environmental*, vol. 184, pp. 182–190, 2016.

[134] Y. Gun, G. Y. Song, V. H. V. Quy, J. Heo, H. Lee, K. S. Ahn, and S. H. Kang, "Joint effects of photoactive TiO2 and fluoride-doping on SnO2 inverse opal nanoarchitecture for solar water splitting," *ACS Applied Materials and Interfaces*, vol. 7, no. 36, pp. 20292–20303, 2015.

[135] Z. Yang, S. Gao, W. Li, V. Vlasko-Vlasov, U. Welp, W. K. Kwok, and T. Xu, "Three-Dimensional Photonic Crystal Fluorinated Tin Oxide (FTO) Electrodes: Synthesis and Optical and Electrical Properties," *ACS Applied Materials and Interfaces*, vol. 3, no. 4, pp. 1101–1108, 2011.

[136] M. Ma, J. K. Kim, K. Zhang, X. Shi, S. J. Kim, J. H. Moon, and J. H. Park, "Double-deck inverse opal photoanodes: Efficient light absorption and charge separation in heterojunction," *Chemistry of Materials*, vol. 26, no. 19, pp. 5592–5597, 2014.

[137] G. Yun, M. Balamurugan, H. S. Kim, K. S. Ahn, and S. H. Kang, "Role of WO3Layers Electrodeposited on SnO2Inverse Opal Skeletons in Photoelectrochemical Water Splitting," *Journal of Physical Chemistry C*, vol. 120, no. 11, pp. 5906–5915, 2016.

[138] S. Zhou, R. Tang, L. Zhang, and L. Yin, "Au Nanoparticles coupled Three-dimensional Macroporous BiVO4/SnO2 Inverse Opal Heterostructure For Efficient Photoelectrochemical Water Splitting," *Electrochimica Acta*, vol. 248, pp. 593–602, 2017.

[139] T. Yang, J. Xue, H. Tan, A. Xie, S. Li, W. Yan, and Y. Shen, "Highly ordered ZnO/ZnFe2O4 inverse opals with binder-free heterojunction interfaces for high-performance photoelectrochemical water splitting," *Journal of Materials Chemistry A*, vol. 6, no. 3, pp. 1210–1218, 2018.

[140] H. Song, S. Oh, H. Yoon, K. H. Kim, S. Ryu, and J. Oh, "Bifunctional NiFe inverse opal electrocatalysts with heterojunction Si solar cells for 9.54%-efficient unassisted solar water splitting," *Nano Energy*, vol. 42, no. August, pp. 1–7, 2017.

[141] E. Eftekhari, P. Broisson, N. Aravindakshan, Z. Wu, I. S. Cole, X. Li, D. Zhao, and Q. Li, "Sandwich-structured TiO2inverse opal circulates slow photons for tremendous improvement in solar energy conversion efficiency," *Journal of Materials Chemistry A*, vol. 5, no. 25, pp. 12803–12810, 2017.

[142] X. Shi, H. Jeong, S. J. Oh, M. Ma, K. Zhang, J. Kwon, I. T. Choi, I. Y. Choi, H. K. Kim, J. K. Kim, and J. H. Park, "Unassisted photoelectrochemical water splitting exceeding 7% solar-to-hydrogen conversion efficiency using photon recycling," *Nature Communications*, vol. 7, no. May, 2016.

[143] M. Curti, J. Schneider, D. W. Bahnemann, and C. B. Mendive, "Inverse Opal Photonic Crystals as a Strategy to Improve Photocatalysis: Underexplored Questions," *Journal of Physical Chemistry Letters*, vol. 6, no. 19, pp. 3903–3910, 2015.

[144] J. Li and T. Zheng, "A comparison of chemical sensors based on the different ordered inverse opal films," *Sensors and Actuators, B: Chemical*, vol. 131, no. 1, pp. 190–195, 2008.

[145] C. Liu, G. Gao, Y. Zhang, L. Wang, J. Wang, and Y. Song, "The naked-eye detection of NH 3-HCl by polyaniline-infiltrated TiO 2 inverse opal photonic crystals," *Macromolecular Rapid Communications*, vol. 33, no. 5, pp. 380–385, 2012.

[146] J. Shin, P. V. Braun, and W. Lee, "Fast response photonic crystal pH sensor based on templated photo-polymerized hydrogel inverse opal," *Sensors and Actuators, B: Chemical*, vol. 150, no. 1, pp. 183–190, 2010.

[147] H. Li, J. Wang, Z. Pan, L. Cui, L. Xu, R. Wang, Y. Song, and L. Jiang, "Amplifying fluorescence sensing based on inverse opal photonic crystal toward trace TNT detection," *Journal of Materials Chemistry*, vol. 21, no. 6, pp. 1730–1735, 2011.

[148] L. Zhang, B. Dong, L. Xu, X. Zhang, J. Chen, X. Sun, H. Xu, T. Zhang, X. Bai, S. Zhang, and H. Song, "Three-dimensional ordered ZnO–Fe3O4 inverse opal gas sensor toward trace concentration acetone detection," *Sensors and Actuators, B: Chemical*, vol. 252, pp. 367–374, 2017.

[149] L. Xia, L. Xu, J. Song, R. Xu, D. Liu, B. Dong, and H. Song, "CdS quantum dots modified CuO inverse opal electrodes for ultrasensitive electrochemical and photoelectrochemical biosensor," *Scientific Reports*, vol. 5, no. June, pp. 1–12, 2015.

[150] X. Huang, J. Chen, Z. Lu, H. Yu, Q. Yan, and H. H. Hng, "Carbon inverse opal entrapped with electrode active nanoparticles as high-performance anode for lithium-ion batteries," *Scientific Reports*, vol. 3, pp. 1–9, 2013.

[151] T. Song, Y. Jeon, M. Samal, H. Han, H. Park, J. Ha, D. K. Yi, J. M. Choi, H. Chang, Y. M. Choi, and U. Paik, "A Ge inverse opal with porous walls as an anode for lithium ion batteries," *Energy and Environmental Science*, vol. 5, no. 10, pp. 9028–9033, 2012.

[152] A. Esmanski and G. A. Ozin, "Silicon inverse-opal-based macroporous materials as negative electrodes for lithium ion batteries," *Advanced Functional Materials*, vol. 19, no. 12, pp. 1999–2010, 2009.

[153] Z. Liang, G. Zheng, W. Li, Z. W. Seh, H. Yao, K. Yan, D. Kong, and Y. Cui, "Sulfur cathodes with hydrogen reduced titanium dioxide inverse opal structure," *ACS Nano*, vol. 8, no. 5, pp. 5249–5256, 2014.

[154] J. H. Kim, J. H. Kim, K. H. Choi, H. K. Yu, J. H. Kim, J. S. Lee, and S. Y. Lee, "Inverse opal-inspired, nanoscaffold battery separators: A new membrane opportunity for high-performance energy storage systems," *Nano Letters*, vol. 14, no. 8, pp. 4438–4448, 2014.

[155] C. O'Dwyer, "Color-Coded Batteries – Electro-Photonic Inverse Opal Materials for Enhanced Electrochemical Energy Storage and Optically Encoded Diagnostics," *Advanced Materials*, vol. 28, no. 27, pp. 5681–5688, 2016.

[156] O. H. Kim, Y. H. Cho, S. H. Kang, H. Y. Park, M. Kim, J. W. Lim, D. Y. Chung, M. J. Lee, H. Choe, and Y. E. Sung, "Ordered macroporous platinum electrode and enhanced mass transfer in fuel cells using inverse opal structure," *Nature Communications*, vol. 4, pp. 1–9, 2013.

[157] J. H. Kim, S. H. Kang, K. Zhu, J. Y. Kim, N. R. Neale, and A. J. Frank, "Ni-NiO core-shell inverse opal electrodes for supercapacitors," *Chemical Communications*, vol. 47, no. 18, pp. 5214–5216, 2011.

[158] A. Einstein, "Einstein diffusion paper," 1905.

[159] B. Sarina and D. Ken A, *Molecular Driving Forces: Statistical Thermodynamics in Chemistry and Biology*. Garland Science, 2003.

[160] R. J. Hunter, *Zeta Potential in Colloid Science*. Academic Press, 1981.

[161] J. W. Swan and E. M. Furst, "A simpler expression for Henry's function describing the electrophoretic mobility of spherical colloids," *Journal of Colloid and Interface Science*, vol. 388, no. 1, pp. 92–94, 2012.

[162] C. Lanczos, *The Variational Principles of Mechanics (Reprint of Fourth Edition of 1970 ed.)*. Dover Publications.

[163] M. A. McLachlan, N. P. Johnson, R. M. De La Rue, and D. W. McComb, "Thin film photonic crystals: Synthesis and characterisation," *Journal of Materials Chemistry*, vol. 14, no. 2, pp. 144–150, 2004.

[164] J. M. Meijer, F. Hagemans, L. Rossi, D. V. Byelov, S. I. Castillo, A. Snigirev, I. Snigireva, A. P. Philipse, and A. V. Petukhov, "Self-assembly of colloidal cubes via vertical deposition," *Langmuir*, vol. 28, no. 20, pp. 7631–7638, 2012.

[165] Y. Masuda, T. Itoh, M. Itoh, and K. Koumoto, "Self-assembly patterning of colloidal crystals constructed from opal structure or NaCl structure," *Langmuir*, vol. 20, no. 13, pp. 5588–5592, 2004.

[166] L. Yang, K. Gao, Y. Luo, J. Luo, D. Li, and Q. Meng, "In situ observation and measurement of evaporation-induced self-assembly under controlled pressure and temperature," *Langmuir*, vol. 27, no. 5, pp. 1700–1706, 2011.

[167] S. K. Rhee, "Surface energies of silicate glasses calculated from their wettability data," *Journal of Materials Science*, vol. 12, no. 4, pp. 823–824, 1977.

[168] K. J. Seu, A. P. Pandey, F. Haque, E. A. Proctor, A. E. Ribbe, and J. S. Hovis, "Effect of surface treatment on diffusion and domain formation in supported lipid bilayers," *Biophysical Journal*, vol. 92, no. 7, pp. 2445–2450, 2007.

[169] S. Babu, *Advances in Chemical Mechanical Planarization (CMP)*. 2016.

[170] A. Avoine, P. N. Hong, H. Frederich, J. M. Frigerio, L. Coolen, C. Schwob, P. T. Nga, B. Gallas, and A. Maître, "Measurement and modelization of silica opal reflection properties: Optical determination of the silica index," *Physical Review B - Condensed Matter and Materials Physics*, vol. 86, no. 16, 2012.

[171] T. Cassagneau and F. Caruso, "Semiconducting polymer inverse opals prepared by electropolymerization," *Advanced Materials*, vol. 14, no. 1, pp. 34–38, 2002.

[172] A. Kojima, K. Teshima, Y. Shirai, and T. Miyasaka, "Organometal halide perovskites as visible-light sensitizers for photovoltaic cells," *Journal of the American Chemical Society*, vol. 131, no. 17, pp. 6050–6051, 2009.

[173] M. M. Lee, J. Teuscher, T. Miyasaka, T. N. Murakami, and H. J. Snaith, "Efficient Hybrid Solar Cells Based on Meso-Superstructured Organometal Halide Perovskites," *Science*, vol. 338, no. 6107, pp. 643–647, 2012.

[174] M. A. Green, A. Ho-Baillie, and H. J. Snaith, "The emergence of perovskite solar cells," *Nature Photonics*, vol. 8, no. 7, pp. 506–514, 2014.

[175] N. G. Park, "Perovskite solar cells: An emerging photovoltaic technology," *Materials Today*, vol. 18, no. 2, pp. 65–72, 2015.

[176] NREL, "NREL chart."

[177] H. S. Jung and N. G. Park, "Perovskite solar cells: From materials to devices," *Small*, vol. 11, no. 1, pp. 10–25, 2015.

[178] T. C. Sum and N. Mathews, "Advancements in perovskite solar cells: Photophysics behind the photovoltaics," *Energy and Environmental Science*, vol. 7, no. 8, pp. 2518–2534, 2014.

[179] W. J. Yin, T. Shi, and Y. Yan, "Unique properties of halide perovskites as possible origins of the superior solar cell performance," *Advanced Materials*, vol. 26, no. 27, pp. 4653–4658, 2014.

[180] S. Colella, E. Mosconi, P. Fedeli, A. Listorti, F. Gazza, F. Orlandi, P. Ferro, T. Besagni, A. Rizzo, G. Calestani, G. Gigli, F. De Angelis, and R. Mosca, "MAPbI3-xClx mixed halide perovskite for hybrid solar cells: The role of chloride as dopant on the transport and structural properties," *Chemistry of Materials*, vol. 25, no. 22, pp. 4613–4618, 2013.

[181] Q. A. Akkerman, V. D'Innocenzo, S. Accornero, A. Scarpellini, A. Petrozza, M. Prato, and L. Manna, "Tuning the optical properties of cesium lead halide perovskite nanocrystals by anion exchange reactions," *Journal of the American Chemical Society*, vol. 137, no. 32, pp. 10276–10281, 2015.

[182] G. Niu, X. Guo, and L. Wang, "Review of recent progress in chemical stability of perovskite solar cells," *Journal of Materials Chemistry A*, vol. 3, no. 17, pp. 8970–8980, 2015.

[183] D. Shi, V. Adinolfi, R. Comin, M. Yuan, E. Alarousu, A. Buin, Y. Chen, S. Hoogland, A. Rothenberger, K. Katsiev, Y. Losovyj, X. Zhang, P. A. Dowben, O. F. Mohammed, E. H. Sargent, and O. M. Bakr, "Low trap-state density and long carrier diffusion in organolead trihalide perovskite single crystals," *Science*, vol. 347, no. 6221, pp. 519–522, 2015.

[184] S. D. Stranks, G. E. Eperon, G. Grancini, C. Menelaou, M. J. P. Alcocer, T. Leijtens, L. M. Herz, A. Petrozza, J. Henry, S. D. Stranks, G. E. Eperon, G. Grancini, C. Menelaou, M. P. Alcocer, T. Leijtens, L. M. Herz, A. Petrozza, and H. Snaith, "Electron-Hole Diffusion Lengths Exceeding 1 Micrometer in an Organometal Trihalide Perovskite Absorber Published by : American," *Science*, vol. 342, no. 6159, pp. 341–344, 2013.

[185] W. Dong, T. Zhang, X. Chen, B. Wang, and B. Zhu, "Charge transport study of perovskite solar cells through constructing electron transport channels," *Physica Status Solidi (A)*, vol. 214, no. 10, 2017.

[186] W. Kim, J. Park, H. Kim, Y. Pak, H. Lee, and G. Y. Jung, "Sequential Dip-spin Coating Method: Fully Infiltration of MAPbI3-xClx into Mesoporous TiO2 for Stable Hybrid Perovskite Solar Cells," *Electrochimica Acta*, vol. 245, pp. 734–741, 2017.

[187] T. Leijtens, B. Lauber, G. E. Eperon, S. D. Stranks, and H. J. Snaith, "The Importance of Perovskite Pore Filling in Organometal Mixed Halide Sensitized TiO 2 - Based Solar Cells," *Physical Chemistry Letters*, vol. 5, pp. 1096–1102, 2014.

[188] H.-s. Kim, J.-w. Lee, N. Yantara, P. P. Boix, S. A. Kulkarni, S. Mhaisalkar, M. Gratzel, and N.-g. Park, "High Efficiency Solid-State Sensitized Solar Cell-Based on Submicrometer Rutile TiO 2 Nanorod and CH3NH3PbI3 Perovskite Sensitizer," *Nano Letters*, vol. 13, pp. 2412–2417, 2013.

[189] H. Chen and S. Yang, "High-quality perovskite in thick scaffold: a core issue for hole transport material-free perovskite solar cells," *Science Bulletin*, vol. 61, no. 21, pp. 1680–1688, 2016.

[190] J.-P. Niemelä, G. Marin, and M. Karppinen, "Titanium dioxide thin films by atomic layer deposition: a review," *Semicond. Sci. Technol*, vol. 32, no. 0935005, 2017.

[191] J. Yang, B. D. Siempelkamp, E. Mosconi, F. De Angelis, and T. L. Kelly, "Origin of the Thermal Instability in CH3NH3PbI3 Thin Films Deposited on ZnO," *Chemistry of Materials*, vol. 27, no. 12, pp. 4229–4236, 2015.

[192] S. L. Triana, Kusumandari, and R. Suryana, "Effect of wet etching process on the morphology and transmittance of fluorine doped tin oxide (FTO)," *Journal of Physics: Conference Series*, vol. 776, no. 1, 2016.

[193] Y. Masuda, "Self-assembly and Patterning of Nanocrystals," in *Nanocrystal*, 2011.

[194] G. Yun, M. Balamurugan, K.-S. Ahn, S.-K. Lee, S. H. Kang, and D.-H. Lim, "Dual roles of a flouride-doped SnO2/TiO2 bilayer based on inverse opal/-nanoparticle structure for water oxidation," *Journal of the Korean Physical Society*, vol. 72, no. 2, pp. 260–269, 2018.

[195] S. C. Riha, B. M. Klahr, E. C. Tyo, S. Seifert, S. Vajda, M. J. Pellin, T. W. Hamann, and A. B. Martinson, "Atomic layer deposition of a submonolayer catalyst for the enhanced photoelectrochemical performance of water oxidation with hematite," *ACS Nano*, vol. 7, no. 3, pp. 2396–2405, 2013.

[196] S. K. Karuturi, L. Liu, L. T. Su, A. Chutinan, N. P. Kherani, T. K. Chan, T. Osipowicz, and A. I. Yoong Tok, "Gradient inverse opal photonic crystals via spatially controlled template replication of self-assembled opals," *Nanoscale*, vol. 3, no. 1, p. 4951, 2011.

[197] M. Kabir, M. Kabir, F. Nigar, S. Ahmed, A. Mustafa, and M. Ahsan, "Preparation and characterization of rice husk ash (RHA)-TiO2 / ZnO composites and its application in treating effluents from textile industries," *Bangladesh Journal of Scientific and Industrial Research*, vol. 47, no. 4, pp. 445–448, 2013.

[198] D. Su, C. Wang, H. Ahn, and G. Wang, "Octahedral tin dioxide nanocrystals as high capacity anode materials for Na-ion batteries," *Physical Chemistry Chemical Physics*, vol. 15, no. 30, pp. 12543–12550, 2013.

[199] N. J. Jeon, J. H. Noh, Y. C. Kim, W. S. Yang, S. Ryu, and S. I. Seok, "Solvent engineering for high-performance inorganic–organic hybrid perovskite solar cells," *Nature Materials*, vol. 13, no. July, pp. 897–903, 2014.

[200] N. Ahn, D. Y. Son, I. H. Jang, S. M. Kang, M. Choi, and N. G. Park, "Highly Reproducible Perovskite Solar Cells with Average Efficiency of 18.3% and Best Efficiency of 19.7% Fabricated via Lewis Base Adduct of Lead(II) Iodide," *Journal of the American Chemical Society*, vol. 137, no. 27, pp. 8696–8699, 2015.

[201] M. Kuang, J. Wang, and L. Jiang, "Bio-inspired photonic crystals with superwettability," *Chemical Society Reviews*, vol. 45, no. 24, pp. 6833–6854, 2016.

[202] L.-Y. Chen, C.-H. Lai, P.-W. Wu, and S.-K. Fan, "Electrowetting of Superhydrophobic ZnO Inverse Opals," *Journal of The Electrochemical Society*, vol. 158, no. 8, p. P93, 2011.

[203] W. Hong, H. Li, X. Hu, B. Zhao, F. Zhang, and D. Zhang, "Independent multifunctional detection by wettability controlled inverse opal hydrogels," *Chemical Communications*, vol. 48, no. 38, pp. 4609–4611, 2012.

[204] K. Chen and H. Tüysüz, "Morphology-Controlled Synthesis of Organometal Halide Perovskite Inverse Opals," *Angewandte Chemie - International Edition*, vol. 54, no. 46, pp. 13806–13810, 2015.

[205] Z. Yuan, Y. Yang, Z. Wu, S. Bai, W. Xu, T. Song, X. Gao, F. Gao, and B. Sun, "Approximately 800-nm-Thick Pinhole-Free Perovskite Films via Facile Solvent Retarding Process for Efficient Planar Solar Cells," *ACS Applied Materials and Interfaces*, vol. 8, no. 50, pp. 34446–34454, 2016.

[206] B. Conings, A. Babayigit, M. T. Klug, S. Bai, N. Gauquelin, N. Sakai, J. T.-w. Wang, J. Verbeeck, H.-g. Boyen, and H. J. Snaith, "A Universal Deposition Protocol for Planar Heterojunction Solar Cells with High Efficiency Based on Hybrid Lead Halide Perovskite Families," *Advanced Materials*, vol. 28, pp. 10701–10709, 2016.

[207] C.-h. Chiang and C.-g. Wu, "A Method for the Preparation of Highly Oriented MAPbI3 Crystallites for High-Efficiency Perovskite Solar Cells to Achieve an 86% Fill Factor," *ACS Nano*, vol. 12, pp. 10355–10364, 2018.

[208] X. Li, D. Bi, C. Yi, J. Luo, S. M. Zakeeruddin, A. Hagfeldt, and M. Gratzel, "A vacuum flash – assisted solution process for high-efficiency large-area perovskite solar cells," *Science*, vol. 353, no. 6294, 2016.

[209] B. Ding, Y. Li, S.-Y. Huang, Q.-Q. Chu, C.-X. Li, C.-J. Li, and G.-J. Yang, "Material nucleation/growth competition tuning towards highly reproducible planar perovskite solar cells with efficiency exceeding 20%," *Journal of Materials Chemistry A*, vol. 5, no. 15, p. 6840, 2017.

[210] B. Qi and J. Wang, "Fill factor in organic solar cells," *Phys.Chem.Chem.Phys*, vol. 15, pp. 8972–8982, 2013.

[211] A. Gómez-Núnez, S. Alonso-Gil, C. López, P. Roura, and A. Vilà, "Role of Ethanolamine on the Stability of a Sol-Gel ZnO Ink," *Journal of Physical Chemistry C*, vol. 121, no. 42, pp. 23839–23846, 2017.

[212] S. Wu, S. Yuan, L. Shi, Y. Zhao, and J. Fang, "Preparation, characterization and electrical properties of fluorine-doped tin dioxide nanocrystals," *Journal of Colloid and Interface Science*, vol. 346, no. 1, pp. 12–16, 2010.

[213] L. M. Sikhwivhilu, S. K. Pillai, and T. K. Hillie, "Influence of Citric Acid on SnO 2 Nanoparticles Synthesized by Wet Chemical Processes," *Journal of Nanoscience and Nanotechnology*, vol. 11, pp. 4988–94, 2011.

[214] J. Li, Y. Cai, and M. Zhang, "Preparation of SnS 2 thin films by chemical bath deposition," *Materials Science Forum*, vol. 663-665, pp. 104–107, 2011.

[215] H. SaarenÄA, T. Niemi, A. Tukiainen, H. Lemmetyinen, and N. Tkachenko, "Aluminum doped zinc oxide films grown by atomic layer deposition for organic photovoltaic devices," *Solar Energy Materials and Solar Cells*, vol. 94, pp. 1379–1383, 2010.

[216] E. Guziewicz, M. Godlewski, L. Wachnicki, T. A. Krajewski, G. Luka, S. Gieraltowska, R. Jakiela, A. Stonert, W. Lisowski, M. Krawczyk, J. W. Sobczak, and A. Jablonski, "ALD grown zinc oxide with controllable electrical properties," *Semicond. Sci. Technol*, vol. 27, pp. 74011–11, 2012.

[217] R. Huang, S. Ye, K. Sun, K. S. Kiang, C. H. . Kees, and . De Groot, "Fermi Level Tuning of ZnO Films Through Supercycled Atomic Layer Deposition," *Nanoscale research letters*, vol. 12, p. 541, 2017.

[218] Z. Baji, Z. Lábadi, Z. E. Horváth, M. Fried, B. Szentpáli, and I. Bársony, "Temperature dependent in situ doping of ALD ZnO," *Journal of Thermal Analysis and Calorimetry*, vol. 105, no. 1, pp. 93–99, 2011.

[219] G. Luka, T. A. Krajewski, B. S. Witkowski, G. Wisz, I. S. Virt, E. Guziewicz, and M. Godlewski, "Aluminum-doped zinc oxide films grown by atomic layer deposition for transparent electrode applications," *Journal of Materials Science: Materials in Electronics*, vol. 22, pp. 1810–1815, dec 2011.

[220] Y. Geng, L. Guo, S.-S. Xu, Q.-Q. Sun, S.-J. Ding, H.-L. Lu, and D. W. Zhang, "Influence of Al Doping on the Properties of ZnO Thin Films Grown by Atomic Layer Deposition," *J. Phys. Chem. C*, vol. 115, pp. 12317–12321, 2011.

[221] J. Li, Z. Yang, Z. Chai, J. Qiu, and Z. Song, "Preparation and upconversion emission enhancement of SiO2 coated YbPO4: Er3+ inverse opals with Ag nanoparticles," *Optical Materials Express*, vol. 7, no. 10, p. 3503, 2017.

[222] A. K. Srivastava, S. Thota, and J. Kumar, "Preparation, microstructure and optical absorption behaviour of NiO thin films," *Journal of Nanoscience and Nanotechnology*, vol. 8, no. 8, pp. 4111–4115, 2008.

[223] A. Singh, S. K. Gupta, and A. Garg, "Inkjet printing of NiO films and integration as hole transporting layers in polymer solar cells," *Scientific Reports*, vol. 7, no. 1, pp. 1–12, 2017.

[224] T. Lampe, T. D. Schmidt, M. J. Jurow, P. I. Djurovich, M. E. Thompson, and W. Brütting, "Dependence of Phosphorescent Emitter Orientation on Deposition Technique in Doped Organic Films," *Chemistry of Materials*, vol. 28, no. 3, pp. 712–715, 2016.

[225] J. P. Markham, S. C. Lo, S. W. Magennis, P. L. Burn, and I. D. Samuel, "High-efficiency green phosphorescence from spin-coated single-layer dendrimer light-emitting diodes," *Applied Physics Letters*, vol. 80, no. 15, pp. 2645–2647, 2002.

[226] R. Sondergaard, M. Hösel, D. Angmo, T. T. Larsen-Olsen, and F. C. Krebs, "Roll-to-roll fabrication of polymer solar cells," *Materials Today*, vol. 15, no. 1-2, pp. 36–49, 2012.

[227] A. Sandstrom, H. F. Dam, F. C. Krebs, and L. Edman, "Ambient fabrication of flexible and large-area organic light-emitting devices using slot-die coating," *Nature Communications*, vol. 3, 2012.

[228] J. Park, J. Lee, Y. Noh, K. H. Shin, and D. Lee, "Flexible ultraviolet photodetectors with ZnO nanowire networks fabricated by large area controlled roll-to-roll processing," *Journal of Materials Chemistry C*, vol. 4, no. 34, pp. 7948–7958, 2016.

[229] L. Wengeler, B. Schmidt-Hansberg, K. Peters, P. Scharfer, and W. Schabel, "Investigations on knife and slot die coating and processing of polymer nanoparticle films for hybrid polymer solar cells," *Chemical Engineering and Processing: Process Intensification*, vol. 50, no. 5-6, pp. 478–482, 2011.

[230] H. Yang and P. Jiang, "Large-scale colloidal self-assembly by doctor blade coating," *Langmuir*, vol. 26, no. 16, pp. 13173–13182, 2010.

[231] Y. L. Ko, H. P. Tsai, K. Y. Lin, Y. C. Chen, and H. Yang, "Reusable macroporous photonic crystal-based ethanol vapor detectors by doctor blade coating," *Journal of Colloid and Interface Science*, vol. 487, pp. 360–369, 2017.

[232] P. Gao, J. He, S. Zhou, X. Yang, S. Li, J. Sheng, D. Wang, T. Yu, J. Ye, and Y. Cui, "Large-Area Nanosphere Self-Assembly by a Micro-Propulsive Injection Method for High Throughput Periodic Surface Nanotexturing," *Nano Letters*, vol. 15, no. 7, pp. 4591–4598, 2015.

[233] M. Parchine, J. McGrath, M. Bardosova, and M. E. Pemble, "Large Area 2D and 3D Colloidal Photonic Crystals Fabricated by a Roll-to-Roll Langmuir-Blodgett Method," *Langmuir*, vol. 32, no. 23, pp. 5862–5869, 2016.

[234] T. Kohoutek, M. Parchine, M. Bardosova, H. Fudouzi, and M. Pemble, "Large-area flexible colloidal photonic crystal film stickers for light trapping applications," *Optical Materials Express*, vol. 8, no. 4, p. 960, 2018.

[235] D. Ge, L. Yang, G. Wu, and S. Yang, "Spray coating of superhydrophobic and angle-independent coloured films," *Chemical Communications*, vol. 50, no. 19, pp. 2469–2472, 2014.

[236] Q. Zhao, C. E. Finlayson, D. R. Snoswell, A. Haines, C. Schäfer, P. Spahn, G. P. Hellmann, A. V. Petukhov, L. Herrmann, P. Burdet, P. A. Midgley, S. Butler, M. Mackley, Q. Guo, and J. J. Baumberg, "Large-scale ordering of nanoparticles using viscoelastic shear processing," *Nature Communications*, vol. 7, pp. 1–10, 2016.